Modeling the Active Sites of Copper Monooxygenase Enzymes

A Dissertation
SUBMITTED TO THE FACULTY OF
UNIVERSITY OF MINNESOTA
BY

Benjamin David Neisen

IN PARTIAL FULFILLMENT OF THE REQUIREMENTS
FOR THE DEGREE OF
DOCTOR OF PHILOSOPHY

William B. Tolman, Advisor

July, 2017

© Benjamin D. Neisen

Acknowledgements

It has been said that nobody achieves anything on their own. I am a firm believer that this statement is true for everything in life and it is especially true in mine. My graduate career has been a series of collaborative works both inside and outside the lab, and it is those collaborators whom I wish to thank. My friends and family have given their unrelenting support over the years and I believe this makes any of my achievements as much theirs as it is mine.

I particularly would like to acknowledge my advisor Professor William B. Tolman for letting me be a part of his lab and showing me what it means to be an independent researcher. The freedom he has given me in my projects and pursuits has made my time at Minnesota all the more rewarding. Additionally, I would like to thank Dr. Victor Young Jr. who allowed me to work alongside him as the X-ray crystallography TA and learn technical skills that greatly enhanced my research.

Moreover, I would like to thank my labmates for the years of fun we have had together. More often than not, the problems I faced in my research could be solved over a cup of coffee with Debanjan Dhar, Gereon Yee, Pavlo Solntsev, and Andrew Spaeth. I may have never enjoyed talking about chemistry more than during our morning coffee.

My final acknowledgement is to the wonderfully talented and intelligent Gabriella Perell. She has been an outstanding source of support and I am absolutely blessed to have her in my life. Her love and words of encouragement kept me going through the worst of my obstacles and I am forever grateful for all she has done.

Dedication

Dedicated to my parents, Joel and LuAnn Neisen, who have been unwavering in their love and support. I love you both and hope to make you proud.

Abstract of the Dissertation

Mechanistic investigation of copper-oxygen intermediates relevant to the oxygenation reactions of copper monooxygenase enzymes is a long-standing goal of bioinorganic chemists. To elucidate and understand the key species in copper monooxygenase pathways, small molecule synthetic chemistry has been employed to discretely generate and characterize individual species of interest. In Chapter 1, previous enzymatic and modeling work with respect to copper monooxygenase chemistry is discussed and current mechanistic proposals are explored in detail.

Chapter 2 describes modeling studies of monocopper sites and the influence of secondary sphere hydrogen bonding interactions on their redox behavior. A series of monocopper complexes with secondary sphere hydrogen bond interactions were determined to result in large increases of the electrochemical potentials of the Cu^{III}/Cu^{II} redox couple when compared to non-hydrogen bound analogs. The hydrogen bonding model systems provide evidence for the structure-function relationship of secondary coordination influences on metal-containing active sites.

Chapter 3 discusses development of a previously undescribed dinucleating macrocyclic ligand, designed to support dicopper-oxygen cores relevant to the enzyme particulate methane monooxygenase (pMMO). Attempts to generate dicopper-hydroxo type cores resulted in hydrolytic products found to be dicopper complexes that were crystallographically characterized. Observed “paddle wheel” type configurations with cis-labile coordination sites in the dicopper complexes represent a class of compounds with diverse coordination chemistry.

The final chapter (Chapter 4) describes the synthesis and characterization of a formal Cu^{III}-alkylperoxo core utilizing spectroscopic and computational methods. The Cu^{III}-alkylperoxo complex has been shown to undergo proton-coupled electron-transfer

(PCET) reactions with weak O-H bond substrates. The Cu^{III}-alkylperoxo core is considered to be a model system of a Cu^{III}-OOH core, proposed to be a possible reactive intermediate in lytic polysaccharide monooxygenase (LPMO).

Table of Contents

List of Figures

List of Schemes

List of Tables

Chapter 1

Copper Monooxygenases: Understanding their Mechanisms

1.1 Introduction

Approximately one third of all enzymes that have been discovered have been shown to utilize transition metals to perform their biological function.[1] These metalloenzymes perform a wide array of roles in nature (e.g. DNA/RNA polymerization, O_2 transport, hydrolysis, neurotransmitter regulation, reduction of radical oxygen species, etc.).[1-6] One such role that metalloenzymes have been shown to be particularly adept at is the mediation of the reduction of molecular O_2 for the subsequent oxidation of organic substrates. The redox activity of their metal-containing active site(s) is responsible for their proficiency in performing these oxidation reactions, whereby dioxygen is sequentially reduced to generate metal-bound superoxo, peroxo, hydroxo, and oxo/oxyl intermediates that are postulated to attack strong C-H bonds.[7-9] One such family of metalloenzymes that have been shown to catalyze oxidation chemistry in this manner have been classified as oxygenases. Oxygenases can be further subdivided into two classes; dioxygenases, which transfer both atoms of oxygen to substrate, and monooxygenases, which transfer only one oxygen atom while the other is lost as water.[10] The capability of oxygenases to promote thermodynamically challenging reactions in a selective and efficient manner has made them the target of intense research in the scientific community. Several well-studied examples of copper containing monooxygenases include dopamine β-monooxygenase (DβM),[11,12] peptidylglycine α-hydroxylating monooxygenase (PHM),[13,14] lytic polysaccharide monooxygenase (LPMO),[15] and particulate methane monooxygenase (pMMO).[16] These enzymes all

catalyze C-H bond activation and subsequent oxygenation of a variety of hydrocarbon substrates (Figure 1.1).

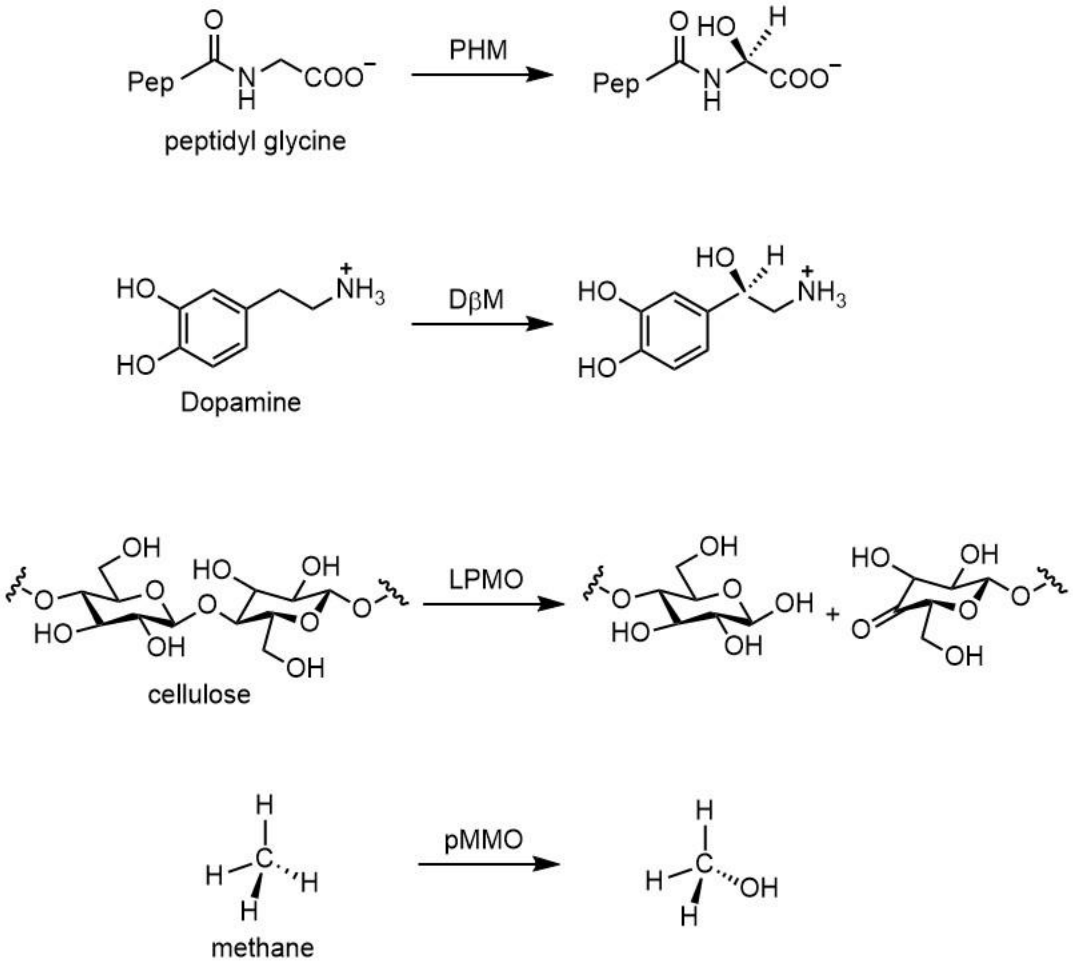

Figure 1.1. Native substrates and respective products of selected examples of copper monooxygenase enzymes.

1.2 Illustrative copper monooxygenases

Copper monooxygenases generally contain either mono- or dicopper active sites where molecular O_2 binds and oxidation of substrate takes place. In the following sections we discuss the copper-oxygen chemistry of this subset of metalloenzymes. To better understand the enzymatic function at the active site the neighboring amino acid

residues and configuration of the ligand environment about the copper center must be assessed such that trends in structure-function relationship can be ascertained.

1.2.1 Monocopper oxygenase active sites

The enzymes PHM, DβM, and LPMO all are monooxygenases that have been shown to have a single copper ion in their respective active sites. It should be noted that DβM and PHM are closely related and have nearly identical active sites. Although they are often classified as containing monocopper active sites, both enzymes have an ancillary copper site ~11 Å away from the O_2 binding copper site, across the protein interface of two protein subunits (Figure 1.2).[11,17] No bonding interactions or electronic coupling between the two copper centers has been detected by extended X-ray absorption fine structure (EXAFS) methods or by electron paramagnetic resonance (EPR) spectroscopy.[18,19] For the sake of discussion we will focus our analysis of the copper-oxygen chemistry and substrate binding at the Cu_M copper site.

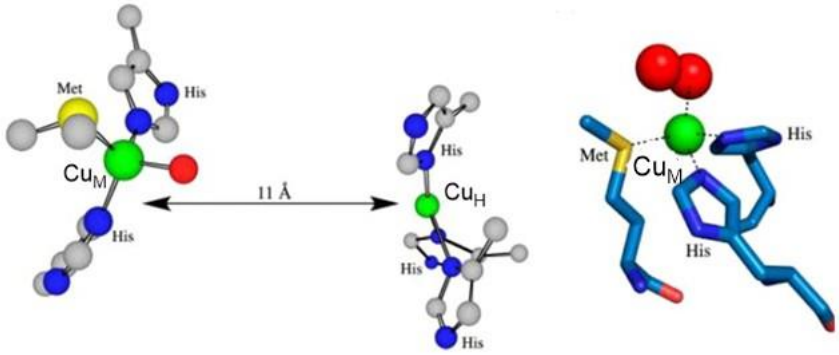

Figure 1.2. Depiction of PHM active site resting state with Cu_M and Cu_H sites (left) oxygenated Cu_M active site with bound dioxygen. Adapted from ref. 18.

The Cu_M site is shown to be coordinated by two nitrogens of nearby histidine residues as well as a sulfur from a methionine residue. This site has been shown to be responsible for O_2 binding as is evidenced crystallographically in the oxygenated form of

PHM (shown in Figure 1.2). It is believed that binding and subsequent oxygenation of peptidyl glycine and dopamine substrate occurs at the Cu_M site of both PHM and DβM, respectively.[19]

An alternative monocopper monooxygenase enzyme is LPMO, which differs from the active sites of DβM and PHM in several ways. First, the active site is found at the surface of the enzyme (Figure 1.3) as opposed to buried within the protein-protein interface of its subunits as is observed for the Cu_M sites of PHM and DβM. This active site location is rationalized by the nature of LPMO's substrates, which are large polysaccharidic chains that are incapable of diffusion to internal active sites. Secondly there are no ancillary copper sites analogous to the Cu_H sites in DβM and PHM, so no electron transfer from secondary metal sites is proposed for LPMO.

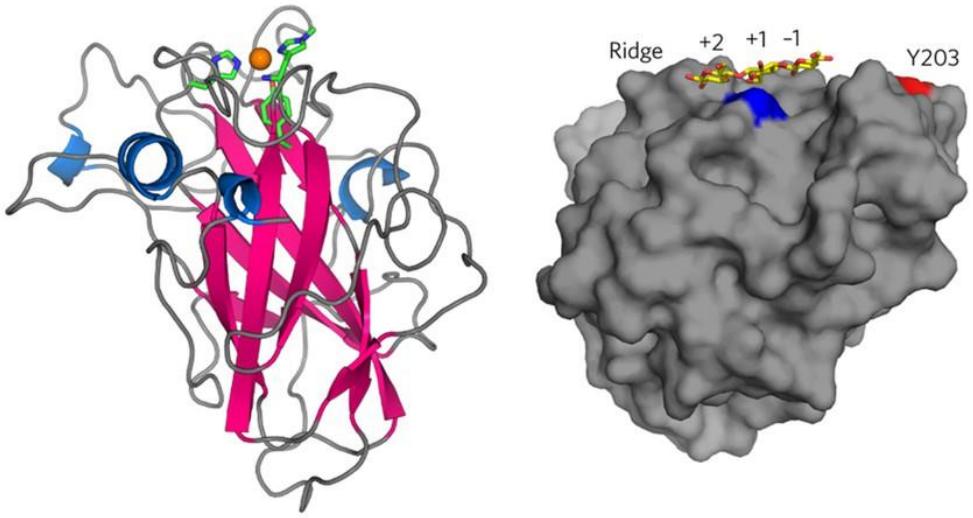

Figure 1.3. Ribbon representation of crystal structure of LPMO (left) and space filling model of LPMO crystal structure shown bound to polysaccharide substrate (right). Adapted from ref. 20.

The final major difference of LPMO from the other described monocopper sites is its unique primary coordination sphere about its copper center. The peripheral copper active site has been shown to be coordinated by two separate histidine residues. One histidine residue binds in a typical imidazole-bound fashion while the other is an N-

terminal histidine which coordinates in a bidentate mode through both its imidazole nitrogen and its amino terminus. This highly conserved bidentate binding mode of an N-terminal histidine has been dubbed the "histidine brace" motif (Figure 1.4).[21] Another interesting feature surrounding the histidine brace motif is that certain variants of LPMO exhibit methylation at one of the imidazolium nitrogens of the N-terminal residue. Additionally a nearby tyrosine is sometimes observed near the axial position of the copper although this residue is not found in all LPMO variants. The significance of the histidine brace is not fully understood but is thought to perform a crucial role in the LPMO mechanism.[20,22-24]

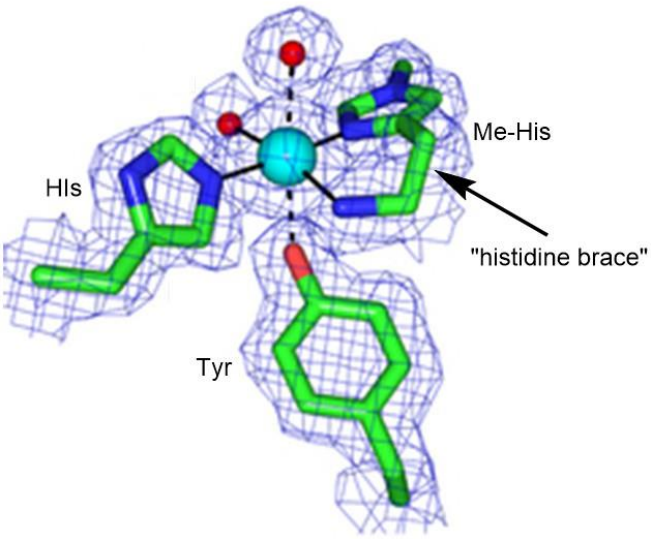

Figure 1.4. Fungal LPMO copper active site shown with histidine brace binding motif. Adapted from ref. 20.

Recent X-ray and neutron diffraction studies of the LPMO active site suggest the amino terminal residue may undergo deprotonation at physiological pH.[25] In this work isotopically labeled D_2O was used to exchange all acidic protons with deuterium in the LPMO enzyme. Crystallization of the partially deuterated enzyme followed by neutron diffraction experiments allowed visualization of the occupancy of deuterons on the amino

terminal tail (Figure 1.5). In several of the metallated active sites a monocopper core was observed coordinated to an activated dioxygen ligand in both end-on and side-on configuration which the authors assigned as a peroxo ligand based on the O-O bond distance (~1.4 Å). The authors claim that in the active sites with end-on peroxo bound ligands, the amino terminus is best modeled as a ND^- with a deuteron missing. This crystallographic work suggests that a deprotonation of the histidine brace may be mechanistically relevant.

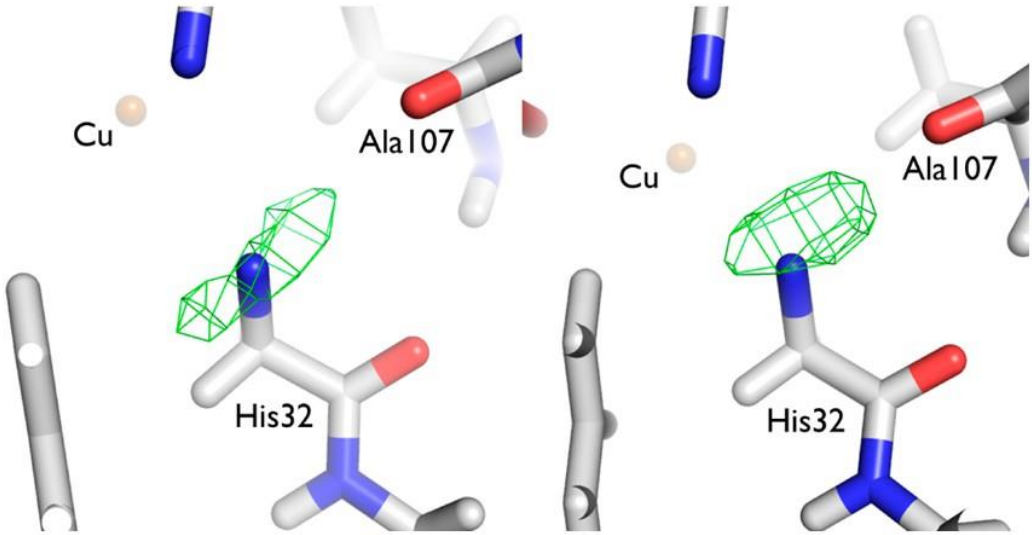

Figure 1.5. Active site of the two LPMO molecules in the asymmetric unit, showing Fo − Fc nuclear difference density (green) contoured at 3.0σ corresponding to (left) a ND_2 in molecule A and (right) a putative ND^- species in molecule B, with the deuterium pointing toward the carbonyl of Ala107. Reprinted with permission from ref. 25.

1.2.2 Mechanistic proposals for monocopper monooxygenases

All monooxygenase enzymes must first reduce dioxygen to generate reactive metal-bound oxygen intermediates. In general, initial reaction of a Cu^I center with O_2 is thought to yield a formal Cu^{II}-superoxo intermediate. The ability of Cu^I to perform one-

electron reduction of molecular O_2 to give superoxide and Cu^{II} is well-known and well-characterized.[7] Some potential mechanisms invoke the Cu^{II}-superoxo species as being responsible for hydrogen atom abstraction from substrate (Shown in Figure 1.6).[26]

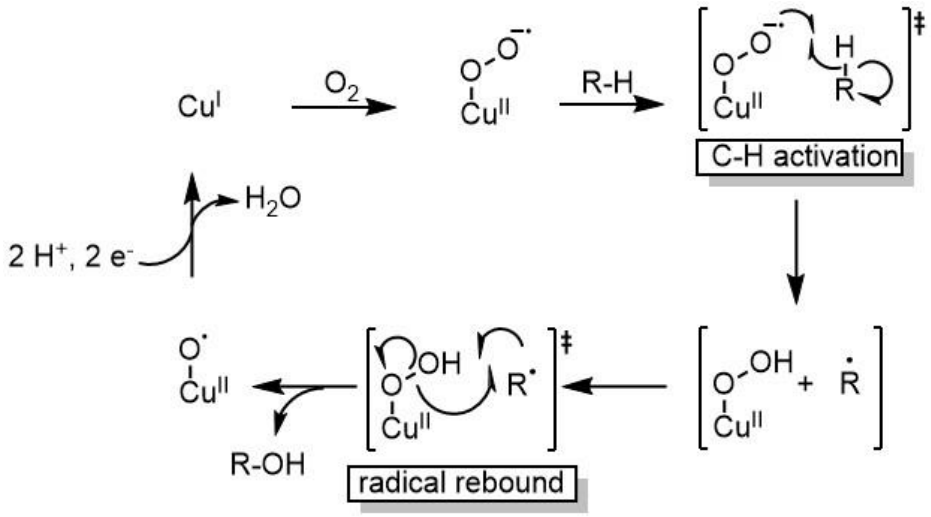

Figure 1.6. Generic mechanistic proposal for Cu^{II}-superoxo as the reactive intermediate in monocopper monooxygenases.

In the above mechanism, the initial C-H bond activation produces a Cu^{II}-OOH species and a carbon radical (R•). It has been suggested that before R• can diffuse away from the active site the Cu^{II}-OOH species, a radical rebound pathway is followed whereby homolytic cleavage of the O-O bond occurs concertedly with formation of a C-OH bond via trapping of the carbon radical.[27] After radical rebound a formally Cu^{II}-oxyl species is left, which with the addition of two protons and two electrons can be reduced back to the starting Cu^{I} core to restart the catalytic cycle.

Alternate proposals have suggested that the Cu^{II}-superoxo is not responsible for C-H bond activation and instead that a Cu^{II}-oxyl is the responsible oxidant.[28,29] This idea is supported by theoretical work arguing that oxidation by a Cu^{II}-oxyl is much more favorable than by the superoxo species. Thus, a mechanism can be proposed for a monocopper site whereby the initially formed Cu^{II}-superoxo is cleaved by two protons

and two electrons to afford the Cu^{II}-oxyl core (Figure 1.7). The Cu^{II}-oxyl can abstract an H-atom from the substrate and subsequent radical rebound by a Cu^{II}-OH intermediate generates hydroxylated product and the regenerated Cu^{I} core.

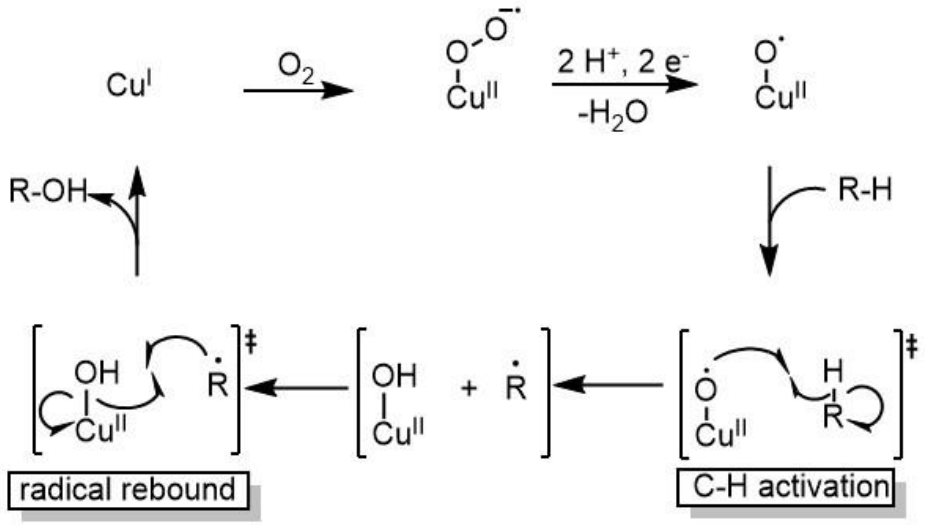

Figure 1.7. Generic mechanistic proposal for Cu^{II}-oxyl as the reactive intermediate in monocopper monooxygenases.

In PHM and DβM an alternative mechanism whereby a Cu^{II}-OOH species is the reactive copper intermediate has also been investigated.[19,30] It was suggested that C-H bond activation by this species occurs in concert with O-O bond cleavage to produce the desired hydroxylation chemistry (Figure 1.8). This type of reactivity of a Cu^{II}-OOR species has been supported both in synthetic models systems and computational models.[31,32] However, studies involving ^{18}O-labeling kinetic experiments of PHM have suggested that, although Cu^{II}-OOH may lie on the mechanistic pathway, an initial O-O bond cleavage prior to C-H bond activation to generate a Cu^{II}-oxyl is more likely.[33] Regardless of whether it is the reactive species in the monooxygenase mechanism, a Cu^{II}-OOH core can be considered as another possible intermediate along the reaction pathway.

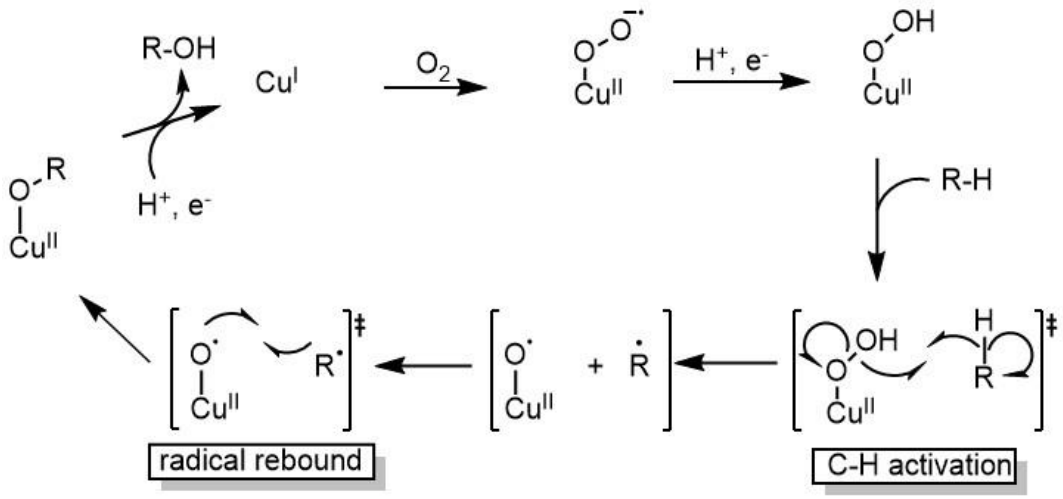

Figure 1.8. Generic mechanistic proposal for Cu^{II}-OOH as the reactive intermediate in monocopper monooxygenases.

More recent synthetic and computational works have suggested another possible copper-oxygen species for consideration in copper monooxygenase mechanisms is the Cu^{III}-OH core.[23,29,34-36] These reports suggest that the Cu^{III}-OH species is competent for performing HAT from hydrocarbon substrates. This work frames the Cu^{III}-OH as the formally protonated Cu^{II}-oxyl core. In light of the crystallographic studies on the active site of LPMO which suggest the amino terminus of the histidine brace moiety in LPMO can be deprotonated, it has been suggested that in LPMO a deprotonated NH^- terminus could stabilize a Cu^{III}-OH core and may exist as a tautomeric form of the fully protonated NH_2 terminus with a Cu^{II}-oxyl core. The mechanism for Cu^{III}-OH as the reactive intermediate in LPMO has been proposed to proceed as shown in Figure 1.9.[20,23,25] This mechanistic proposal for Cu^{III}-OH is analogous to that involving Cu^{II}-oxyl species, except tautomerization with the amino terminus (or another proton transfer pathway) occurs to give a Cu^{III}-OH unit which participates in the C-H bond activation step. Subsequent reprotonation of the NH^- tail gives a Cu^{II}-OH core that can undergo radical rebound and regeneration of Cu^{I} to complete the catalytic cycle.

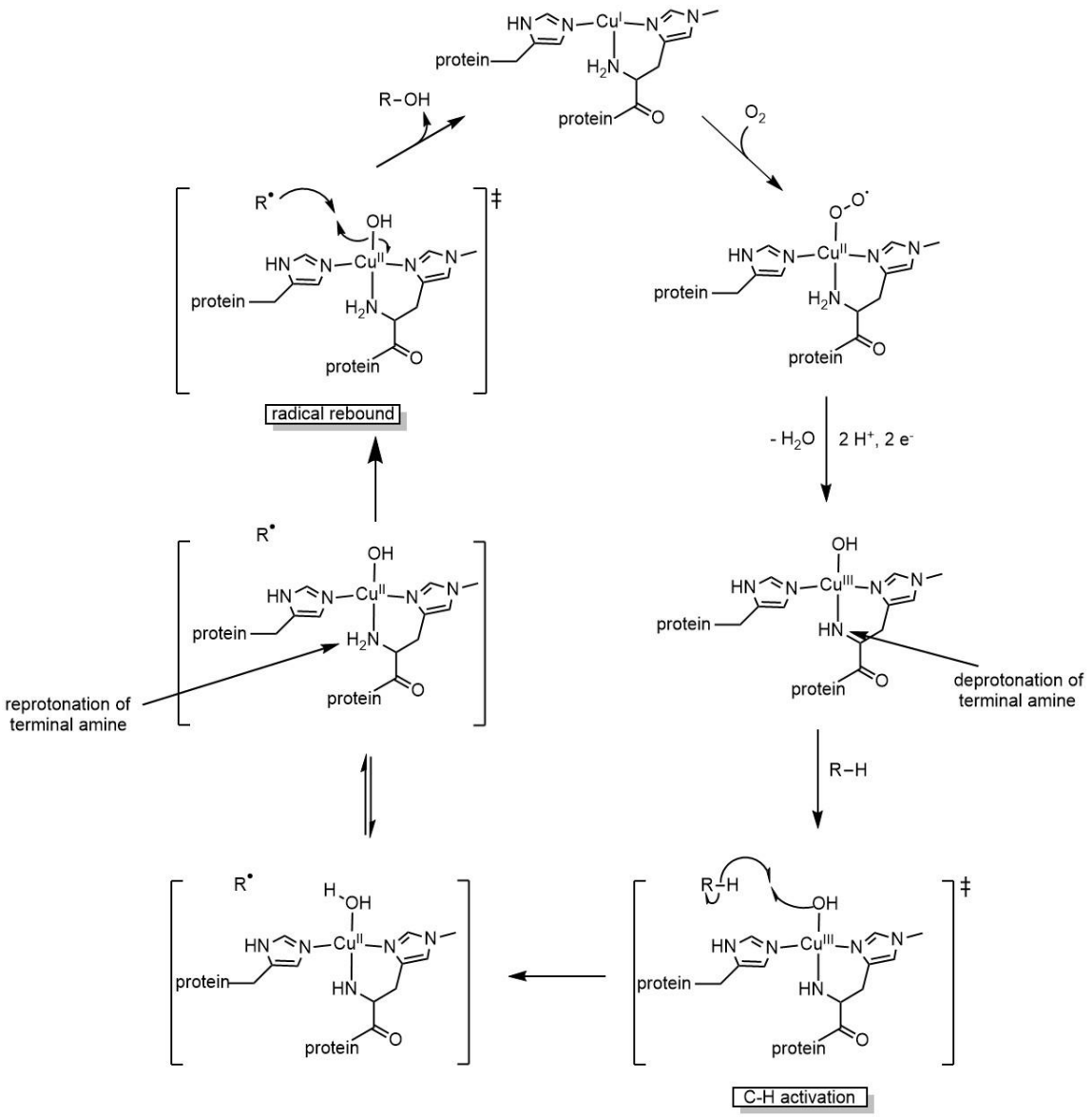

Figure 1.9. Mechanistic proposal for Cu^{III}-OH as the reactive species in LPMO active site whereby deprotonation of amino terminus stabilizes the Cu^{III}-OH core.

1.2.3 Dicopper monooxygenase active sites

Dicopper active sites have been identified for several copper monooxygenase enzymes. Two specific dicopper monooxygenases we will discuss in this section are tyrosinase and pMMO. Tyrosinase is a well-known dicopper enzyme that is implicated in the catalysis of both the hydroxylation of phenol and the conversion of catechol to

quinone. Its active site consists of two copper centers each coordinated by three imidazolium nitrogens of neighboring histidine residues (Figure 1.10). Crystallographic studies of the reduced $Cu^{I}Cu^{I}$ form of tyrosinase put the Cu-Cu distance at ~4.2 Å, where the copper centers are close enough to engage in cooperative dioxygen chemistry as opposed to the non-coupled copper centers observed for PHM and DβM.[37]

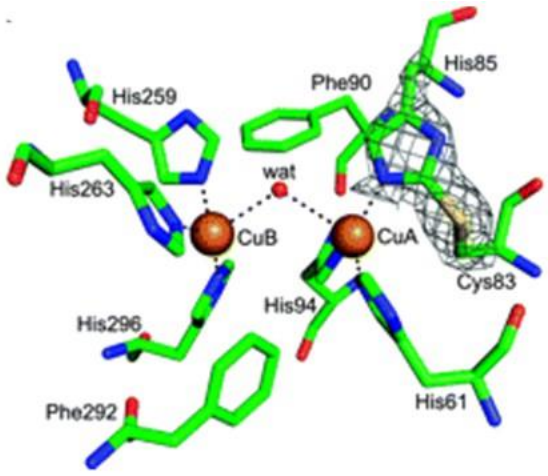

Figure 1.10. Depiction of structure of the $Cu^{I}Cu^{I}$ binuclear active site of *Agaricus bisporus* mushroom tyrosinase. Reproduced with permission from ref. 37.

The structural determination of the active site of pMMO has been a topic of intense research among biochemists. Early after the discovery of pMMO, the metal responsible for its chemistry, location of its active site, the nuclearity were all initially ambiguous.[38] Mutagenesis studies in conjunction with metal titration experiments have assigned the active site of pMMO to be located in the spmoB subunit of the enzyme (Figure 1.11).[16,39] Crystallographic work has identified a metal coordination site near the N-terminal histidine residue that can equally be modeled as a mono- or dicopper site (right side of Figure 1.10),[40] a tricopper alternative has also been suggested.[41] EXAFS studies potentially indicate a dicopper core with a Cu-Cu distance at ~2.6 Å, a full 1.6 Å shorter than that of the tyrosinase dicopper core.[42] EXAFS and EPR studies have been used to bolster the assignment of the pMMO active site as having two copper centers but

the debate of the actual nuclearity is ongoing.[43,44] It has been noted that the copper core exhibits a histidine brace motif analogous to what has been observed for the monocopper enzyme LPMO. The terminal histidine is highly conserved across pMMO variants and is proposed to play a role in its catalytic mechanism, possibly through deprotonation events as proposed for LPMO although no experimental evidence has been obtained to support this notion.

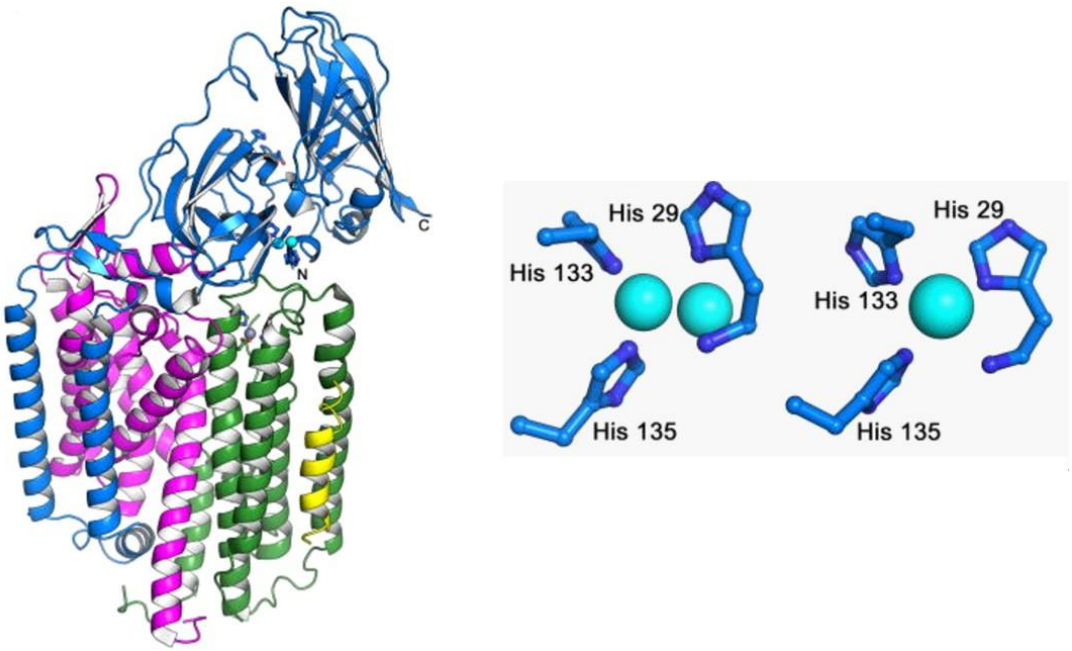

Figure 1.11. Crystal structure of trimeric pMMO enzyme with spmoB subunit shown in blue (left) and proposed copper active site with N-terminal histidine brace motif modeled as a single copper and dicopper core. Reproduced with permission from ref. 40.

1.2.4 Mechanistic proposals for dicopper monooxygenases

Dicopper activation of molecular dioxygen has been observed in both biological and synthetic systems. The reaction of molecular O_2 with two Cu^I centers is known to involve the two-electron reduction of O_2 to produce a variety of peroxo and oxo bound dicopper cores. Several cores known to be generated from this reaction include dicopper(II) peroxo species in both end-on (μ-η^1:η^2-peroxo)Cu^{II}_2 and side-on (μ-η^2:η^2-peroxo)Cu^{II}_2 geometries, as well as the high-valent bis(μ-oxo)Cu^{III}_2 core. In the case of

tyrosinase, the mechanism has been elucidated through extensive spectroscopic and crystallographic studies that have shown strong support for the possibility of the reactive intermediate to be the side-on (μ-η^2:η^2-peroxo)Cu^{II}_2 core.[45,46] A proposed mechanism accepted for a (μ-η^2:η^2-peroxo)Cu^{II}_2 reactive species in tyrosinase is shown in Figure 1.12.

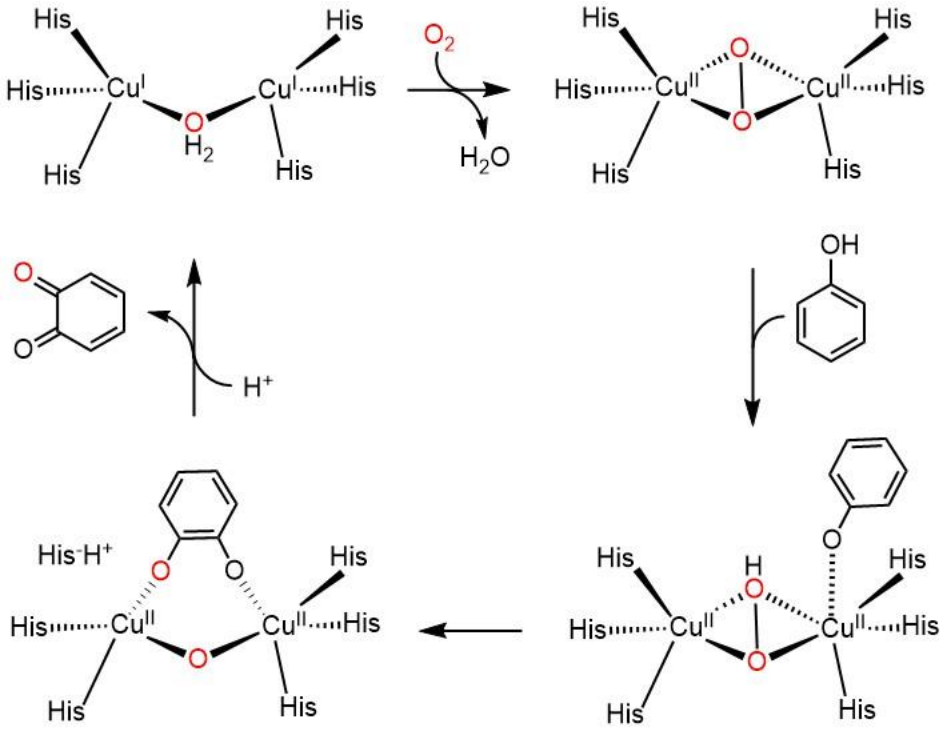

Figure 1.12. Mechanistic proposal for oxidation of phenol substrate by a (μ-η^2:η^2-peroxo)Cu^{II}_2 reactive core in tyrosinase.

In the tyrosinase mechanism shown above, a side-on peroxo bridge with two Cu^{II} ions is generated upon initial O_2 reduction by the (μ-aqua)Cu^{I}_2 core. The bridging peroxide ligand then abstracts a proton from the phenolic hydroxyl group. Subsequently, deprotonated phenoxide group then binds to the sixth coordination site of one of the copper centers. The six ligands coordinated to this copper arrange as a square bipyramidal geometry and the *ortho*- position of the bound substrate approaches the peroxo group and an oxygen atom from the peroxide is then added at the *ortho*- position.

A catecholate intermediate is formed and stabilized by spanning the two copper centers. To form the catecholate intermediate one of the histidine residues becomes unbound. This resulting intermediate can be further oxidized by the Cu^{II} centers, resulting in the formation of quinone and the regenerated (μ-aqua)Cu^{I}_2 core.

Alternate proposals have suggested that the (μ-η^2:η^2-peroxo)Cu^{II}_2 is not the reactive intermediate and instead an isomerization to the bis(μ-oxo)Cu^{III}_2 species occurs prior to initial activation of phenol.[47] The reversible isomerization of (μ-η^2:η^2-peroxo)Cu^{II}_2 to bis(μ-oxo)Cu^{III}_2 has been shown to occur in many synthetic dicopper examples (Figure 1.13).[48-50] The evidence for these mechanistic proposals is largely based on synthetic modeling experiments whereby bis(μ-oxo)Cu^{III}_2 intermediates, identified by UV-vis and resonance Raman spectroscopy, were shown to undergo aromatic substitution of phenolic substrate.[47] These proposals have been corroborated by DFT calculations[47] but evidence for a bis(μ-oxo)Cu^{III}_2 intermediate in the native tyrosinase enzyme has yet to be observed.

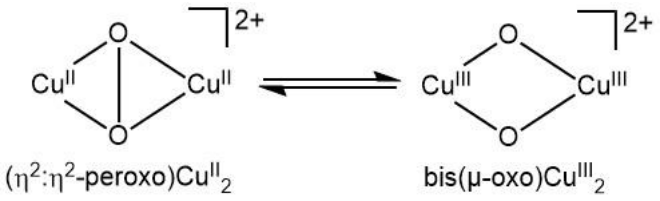

Figure 1.13. Reversible isomerization of (μ-η^2:η^2-peroxo)Cu^{II}_2 to bis(μ-oxo)Cu^{III}_2.

Much less is known about the mechanism by which methane hydroxylation occurs in pMMO, particularly because the structure of the active site is still under debate. Nonetheless, different copper species have been proposed as possible oxidants. Oxygenation experiments of the spmoB subunit using either O_2 or H_2O_2 resulted in the formation of a UV-vis feature at 345 nm which the authors attribute to be consistent with the formation of a side-on (μ-η^2:η^2-peroxo)Cu^{II}_2 complex (Figure 1.14).[40] Further

computational molecular modeling work has been performed, optimizing potential oxygenated states from the predicted resting state of pMMO.[51] This theoretical work supported the identification of the 345 nm feature as a μ-η^2:η^2 -peroxo-Cu^{II}_2 species albeit with puckering of the core.

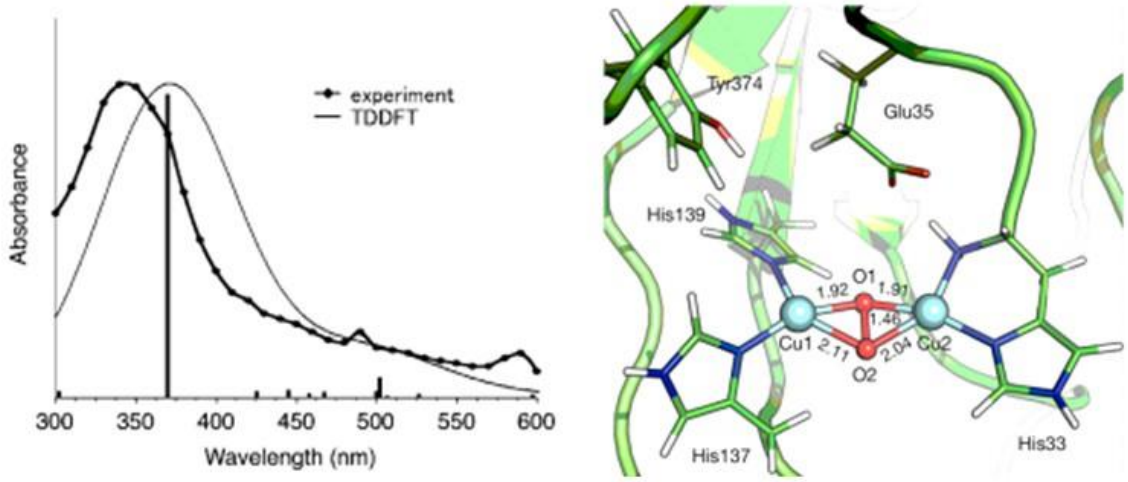

Figure 1.14 Experimental UV-vis spectrum of oxygenated spmoB subunit of pMMO and overlaid TDDFT simulate spectrum for a μ-η^1:η^2 -peroxo-Cu^{II}_2 complex (left) and TDDFT optimized μ-η^2:η^2-peroxo-Cu^{II}_2 core in pMMO active site (right). Reproduced with permission from ref. 51.

Other computational work using density functional theory (DFT) has suggested a series of possible mixed valent bis-μ(oxo)$Cu^{II}Cu^{III}$ cores with various protonation states.[52,53] These cores have been proposed based on their calculated activation energies for C-H bond activation of methane where the reaction barrier for the bis(μ-oxo)$Cu^{II}Cu^{III}$ is calculated to be 16.1 kcal/mol as opposed to 44.0 kcal/mol for the bis(μ-oxo)Cu^{III}_2 core.[52] The proposed mixed-valent reactive dicopper intermediate for pMMO is depicted in Figure 1.15.

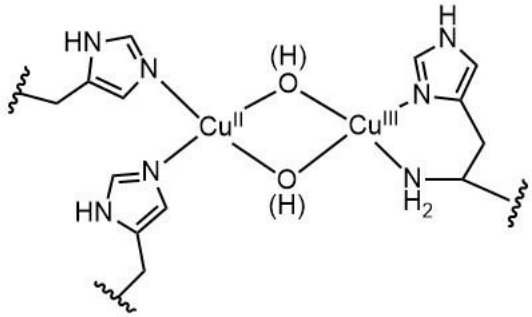

Figure 1.15. Depiction of the proposed mixed-valent bis(μ-oxo/hydroxo)$Cu^{II}Cu^{III}$ intermediate in the pMMO active site.

1.3 Modeling reactive species for copper monooxygenase chemistry

Synthetic modeling approaches to understanding copper-oxygen chemistry can provide important fundamental chemical insights into copper monooxygenase reactivity. This section discusses selected examples of synthetic attempts to model proposed reactive intermediates in copper monooxygenase chemistry. The viability of these copper-oxygen species as potential reactive intermediates is analyzed in the context of these model complexes and their observed structural, spectroscopic, and reactivity characteristics.

1.3.1 Cu^{II}-superoxo model systems

The Cu^{II}-superoxo core has many synthetic models reported in literature that have shown to exhibit both end-on (η^1) and side-on (η^2) coordination modes. Additionally, Cu^{II}-superoxo cores have also been found to lie on an electronic continuum in which certain complexes are better described as Cu^{III}-peroxo cores. This electronic continuum is evidenced by several crystallographic examples shown in Figure 1.16, where assignments for each electronic configuration on the superoxo-peroxo continuum are noted.[26,54-56] As such, both electronic states should be considered when discussing $[Cu(OO)]^+$ cores.

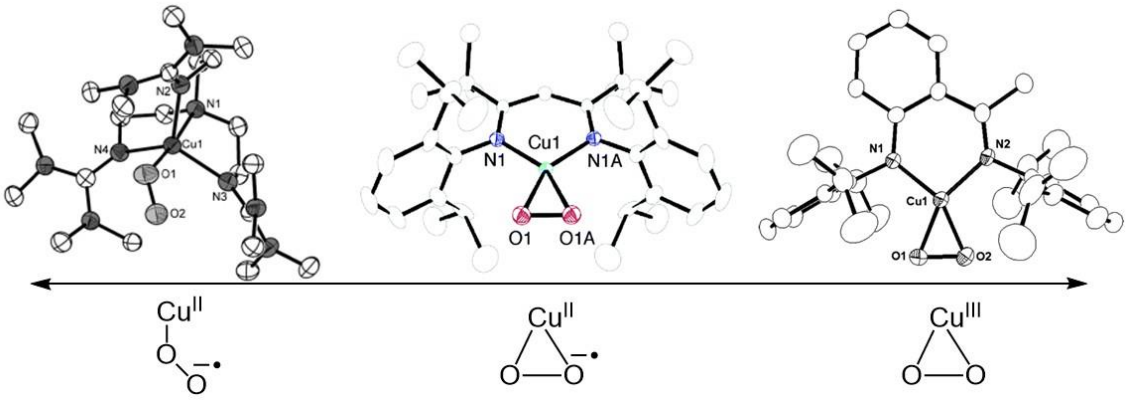

Figure 1.16. Crystal structures of $[Cu(OO)]^+$ complexes with different electronic configurations and binding modes. Reproduced with permission from refs 26, and 54-56.

Regardless of the myriad of spectroscopic and structural techniques which have elucidated the nature of $[Cu(OO)]^+$ cores in a variety of supporting ligand frameworks, $[Cu(OO)]^+$ complexes have consistently been shown to exhibit only moderate capability as PCET reagents. A literature report of a $[Cu(OO)]^+$ complex supported by a benzimidazole-based N_3S ligand boasts the activation of the strongest reported C-H bond by a $[Cu(OO)]^+$ system whereby 9,10-dihydroanthracene (DHA) with a bond strength of ~77 kcal/mol was shown to be converted to anthracene with a pseudo-first order rate constant of 0.002 s^{-1} at -60 °C (Scheme 1.1).[57] It should be noted that the BDE of 77 kcal/mol for DHA is much lower than any of the native enzymatic substrates of copper monooxygenases. Thus, whether a $[Cu(OO)]^+$ intermediate should be considered as the primary reactive species in any of the monooxygenase mechanisms is currently a point of contention.[28,29]

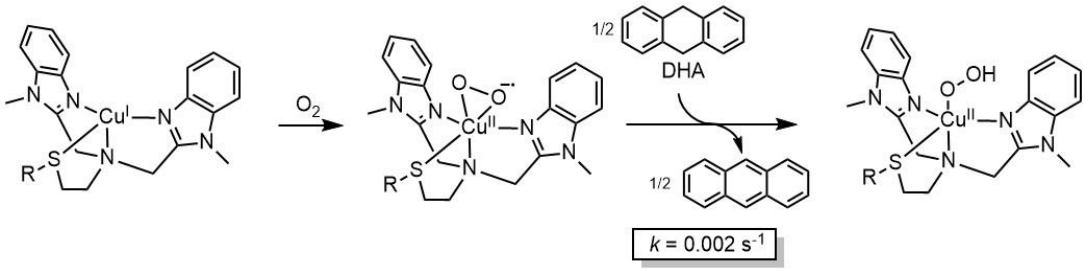

Scheme 1.1. Literature example of a Cu^{II}-superoxo complex performing PCET from DHA to give anthracene a Cu^{II}-OOH species. Adapted from reference 57.

1.3.2 Cu^{II}-oxyl characterization

The Cu^{II}-oxyl has been heavily favored as an intermediate of interest as several computational works have predicted it to be a powerful oxidant, capable of abstraction of strong C-H bonds.[28,36,58-60] Direct experimental evidence for a Cu^{II}-oxyl core has previously been reported by a mass spectrometry experiment whereby features corresponding to $[Cu(O)]^+$ cores supported by phenanthroline and bipyridine frameworks were observed in the gas phase (Figure 1.17).[59,61] Additionally, a diatomic $[Cu(O)]^+$ molecule with no supporting ligand framework was also observed in mass spectrometric analysis.[60] The Cu^{II}-oxyl core, although an attractive target remains uncharacterized outside of gas phase studies, so little experimental evidence exists with which to bolster its assignment as a reactive intermediate in copper monooxygenases.

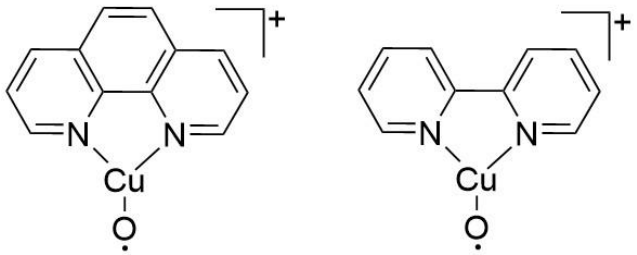

Figure 1.17. Depiction of gas phase [Cu(O)]+ complexes generated by collision induced dissociation methods (refs 59 and 61).

1.3.3 Cu^{II}-OOR model systems

Model systems of Cu^{II}-OOR (R = alkyl, H) are often not particularly stable as the O-O bond has a tendency to cleave at higher temperatures (>-40 °C). Low temperature IR and Raman studies have established the existence of such cores in a variety of complexes.[62-64] A significant difficulty associated with the study of Cu^{II}-OOR complexes is that they have been shown to be prone to decomposition whereby intramolecular hydroxylation of ligand backbones occurs.[65-67] Only two crytallographically characterized Cu^{II}-OOR complexes have been reported, a Cu^{II}-OOCm (Cm = cumyl) structure[68] and a Cu^{II}-OOH structure where the Cu^{II}-OOH is stabilized by intramolecular hydrogen bonds to the proximal oxygen (Figure 1.18).[69]

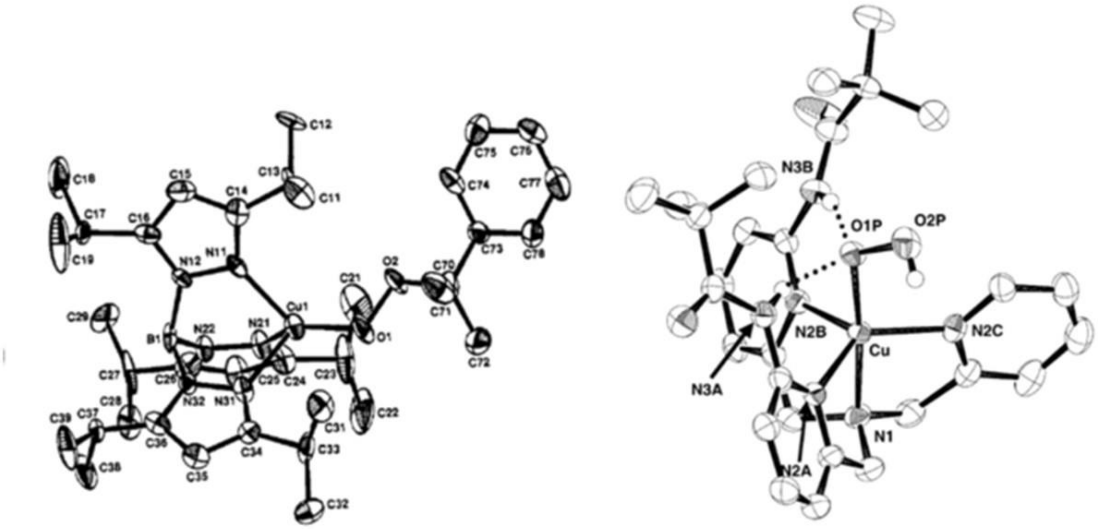

Figure 1.18. Crystal structure of a tris(pyrazole)borate supported Cu^{II}-OOCm core (left) and the crystal structure of a TPA based Cu^{II}-OOH complex with intramolecular hydrogen bonding interactions to proximal oxygen of –OOH ligand. Reproduced with permission from ref. 7.

Through reaction product analysis, it has been shown that Cu^{II}-OOR systems can attack weak C-H bonds. For example, cyclohexadiene (BDE ~ 76 kcal/mol) has been shown to be converted to benzene.[32] Notably, no synthetic examples of Cu^{II}-OOR

complexes have been shown to react with exogenous hydrocarbon substrates containing C-H bond BDE's on par with native monooxygenase substrates. Typical mechanistic proposals invoke concerted C-H bond activation with homolytic O-O bond cleavage such that oxidized products and Cu^{II}-OH complexes are obtained (Scheme 1.2). The ability of Cu^{II}-OOR to abstract C-H bonds in model systems suggests that these cores should be considered as reactive intermediates in monooxygenase mechanisms.

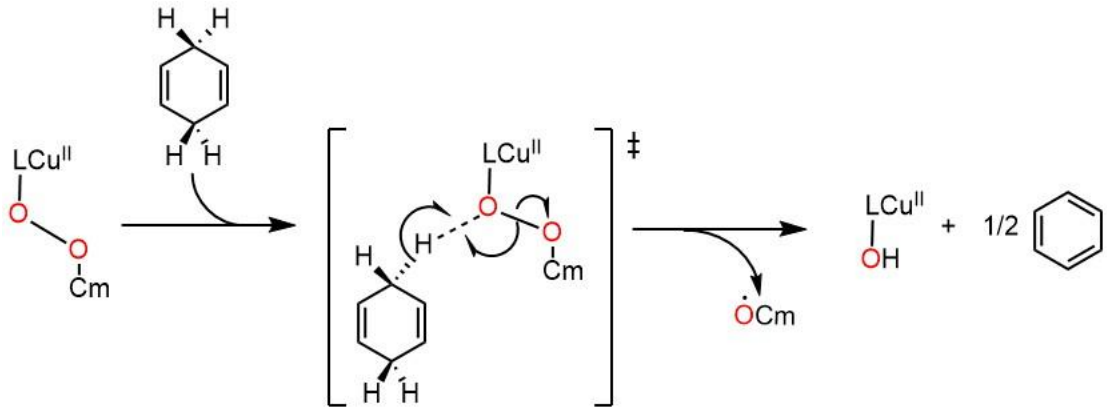

Scheme 1.2. Proposed mode of C-H bond activation of CHD for $LCu^{II}OOCm$ complexes through concerted HAT and homolytic O-O bond cleavage transition state.

1.3.4 Cu^{III}-OH model systems

Synthetic complexes containing a Cu^{III}-OH core supported by pyridine and piperdine dicarboxamido frameworks (**L1a**$^{2-}$ - **L1d**$^{2-}$) have been reported (Figure 1.19).[23,35,70] The Cu^{III}-OH is the formally protonated version of the Cu^{II}-oxyl core and as such can be thought of as a more synthetically accessible analog.

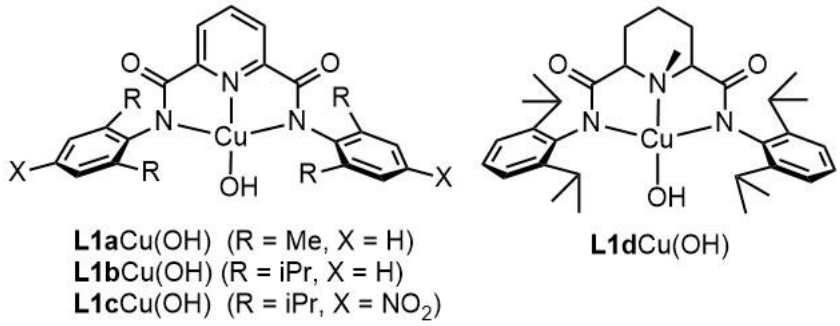

Figure 1.19. Reported Cu^{III}-OH complexes with several dicarboxamide ligand variations.

The generation of the Cu^{III}-OH complexes can be achieved by the one-electron oxidation of a Cu^{II}-OH precursor. In these model systems, C-H bond activation of common hydrocarbon substrates has been shown to be rapid. In 1,2-diflurobenzene (1,2-DFB) at -25 °C reactions of **L1b**Cu^{III}(OH) with DHA were found to have a second order rate constant of 50 $M^{-1}s^{-1}$ (Scheme 1.3). This translates to a rate five orders of magnitude faster than the fastest reported Cu^{II}-superoxo complex, albeit under slightly different experimental conditions.[23,57] The high rates of reactivity with C-H bonds are key indicators that the Cu^{III}-OH unit may be biologically relevant.

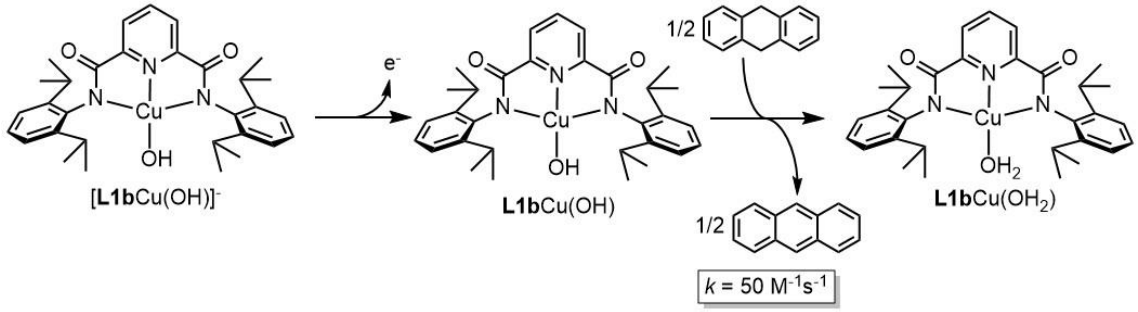

Scheme 1.3. Single electron oxidation of [**L1b**Cu^{II}(OH)]$^-$ to give the corresponding **L1b**Cu^{III}(OH) species, capable of C-H bond activation of DHA to produce anthracene and **L1b**$Cu^{II}(OH_2)$ (ref. 23).

The reactions of **L1b**Cu^{III}(OH) with hydrocabons results in the formation of a new O-H bond to give the aqua adduct **L1b**$Cu^{II}(OH_2)$. The thermodynamic parameters for this PCET process[71] were determined ($E_{1/2}$ (Cu^{III}/Cu^{II}) = -74 mV vs. Fc^+/Fc, p*K*a ~ 18.8) which led to the calculation of the BDE of the aqua adduct O-H bond to be ~90 kcal/mol (Table 1.1). This high BDE represents a strong thermodynamic driving force for the PCET reaction, which is consistent with the high observed rates of reaction with organic substrates. Perturbation of the electronic environment of the Cu^{III}-OH cores by employing the more electron deficient ligand **L1c**$^{2-}$ resulted in an increase in the BDE (~91 kcal/mol) whereas the more electron rich ligand **L1d**$^{2-}$ decreased the BDE (~88 kcal/mol). These small BDE differences were found to roughly parallel differences in rates of PCET reactions with C-H bonds.[35]

Table 1.1. Thermodynamic parameters for selected $[Cu(OH)]^{2+}$ complexes (ref. 35).

Complex	**$E_{1/2}$ (vs. Fc^+/Fc)**	**p*K*a**	**BDE (kcal/mol)**
L1b Cu(OH)	-0.074 V	18.8 ± 1.8	90 ± 3
L1c Cu(OH)	+0.124 V	16.2 ± 2.2	91 ± 3
L1d Cu(OH)	-0.260 V	20 ± 2	88 ± 3

Overall, with the clear characterization of the Cu^{III}-OH core by a variety of methods and the demonstration of its ability of it to perform PCET from relatively strong C-H bonds, the viability of the Cu^{III}-OH unit as a possible intermediate for C-H bond activation in monooxygenases has been demonstrated. In the context of LPMO, these models are particularly of interest due the amino-terminus deprotonation proposals discussed in Section 1.2.2 whereby the active the Cu^{III}-OH core is theorized to be stabilized by the monoanionic NH^- tail. Yet, the synthetic Cu^{III}-OH complexes have shown no propensity for radical rebound to generate oxygenated products. We speculate that the dianionic pyridine dicarboxamido framework does not support the Cu^I unit that

would be expected to form upon radical rebound. Moreover, no rebound mechanism has ever been suggested from a Cu^{II}-aqua species, even in biological systems. Serious consideration of the Cu^{III}-OH as a biological intermediate for hydroxylation of substrates thus demands new proposals for copper monooxygenase mechanisms.

1.3.5 (μ-η²:η²-peroxo)Cu^{II}_2 model systems

Model compounds of dicopper-oxygen cores are vast in number. It is well-described in literature that small perturbations to electronic or steric environment about the copper core can affect the formation of a particular core.[49,72,73] In the context of modeling the active site of tyrosinase, even simple monodentate ligand model systems have proven to be act as reasonable models. Substituted imidazole ligands at low temperature (-125 °C) in 2-methyl tetrahydrofuran (MeTHF) were shown to be capable of producing nearly identical UV-vis spectra to what is observed in native tyrosinase enzyme when complexed with Cu^{I} and subsequently reacted with O_2 (Figure 1.20).[74] The core was unambiguously identified as a (μ-η²:η²-peroxo)Cu^{II}_2 species in conjunction with Cu K-edge X-ray absorption spectroscopy (XAS) and EPR spectroscopy. In addition to being a structural and spectroscopic model for the tyrosinase active site, it was noted that these complexes are also functional models with reactions with exogenous phenolates occurring at reasonable rates even at low temperatures (k = 0.2–0.3 M^{-1} s^{-1}).

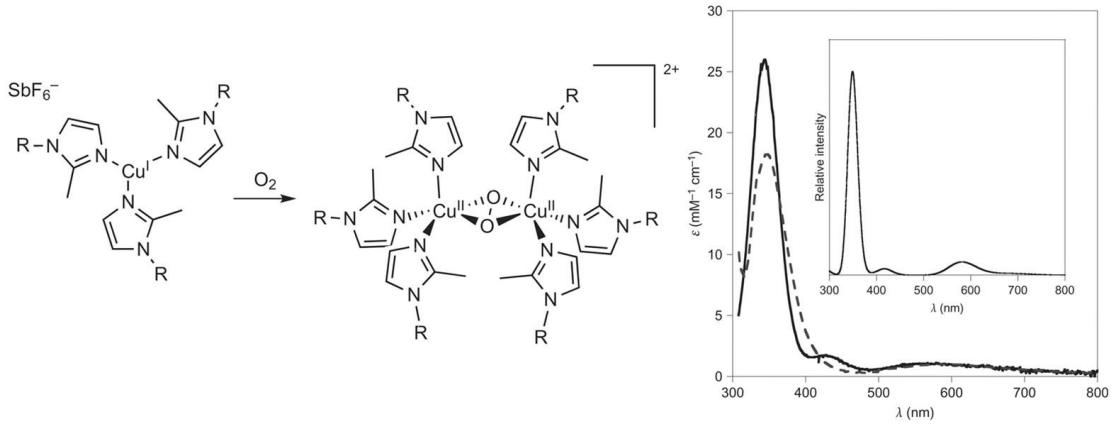

Figure 1.20. Preformed Cu^{I}(imidazole)$_3$ complex reacting with oxygen to give a μ-η2 :η2 -peroxo-Cu^{II}_2 complex (left) and overlaid UV-vis spectra of native oxy-tyrosinase enzyme and the imiadozle supported (μ-η^2:η^2-peroxo)Cu^{II}_2 complex at -125 °C in MeTHF (right). Reproduced with permission from ref. 74.

1.3.6 Bis(μ-oxo)Cu^{III}_2 model systems

Additional synthetic examples have alternatively implicated bis(μ-oxo)Cu^{III}_2 cores as possible reactive intermediates in tyrosinase and pMMO.[75-78] Complexes utilizing simple bidentate amine donors have shown to generate bis(μ-oxo)Cu^{III}_2 cores and in certain cases have been shown to be proficient at the aromatic substitution of phenolic substrates.[47] The observed reactivity with phenols suggest that the bis(μ-oxo)Cu^{III}_2 cannot be discounted as a reactive intermediate in the tyrosinase mechanism. Additionally, similar studies employing histamine ligands to reproduce "histidine-brace" type coordination geometries revealed stabilization of bis(μ-oxo)Cu^{III}_2 cores at low temperatures (-125 °C) as shown in Figure 1.21.[75,76] From this work the bis(μ-oxo)Cu^{III}_2 has been counted among the possible reactive intermediates for pMMO as well.

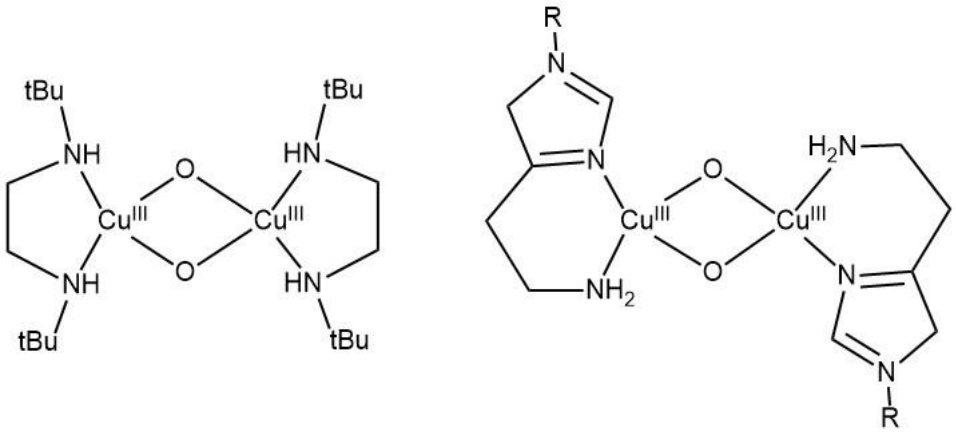

Figure 1.21. Selected examples of bis(μ-oxo)Cu^{III}_2 employing simple bidentate ligands (ref. 47,75).

1.3.7 $Cu^{II}Cu^{III}$ mixed-valent model systems

Many attempts have been made to generate model systems of the computationally proposed mixed-valent $Cu^{II}Cu^{III}$ cores for pMMO. Only two independent reports of complexes containing dicopper $Cu^{II}Cu^{III}$ cores have been published.[79,80] In one such model complex, a μ(hydroxo)Cu^{II}_2 core with a short Cu-Cu 2.66 Å distance (pMMO Cu-Cu ~2.6 Å) was generated using a tetraanionic macrocyclic supporting ligand having two pyridine dicarboxamido pockets tethered together by phenyl linkers (Scheme 1.4).[79] This complex was shown to undergo one and two-electron oxidation reactions, producing mixed valent (μ-hydroxo)$Cu^{II}Cu^{III}$ and (μ-hydroxo)Cu^{III}_2 complexes, respectively. Preliminary reactivity studies of the (μ-hydroxo)$Cu^{II}Cu^{III}$ complex with DHA showed formation of anthracene albeit at relatively slow rates (k = 0.0031 s^{-1}). This level of reactivity is a far reach from the activation of methane C-H bonds as seen in native pMMO.

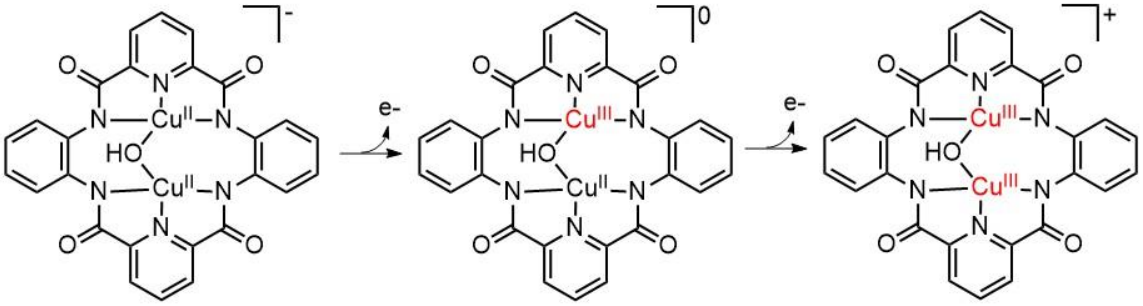

Scheme 1.4. One and two electron oxidation of μ(hydroxo)Cu^{II}_2 macrocyclic comlex to give (μ-hydroxo)$Cu^{II}Cu^{III}$ and (μ-hydroxo)Cu^{III}_2 complexes, respectively (ref. 79).

1.4 Research goals and objectives

The work described herein explores related efforts to employ ligand design to further investigate the properties of the $[Cu^{III}(OH)]^{2+}$ cores as well as other potentially biorelevant high valent units. In the next chapter, secondary coordination hydrogen-bonding effects are studied using two mononucleating macrocyclic ligands with varying intramolecular hydrogen bonding modes. The secondary coordination sphere effects are observed structurally in a crystallographic analysis of a series of pyridine dicarboxamido complexes and their effects on the electronic environment of the copper center determined by electrochemical studies of the effective Cu^{III}/Cu^{II} redox potentials. These studies are discussed in the context of metalloenzyme coordination environments and the enzymatic modulation of redox potential by secondary coordination sphere interactions.

Chapter 3 presents work done to develop a new macrocyclic ligand framework containing two pyridine dicarboxamido pockets conducive for binuclear chemistry relevant to pMMO. The ligand was designed with the intention of generating two Cu^{III}-OH units in close proximity such that C-H bond activation and radical rebound steps might become possible. We hypothesized that a single Cu^{III}-OH unit would perform PCET as has been described in previous systems while a second still near the radical

species will be able to undergo radical rebound to generate the respective hydroxylated product and a solvato copper species. In this third chapter, we describe the synthesis of this new ligand framework and the crystallographic analysis of several new dicopper compounds supported by this tetraanionic framework.

Finally, in Chapter 4 work towards generation of a new $[Cu(OOR)]^{2+}$ core (R = alkyl) is discussed. In this work two novel high-valent Cu-alkylperoxo cores are characterized and their spectroscopic properties assessed by a variety of techniques. Propensities of these $[Cu(OOR)]^{2+}$ cores to undergo PCET reactions towards C-H and O-H bond substrates is also assessed and discussed in the context of the analogous $[Cu(OH)]^{2+}$ complexes. Possible implications for a proton transfer from the amino-terminus to a Cu^{II}-superoxo intermediate to generate a formally Cu^{III}-OOH species as a reactive intermediate in LPMO are proposed, analogous to what has been proposed for a Cu^{III}-OH mechanism previously.

Chapter 2

Unique Coordination Chemistry of Novel Monocopper Macrocyclic Complexes and the Effects of Secondary Sphere Hydrogen Bonding on Redox Behavior[a]

[a]The results presented in this chapter were previously published in:

Benjamin D. Neisen, Pavlo Solntsev, Mohammad R. Halvagar, and William B. Tolman Secondary Sphere Hydrogen Bonding in Monocopper Complexes of Potentially Dinucleating Bis(carboxamide) Ligand. *Eur. J. Inorg. Chem.* **2015**, 36, 5856–5863.

2.1 Introduction

By understanding the properties and reactivity of copper-oxygen intermediates implicated in reactions of metalloenzymes and other catalysts, progress toward the development of new oxidation processes may be achieved.[81] Motivated by intriguing proposals for such intermediates, including $[CuO]^{+}$ species in enzymes such as peptidylglycine monooxygenase,[82] dopamine β-monooxygenase (DBM),[58] and lytic polysaccharide monooxygenase (LPMO)[24,28] and $[CuOCu]^{n+}$ (n = 2–4) species in particulate methane monooxygenase (pMMO)[52,53] and heterogeneous Cu-doped zeolites,[83] we and others have targeted for synthesis and detailed study reactive mono- and dicopper complexes containing these and related cores.[84,] In previous work,[23,34,35,79,85] the novel compounds [**L1a**Cu(OH)], [**L1b**Cu(OH)] and [**L2**Cu_2(OH)] were successfully prepared and proposed to contain Cu^{III}-OH^{+} and $[Cu^{II/III}(OH)Cu^{III}]^{4+/5+}$ moieties (Figure 2.1). The powerful electron donating ability of the ligand carboxamido donors was critical for stabilizing the reactive oxidized cores of these complexes.

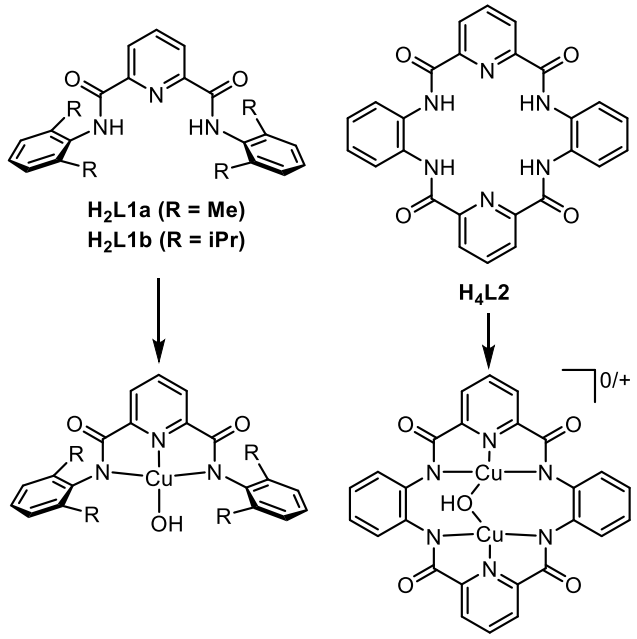

Figure 2.1. Ligands and complexes of previously described pyridine dicarboxamido systems and the oxidized copper-hydroxo cores that they support.

Concerned about the potential redox noninnocence of the *ortho*-phenylenediamine linkers in **L2**, and with the aim of further enhancing the carboxamido electron donating properties and thus further stabilizing oxidized copper species to enable more complete characterization, we turned to the analogous ligands $\mathbf{L3^{4-}}$[86] comprising simple ethylene linkers. This chapter describes how efforts to isolate dicopper complexes of $\mathbf{L3^{4-}}$ have failed, leading instead to the discovery of a new class of monocopper complexes that feature hydrogen bonding from the free carboxamide N-H groups in the doubly protonated form of the ligand ($\mathbf{H_2L3^{2-}}$) to the fourth ligand coordinated to the Cu^{II} ion (Scheme 2.1).

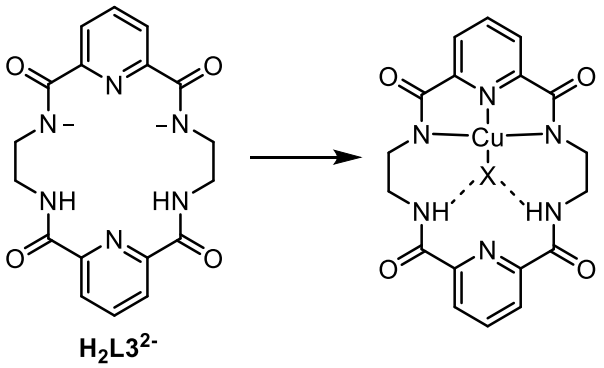

H_2L3^{2-}

Scheme 2.1. Generic depiction of H_2L3^{2-} and its copper bound complexes with intramolecular hydrogen bonding.

Such interactions model secondary sphere hydrogen bonding in important metalloenzyme active sites.[6,87,88] It is understood that hydrogen bond donating and accepting residues in the second coordination sphere of enzyme active sites have an effect on the redox potential of the metal center. In previously reported enzymatic studies the direction and magnitude of a shift in potential is not always obvious, with reports of second-sphere residues both raising and lowering the redox potential. For instance, in Fe Superoxide Dismutase (SOD), a glutamine residue (Q69) acting as a hydrogen bond donor to the inner sphere of the iron has been implicated in lowering the potential by −220 mV.[88] Conversely, increasing H-bond donation in the Fe-S protein rubredoxin has been shown to modulate the potential up to +126 mV.[87] A number of studies aimed at understanding how such hydrogen bonding influences metal complex reactivity and redox properties have also been published.[89-92]

In model complex work there is a much more obvious trend of second-sphere H-bonding interactions raising the redox potential of the metal as compared to the analogous complex with little to no second sphere interactions. Particularly relevant in the present context is recent work in which hydrogen bonding groups were introduced as unconstrained appendages in bis(carboxamido)pyridine ligands to evaluate their effects

on redox potentials and/or catalytic activity of Cu^{II} complexes.[93] The work in this chapter encompasses the evaluation of the structures of a series of monocopper complexes of $\mathbf{H_2L3^{2-}}$ and the new purposefully mononucleating ligands $\mathbf{H_2L4a^{2-}}$ and $\mathbf{H_2L4b^{2-}}$ in which the carboxamide N-H groups are held in place by the macrocycle (Figure 2.2). Different secondary sphere interactions were observed, and their role in influencing the redox properties of a subset of the compounds prepared was examined.

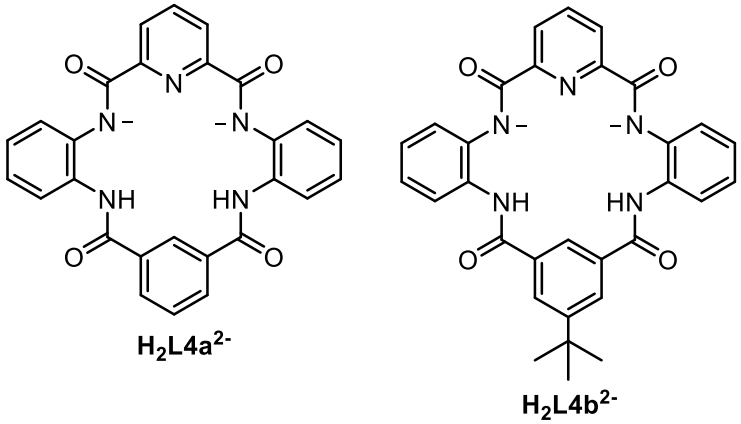

Figure 2.2. Purposefully mononucleating macrocyclic ligand $\mathbf{H_2L4a^{2-}}$ and $\mathbf{H_2L4b^{2-}}$.

2.2 Synthesis and characterization of ligands

2.2.1 Synthesis of macrocyclic proligand H_4L3

The ligand precursor **H_4L3** was prepared using a modified version of a published method (Scheme 2.2).[86] A mixture of 2,6-pyridine dicarboxylic acid and ethylene diamine was reacted in the presence of triphenyl phosphite and pyridine at 100 °C to afford target macrocycle **H_4L3** (9.04 g, 40%). Triphenyl phosphite and pyridine are used to generate the N-phosphonium salt in-situ which creates a good leaving group to afford carboxamides when reacted with primary amines (Scheme 2.3).[94] The condensation to give the pyridine carboxamide macrocycle **H_4L3** is thought proceed through this mechanism.

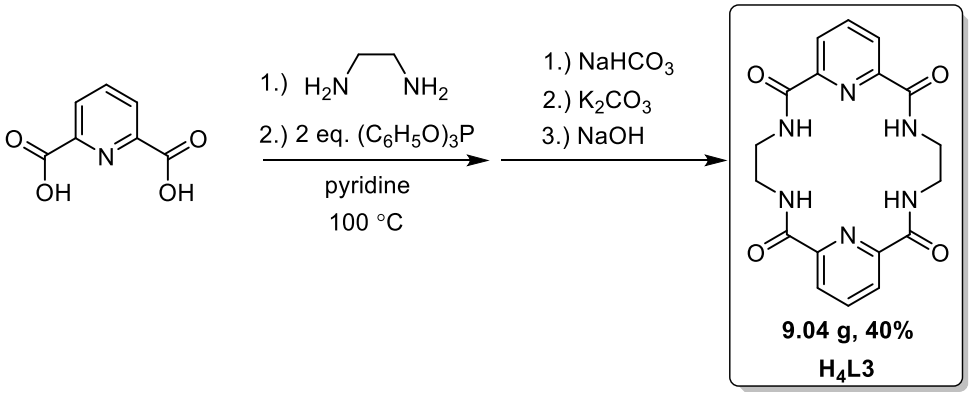

Scheme 2.2. Synthetic route of proligand **H4L3.**

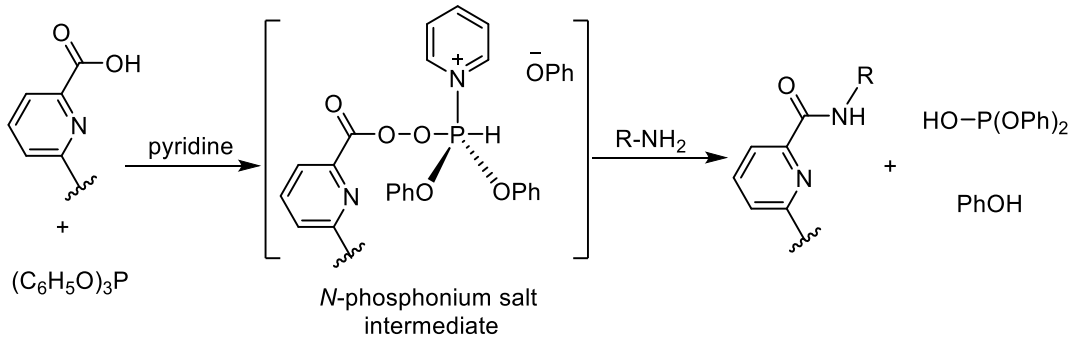

Scheme 2.3. Synthetic route to form carboxamide from carboxylic acid group, pyridine and triphenyl phosphite.

Characterization of **H4L3** by ^{1}H nuclear magnetic resonance (NMR) spectroscopy displays an expected singlet at 9.45 ppm consistent with four carboxamide protons (Figure 2.3) as well as features in the aromatic region (8.14 – 8.21 ppm) consistent with six pyridyl protons. In the alkyl region we observe a singlet at 3.60 ppm that can be assigned as eight equivalent ethylene protons of the linker groups. Additionally, elemental analysis of the product supports the assignment of this compound as **H4L3**.

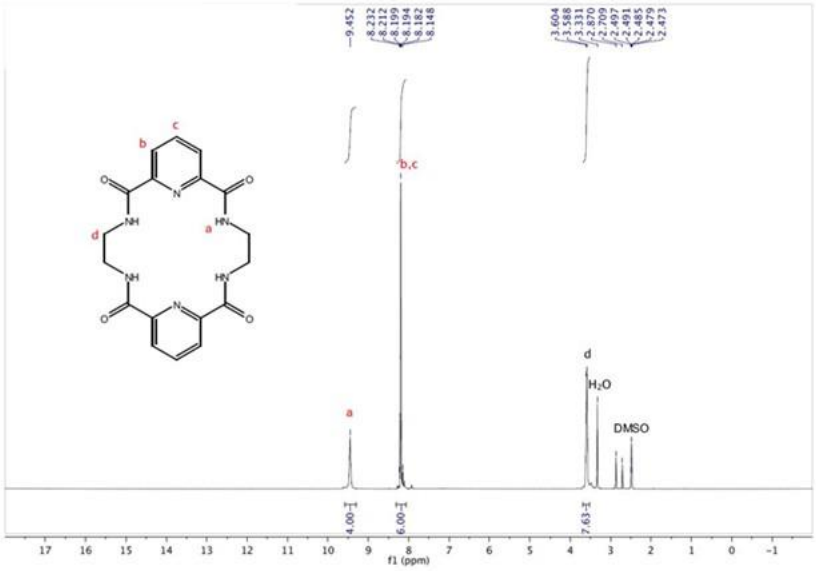

Figure 2.3. ^{1}H NMR spectrum (300 MHz) of **H_4L3** taken in DMSO-*d6*.

2.2.2 Synthesis of macrocyclic proligands H_4L4a and H_4L4b

The synthesis of the macrocyclic precursors **H_4L4a** and **H_4L4b** involved use of procedures modified from previously reported work (Scheme 2.4).[95] Unlike the synthesis of **H_4L3**, the synthesis of both macrocycles requires initial formation of a hemicycle precursor (*N2,N6*-bis(2-aminophenyl)pyridine-2,6-dicarboxamide). An initial Boc protection reaction of commercially available 1,2-phenylene diamine yields *N*-Boc-phenylene diamine (21.9 g, 70.4%). The protected product is then allowed to react with 2,6 pyridine dicarbonyl dichloride to afford the protected condensation product which can be subsequently deprotected using trifluoroacetic acid to give the free *N2,N6*-bis(2-aminophenyl)pyridine-2,6-dicarboxamide (8.68 g, 80%) (Scheme 2.4).

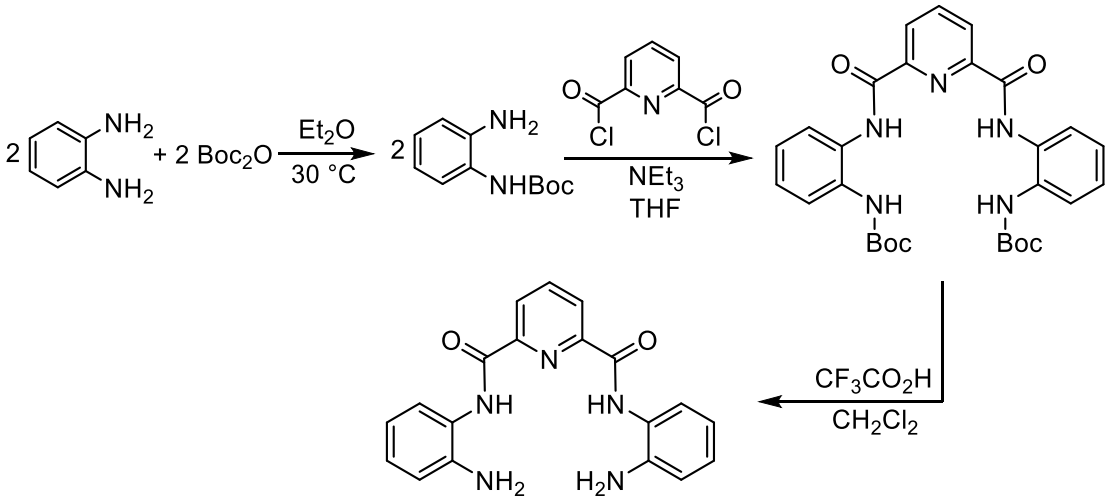

Scheme 2.4. Synthesis of hemicyclic precursor *N2*,*N6*-bis(2-aminophenyl)pyridine-2,6-dicarboxamide.

With the hemicycle precursor in hand, a final condensation step using either isopthalyl dichloride for **H4L4a** or 5-*tert*-butyl-isopthalyl dichloride for **H₄L4b** was performed similarly to the condensation reaction of *N*-Boc-phenylene diamine with 2,6-pyridinedicarbonyl dichloride in the second step of scheme 2.4. It was observed, however, that this final step required refluxing temperatures in THF in order to obtain product in appreciable yields. After recrystallization, crystalline samples of both **H₄L4a** (0.94 g, 68%) and **H₄Lb** (1.85 g, 60%) were obtained (Scheme 2.5).

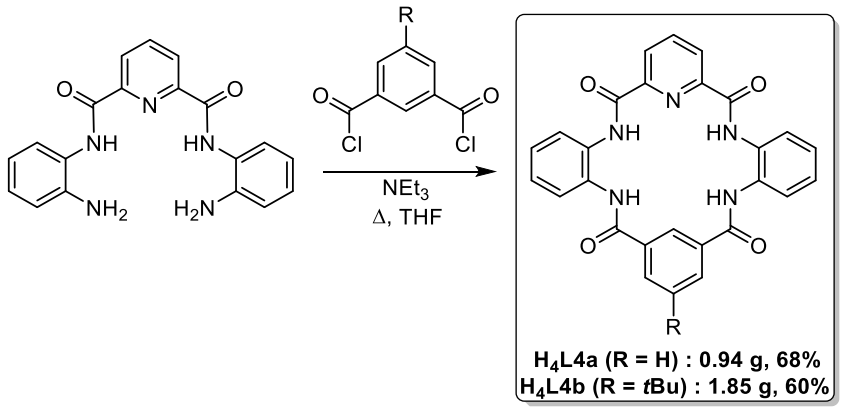

Scheme 2.5. Synthesis of proligands **H₄L4a** and **H₄L4b.**

Characterization of **H$_4$La** and **H$_4$Lb** by ^{1}H NMR spectroscopy reveals two sets of carboxamide protons, consistent with a macrocycle with a pyridine dicarboxamide pocket and a benzene dicarboxamide pocket (Figure 2.4-2.5). In both macrocycles eleven aromatic protons corresponding to the phenylene linkers and six pyridyl protons were observed in the aromatic region of the NMR spectrum (7.3 – 8.5 ppm). The phenyl group opposite the pyridine ring shows three protons in the aromatic region for **H$_4$La** and two protons for **H$_4$Lb**. A singlet at ~10.2 ppm was assigned as the proton *ortho*- to both carboxamide groups on the phenyl pocket of the macrocycle. The large downfield shift of this aromatic proton is consistent with a phenyl proton flanked by two carboxamide groups based on other literature examples of similar compounds.[126] Additionally, the ^{1}H NMR spectrum of **H$_4$Lb** exhibits a feature (~1.34 ppm) in the alkyl region consistent with the nine protons of the appended *tert*-butyl group. Elemental analysis of the isolated products further support the assignment as **H$_4$L4a** and **H$_4$L4b**.

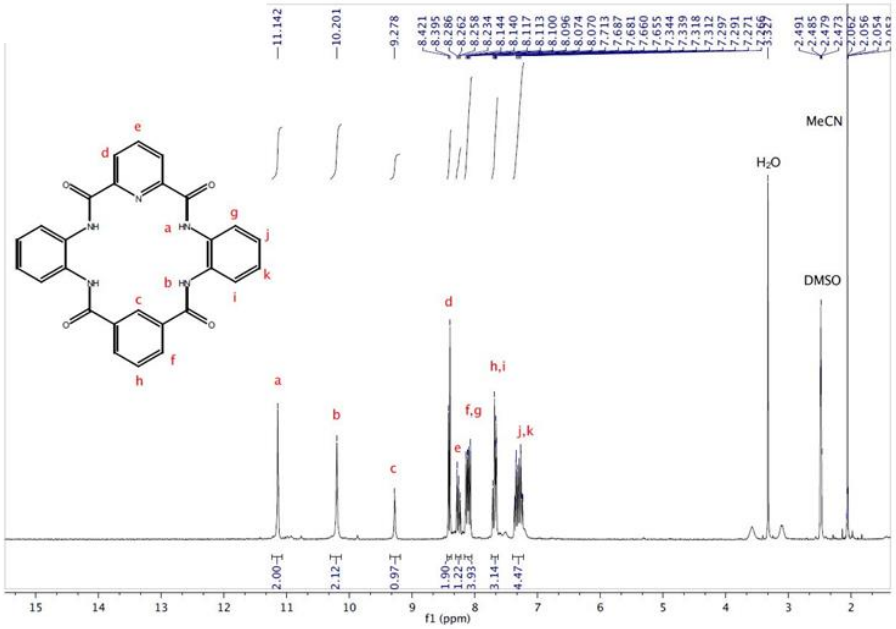

Figure 2.4. ^{1}H NMR spectrum (300 MHz) of **H$_4$L4a** in DMSO-d_6.

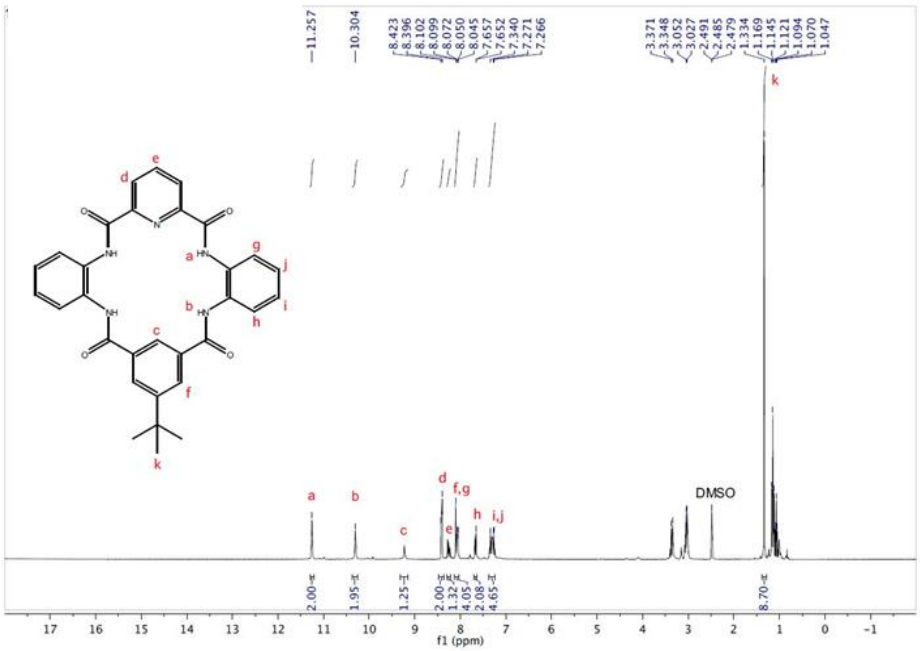

Figure 2.5. ^{1}H NMR spectrum (300 MHz) of **H_4L4b** in DMSO-d_6.

2.3 Synthesis and spectroscopic characterization of macrocyclic Cu^{II} complexes

2.3.1 H_2L3^{4-} Monocopper Complexes

After initial attempts to generate dicopper complexes of **$L3^{4-}$** by treating **H_4L3** with excess base in the presence of copper(II) salts (≥2 equiv) only yielded monocopper complexes **1–3**, a more purposeful synthesis was developed. Metallation of **H_2L3^{2-}** to generate monocopper compounds [NMe_4][**H_2L3**Cu(Cl)] ([NMe_4][**1**]) and [NMe_4][**H_2L3**Cu(OAc)] ([NMe_4][**2**]) were performed using similar procedures, wherein the ligand was dissolved in a degassed water/pyridine mixture and different copper salts were introduced to give corresponding copper species of interest. It was observed that in the cases where chloride or acetate copper(II) salts were employed, [NMe_4][**1**] (0.236 g, 58%) and [NMe_4][**2**] (0.187 g, 42%) were generated, respectively (Scheme 2.6). Conversely, when copper(II)trifluoromethanesulfonate ($Cu(OTf)_2$) was used as the metal source, formation of a monocopper hydroxide complex was observed,

[NMe_4][**H_2L3**Cu(OH)] ([NMe_4][**3**]) (53 mg, 12%). The poor coordination of triflato-anions to the copper center explains why a hydroxide ligand coordinates in the fourth coordination site of copper, unlike in the anionic complexes **1** and **2**.

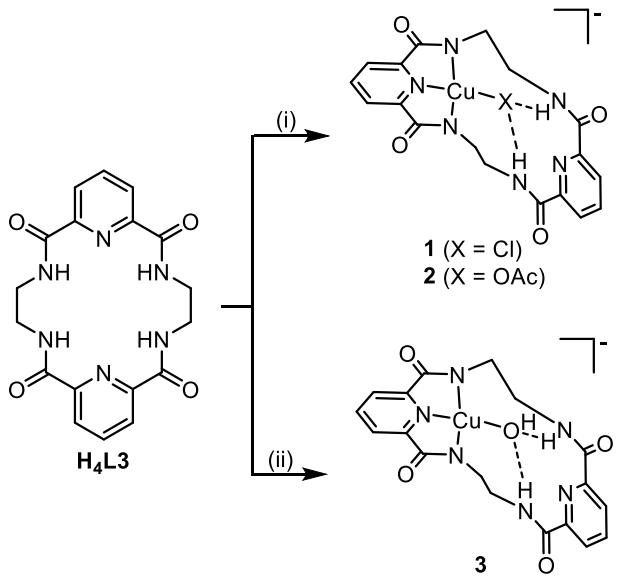

Scheme 2.6. Synthetic preparation of complexes **1**, **2**, and **3** (i) NMe_4OH (2 eq.), CuX_2 (X = Cl, OAc), (ii). NMe_4OH (3 eq.), $Cu(OTf)_2$.

The mononucleated complexes of $\mathbf{H_2L3^{2-}}$ were characterized in solution by electron paramagnetic resonance (EPR) spectroscopy (**1 – 3**) (Figure 2.6-2.8) as well as negative mode high resolution electrospray ionization mass spectrometry (HR-ESI-MS, **1** and **2**) (Figure 2.6-2.7). The axial and pseudo-axial spectra observed in the EPR spectra of **1-3** are consistent with monocopper(II) $S = 1/2$ complexes coordinated in square planar geometry. The EPR parameters were extracted from simulations of the experimental spectra (Table 2.1). Notably, the EPR parameters for **3** differ from those of [**L1b**Cu(OH)]$^-$ previously reported, suggesting perturbations to the electronic environment of the Cu^{II} center.

Negative mode HR-ESI-MS allowed identification of features that could be simulated with expected molecular formulae of anions **1** and **2**. The simulation of the

isotopic patterns confirm that the parent peaks are monocopper complexes of the doubly deprotonated ligand $\mathbf{H_2L3^{2-}}$ with respective chlorido and acetato ligands. The assignment of mononucleated species is in agreement with the EPR spectra of **1** and **2** species in solution where no evidence of a $\mathbf{L3^{4-}}$ dicopper species is observed.

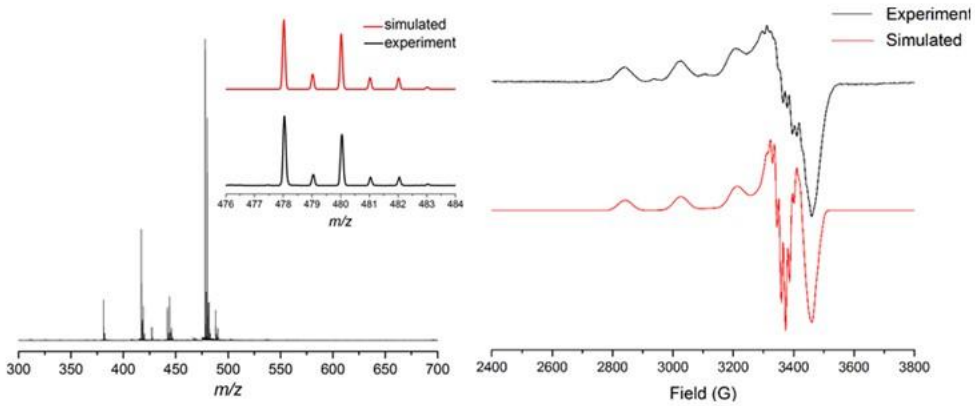

Figure 2.6. For [NMe_4][$\mathbf{H_2L3}$Cu(Cl))] ([NMe_4][**1**]): (left) negative ion mode HR-ESI-MS with the inset showing the experimental (bottom, black) and simulated (top, red) peak envelope for the ion [$\mathbf{H_2L3}$Cu(Cl)]$^-$ (right) experimental (top, black) and simulated (bottom, red). EPR spectrum (X-band, 30K). EPR parameters are listed in Table 2.1.

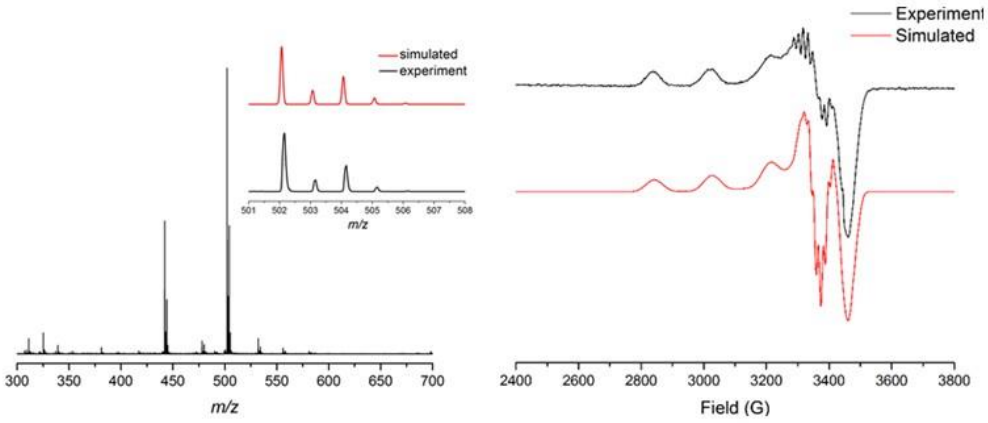

Figure 2.7. For [NMe_4][$\mathbf{H_2L3}$Cu(OAc)] ([NMe_4][**2**]): (left) negative ion mode HR-ESI-MS with the inset showing the experimental (bottom, black) and simulated (top, red) peak envelope for the ion [$\mathbf{H_2L4}$Cu(OAc)]$^-$. (right) experimental (top, black) and simulated (bottom, red). EPR spectrum (X-band, 30K). EPR parameters are listed in Table 2.1.

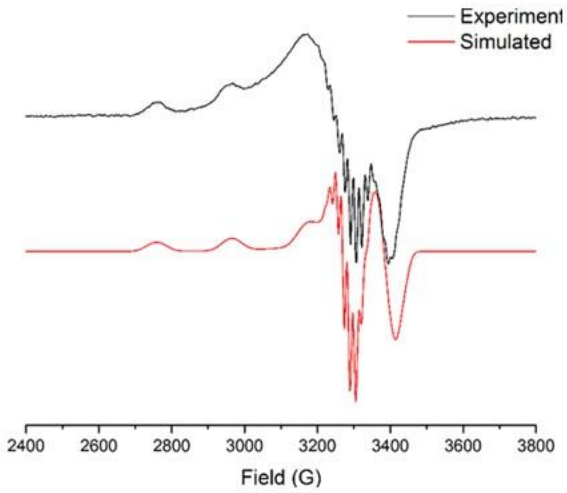

Figure 2.8. For [NMe_4][**H_2L3**Cu(OH)] ([NMe_4][**3**]): experimental (top, black) and simulated (bottom, red) EPR spectrum (X-band, 30K). EPR parameters are listed in Table 2.1.

Table 2.1. EPR Parameters Derived from Simulations of Experimental X-Band Spectra[a]

Compound	g_x	g_y	g_z	A // (Cu)	$A(N_{am})$	$A(N_{Py})$
[NBu_4][**L1b**Cu(OH)]	2.032	2.055	2.185	196	17.7	13.4
[NMe_4][**H_2L**4Cu(Cl)] (**1**)	2.05	2.06	2.21	190	14	14
[NMe_4][**H_2L4**Cu(OAc)] (**2**)	2.05	2.07	2.21	200	17	17
[NMe_4][**H_2L4**Cu(OH)] (**3**)	2.05	2.05	2.187	210	15	15
[NMe_4][**H_2L4a**Cu(OAc)] (**8**, R = H)	2.05	2.06	2.21	190	15	15
[NMe_4][**H_2L4b**Cu(Cl)] (**9,** R = *t*Bu)	2.05	2.05	2.21	185	16	16

[a] Measured in DMF at 30K. Units of A are in 10^{-4} cm^{-1}.

X-ray crystallographic determination of anionic species **1-3** revealed interesting structural characteristics. The chlorido (**1**), acetato (**2**), and hydroxido (**3**) ligands are all engaged in intramolecular hydrogen bonding to the two carboxamide N-H groups (Figure 2.9). This hydrogen bond interaction was indicated by the NH···X and N···X (X = Cl, OAc, OH) distances which are all well within range of standard hydrogen bond distances (Table 2.2).[96] Classically, hydrogen bond donor-acceptor distances of 2.2 – 2.5 Å are considered "strong, mostly covalent", distances ranging from 2.5 – 3.2 Å are considered "moderate, mostly electrostatic", and distances of 3.2 – 4.0 Å are considered "weak,

electrostatic."[96] For example, **2** is considered to have a moderate hydrogen bond interaction with distances of O1···H4 = 2.202 Å, O1···H6 = 2.197 Å, O1···N4 = 3.003(2) Å, and O1···N6 = 3.002(2) Å.

Focusing on the primary coordination sphere of the copper(II) center, comparable parameters are observed with respect to related complexes reported previously for copper(II) complexes of other carboxamido complexes.[13] There is a slight elongation of the Cu-X (X = OH, Cl) distance in **1** and **3** compared to analogous systems without hydrogen bonding, as in the case for [**L1b**Cu(OH)]$^-$ vs. **3** where the Cu-OH distances are 1.863 Å and 1.884 Å respectively.[8] The elongation of the Cu-X distances aside, the geometry about the copper(II) center is nearly identical to the non-hydrogen bonded systems. HR-ESI-MS and EPR spectroscopy of **1-3** appear to be in agreement with the solid-state structures observed by crystallography suggesting the species are conserved in solution state.

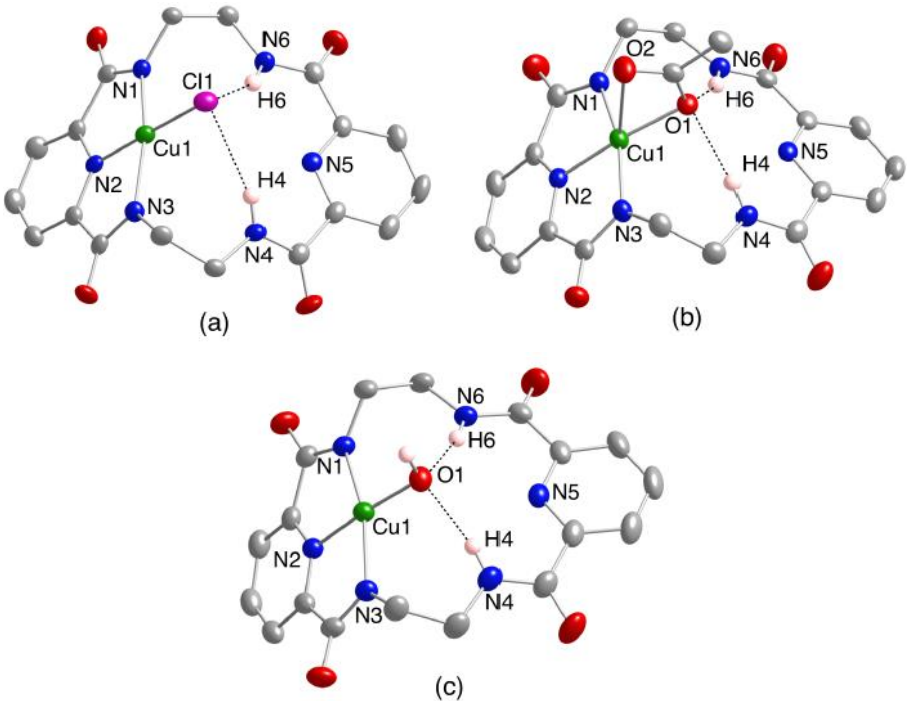

Figure 2.9. Representations of the anionic portions of the X-ray structures of (a) [NMe$_4$][**H$_2$L3**Cu(Cl)] ([NMe$_4$][**1**]), (b) [NMe$_4$][**H$_2$L3**Cu(OAc)] ([NMe$_4$][**2**]), and (c) [NMe$_4$][**H$_2$L3**Cu(OH)] ([NMe$_4$][**3**]), showing all nonhydrogen atoms as 50% thermal ellipsoids and hypothesized hydrogen bonds as dashed lines. Reproduced with permission from ref. 97.

Table 2.2. Selected Interatomic Distances (Å) and Angles (deg) for [NMe$_4$][**H$_2$L3**CuCl] ([NMe$_4$][**1**]), [NMe$_4$][**H$_2$L3**Cu(OAc)] ([NMe$_4$][**2**]), and [NMe$_4$][**H$_2$L3**Cu(OH)] ([NMe$_4$][**3**]).

[NMe$_4$][**H$_2$L3**CuCl] ([NMe$_4$][**1**])					
Cu1 – N1	1.986(2)	N4• • •O1	3.393(3)	N2 – Cu1 – O1	178.75(7)
Cu1 – N2	1.926(2)	N6• • •O1	3.390(2)	N2 – Cu1 – N1	80.40(9)
Cu1 – N3	1.984(2)	H4• • •O1	2.602	O1 – Cu1 – N1	99.99(7)
Cu1 – O1	2.2408(8)	H6• • •O1	2.628	N2 – Cu1 – N3	80.78(10)
				O1 – Cu1 – N3	98.77(7)
				N1 – Cu1 – N3	161.01(10)

[NMe_4][**H_2L3**Cu(OAc)] ([NMe_4][**2**])					
Cu1 – N1	1.980(2)	N4• • •O1	3.003(2)	N2 – Cu1 – O1	171.46(6)
Cu1 – N2	1.920(2)	N6• • •O1	3.002(2)	N2 – Cu1 – N1	80.97(7)
Cu1 – N3	1.991(2)	H4• • •O1	2.202	O1 – Cu1 – N1	99.43(6)
Cu1 – O1	1.937(2)	H6• • •O1	2.197	N2 – Cu1 – N3	80.73(7)
Cu1 – O2	2.636(2)			O1 – Cu1 – N3	98.11(6)
				N1 – Cu1 – N3	161.31(7)
[NMe_4][**H_2L3**Cu(OH)] ([NMe_4][**3**])					
Cu1 – N1	2.005(2)	N4• • •O1	2.890(2)	N2 – Cu1 – O1	172.85(7)
Cu1 – N2	1.931(2)	N6• • •O1	2.865(2)	N2 – Cu1 – N1	80.08(7)
Cu1 – N3	2.002(2)	H4• • •O1	2.038	O1 – Cu1 – N1	99.69(6)
Cu1 – O1	1.884(1)	H6• • •O1	2.055	N2 – Cu1 – N3	80.27(7)
				O1 – Cu1 – N3	99.59(7)
				N1 – Cu1 – N3	160.25(7)

A separate set of neutral monocopper compounds was also identified when metallation of **H_4L3** was attempted using potassium hydride in dimethyl sulfoxide (DMSO) (Scheme 2.7). Solid, highly insoluble crystals from the same reaction mixture were formed and identified by single crystal X-ray diffraction as two distinct variations of neutral DMSO adducts. One compound was found to be the coordination polymer [**H_2L3**Cu(DMSO)]$_n$ (**4**) and the other a solvato-adduct [**H_2L3**Cu(DMSO)]•DMSO (**5**). No synthetic conditions were identified that could discriminately generate one species preferentially over the other. Both compounds **4** and **5** were found to be insoluble in all typical organic solvents, making further studies of these compounds in solution impossible.

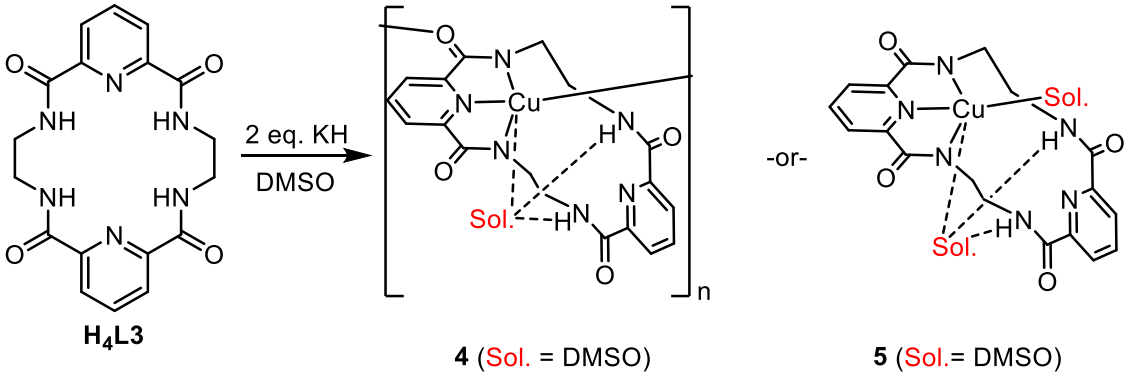

H_4L3 **4** (Sol. = DMSO) **5** (Sol.= DMSO)

Scheme 2.7. Synthetic route to afford [**H_2L3**Cu(DMSO)]$_n$ (**4**) and [**H_2L3**Cu(DMSO)]•DMSO **(5)**.

The X-ray structure of **4** showed it to be a one-dimensional coordination polymer where each copper is bound through the O1 oxygen of the neighboring carbonyl group (Figure 2.10 a, b). The second neutral monocopper species **5** was found to be a solvato adduct, wherein the DMSO occupies the fourth coordination position at the equatorial site (**5**) (Figure 2.10 c, d). Interestingly both of these structures exhibit hydrogen bonding interactions, but not in the same way as observed in **1**, **2**, and **3**. In complexes **4** and **5** the carboxamide protons are not engaged in hydrogen bond donation to the equatorial ligand of the copper center but rather are hydrogen bound to a separate DMSO solvent molecule located near the axial position of the copper (figure 2.11). The donor-acceptor distances are N4···O2 = 2.972(6) Å and N6···O2 = 2.958(6) Å (Table 2.3), both consistent with moderately strong hydrogen bond interactions.

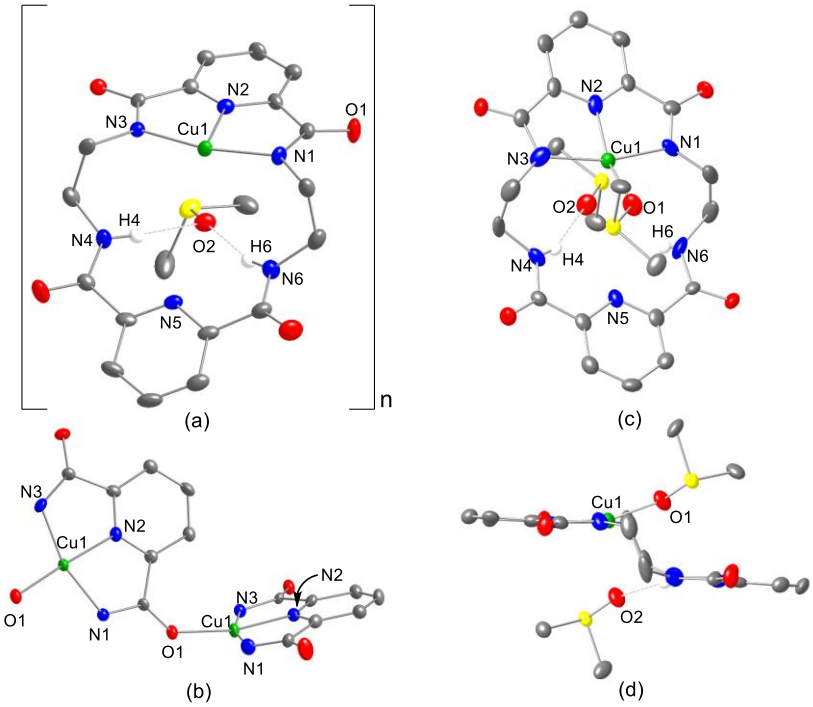

Figure 2.10. X-ray structures of (a) repeat unit of **H$_2$L3**Cu(DMSO) coordination polymer (**4**), (b) representation of polymeric chain of **4**, (c) [**H$_2$L3**Cu(DMSO)]•DMSO (**5**) solvato-adduct front-on view, and (d) solvato-adduct **5** side-on view showing all nonhydrogen atoms as 50% thermal ellipsoids and hypothesized hydrogen bonds as dashed lines.

Table 2.3. Selected Interatomic Distances (Å) and Angles (deg) for [**H$_2$L3**Cu(DMSO)]$_n$ **(4)** and **H$_2$L3**Cu(DMSO)•DMSO **(5).**

[**H$_2$L3**Cu(DMSO)]$_n$ **(4)**					
Cu1 – N1	1.987(4)	N4• • •O2	2.972(6)	N2 – Cu1 – O1	169.83(17)
Cu1 – N2	1.911(4)	N6• • •O2	2.958(6)	N2 – Cu1 – N1	80.35(18)
Cu1 – N3	1.967(4)	H4• • •O2	2.155	O1 – Cu1 – N1	97.35(15)
Cu1 – O1	1.923(3)	H6• • •O2	2.114	N2 – Cu1 – N3	81.91(18)
				O1 – Cu1 – N3	100.48(16)
				N1 – Cu1 – N3	162.14(17)

H_2L3 Cu(DMSO)•DMSO **(5)**					
Cu1 – N1	2.083(6)	N4• • •O2	3.077(6)	N2 – Cu1 – O1	160.27(23)
Cu1 – N2	1.858(6)	N6• • •O2	2.887(5)	N2 – Cu1 – N1	81.93(23)
Cu1 – N3	2.066(6)	H4• • •O2	2.319	O1 – Cu1 – N1	104.49(23)
Cu1 – O1	1.902(5)	H6• • •O2	2.074	N2 – Cu1 – N3	81.64(24)
				O1 – Cu1 – N3	91.69(22)
				N1 – Cu1 – N3	163.46(22)

The change in hydrogen bond acceptor in these molecules can be rationalized by the lack of a charged fourth ligand on the copper center. A neutral ligand occupying this site is less likely to accept a hydrogen bond when bound to copper than a negatively charged ligand such as chlorido or hydroxido as observed in **1** and **3**, respectively. This diversity in hydrogen bond donor-acceptor pair orientation between **1-3** and **4-5** may be viewed as biologically pertinent. Dynamic donor-acceptor pair interactions are often speculated as one way in which metalloenzymes control substrate bonding and reactivity at their active sites.[89,91] The diversity in binding modes of $\mathbf{H_2L3^{2-}}$ copper complexes is a nice example of this dynamic secondary coordination interaction as a function of the metal center's primary coordination sphere

2.3.2 H_2L3^{4-} dicopper and tricopper carbonato complexes

During the course of this work, the anionic compound **3** was found to readily react with atmospheric CO_2(g) to afford multinuclear carbonato complexes that could be readily crystallized (Scheme 2.8). It was observed that from randomly selected crystals from the same mixture two different species could be observed by single crystal X-ray diffraction crystallography. A binuclear complex $[NMe_4]_2[(\mathbf{H_2L3}Cu)_2(CO_3)]$ ($[NMe_4][\mathbf{6}]$)

with a bridging dianionic carbonate molecule was identified along with a trinuclear complex $[NMe_4]_2[(\mathbf{H_2L3}Cu)_3(CO_3)]$ ($[NMe_4][\mathbf{7}]$) with a dianionic carbonato molecule also bridging the three copper centers (Figure 2.11, Table 2.4). Anionic compound **7** was also observed by negative mode ESI-MS, where the isotopic pattern, along with the mass-to-charge ratio (*m/z* = 695.754), matches with what is predicted for the dianionic tricopper complex (Figure 2.12). Simulation of the observed isotopic pattern of the feature confirms three coppers are present.

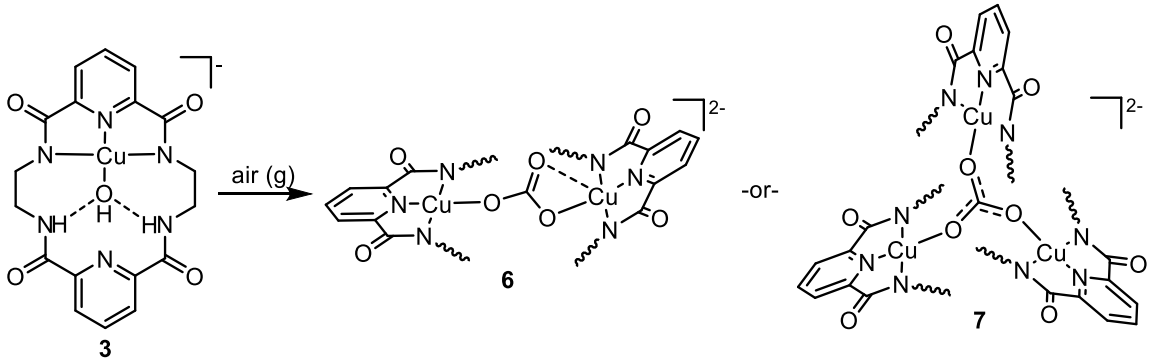

Scheme 2.8. Reaction of **3** with ambient atmosphere to afford **6** and **7**.

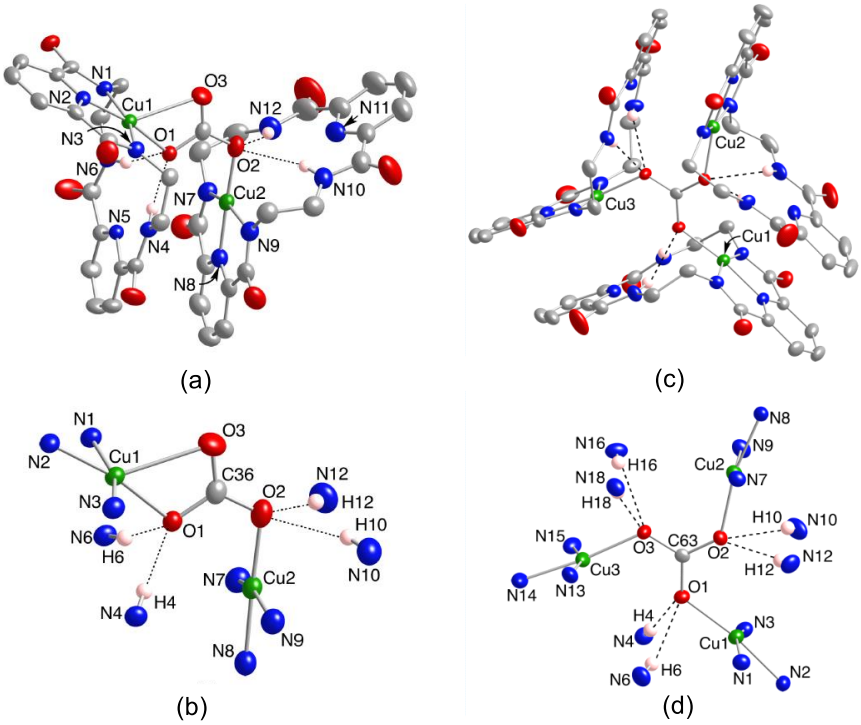

Figure 2.11. (a) Representation of the anionic portion of the X-ray structure of $[NMe_4]_2[(\mathbf{H_2L3}Cu)_2(CO_3)]$ ($[NMe_4]_2$**[6]**), showing all nonhydrogen atoms as 50% thermal ellipsoids and hypothesized hydrogen bonds as dashed lines. (b) Expanded view of core, with all carbon atoms (except C36) omitted. (c) Representation of the anionic portion of the X-ray structure of $[NMe_4]_2[(\mathbf{H_2L3}Cu)_3(CO_3)]$ ($[NMe_4]_2$**[7]**), showing all nonhydrogen atoms as 50% thermal ellipsoids and hypothesized hydrogen bonds as dashed lines. (d) Expanded view of core, with all carbon atoms (except C63) omitted. Reprinted with permission from ref. 97.

Table 2.4. Selected Interatomic Distances (Å) and Angles (deg) for $[NMe_4]_2[(\mathbf{H_2L3}Cu)_2(CO_3)]$ ($[NMe_4]$**[6]**) and $[NMe_4]_2[(\mathbf{H_2L3}Cu)_3(CO_3)]$ ($[NMe_4]$**[7]**).

$[NMe_4]_2[(\mathbf{H_2L3}Cu)_2(CO_3)]$ ($[NMe_4]$**[6]**)					
Cu1 – N1	1.982(2)	N4• • •O1	2.957(4)	N2 – Cu1 – O1	169.46(8)
Cu1 – N2	1.931(2)	N6• • •O1	3.024(4)	N2 – Cu1 – N1	80.38(9)
Cu1 – N3	1.982(2)	H4• • •O1	2.106	O1 – Cu1 – N1	99.96(8)
Cu1 – O1	1.960(2)	H6• • •O1	2.170	N2 – Cu1 – N3	80.32(9)
Cu1 – O3	2.543(3)	N10• • •O2	3.194(5)	O1 – Cu1 – N3	98.30(8)

Cu2 – N7	1.991(2)	N12• • •O2	3.128(5)	N1 – Cu1 – N3	160.32(9)
Cu2 – N8	1.919(2)	H10• • •O2	2.019	N8 – Cu2 – O2	177.96(9)
Cu2 – N9	2.019(3)	H12• • •O2	1.908	N8 – Cu2 – N7	80.84(10)
Cu2 – O2	1.908(2)			O2 – Cu2 – N7	99.76(10)
				N8 – Cu2 – N9	80.50(10)
				O2 – Cu2 – N9	98.68(10)
				N7 – Cu2 – N9	160.35(10)

$[NMe_4]_2[(\mathbf{H_2L3}Cu)_3(CO_3)]$ ($[NMe_4][\mathbf{7}]$)

Cu1 – N1	1.979(3)	N4• • •O1	3.045(4)	N2 – Cu1 – O1	171.37(12)
Cu1 – N2	1.923(3)	N6• • •O1	3.167(4)	N2 – Cu1 – N1	80.68(14)
Cu1 – N3	1.991(3)	H4• • •O1	2.219	O1 – Cu1 – N1	100.31(12)
Cu1 – O1	1.945(3)	H6• • •O1	2.395	N2 – Cu1 – N3	80.35(14)
Cu2 – N7	1.979(3)	N10• • •O2	3.108(4)	O1 – Cu1 – N3	97.95(12)
Cu2 – N8	1.919(3)	N12• • •O2	3.140(4)	N1 – Cu1 – N3	160.75(14)
Cu2 – N9	1.975(3)	H10• • •O2	2.440	N8 – Cu2 – O2	168.19(12)
Cu2 – O2	1.949(3)	H12• • •O2	2.421	N8 – Cu2 – N7	80.36(13)
Cu3 – N13	1.987(4)	N16• • •O3	3.090(5)	O2 – Cu2 – N7	99.71(12)
Cu3 – N14	1.931(3)	N18• • •O3	2.984(5)	N8 – Cu2 – N9	80.87(13)
Cu3 – N15	1.977(4)	H16• • •O3	2.503	O2 – Cu2 – N9	98.46(12)
Cu3 – O3	1.942(3)	H18• • •O3	2.398	N7 – Cu2 – N9	161.21(13)
				N14 – Cu3 – O3	173.86(13)
				N14 – Cu3 – N13	80.08(16)
				O3 – Cu3 – N13	98.16(13)
				N14 – Cu3 – N15	81.17(16)
				O3 – Cu3 – N15	99.94(13)
				N13 – Cu3 – N15	160.54(14)

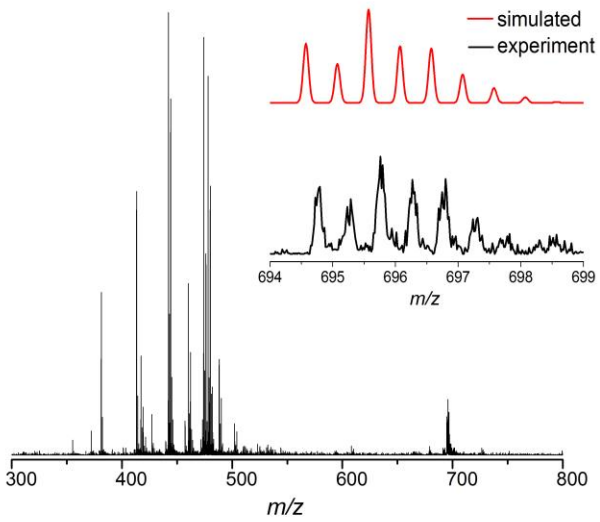

Figure 2.12. For $[NMe_4]_2[(\mathbf{H_2L3}Cu)_3(CO_3)]$ ($[NMe_4]_2[\mathbf{7}]$): negative ion mode HR-ESI-MS with the inset showing the experimental (bottom, black) and simulated (top, red) peak envelope for the ion $[(\mathbf{H_2L3})Cu)_3(CO_3)]^{2-}$.

In the dicopper complex **6**, the carbonato ligand is coordinated in a monodentate fashion to Cu2 and in a bidentate fashion to Cu1. In the tricopper complex **7** the carbonate adopts a monodentate binding mode with each Cu(II) ion. Complete delocalization of the C=O double bond in the carbonate is evidenced by the essentially identical C-O bond distances. These binding modes are both precedented in the copper coordination chemistry literature,[98-101] albeit normally not found as individually attainable cores from a single starting compound as we have described herein.

2.3.3 H_2L4a^{2-} and H_2L4b^{2-} monocopper complexes

H_4L4a and **H_4Lb** were synthesized intentionally in order to only allow a single copper to coordinate while still allowing for the possibility of intramolecular hydrogen bond donation. Additionally, **H_2L4a^{2-}** and **H_2Lb^{2-}** contain aromatic carboxamide donors

akin to **L1b**$^{2-}$, making them closer ligand analogs to the non-hydrogen bound systems than **H$_2$L3**$^{2-}$ complexes. The goal was to generate compounds analogous to **1-3** as additional comparison points in the analysis of the secondary coordination sphere effects.

H$_4$L4a and **H$_4$Lb** were metallated using similar methods as those employed in the metalation of the macrocycle **H$_4$L3**. Using organic solvents and NMe_4OH as a deprotonation reagent, several new compounds were isolated. In cases where $Cu(OAc)_2$•H_2O or $CuCl_2$ were used, monocopper complexes [NMe_4][**H$_2$L4a**Cu(OAc)] ([NMe_4][**8**]) and [NMe_4][**H$_2$L4b**Cu(Cl)] ([NMe_4][**9**]) were formed, respectively (Scheme 2.9). Characterization of these compounds by frozen solution EPR spectroscopy was performed. Similar to the compounds **1-3**, pseudo-axial features consistent with square planar S = ½ monocopper complexes are observed, consistent with their supposed structures (Figure 2.13-2.14). Negative ion mode HR-ESI-MS displayed predicted parent features at *m/z* = 597.136 corresponding to anionic compound **8** and at m/z = 631.134 corresponding to anionic compound **9** (Figure 2.13-2.14). Simulation of the isotropic patterns were consistent with the presence of a single copper ion.

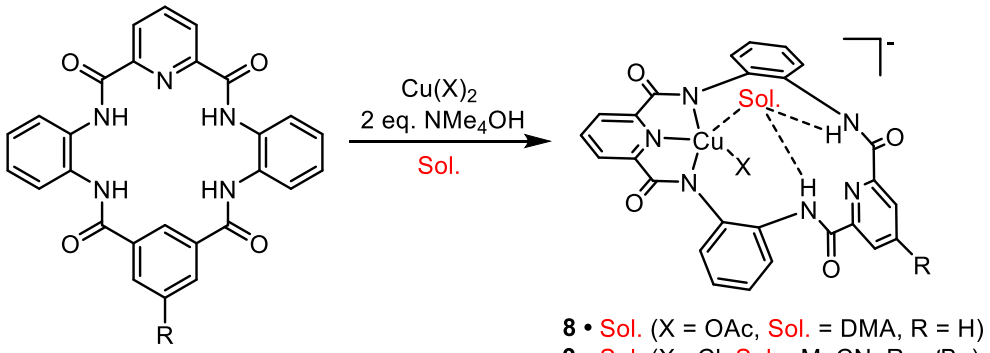

Scheme 2.9. Synthetic scheme for generation of metallated complexes **8** and **9.**

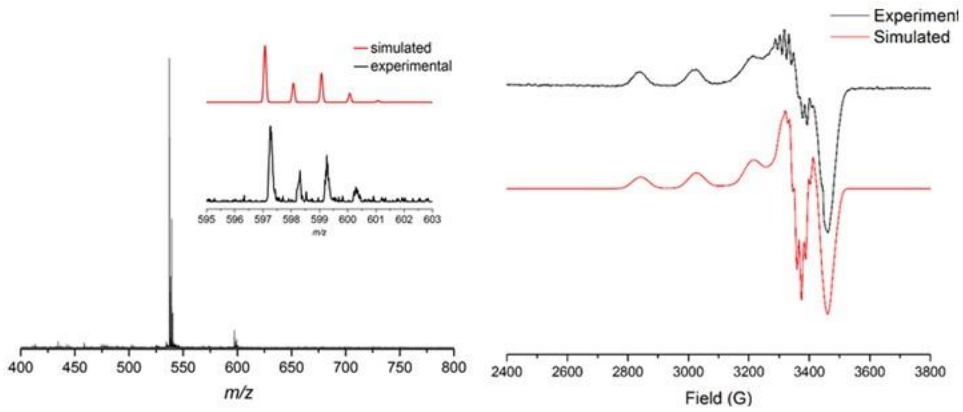

Figure 2.13. [NMe_4][**H_2L4a**Cu(OAc)] ([NMe_4][**8**]): (left) negative ion mode HR-ESI-MS with the inset showing the experimental (bottom, black) and simulated (top, red) peak envelope for the ion [**H_2L4a**Cu(OAc)]$^-$. (right) experimental (top, black) and simulated (bottom, red) EPR spectrum (X-band, 30K). EPR parameters are listed in Table 2.1.

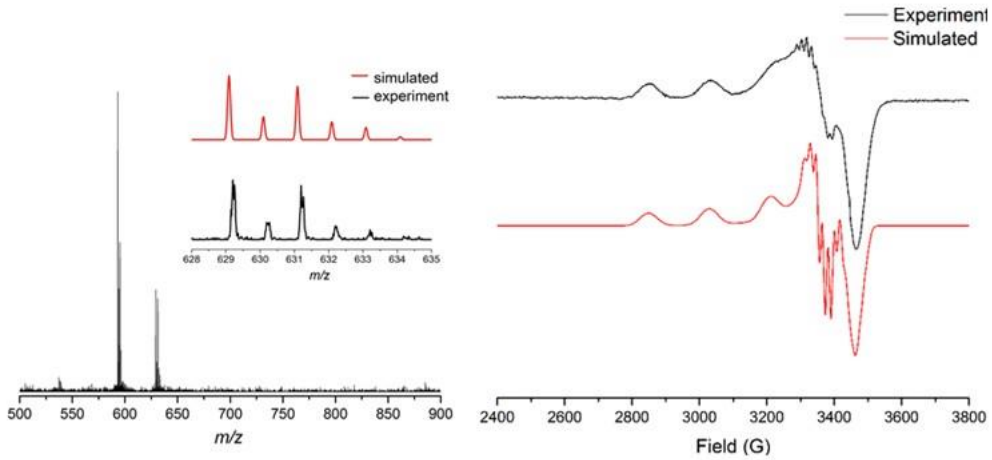

Figure 2.14. [NMe_4][**H_2L4b**Cu(Cl)] ([NMe_4][**9**]): (left) negative ion mode HR-ESI-MS with the inset showing the experimental (bottom, black) and simulated (top, red) peak envelope for the ion [**H_2L4b**Cu(Cl)]$^-$. (right) experimental (top, black) and simulated (bottom, red) EPR spectrum (X-band, 30K). EPR parameters are listed in Table 2.1.

X-ray crystallographic determination of the structures of anionic **H_2L4a**$^{2-}$ and **H_2L4b**$^{2-}$ monocopper complexes was performed upon crystallization from DMA or MeCN for [NMe_4][**8**] and [NMe_4][**9**], respectively (Figure 2.15). Standard primary coordination sphere bond metrics were observed in the structure, but, most notably, a change in hydrogen bonding mode was observed. Instead of the carboxamide protons

interacting with the chlorido or acetato ligands as previously observed in anionic compounds **1** and **2**, the carboxamide donors were hydrogen bonded to separate solvent molecules of DMA in **8** and CH_3CN in **9**, respectively. This donor-acceptor orientation is similar to what is observed in complexes **4** and **5**. The donor-acceptor distances are N4···O7 = 3.096(5) Å and N5···O7 = 3.164(3) Å in the structure of $[NMe_4]$[**8**]•DMA and N4···N6 = 3.348(3) Å and N5···N6 = 4.013(3) Å in the structure of $[NMe_4]$[**9**]•CH_3CN (Table 2.5). These donor-acceptor distance suggest these interactions are rather weak when compared to the donor-acceptor distance of ~2.9 Å observed in complex **3**.

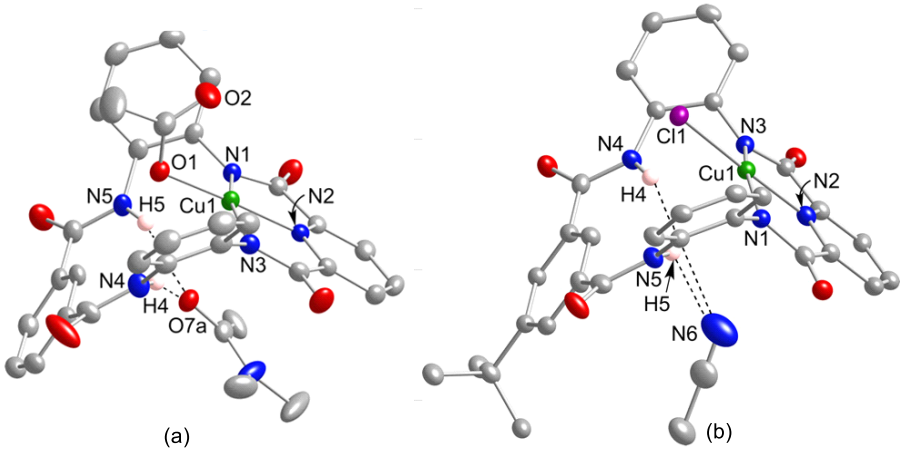

Figure 2.15. (a) Representations of the anionic portion of the X-ray structures of (a) $[NMe_4]$[**H_2L4a**Cu(OAc)]•DMA ($[NMe_4]$[**8**]•DMA, R = H) and (b) $[NMe_4]$[**$H_2$4b**Cu(Cl))]•CH_3CN ($[NMe_4]$[**9**] •CH_3CN, R= *t*Bu), showing all nonhydrogen atoms as 50% thermal ellipsoids and hypothesized hydrogen bonds as dashed lines. Reproduced with permission from ref. 97.

Table 2.5. Selected Interatomic Distances (Å) and Angles (deg) for [NMe_4][**H_2L4a**Cu(OAc)]•DMA ([NMe_4][**8**]•DMA) and [NMe_4][**H_2L4b**Cu(Cl)]•CH_3CN ([NMe_4][**9**]•CH_3CN).

[NMe_4][**H_2L4a**Cu(OAc)]•DMA ([NMe_4][**8**]•DMA)					
Cu1 – N1	2.005(2)	N4• • •O7	3.096(5)	N2 – Cu1 – O1	177.84(6)
Cu1 – N2	1.915(2)	N5• • •O7	3.164(3)	N2 – Cu1 – N1	80.55(6)
Cu1 – N3	2.018(2)	H4• • •O7	2.183	O1 – Cu1 – N1	100.68(6)
Cu1 – O1	1.912(1)	H5• • •O7	2.691	N2 – Cu1 – N3	81.00(7)
Cu1 – O2	2.819(2)			O1 – Cu1 – N3	97.65(6)
				N1 – Cu1 – N3	161.14(7)
[NMe_4][**H_2L4b**Cu(Cl)]•CH_3CN ([NMe_4][**9**]•CH_3CN)					
Cu1 – N1	2.043(2)	N4• • •N6	3.348(3)	N2 – Cu1 – O1	178.05(5)
Cu1 – N2	1.918(2)	N5• • •N6	4.013(3)	N2 – Cu1 – N1	80.56(7)
Cu1 – N3	2.021(2)	H4• • •N6	2.602	O1 – Cu1 – N1	99.81(5)
Cu1 – Cl1	2.185(5)	H5• • •N6	2.628	N2 – Cu1 – N3	80.23(6)
				O1 – Cu1 – N3	99.62(5)
				N1 – Cu1 – N3	159.62(7)

The rationale for the change in hydrogen bonding mode in **8** and **9** is not completely understood. We speculate that it may be due to the lack of charge build-up in the primary coordination sphere of the copper ion due to the less electron donating nature of the aromatic carboxamido donors as opposed to the alkyl carboxamido donors in the ligand $\mathbf{H_2L3^{2-}}$. It is also possible that this donor-acceptor interaction is dynamic when in solution state and the observed solid state structures are not reflective of the structure of **8** and **9** when dissolved.

2.3.4 H_2L4a^{2-}dicopper μ-hydroxo complex

Attempts to generate the analogous monocopper-hydoxido species to **3** in the **H_2L4a^{2-}** or **H_2L4b^{2-}** framework proved to be unfruitful. Generation of hydroxido- species using these macrocylces with aromatic phenylene linkers, as opposed to its ethylene bridged counterpart, resulted in formation of [NMe_4][(**H_2L4b**Cu)$_2$(OH)] ([NMe_4][**10**]) (Scheme 2.10). This new species consists of a dicopper μ-hydroxido core, wherein two monometallated macrocycles bridge through a single hydroxide ligand (Figure 2.16). The species [NMe_4][**10**]•CH_3CN was observed by single crystal X-ray crystallographic studies and is believed to be the thermodynamic product of the metallation conditions described in scheme 2.8

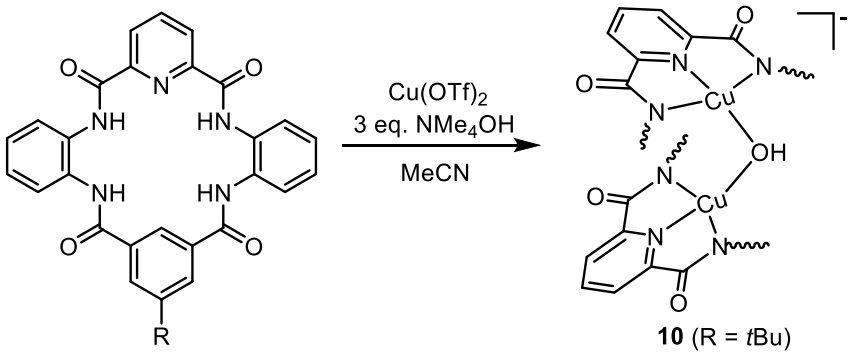

Scheme 2.10. Synthetic preparation of metallated complex [NMe_4][(**H_2L4b**Cu)$_2$(OH)]•CH_3CN ([NMe_4][**10**]•CH_3CN).

Analysis of the crystal structure of **10** reveals standard N-Cu distances in the primary coordination sphere but with a Cu1-O1 distance of 1.936(3) Å and Cu2-O1 distance of 1.890(3) Å (Table 2.6). The difference in distance between the copper-hydroxo bond lengths suggest the hydroxo is more strongly bound to Cu2 than Cu1. Additionally the two macrocylces are canted two one another and exhibit a Cu1-O1-Cu2 bond angle of 127.81°. The dicopper(II) μ-hydroxo motif is not uncommon in copper(II) compounds and is often observed in systems that do not have appropriate steric bulk to

prevent such species from forming.[102] Notably, the carboxamide protons are pointed away from the hydroxide and instead interact with a CH_3CN molecule and a carbonyl oxygen of a neighboring complex. We speculate that the absence of hydrogen-bonding from the carboxamide protons to the hydroxo allows for its lone pairs to participate in coordination to a second copper and ultimately results in formation of the anionic complex **10**.

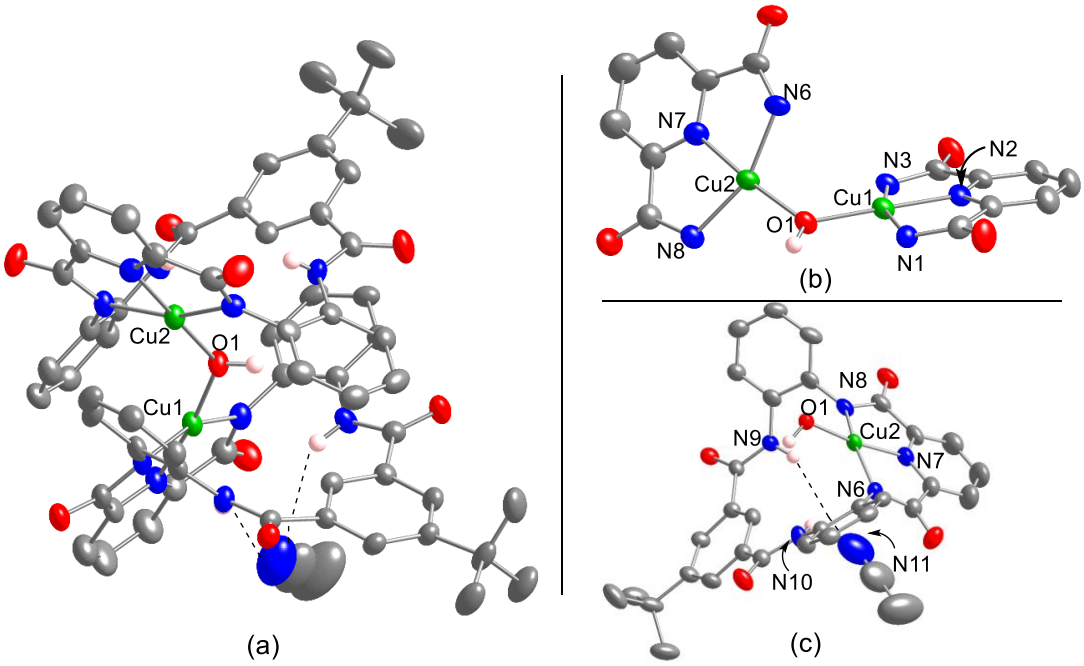

Figure 2.16. (a) Representations of the anionic portion of the X-ray structure of (a) $[NMe_4][(\mathbf{H_2L4b}Cu)_2(OH)]\bullet MeCN$ ($[NMe_4][\mathbf{10}]\bullet CH_3CN$), (b) close up of the dicopper hydroxo core, and (c) the portion of $[NMe_4][\mathbf{10}]$ that contains hydrogen bonding to a molecule of CH_3CN showing all nonhydrogen atoms as 50% thermal ellipsoids and hypothesized hydrogen bonds as dashed lines.

Table 2.6. Selected Interatomic Distances (Å) and Angles (deg) for [NMe_4][(**H_2L4b**Cu)$_2$(OH)]•MeCN ([NMe_4][**10**]).

[NMe_4][(**H_2L4b**Cu)$_2$(OH)]•MeCN ([NMe_4][**10**])					
Cu1 – N1	2.015(5)	N4• • •O8	4.079(3)	N2 – Cu1 – O1	179.15(13)
Cu1 – N2	1.903(3)	N5• • •O8	3.112(4)	N2 – Cu1 – N1	80.86(13)
Cu1 – N3	2.037(3)	H4• • •O8	3.313	O1 – Cu1 – N1	99.40(12)
Cu1 – O1	1.936(3)	H5• • •O8	2.345	N2 – Cu1 – N3	80.22(13)
Cu2 – N6	2.019(3)	N9• • •N11	4.304(5)	O1 – Cu1 – N3	99.43(12)
Cu2 – N7	1.903(3)	N10• • •N11	3.685(2)	N1 – Cu1 – N3	159.92(13)
Cu2 – N8	2.040(3)	H9• • •O8	3.569	N7 – Cu2 – O1	172.50(13)
Cu2 – O1	1.890(3)	H10• • •O8	2.920	N7 – Cu2 – N6	80.82(14)
				O1 – Cu2 – N6	102.97(12)
				N7 – Cu2 – N8	80.31(14)
				O1 – Cu2 – N8	97.06(13)
				N6 – Cu2 – N8	158.18(14)

2.4 Electrochemistry of copper complexes

2.4.1 Cyclic voltammetry of monocopper hydroxo complexes

Cyclic voltammetry (CV) experiments using [NBu_4][**L1b**Cu(OH)] and [NMe_4][**3**] were performed in DMA using NBu_4PF_6 (0.1 M) as electrolyte. For [NBu_4][**L1b**Cu(OH)], a reversible redox feature assigned to the $Cu^{III/II}$ redox couple of interest was observed and the $E_{1/2}$ was calculated to be -67 mV vs. the Fc^+/Fc redox couple (Figure 2.17). In the CV measurement of **3** at the same scan rate (500 mV/s), an irreversible oxidation was observed at +310 mV. Upon increasing the scan rate (2000 – 4000 mV/s), the corresponding cathodic feature of **3** became more pronounced, giving

current ratio values (i_{pa}/i_{pc}) of ~3.16 and ~2.13 at 2000 and 4000 mV/s respectively. In a perfectly reversible system i_{pa}/i_{pc} = 1, where the current intensity of the anodic and cathodic features are equivalent.

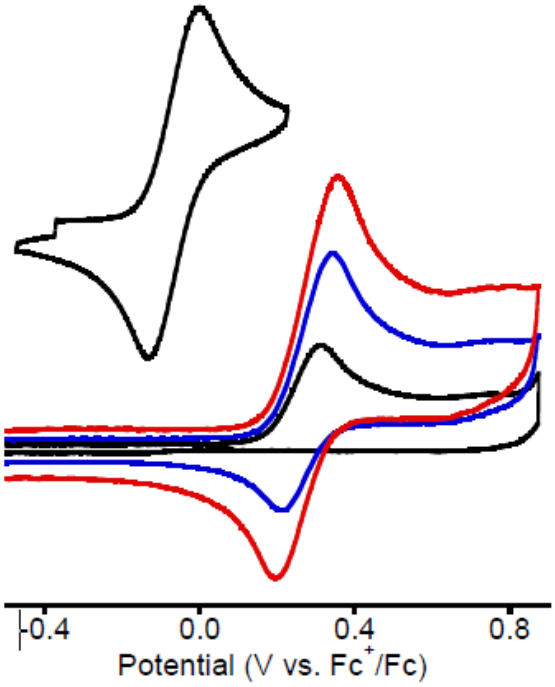

Figure 2.17. Cyclic voltammograms (0.1 M Bu_4NPF_6, Pt electrode) of (a) the complexes (i) [(**L1b**)CuOH]$^-$ and (ii) [**H$_2$L3**Cu(OH)]$^-$ (**3**) in DMA. Scan rates: (i) 500 mV/s, (ii) 500 (black), 2000 (blue), 4000 (red) mV/s. Reprinted with permission from ref. 97.

The scan rate dependence that is observed for **3** is consistent with the oxidized complex undergoing a chemical reaction. We propose that the oxidized species ([**H$_2$L3**LCu(OH)] (**3**$^+$)) forms and the rate at which it reacts/decays is on the order of the rate that the electrochemical sweep is occurring in the CV experiments (Scheme 2.11). At higher scan rates the species **3**$^+$ is then able to be reduced back to the starting compound **3** as the electrochemical redox process begins to outcompete the decay rate.

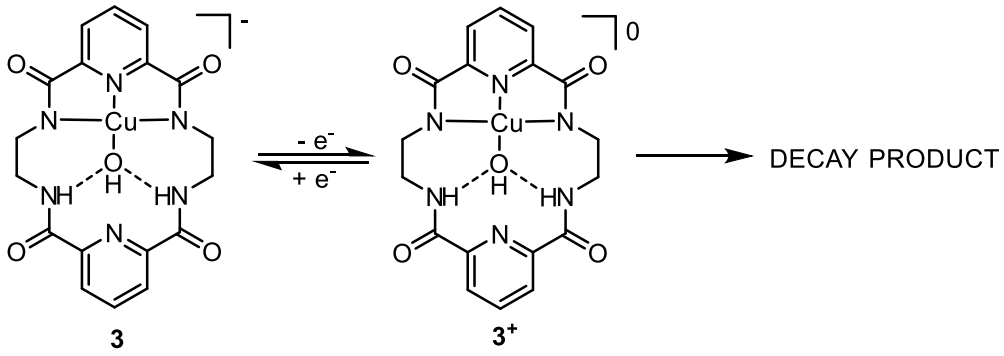

Scheme 2.11. Generic scheme for reaction side decay pathway of oxidized species $\mathbf{3}^{+}$.

An approximate $E_{1/2}$ value for the $Cu^{III/II}$ redox couple of **3** was calculated from its CV data to be ~+284 mV vs. Fc^{+}/Fc (Table 2.7). Compared to the measured [**L1b**Cu(OH)]$^{-}$ redox couple, a difference in $E_{1/2}$ ~ +350 mV is apparent between our two monocopper hydroxido systems. This electrochemical difference is large and positive, consistent with what might be expected for the presence of strong hydrogen bond donors. Yet, whether this shift can be wholly attributed to the presence of hydrogen bond donation cannot be ascertained from only two points of comparison. To better understand the hydrogen bonding relationship with $E_{1/2}$ we went on to compare the chlorido series of these macrocyclic monocopper complexes.

Table 2.7. Redox potentials for the indicated copper complexes.[a] Adapted from ref. 97.

Compound	**Solvent**	$\boldsymbol{E_{1/2}}$ **(mV)**[b]
[**L1b**Cu(OH)]$^{-}$	DMA	-67
[$\mathbf{H_2}$**L3**Cu(OH)]$^{-}$ (**3**)	DMA	+284
[**L1b**Cu(Cl)]$^{-}$	CH_3CN	+338
[$\mathbf{H_2}$**L3**Cu(Cl)]$^{-}$ (**1**)	CH_3CN	+632
[$\mathbf{H_2}$**L4b**Cu(Cl)]$^{-}$ (**9**)	CH_3CN	+581

[a]Conditions: room temperature, 0.1 M Bu_4NPF_6, Pt electrode.[b]vs. Fc^{+}/Fc.

2.4.2 Cyclic voltammetry of monocopper chlorido complexes

Cyclic voltammetry data of the complexes [NBu_4][**L1b**Cu(Cl)], [NMe_4][**1**], and [NMe_4][**8**] were obtained in acetonitrile using NBu_4PF_6 (0.1 M) as electrolyte (Figure 2.18). It was necessary to switch solvents to acetonitrile in the CV experiments of the monocopper chlorido complexes as they have much higher redox potentials that are unobservable in DMA's electrochemical solvent window. Under these electrochemical conditions, a reversible redox feature of [**L1b**Cu(Cl)]$^-$ was observed with an $E_{1/2}$ of approximately +338 mV vs. Fc^+/Fc (Table 2.7), much higher than that of the measured $E_{1/2}$ -67 mV for its analog [**L1b**Cu(OH)]$^-$. Compound [NMe_4][**1**] was found to have a quasi-reversible redox feature at a scan rate of 500 mV/s (i_{pa}/i_{pc} = 14.1) and showed only modestly increased reversibility at higher scan rates of 2000 mV/s (i_{pa}/i_{pc} = 6.5) and 4000 mV/s (i_{pa}/i_{pc} = 5.9). An $E_{1/2}$ value for the supposed Cu^{III}/Cu^{II} couple of **1** was approximated to be +632 mV/s. Fc^+/Fc, 294 mV higher than the redox couple of [**L1b**Cu(Cl)]$^-$.

Compound **9** was also found to have a quasi-reversible redox feature with a larger scan rate dependence than **1,** where i_{pa}/i_{pc} = 3.9 at 500 mV/s and i_{pa}/i_{pc} = 2.0 at 4000 mV/s. The $E_{1/2}$ value for **9** was calculated to be +581 mV vs. Fc^+/Fc (Table 2.7). Interestingly, the $E_{1/2}$ of **9** value is only ~50 mV lower than compound **1**. The similarity in $E_{1/2}$ values between **9** and **1** suggests that both compounds experience secondary coordination sphere interactions that are responsible for the raise of their observable Cu^{III}/Cu^{II} redox potential relative to the complex [**L1b**Cu(Cl)]$^-$.

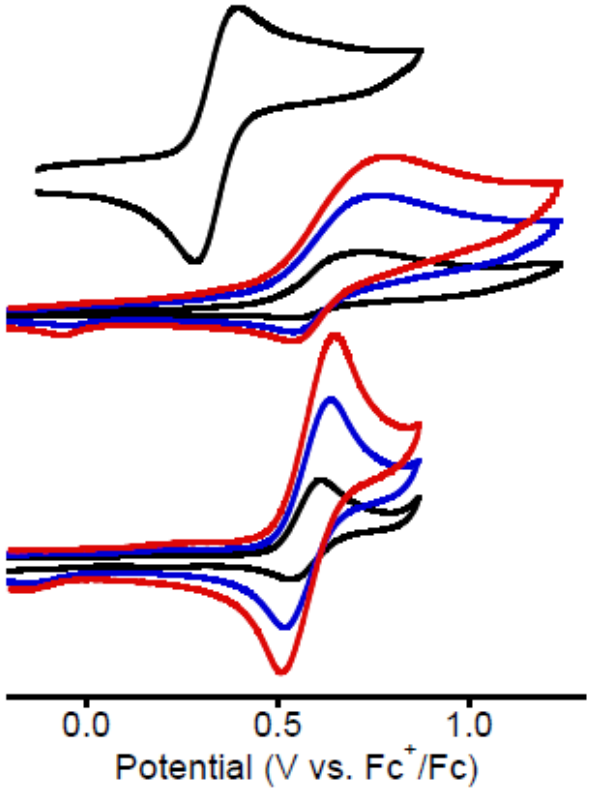

Figure 2.18. Cyclic voltammograms of (i) [**L1b**Cu(Cl)]$^{-}$, (ii) [**H$_2$L3**Cu(Cl)]$^{-}$ (**1**), and (iii) [**H$_2$L4b**Cu(Cl)]$^{-}$ (**9**, R = *t*Bu) in CH_3CN. Scan rates:, (i) 100 mV/s, (ii, iii) 500 (black), 2000 (blue), 4000 (red) mV/s. Reproduced with permission from ref. 97.

Comparison between the non-hydrogen bonded systems relative to the two macrocyclic complexes **1** and **9** with potential hydrogen-bond donors again shows a large positive difference in the $Cu^{III/II}$ redox couple. The difference in $E_{1/2}$ values is +294 mV between [**L1b**Cu(Cl)]$^{-}$ and **1**. Similarly, a +243 mV difference was found between [**L1b**Cu(Cl)]$^{-}$ and **9**. The relative potentials of all the new macrocylic complexes measured, with respect to their non-hydrogen bonded **L1b**$^{2-}$ monocopper counterparts, consistently showed large positive shifts in all cases, albeit with larger overall shifts observed in the monocopper hydroxide complexes. The larger observed shift in the hydroxide series may be a result of hydroxide ligands engaging in stronger hydrogen

bond interactions with the carboxamide protons as is evidenced by their shorter donor-acceptor distances relative to the chlorido analogs in their respective X-ray crystal structures.

2.5 Conclusions

Treatment of macrocyclic proligand **H_4L3** with base and Cu(II) salts results in the formation of complexes in which **H_2L3^{2-}** binds to a single Cu(II) ion. Monoanionic compounds **1-3** and neutral DMSO adducts **4** and **5** were generated depending on the specific metallation conditions employed. Carbonato-bound complexes **6** and **7** were also found to form upon the reaction of **3** with ambient carbon dioxide. X-ray crystallographic studies of compound **1-3** and **6-7** revealed intramolecular hydrogen bonding between the carboxamide N-H groups to the fourth ligand (Cl, OAc, OH, or CO_3^{2-}) bound to the Cu(II) ion. Alternate hydrogen bonding interactions in the same **H_2L3^{2-}** ligand framework were observed in the neutral species **4** and **5**, where in carboxamide N-H groups hydrogen bond with DMSO molecules that do not occupy the fourth ligand site of the Cu(II) center.

The macrocyclic proligands **H_4L4a** and **H4L4b** were synthesized and used to generate **8** and **9**, analogous monocopper compounds to complexes **1-3**. A monocopper hydroxo core could not be isolated using these ligand frameworks and instead resulted in formation of the dicopper(II) μ-hydroxo species **10**. X-ray crystallography of **8** and **9** revealed hydrogen bonding from the carboxamide protons in to molecules of DMA and CH_3CN respectively. The observed hydrogen bond orientation was more akin to that observed in the structures of **4** and **5** where the hydrogen bond acceptors are solvate molecules located near the axial postion of the Cu(II) center.

Electrochemical measurements of these macrocyclic monocopper compounds indicated that secondary coordination sphere hydrogen bonding interactions result in a

significant positive rise in the $Cu^{III/II}$ redox potential. We surmise that these shifts are not due to the ethyl linkers, as we observe a similar increase in the redox potential for the monocopper complex **9** supported by the purposefully mononucleating ligands $\mathbf{H_2L4a^{2-}}$ and $\mathbf{H_2L4b^{2-}}$ that features aryl groups on the carboxamido donors. While the X-ray structures of complexes of $\mathbf{H_2L4a^{2-}}$ and $\mathbf{H_2L4b^{2-}}$ show a different hydrogen bonding pattern involving interactions between the carboxamide N-H groups and solvate molecules, we speculate that intramolecular hydrogen bonding in solution underlies the observed redox potential for **9**. Additional influences of the secondary sphere interactions in the various complexes we have prepared on their reactivity are the subject of continuing research.

2.6 Experimental section

2.6.1 Materials and methods.

All reactions and manipulations were performed under an inert gas atmosphere using Schlenk techniques or a Glove box unless otherwise noted. HPLC grade Water was distilled and degassed by one freeze–pump–thaw cycle. The solvents tetrahydrofuran (THF), diethyl ether (Et_2O), pentane, dichloromethane (CH_2Cl_2) were passed through solvent purification columns (Glass Contour, Laguna, CA). Pyridine and ethylene diamine were purified by distillation prior to use. All chemicals were purchased from Aldrich and used without purification unless stated otherwise. Perpendicular-mode X-band (9.62 GHz) EPR spectra were recorded on a Bruker Elexsys E500 spectrometer. Simulations were performed using Bruker SimFonia software (version 1.25). Electrospray ionization mass spectrometry (ESI-MS) was performed on a Bruker Bio-TOF II instrument. Cyclic voltammetry (CV) was performed in a three electrode cell with Ag^+/Ag reference electrode, platinum auxiliary electrode, and platinum working electrode

and analyzed with BASi Epsilon software. Tetrabutylammonium hexafluorophosphate (Bu_4NPF_6) was used as the supporting electrolyte.

2.6.2 Preparation of compounds

H_4L3. The synthesis of **H_4L3** was procedure modified relative to that previously reported. This procedure was not performed using Schlenk line techniques. The compound 2, 6-pyridine dicarboxylic acid (20 g, 0.120 mol) was dissolved in dry pyridine (250 mL) at 100 °C. To this homogeneous solution, stirred by a mechanical stirrer, was added a solution of ethylene diamine (6.5 mL, 0.120 mol) and pyridine (1 mL) dropwise from a syringe. A white solid formed and the mixture was stirred for 10 min. Triphenyl phosphite (63 mL, 0.240 mol) was then added to the reaction solution via an addition funnel and the mixture was stirred at 100 °C for an additional 5 h. The solution was then cooled to room temperature and stirred for an additional 12 h, after which the mixture was concentrated by removing the pyridine by distillation. The resulting white slurry was then washed with distilled water (2 × 50 mL), a 0.1 M solution of $NaHCO_3$ (2 × 200 mL), a 0.1 M solution of K_2CO_3 (2 × 200 mL), and 0.1 M solution of NaOH (2 × 200 mL). MeOH (40 mL) was added to the washed product and the mixture was refluxed for 40 min, cooled, and the solid collected via filtration using a Büchner funnel. After washing the white solid with additional MeOH (2 × 30 mL) and Et_2O (2 × 30 mL), it was allowed to dry in air. This white solid was then refluxed once more with 180 mL of DMF for 10 min, filtered while hot, and the filtrate allowed to cool to room temperature, producing white crystals of **H_4L3** (9.04 g, 40%). ^{1}H-NMR (DMSO-*d*6, 300 MHz) δ (ppm): 9.46 (s, 4H, NHCO), 8.24-8.17 (m, 6H, CH^{Py}), 3.61-3.60 (m, 8H, CH_2). Anal. Calcd for $C_{18}H_{18}N_6O_4$: C, 56.54; H, 4.75; N, 21.98. Found: C, 56.67; H, 4.71; N, 21.97.

***N*-Boc-1, 2-phenylenediamine.** A procedure modified relative to that previously reported was used. This procedure was not performed using Schlenk line techniques. 1, 2-phenylenediamine (16.2 g, 0.150 mol) was added to 100% EtOH (300 mL) and the mixture was slowly heated to 30 ° C until a clear yellow solution was obtained. A solution of Boc_2O (33.0 g, 0.150 mol) in EtOH (65 mL) was added dropwise over a 90 min period, keeping the temperature at 30 °C. After completing the addition the mixture was left to stir for 30 min, after which the volatiles were removed under vacuum to yield a white solid. To the raw product Et_2O (20 mL) and hexanes (20 mL) were added and a white solid was filtered off using Büchner funnel, washed with additional hexanes (20 mL), and the white crystalline product was dried in air. An additional amount of the product was obtained by slow evaporation of the filtrate over 2 d. The white crystals were collected by filtration, washed with hexane (2 × 10 mL), and dried in air (21.9 g, 70.4%). The ^1H NMR spectrum matched that which was reported.[16,17] This compound was carried on as a precursor for the synthesis of the hemicycle, N2,N6-bis(2-aminophenyl)pyridine-2,6-dicarboxamide.

***N2,N6*-bis(2-aminophenyl)pyridine-2,6-dicarboxamide**. A procedure modified relative to that previously reported was used. Pyridine 2,6-dicarbonyl dichloride (5.0 g, 0.025 mol) was dissolved in dry THF (50 mL) and added dropwise to a solution of N-Boc-1,2-phenylenediamine (10.41 g, 0.050 mol) and NEt_3 in THF (300 mL) over 10 h. After the addition was complete, the mixture was stirred for 2 h and the resulting white solid was collected by filtration, washed with Et_2O (2 × 20 mL), and dried under vacuum. Next, the dried product was added to a mixture of CH_2Cl_2 (100 mL) and CF_3CO_2H (50 mL) and the mixture was stirred for 2 h. It was then carefully poured into aqueous NaOH (2M, 500 mL). The solution was immersed in an ice bath and allowed to cool. Additional CH_2Cl_2 (~900 mL) was added to dissolve all of the product, and the CH_2Cl_2 layer was

washed with water (3 × 200 mL), dried over Na_2SO_4, and volatiles removed under vacuum to afford yellow solid. Recrystallization of this yellow solid from CH_2Cl_2 (100 mL) and Et_2O (100 mL) at 0 °C yielded pure compound **5** (8.68 g, 80%). ^{1}H-NMR matched reported values in literature.

H_4L4a (R = H). A procedure modified relative to that previously reported was used.17 A solution of isophthalic dichloride (1.18 g, 0.0058 mol) in dry THF (60 mL) was added dropwise over 12 h to a refluxing solution of N2,N6-bis(2-aminophenyl)pyridine-2,6-dicarboxamide (2.0 g, 0.0058 mol) in a mixture of THF (250 mL) and NEt_3 (20 mL), all under Argon atmosphere. The mixture was cooled to room temperature, left to stir for an additional 24 h, filtered, and then solvent removed from the filtrate under vacuum to give a sticky brown solid. Addition of MeOH (300 mL) generated a white suspension that was filtered. The filtrate was collected and concentrated to ~50 mL and Et_2O (50 mL) was added to give a white powder that was collected by filtration and then washed with Et_2O (3 × 30 mL). The powder was redissolved in DMF (10 mL) and recrystallized with the addition of Et_2O (20 mL) at 0 °C over 24 hours to yield the product, which was dried under vacuum (0.94 g, 68%). ^{1}H-NMR (DMSO-d6, 300 MHz) δ (ppm): 11.15 (s, 2H, NHCO), 10.21 (s, 2H, NHCO), 9.28 (s, 1H, CH), 8.43-8.40 (d, 2H, CHPy), 8.29-8.24 (m, 1H, CHPy), 8.15-8.07 (m, 4H, CH), 7.72-7.66 (m, 2H, CH), 7.37-7.25 (m, 4H, CH). Anal Calcd for $C_{30}H_{26}N_6O_5$ (**H_4L4a (R=H)** with one molecule of DMF) C, 65.45; H, 4.76; N, 15.26. Found: C, 64.57; H, 4.70; N, 15.32.

H_4L4b (R = *t*Bu). H_4L4b was synthesized analogously to **H_4L4a (R' = H)** except 5-tert-butyl-isophthalic dichloride was used instead of isopthalic dichloride (1.85 g, 60.2%). 1H-NMR (DMSO-d6, 300 MHz) δ (ppm): 11.25 (s, 2H, NHCO), 10.30 (s, 2H, NHCO), 9.22 (s, 1H, CH), 8.42-8.39 (d, 2H, CHPy), 8.28-8.22 (m, 1H, CHPy), 8.10-8.04

(m, 4H, CH), 7.68-7.65 (m, 2H, CH), 7.36-7.26 (m, 4H, CH), 1.33 (s, 9H, CH3). Calcd for $C_{34}H_{34}N_6O_5$ (**H_4L4b (R' = *t*Bu)** with one molecule of DMF): C, 67.31; H, 5.65; N, 13.85. Found: C, 67.02; H, 6.01; N, 13.80.

[NMe_4][(H_2L3)Cu(Cl)] ([NMe_4][1]). To a solution of **H_4L3** (300 mg, 0.78 mmol) in 1:3 water (3 mL)/pyridine (9 mL) was added a solution of NMe_4OH in MeOH (0.38 mL, 0.0017 mol, 2.18 M). Upon addition of base and with vigorous stirring, a clear, yellow solution resulted. An equivalent of $CuCl_2$ (105 mg, 0.78 mmol) was added slowly to the yellow solution, which gradually turned green and eventually purple upon stirring. After allowing to stir for 12 h, the solvent was removed under vacuum and the resulting purple powder was dissolved in DMF (5 mL). Vapor diffusion of Et_2O into the solution afforded the product as purple crystals which were dried under vacuum (0.236 g, 58%). HR-MS (ESI-, CH_3OH): *m/z* = 478.137. Calcd. for **1** : 478.022. Anal. Calcd for $C_{22}H_{28}ClCuN_7O_4$: C, 47.74; H, 5.10; N, 17.71. Found: C, 47.79; H, 5.14; N, 17.24.

[NMe_4][(H_2L3)Cu(OAc)] ([NMe4][2]). Compound **2** was prepared analogously to **1** except $Cu(OAc)_2{\cdot}H_2O$ was used instead of $CuCl_2$ (0.187 g, 42%). HR-MS (ESI-, CH3OH): *m/z* = 502.032. Calcd for **2 :** 502.066. Anal. Calcd for $C_{24}H_{31}CuN_7O_6$: C, 49.95; H, 5.41; N, 16.99. Found: C, 49.26; H, 5.59; N, 16.74.

[NMe_4][(H_2L4)Cu(OH)] ([NMe_4][3]). The compound **H_4L3** (300 mg, 0.78 mmol) was added to a degassed solution of 1:3 water/pyridine. Subsequently, 0.55 mL (0.0025 mol) of a 2.18 M NMe_4OH solution in water was added to this solution resulting in a yellow color. An equivalent of $Cu(OTf)_2$ (280 mg, 0.78 mmol) was added slowly to the solution resulting in a slight green color that turned purple after stirring for several minutes. The solution was left to stir for 12 hours and then the solvent was removed under high vacuum. The resulting purple powder was dissolved in DMF (10 mL) and an equivalent amount of Et_2O (10 mL) was added and placed in a vial and left to sit under

Nitrogen atmosphere at room temperature. After 5 days purple crystals were observed on the sides of the vial that were found to be [NMe_4][**3]** (53 mg, 12%). Anal Calcd for $C_{22}H_{29}CuN_7O_5$: C, 49.39; H, 5.46; N, 18.32. Found: C, 49.05; H, 5.93; N, 17.97.

[H_2L3Cu(DMSO)]$_n$ (4) and H_2L3Cu(DMSO)$_2$ (5). The compound **H_4L3** (300 mg, 0.78 mmol) and Potassium hydride was dissolved in 10 mL of DMSO and allowed to stir until all bubbling ceased and all reagents were fully dissolved. To this solution was added Cu(OTf)$_2$ salt and the mixture allowed to stir for 4 hours to afford a purple solution. To this solution 8 mL of DCM was layered added and the resulting mixture left in a -20 °C freezer. After 24 hours purple crystals were afforded and identified as a mixture of compounds **4** and **5** by X-ray crystallography. Because the product was identified as a mixture, no CHN analysis was attempted.

[NMe_4]$_2$[(H_2L3Cu)$_2CO_3$] ([NMe_4]$_2$[6]) and [NMe_4]$_2$[(H_2L3Cu)$_3CO_3$] ([NMe_4]2[7]). Compound **3** (200mg, 0.40 mmol) was dissolved in 10 mL of DMF was left open to atmospheric CO2 for over 24 hours. Upon Et_2O vapor diffusion into the DMF solution, purple crystals were isolated and identified as a mixture of **6** and **7** by X-ray crystal structrures of randomly selected crystals. An ESI-mass spectrum of one crystal was consistent with **7** (ESI-, CH_3OH): *m/z* = 695.754. Calc for **7**: 695.571. Because the product was identified as a mixture, no CHN analysis was attempted.

[NMe4][H_2L4aCu(OAc)] ([NMe_4][8]). To a solution of ligand **H_4L4a** (R = H) (200 mg, 0.4 mmol) in 10 mL of dry DMA, 0.13 mL (0.6 mmol) of a 2.18 M NMe_4OH solution in MeOH was added and the solution was left to stir for 10 min. resulting in a clear yellow solution. To this yellow solution an equivalent of Cu(OAc)$_2$·H_2O (80 mg, 0.4 mmol) was added resulting in a green color change of the solution. The reaction was left to stir at room temp for 2 hours and then filtered. The solvent was removed under vacuum to afford a green powder. The powder was dissolved in acetone (10 mL), filtered,

and the solvent removed to afford [NMe_4][**8**]. (125 mg, 62%). Crystals of [NMe_4][**8**] were obtained by slow evaporation of Et_2O into a concentrated solution of [NMe_4][**8**] in dry DMA. HR-MS (ESI-, CH_3OH): *m/z* = 597.136. Calcd. for **8** : 597.071. Repeated attempts to obtain correct CHN analysis were unsuccessful, which we attribute to incomplete combustion.

[NMe_4][H_2L4bCu(Cl)] ([NMe_4][9]). Compound [NMe_4][**9**] was prepared analogously to [NMe_4][**8**] except $CuCl_2$ was used instead of $Cu(OAc)_2 \cdot H_2O$ and **H_4L4b** was used instead of **H_4L4a** (140 mg, 66%). Crystals of [NMe_4][**9**] were obtained by slow evaporation of Et_2O into a concentrated solution of [NMe_4][**9**] in dry MeCN. HR-MS (ESI-, CH_3OH): *m/z* = 631.134. Calc for **9**: 630.568. Repeated attempts to obtain correct CHN analysis were unsuccessful, which we attribute to incomplete combustion.

[NMe_4][(H_2L4bCu)$_2$(OH)] ([NMe_4][10]). Compound [NMe_4][**10**] was prepared analogously to [NMe_4][**9**] except $Cu(OTf)_2$ was used instead of $CuCl_2$ and an additional equivalent of NMe_4OH (0.9 mmol) was used (110mg, 43%). Crystals of [NMe_4][**10**] were obtained by slow evaporation of Et_2O into a concentrated solution of [NMe_4][**10**] in acetonitrile. These crystals were identified to be [NMe_4][**10**] by X-ray crystallography.

X-ray Crystallography. All crystals were placed onto the tip of a 0.1 mm diameter glass capillary and mounted on a Bruker APEX II Platform CCD diffractometer or a Bruker D8 Photon 100 CMOS diffractometer for data collection. The data collections were carried out using MoKα or CuKα radiation with a graphite monochromator (λ = 0.71073 Å or 1.54184 Å) at 173 K or 123 K respectively. Structure solutions were performed by direct methods using SHELXS-2013 software and refined against F2 using full-matrix-least-squares using SHELXL-97[103] and SHELXL-2013 software. All hydrogen atoms were placed as idealized and refined in a riding approximation. The thermal ellipsoids of the hydrogen atoms were bonded to the parent atom as follows:

$U_{iso}(H) = 1.2U_{eq}(N/C)$ for aromatic, amide, and -CH_2- protons and $U_{iso}(H) = 1.5U_{eq}(N/C)$ for -CH_3 protons, where $U_{eq}=1/3(U_{11}+U_{22}+U_{33})$. The structure for **9** was found to be a non-merohedral twin, in which two twin components are related to each other by a rotation around the a* direction in reciprocal space. The corresponding twin law was found to be 1 0 0 0 −1 0 1 0 −1. The CCDC codes for the deposited data are as follows: 1424005 ($[NMe_4]_2$[**7]**); 1424006 ($[NMe_4]_2$[**6]**); 1424007 ($[NMe_4]$[**1]**); 1424008 ($[NMe_4]$[**2]**); 1424009 ($[NMe_4]$[**3]**); 1424010 ($[NMe_4]$[**8]**); 1424011 ($[NMe_4]$[**9]**).

Chapter 3

Dicopper Complexes of a Naphthalene-Bridged Dinucleating Ligand

3.1 Introduction

Finding new and useful ways to utilize existing energy sources is currently a topic of intense research.[104-107] One particular facet of this research revolves around the conversion of natural gas feedstocks to a more readily usable liquid fuel source, amenable to the existing liquid fuel infrastructure. Liquid methanol production from natural gas, and more specifically from its primary component methane, is one way researchers have attempted to address this problem (Scheme 3.1).[16,108-111] The challenge of this chemical process is twofold. First, conversion of methane to methanol requires selective single oxidation so as to not simply generate carbon dioxide. Second, the C-H bond strength in methane are particularly high, with bond dissociation energies of ~104 kcal/mol. Although mild success has been had with heavy metal and zeolite based catalysts,[112-117] chemists are striving to find faster, cheaper, and more efficient ways to perform this highly desirable chemical process.

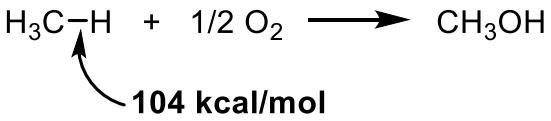

Scheme 3.1. Oxidation scheme of methane to methanol.

The identification of a class of metalloenzymes, methane monooxygenases (MMO's), whose natural function is the conversion of methane to methanol has opened the door to addressing the catalytic problems of these conversions from a bioinorganic standpoint. Methane monooxgenases come in two known forms, an iron containing soluble methane monoxygenase (sMMO),[118-120] and a copper containing particulate methane monooxygenase (pMMO).[40,121,122] The study of these systems has been undertaken to elucidate key mechanistic information of how they perform their chemistry

and give insights into development of catalyst systems capable of similar reactivity.[16,42,75,123,124]

Although the actual nuclearity of the pMMO active site is still hotly debated in the literature, a variety of dicopper-oxygen cores have often been proposed as the active species in its mechanism. Specifically, several papers have discussed the possibility of $Cu^{III}Cu^{III}$ or mixed valent $Cu^{II}Cu^{III}$ cores with possible bridging oxo or hydroxo ligands as being responsible for the initial activation of the methane C-H bond (Figure 3.1).[16,52] The reactivity of these proposed cores for activation and hydroxylation of the C-H bonds of methane has been evaluated by theory, and the provocative results have made these and similar cores synthetic targets. This chapter focuses on our synthetic efforts to generate similar cores as those proposed in pMMO using specific ligands designed to promote the formation of novel dicopper species.

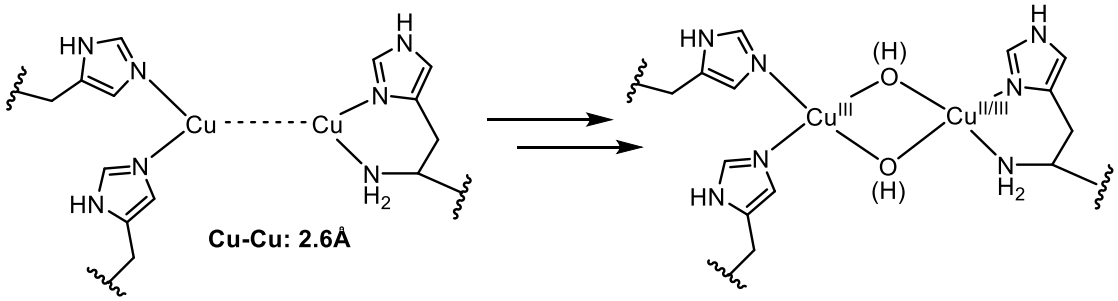

Figure 3.1. Proposed resting state of pMMO going to several reactive cores proposed previously for the oxidation of methane. Protons in parentheses may or may not be present.

Binucleating macrocyclic complexes containing pyridine dicarboxamido moieties have been previously reported by our group using the ligand $\mathbf{L2^{4-}}$ (Figure 3.2).[79] The binucleating capability of $\mathbf{L2^{4-}}$ along with the tetraanionic nature of its framework for stabilization of high-valent metal centers make them attractive from a ligand design standpoint. The one and two-electron oxidation of $[\mathbf{L2}Cu_2(OH)]^-$ yielded putative $Cu^{II}Cu^{III}$ and $Cu^{III}Cu^{III}$ complexes. Importantly, the observed Cu-Cu distances of the $\mathbf{L2^{4-}}$

complexes (~2.7 Å) are close to the Cu-Cu distances predicted in the pMMO active site (~2.6 Å). A shortcoming of the dicopper complexes of $\mathbf{L2}^{4-}$ is the apparent ability to only accommodate a single bridging ligand. To facilitate C-H bond activation and subsequent hydroxylation of substrate, we suspect a second oxo or hydroxo ligand for radical rebound and subsequent hydroxylation is necessary.

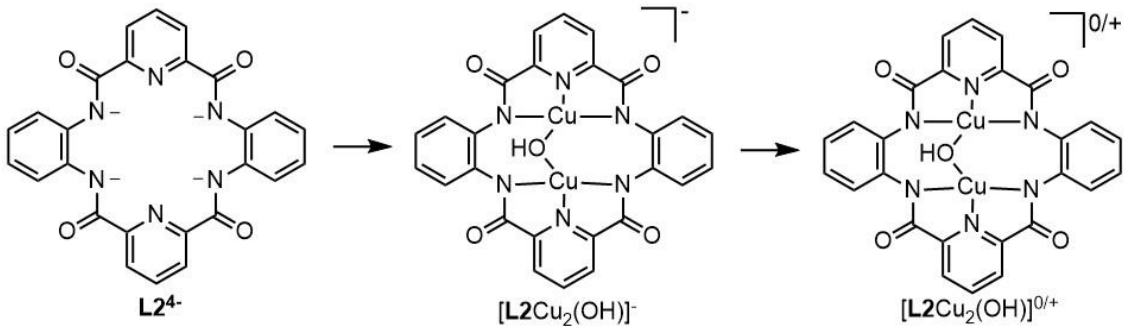

Figure 3.2. Previously reported tetraanionic ligand $\mathbf{L2}^{4-}$, its metallated μ-hydroxo complex $[\mathbf{L2}Cu_2(OH)]^-$ and its oxidized forms $[\mathbf{L2}Cu_2(OH)]^{0/+}$.

We hypothesize that the classical rebound pathway known to occur in reactions of terminal metal-oxos such as those found in enzymes like cytochrome P450 can be extended to dicopper systems. In particular, we suggest that a dicopper(III) complex with two proximal terminal hydroxo ligands can effect hydroxylation alkanes. Initial HAT, known to occur rapidly with mononuclear Cu^{III}-OH complexes, would yield organic radical (R•), which could be trapped by a subsequent "rebound" step as outlined in Figure 3.3. Due to its inherent geometric limitations, $\mathbf{L2}^{4-}$ is unsuitable for supporting dicopper cores with two hydroxo or oxo ligands, preventing study of their competency in the hydroxylation chemistry of organic substrates in these frameworks. We hypothesized that in order to prevent formation of bridging hydroxide complexes that we postulate will be less reactive, a ligand variant of $\mathbf{L2}^{2-}$ with a linker to allow the appropriate geometry is needed.

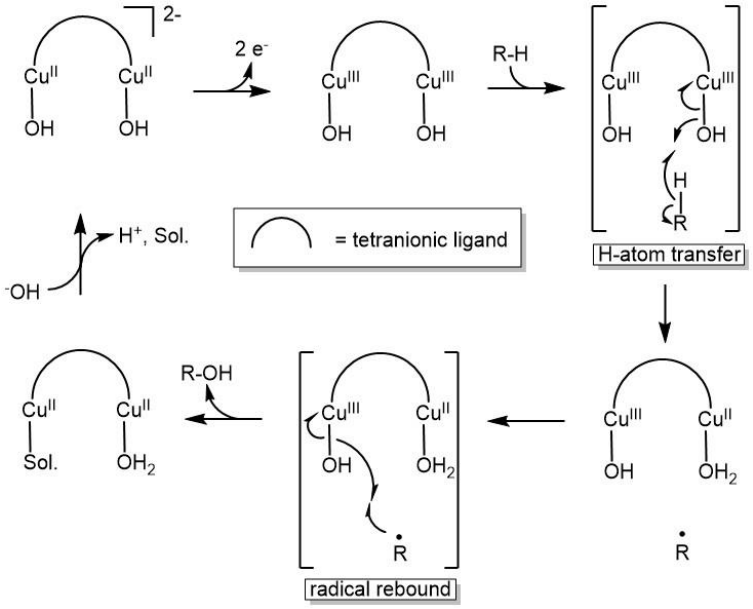

Figure 3.3. Proposed C-H bond activation and hydroxylation reaction mechanisms for terminal bis-hydroxo $[Cu^{III}_2(OH)_2]^{4+}$ core supported by a tetraanionic ligands.

One such ligand variation, described herein, is the macrocyclic ligand **L5^{4-}.** This new macrocycle contains naphthyl linkers that bridge the pyridine dicarboxamide pockets instead of the phenyl linkers employed in **L2^{4-}**. Exploiting the tendency of the pyridine dicarboxamide planes to orient themselves orthogonally to their aromatic groups, we hypothesize that by employing a naphthyl linker we will open up the labile sites such that the dimetallic center can accommodate two ligands. This ligand geometry may be suitable for the generation of the target bis-hydroxo $[Cu^{II}_2(OH)_2]^{2+}$ core to give the compound [**L5**$Cu_2(OH)_2]^{2-}$ (**16,** Figure 3.4**)**. Herein we report the development of a synthesis of **L5^{4-}** and explorations of its copper coordination chemistry. While the ultimate aim of developing a terminal bis(hydroxo)Cu^{III}_2 species was not met, novel structures and reactivity of dicopper compounds were uncovered that will inform further efforts to target models of pMMO.

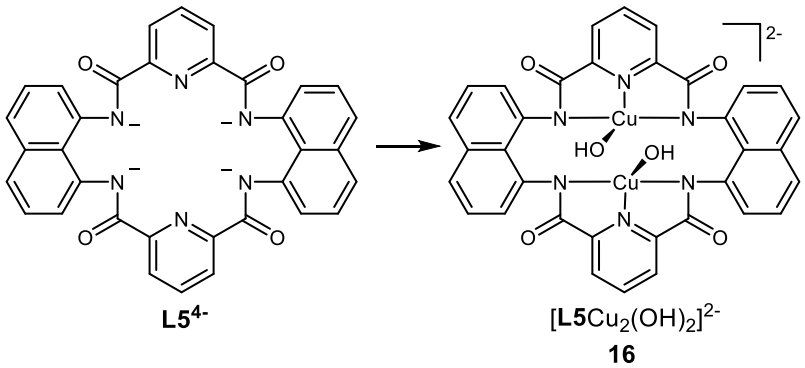

Figure 3.4.Target macrocyclic ligand $\mathbf{L5}^{4-}$ and the proposed dianionic species $[\mathbf{L5}Cu_2(OH)_2]^{2-}$ (**16**).

3.2 Synthesis and characterization of macrocyclic proligand H_4L5

The synthesis of target macrocyclic proligand **H_4L5** was initially attempted using similar methods to those previously described for synthesis of other pyridine dicarboxamide compounds[35,97,125,126] by employing a condensation reaction of 2,6-pyridinedicarbonyl dichloride with a corresponding equivalent of 1,8-diaminonaphthalene. To prevent undesired oligomeric products, slow addition of 1,8-diaminonaphthalene to a solution of the 2,6-pyridinedicarbonyl dichloride and base was performed. When this initial synthetic route was used a red cloudy mixture was observed. This reaction mixture was found to contain two products after workup by NMR spectroscopy and ESI-MS. One of these products was found to be the desired **H_4L5** but only as a minor component (<10%), with a major component of a bright red organic compound (Scheme 3.2). ^{1}H NMR spectroscopy of the isolated red species shows peaks consistent with the three aromatic pyridine protons as well as three equivalent sets of naphthyl aromatic proton signals (Figure 3.5). No signals consistent with carboxamide protons were detected, suggesting that this species was not **H_4L5** or any other carboxamide containing species.

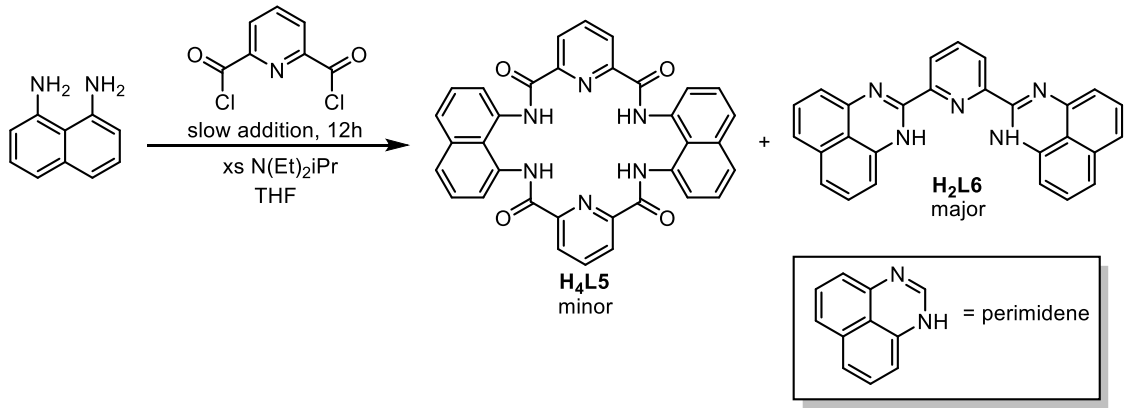

Scheme 3.2. Synthetic procedure with slow addition of 2,6-pyridinedicarbonyl dichloride added slowly to a THF solution of 1,8-diaminonaphthalene in the presence of excess *N*,*N*-diisopropylethylamine.

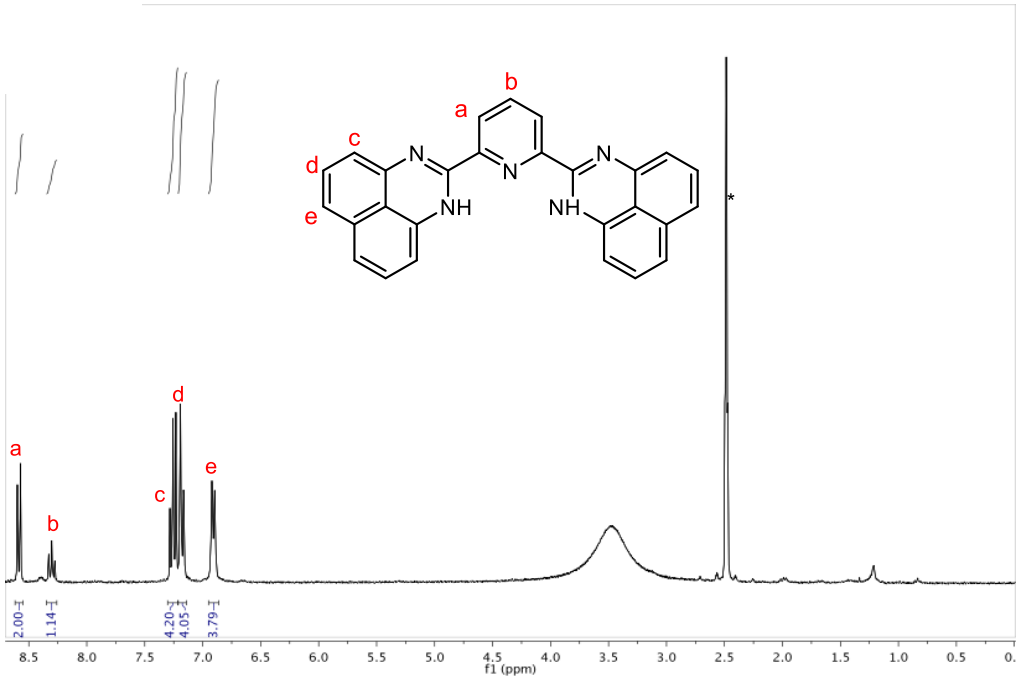

Figure 3.5. ^{1}H NMR spectrum of purified **H_2L6** in DMSO-*d6*.

Crystallization of the red compound and subsequent X-ray crystallography experiments led to the identification of this compound as a 2,6-diperimidine pyridine

compound (**H_2L6**, Figure 3.6). The crystal structure is in agreement with the ^{1}H NMR spectrum shown in Figure 3.5. The structure of **H_2L6** is completely planar suggesting it is fully conjugated throughout the molecule. The formation of this undesired species under the reaction conditions, as described above, can be rationalized by invoking a double condensation mechanism of the diamine with the 2,6-pyridinedicarbonyl dichloride. In this proposed mechanism, the desired condensation of an amino arm with the carbonyl chloride group occurs accompanied by the loss of HCl. After this initial condensation occurs, the carboxamide moiety now contains a free amino group which is free to react with the carbonyl moiety and lose an equivalent of water to result in imine formation. This condensation process is thought to be particularly favorable as it forms a stable six member ring (Scheme 3.3). The proposed reaction route is further supported by ESI-MS data of an aliquot of the reaction solution before completion (~5 min). This ESI-MS data has features which correspond to two intermediate species that have undergone carbonyl chloride condensation to form the carboxamide arms with one (*m/z* = 428.029) and two (*m/z* = 446.006) unreacted amine groups, as well as the final **H_2L6** product at *m/z* = 410.032 (Figure 3.7). Consistent with the mechanism each feature is 18 mass units apart, the mass of the molecule of water that is lost upon imine formation.

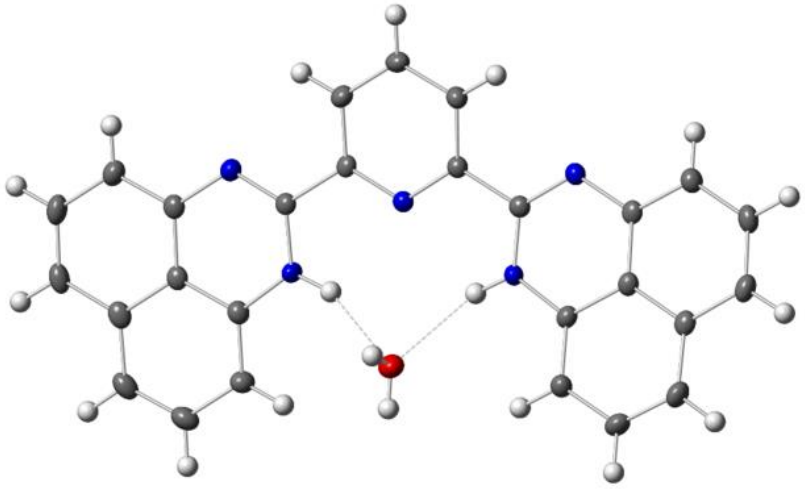

Figure 3.6. Depiction of X-ray crystal structure of **H_2L6** with a molecule of water hydrogen bonding to amide protons. All nonhydrogen atoms shown as 50% thermal ellipsoids and hypothesized hydrogen bonds as dashed lines.

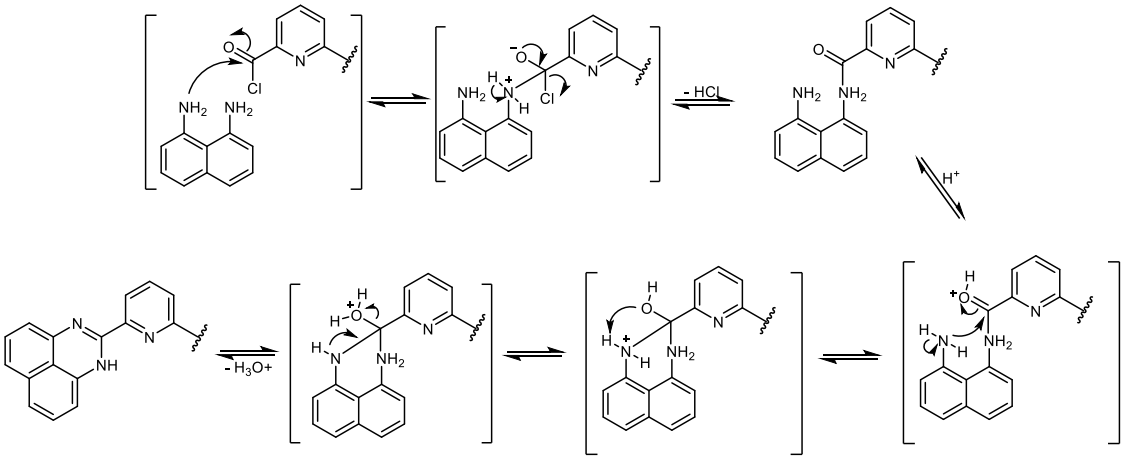

Scheme 3.3. Proposed mechanism for formation of perimidine unit to form **H_2L6.**

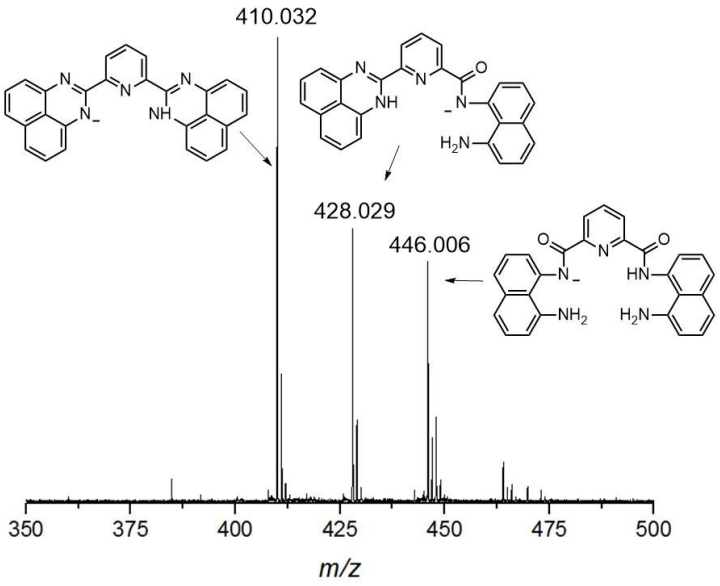

Figure 3.7. Negative ion mode ESI-MS of an aliquot of the reaction mixture of 1,8-diaminonaphthalene with 2,6 pyridinedicarbonyl dichloride after 30 min. of reaction time.

It was discovered that in an alternative synthetic route, if no external base was added to the reaction mixture, **H_2L6** was formed as the exclusive product of the reaction (Scheme 3.4). This observation can be rationalized by the fact that imine formation reactions from amino and carbonyl groups are known to be catalyzed by acid in the proposed mechanism shown in Scheme 3.3. If no external base is added then the initial condensation to form the carboxamide will produce an equivalent of HCl. The HCl is then free to catalyze the next imine condensation reaction. Accumulation of HCl in solution seems to make the formation of **H_2L6** much more favorable, perhaps never allowing **H_4L5** to form under these acidic reaction conditions. This proposed synthetic route may explain the absence of **H_4L5** as a product.

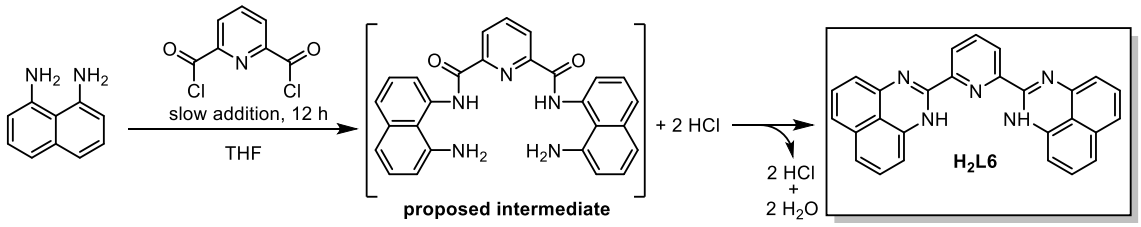

Scheme 3.4. Synthetic procedure with slow addition of 2,6 pyridinedicarbonyl dichloride added slowly to a THF solution of 1,8-diaminonaphthalene with no external base added. Proposed hemicyclic intermediate shown in brackets.

Under the presumption that the carboxamide formation occurs before an imine formation step, the above synthetic procedure was modified with the intention of favoring the production of the target macrocycle **H_4L5**. To limit formation of the proposed hemicyclic intermediates that can undergo intramolecular reactions to form **H_2L6**, 1,8-diaminonaphthalene was added to a concentrated solution of 2,6-pyridinedicarbonyl dichloride with excess base. The change in the order of addition of reagents was meant to take advantage of the supposed difference of rates between the two condensation steps that ultimately form **H_2L6**. Prevention of the hemicyclic intermediate from Scheme 3.4 would be achieved by allowing the amino groups of the 1,8-diaminonaphthalene to react with the 2,6-pyridinedicarbonyl dichloride first and prevent unreacted amino groups to undergo imine formation. This new synthetic method, outlined in Scheme 3.5, can be envisioned to proceed through an alternate hemicyclic intermediate which then can close upon condensation of a second 2,6-pyridinedicarbonyl dichloride group to give **H_4L5**. We were gratified to find that when these new reaction conditions are used, **H_4L5** forms with only small amounts of **H_2L6** observed before purification. Upon recrystallization, **H_4L5** was obtained in 22% yield as a white crystalline solid.

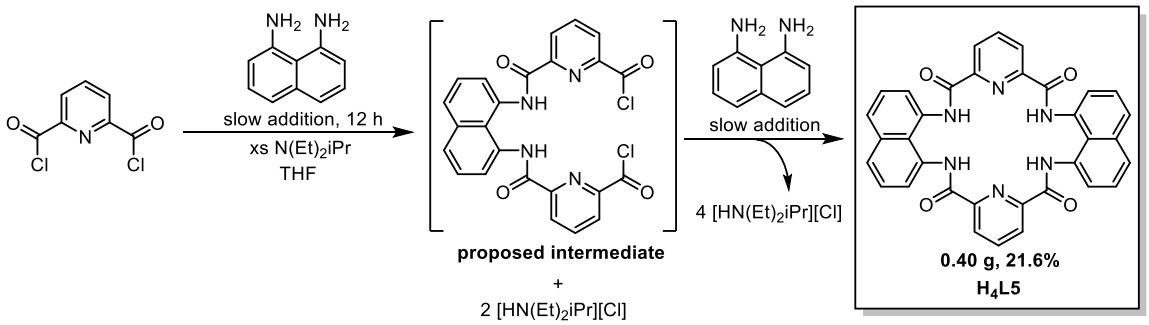

Scheme 3.5. Synthetic procedure with slow addition of 1,8-diaminonaphthalene added slowly to a THF solution of 2,6 pyridinedicarbonyl dichloride in the presence of excess *N*,*N*-diisopropylethylamine. Proposed hemicyclic intermediate shown in brackets.

The product **H4L5** was identified by ^{1}H NMR spectroscopy (Figure 3.8) and HR-ESI-MS (Figure 3.9). The ^{1}H NMR spectrum shows four equivalent protons at 11.27 ppm consistent with the presence of the diagnostic carboxamide protons, as well as aromatic protons consistent with the pyridyl and naphthyl groups. Mass spectrometry also has two features that correspond to a single deprotonated ligand ([**H3L5**]$^{-}$, *m/z* = 577.129) and a second peak corresponding to **H4L5** with a single chloride anion (*m/z* = 613.102). Single crystals of **H4L5** were grown by vapor diffusion of diethyl ether into DMA solutions. X-ray crystallography experiments provided the three-dimensional structure of **H4L5** (Figure 3.10), confirming the formulation of the desired macrocyclic compound. Interestingly, the topology of **H4L5** as seen by the crystal structure is unique in that both pyridyl planes run parallel to one another with the naphthyl bridges running roughly perpendicular to the pyridyl planes. The observed geometry contrasts with that of the previously synthesized compound **H4L2** which contains phenyl bridging groups but is only modestly bent by comparison. Both **H4L5** and **H4L2** contain hydrogen bonding interactions from their carboxamide protons to a molecule of DMA. This type of interaction is typical as carboxamide macrocycles are known to be good receptors for anions and polar organics,[75,96] as noted in Chapter 2.

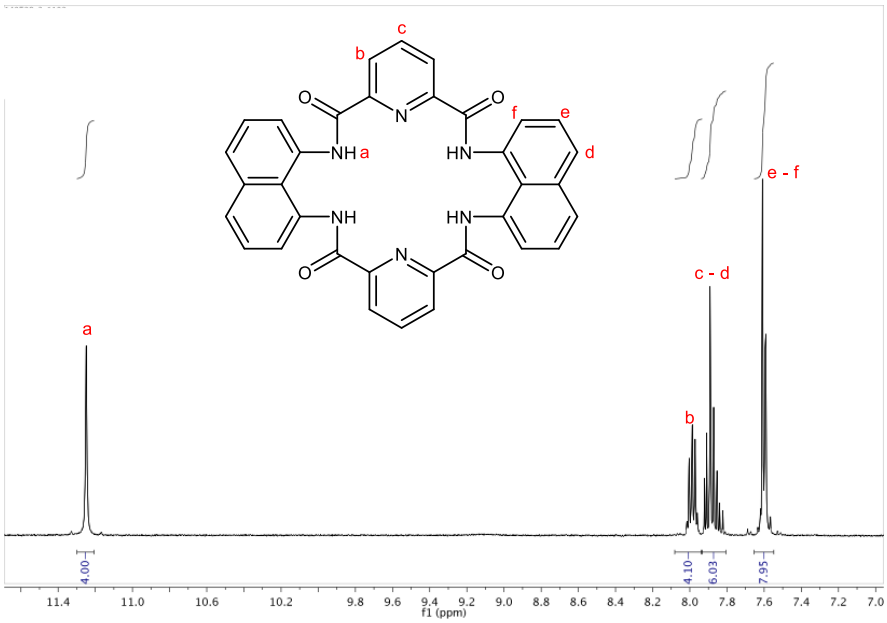

Figure 3.8. ^{1}H NMR spectrum of purified **H_2L5** in DMSO-*d6*.

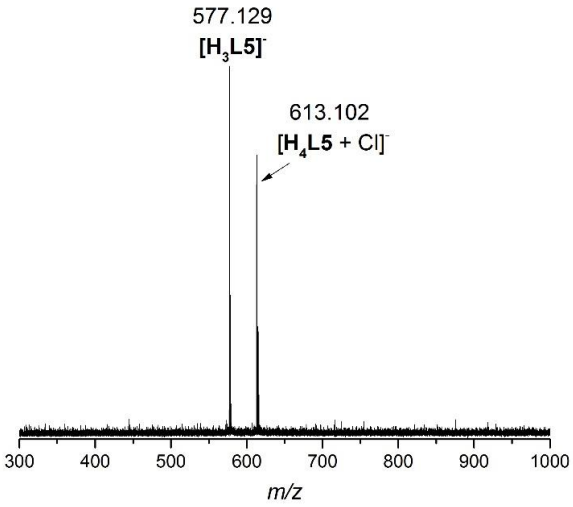

Figure 3.9. Negative mode HR-ESI-MS of **H_4L5** run in MeOH

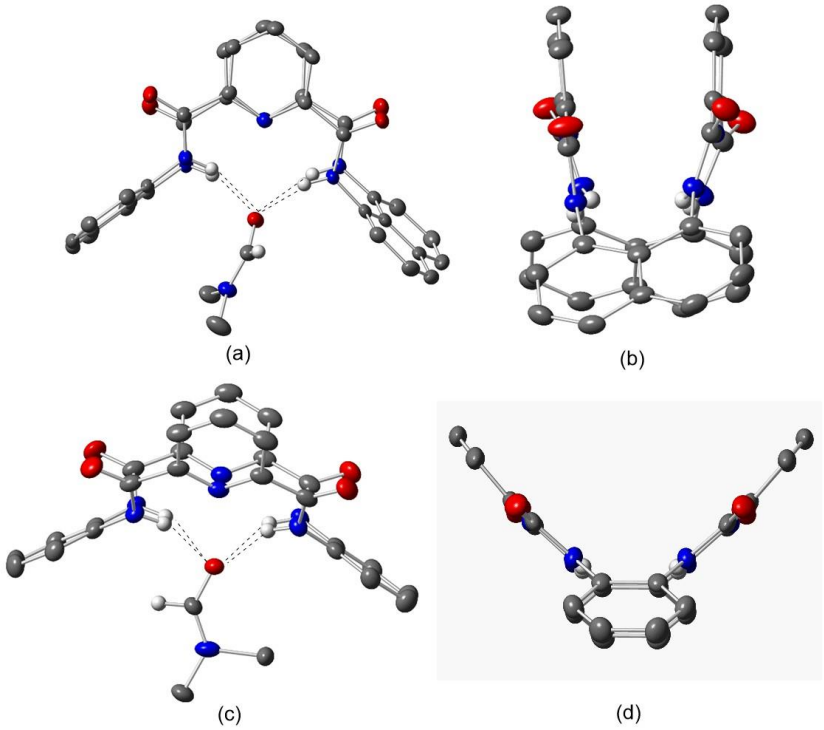

Figure 3.10. Front-on view of X-ray crystal structure of **H_4L5** with DMF molecule hydrogen bonding to carboxamide protons (a), side-on view **H_4L5** with DMF molecule omitted for clarity (b), Front-on view of X-ray crystal structure of **H_4L2** with DMF molecule hydrogen bonding to carboxamide protons (c), and side-on view **H_4L2** with DMF molecule omitted for clarity (d). All nonhydrogen atoms shown as 50% thermal ellipsoids and hypothesized hydrogen bonds as dashed lines.

A final modification for the optimization of the synthetic procedure was performed to increase scale and yield as well as decrease the overall reaction time for the synthesis of **H_4L5**. It was discovered that by cooling the concentrated THF solution of the 2,6-pyridinedicarbonyl dichloride and *N*,*N*-diisopropylethylamine to ~0° C and adding a THF solution of 1,8-diaminonaphthalene over the course of approx. 1 min, **H_4L5** will subsequently precipitate out of the concentrated THF solution and is easily collected by filtration to give the product in 71% yield on a ~ 4 g scale (Scheme 3.6). This method, which is precedented in macrocycle syntheses,[127] can be run on scales

roughly four times greater than that of the slow addition procedures described previously, and does not seem to increase production of larger macrocycles or oligomeric species. The absence of oligomeric species is not fully understood but suggests that **H_4L5** is the most thermodynamically favorable species to form in a concentrated reaction mixture.

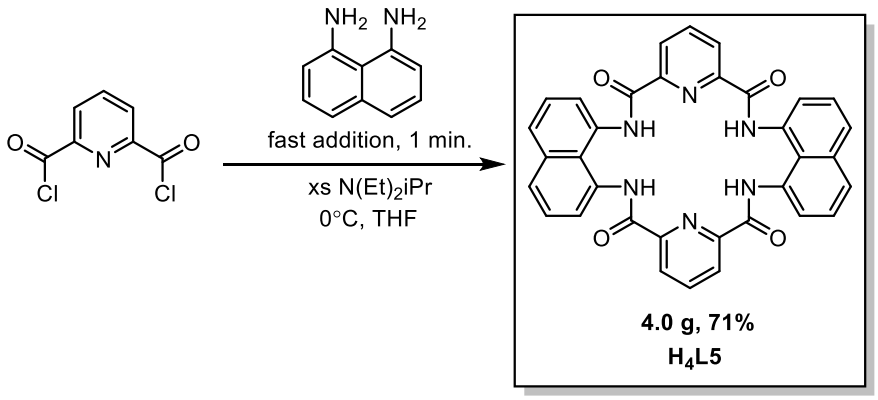

Scheme 3.6. Synthetic procedure of **H_4L5** using fast addition method.

3.3 Synthesis and characterization of copper complexes.

Initial attempts to metallate the macrocycle **H_4L5** to generate dicopper **$L5^{4-}$** complexes involved use of procedures similar to those previously reported for generating dicopper complexes of **$L2^{2-}$**.[79] In an effort to prepare the target compound bis-hydroxo complex **16**, the ligand was deprotonated with excess equivalents of tetramethylammonium hydroxide and $Cu(OTf)_2$ was added (Scheme 3.7). When this reaction was performed in *N*,*N*-dimethyl acetamide (DMA) as a solvent medium, a green product powder was isolated. Isolation of pure bulk product was not able to be obtained but single crystals were able to be grown from diethyl ether diffusion into a solution of DMA. An initial crystal structure of the metallated product was obtained but only isotropic refinement was possible due to the poor quality of the X-ray data (R1 = 10.00). Atom connectivity information of the product was still obtainable, however, allowing identification of the green product as [**L5**Cu_2(OAc)]$^-$ (**11**, Figure 3.11). The X-ray crystal

structure definitively shows both pyridine dicarboxamido pockets occupied by copper(II) centers with a bridging acetato ligand spanning the two metals. **L2**$^{4-}$ has never been shown to be proficient at generating dicopper cores in such a geometry, suggesting the desired topological differences of the macrocycle **L5**$^{4-}$ may be responsible for making a μ(1,3) coordination mode accessible. The two copper centers are in close proximity with a Cu1-Cu2 distance of ~2.7 Å (approximate distance from low quality X-ray data) and square planar geometries with respect to the NNN plane and the acetato ligand (Table 3.1). The primary coordination sphere of the dicopper core is notably similar to that of the crystal structure of $Cu(OAc)_2 \bullet H_2O$ (Cu-Cu: 2.6143(17) Å) which is known to dimerize as a dicopper "paddle-wheel" complex with four bridging μ(1,3) coordinated acetate ligands.[128] The presence of an acetate in the compound led us to speculate that hydrolysis of an in-situ generated hydrolytic intermediate (possibly **16**) may be performing hydrolysis of DMA solvent to afford the acetato complex **11**.

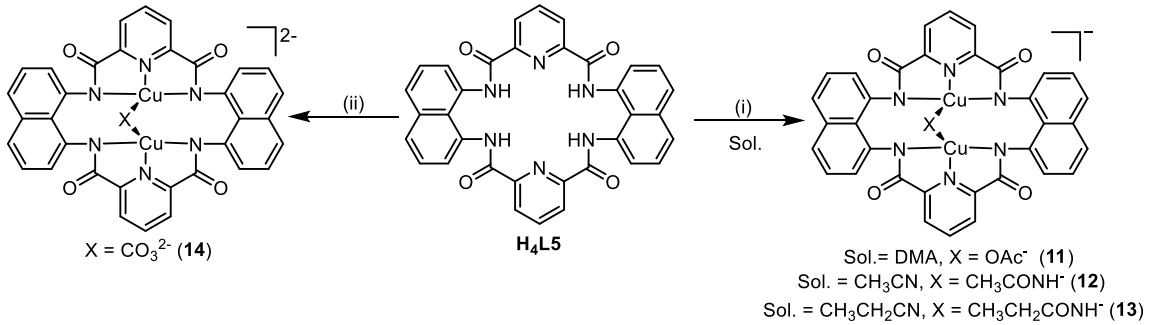

Scheme 3.7. Synthetic procedure for generation of (i) **11-13** with 6 equiv. of NMe_4OH and 2.5 equiv. of $Cu(OTf)_2$ and (ii) **14** with 6 equiv. of NMe_4OH and 2.5 equiv. $Cu(OTf)_2$ in a 1:3 water/pyridine solvent mixture and subsequently exposed to ambient CO_2(g).

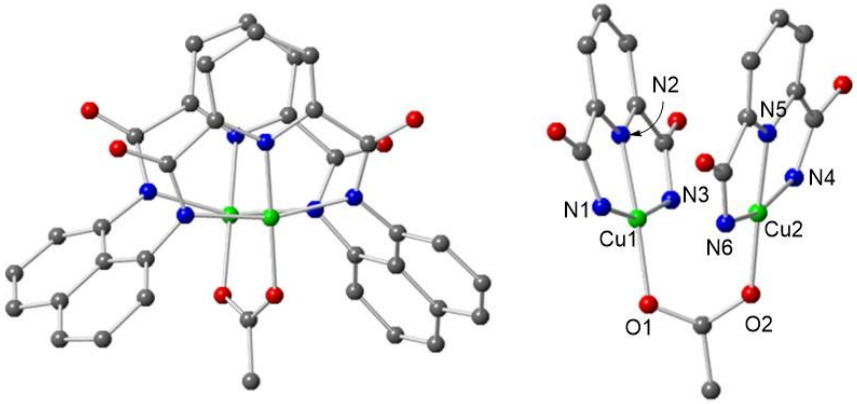

Figure 3.11. Representations of the anionic portion of the X-ray structure of [NMe_4][**L5**Cu_2(OAc)] ([NMe_4][**11**]) from front-on view (left) and the side-on dicopper core with naphthyl linkers omitted for clarity (right). All atoms displayed isotropically.

Table 3.1. Selected interatomic distances (Å) and Angles (deg) for [NMe_4][**L5**Cu_2(OAc)] ([NMe_4][**11**]).

[NMe_4][**L5**Cu_2(OAc)] ([NMe_4][**11**])			
Cu1 – N1	2.01(21)	N2 – Cu1 – O1	176.7(8)
Cu1 – N2	1.90(17)	N2 – Cu1 – N1	80.0(16)
Cu1 – N3	2.02(20)	O1 – Cu1 – N1	100.1(13)
Cu1 – O1	1.90(17)	N2 – Cu1 – N3	80.7(16)
Cu1 – Cu2	2.694(48)	O1 – Cu1 – N3	99.3(12)
Cu2 – N4	2.024(20)	N1 – Cu1 – N3	160.5(14)
Cu2 – N5	1.849(22)	N5 – Cu2 – O1	177.5(9)
Cu2 – N6	2.030(22)	N5 – Cu2 – N4	82.7(16)
Cu2 – O1	1.876(19)	O2 – Cu2 – N4	98.4(14)
		N5 – Cu2 – N6	81.7(16)
		O2 – Cu2 – N6	97.2(13)
		N4 – Cu2 – N6	164.3(16)

To further investigate the metallation chemistry of the new ligand $\mathbf{L5}^{4-}$, other solvents were used in attempts to isolate the desired bis-hydroxo complex $[\mathbf{L5}Cu_2(OH)_2]^{2-}$ (**16**). When acetonitrile is used as a solvent the resulting product was found to be yet another hydrolytic decomposition species $[\mathbf{L5}Cu_2(CH_3CONH)]^-$ (**12**). Again, bulk pure product was not able to be obtained and as such only crude product could be obtained as a green powder. From the crude product several X-ray crystallography quality crystals of this compound were grown by adding potassium triflate to give the potassium salt of **12** (Figure 3.12). The anionic compound **12** contains a similar geometry to that observed in **11** but with an acetamido ligand spanning the dicopper core in the same μ(1,3) fashion. The Cu1-Cu2 distance is 2.780(11) Å (Table 3.2). Again in this structure, both coppers were found to exhibit pseudo square planar geometries with both labile sites coordinated to the oxygen and nitrogen of the acetamido ligand.

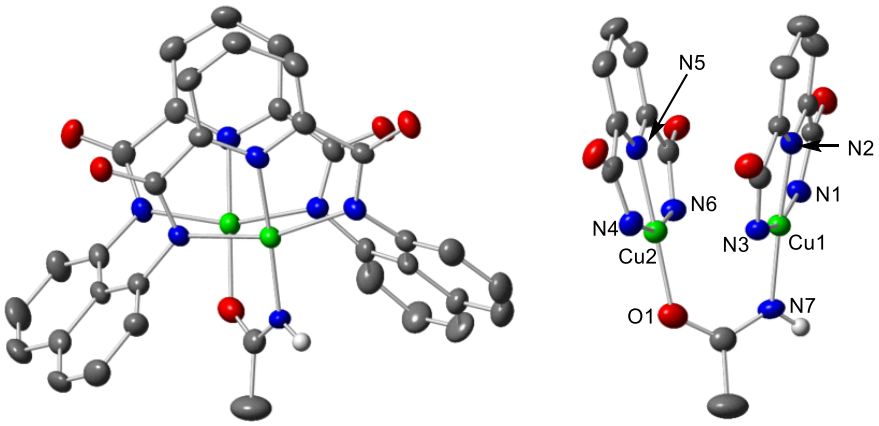

Figure 3.12. Representations of the anionic portion of the X-ray structure of [K][**L5**$Cu_2(CH_3CONH)$] ([K][**12**]) from front-on view (left) and the side-on dicopper core with naphthyl linkers omitted for clarity (right). All nonhydrogen atoms shown as 50% thermal ellipsoids.

Table 3.2. Selected interatomic distances (Å) and Angles (deg) for [K][**L5**$Cu_2(CH_3CONH)$] ([K][**12]**).

[K][**L5**$Cu_2(CH_3CONH)$] ([K][**12]**)			
Cu1 – N1	2.003(5)	N2 – Cu1 – N7	175.53(21)
Cu1 – N2	1.925(5)	N2 – Cu1 – N1	80.17(21)
Cu1 – N3	2.041(5)	N7 – Cu1 – N1	102.42(20)
Cu1 – N7	1.914(5)	N2 – Cu1 – N3	80.62(20)
Cu1 – Cu2	2.780(1)	N7 – Cu1 – N3	96.99(20)
Cu2 – N4	1.994(5)	N1 – Cu1 – N3	160.43(20)
Cu2 – N5	1.927(5)	N5 – Cu2 – O1	178.75(21)
Cu2 – N6	1.999(5)	N5 – Cu2 – N4	79.86(21)
Cu2 – O1	1.922(5)	O1 – Cu2 – N4	99.83(20)
		N5 – Cu2 – N6	80.55(20)
		O1 – Cu2 – N6	99.76(19)
		N4 – Cu2 – N6	160.41(20)

To confirm whether analogous species with other nitriles form under the same conditions that produce **12**, the metallation reaction of $\mathbf{L5^{4-}}$ was run in propionitrile solvent. Upon crystallization of the product and subsequent X-ray analysis, the product of this reaction was found to be [**L5**$Cu_2(CH_3CH_2CONH)]^-$ (**13**) with similar geometric characteristics to those observed in **11** and **12,** again with a short Cu-Cu distance of 2.811(17) Å **(**Table 3.3, Figure 3.13). We took the presence of propionamide as confirmation that hydrolysis of nitriles is a general pathway that may involve an intermediate hydrolytic species such as **16**.

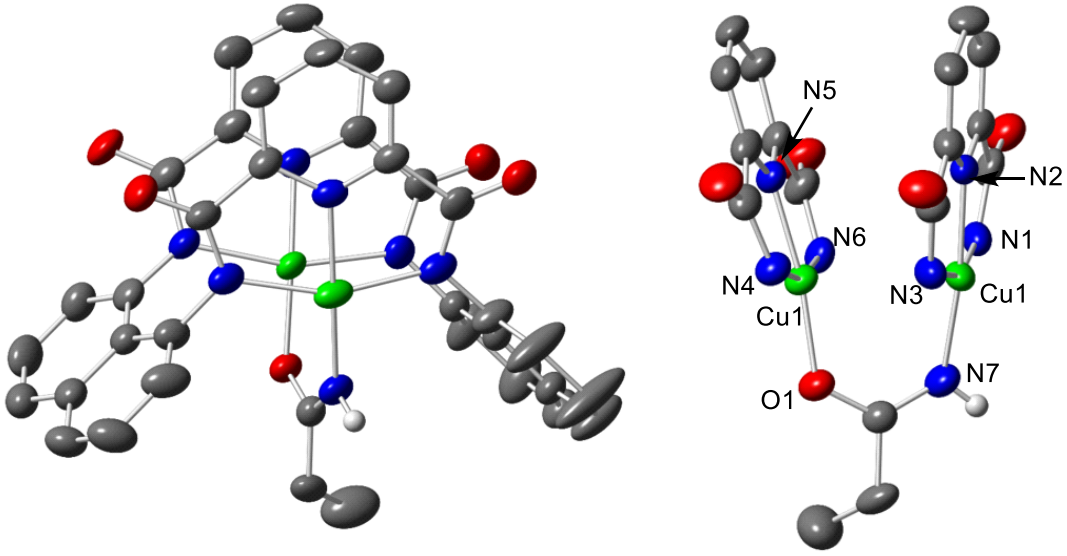

Figure 3.13. Representations of the anionic portion of the X-ray structure of [NMe_4][**L5**Cu_2(CH_3CH_2CONH)] ([NMe_4][**13**]) from front-on view (left) and the side-on dicopper core with naphthyl linkers omitted for clarity (right). All nonhydrogen atoms shown as 50% thermal ellipsoids.

Table 3.3. Selected interatomic distances (Å) and Angles (deg) for [NMe_4][**L5**Cu_2(CH3CH_2CONH)] ([NMe_4][**13**]).

[NMe_4][**L5**Cu_2(CH3CH_2CONH)] ([NMe_4][**13**])			
Cu1 – N1	1.993(7)	N2 – Cu1 – N7	173.01(26)
Cu1 – N2	1.937(6)	N2 – Cu1 – N1	78.94(25)
Cu1 – N3	2.007(6)	N7 – Cu1 – N1	100.76(27)
Cu1 – N7	1.926(6)	N2 – Cu1 – N3	80.26(25)
Cu1 – Cu2	2.812(1)	N7 – Cu1 – N3	99.01(27)
Cu2 – N4	2.022(6)	N1 – Cu1 – N3	158.00(25)
Cu2 – N5	1.918(6)	N5 – Cu2 – O1	171.97(23)
Cu2 – N6	2.020(6)	N5 – Cu2 – N4	80.16(24)
Cu2 – O1	1.906(5)	O1 – Cu2 – N4	98.71(23)
		N5 – Cu2 – N6	81.03(24)

O1 – Cu2 – N6	99.98(23)
N4 – Cu2 – N6	161.18(24)

In order to avoid undesirable solvent hydrolysis and target **16** for synthesis, metallation attempts were then employed using water/pyridine mixtures as the solvent medium. These metallation conditions resulted in dark green solutions, but attempts to crystallize and purify the product under inert atmosphere proved to be difficult. When these reaction solutions were exposed to ambient atmosphere, however, we were able to obtain several X-ray quality crystals from organic solvents. X-ray crystallography revealed the formation of a dianionic complex $[\mathbf{L5}Cu_2(CO_3)]^{2-}$ (**14,** Figure 3.14). This new dianionic species exhibits the μ(1,3) bridge motif observed in complexes **11-13** but with a carbonato ligand acting as the bridging group. A Cu1-Cu2 distance of 2.717(7) Å is observed and the same pseudo square planar geometry about the copper centers is conserved (Table 3.4). Charge balance and bond lengths are consistent with the carbonato unit being fully deprotonated making the complex **14** dianionic, as opposed to the monoanionic complexes **11-13**. Much like the reactions discussed in section 2.3.2, it is believed that a metal-hydroxo intermediate (possibly **16**) may be reacting in a nucleophilic manner with ambient CO_2(g) to produce the carbonato ligand.

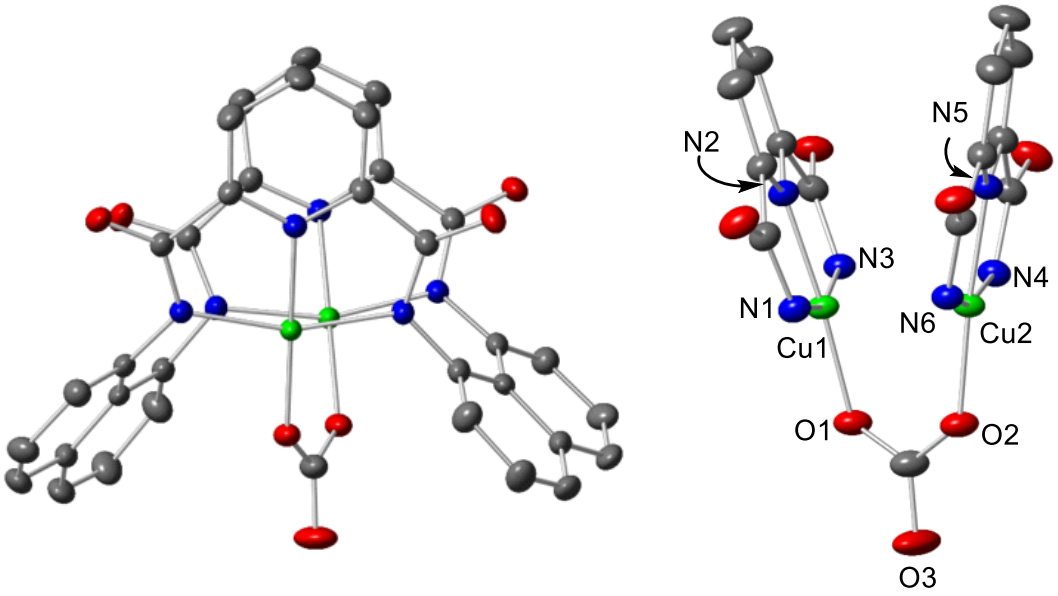

Figure 3.14. Representations of the dianionic portion of the X-ray structure of $[NMe_4]_2$[**L5**$Cu_2(CO_3)$] ($[NMe_4]_2$[**14**]) from front-on view (left) and the side-on dicopper core with naphthyl linkers omitted for clarity (right). All nonhydrogen atoms shown as 50% thermal ellipsoids.

Table 3.4. Selected interatomic distances (Å) and Angles (deg) for $[NMe_4]_2$[**L5**$Cu_2(CO_3)$] ($[NMe_4]_2$[**14**]).

$[NMe_4]_2$[**L5**$Cu_2(CO_3)$] ($[NMe_4]_2$[**14**])			
Cu1 – N1	1.983(2)	N2 – Cu1 – O1	175.47(7)
Cu1 – N2	1.915(2)	N2 – Cu1 – N1	80.53(7)
Cu1 – N3	2.004(2)	O1 – Cu1 – N1	99.11(7)
Cu1 – O1	1.900(2)	N2 – Cu1 – N3	80.72(7)
Cu1 – Cu2	2.7172(7)	O1 – Cu1 – N3	99.66(7)
Cu2 – N4	1.983(2)	N1 – Cu1 – N3	161.23(8)
Cu2 – N5	1.915(2)	N5 – Cu2 – O2	175.47(7)
Cu2 – N6	2.004(2)	N5 – Cu2 – N4	80.53(7)
Cu2 – O2	1.900(2)	O2 – Cu2 – N4	99.11(7)
		N5 – Cu2 – N6	80.72(7)
		O2 – Cu2 – N6	99.66(7)

N4 – Cu2 – N6	161.23(8)

Another solvent change to methanol (MeOH) in these reactions yielded yet another new dicopper species but with a coordination mode that is different from those observed in complexes **11**-**14** (Scheme 3.8). The bulk product could only be obtained as a crude product in the form of a green powder but single crystals for crystallography were able to be grown by diethyl ether diffusion into MeOH solutions of the product. The crystal structure was identified as [**L5**Cu_2(OMe)]$^-$•2(MeOH), a dicopper species with a μ-methoxo monoatomic bridge with two flanking neutral methanol molecules coordinated near the axial positions of the two copper centers (Figure 3.15). This dicopper(II) μ-methoxo moiety has previously been observed crytallographically supported by the ligand **L2**$^{4-}$, also shown in Figure 3.13. This anionic complex, [**L2**Cu_2(OMe)]$^-$•MeOH, contains only a single neutral methanol molecule as opposed to the two methanol molecules observed in **15**.

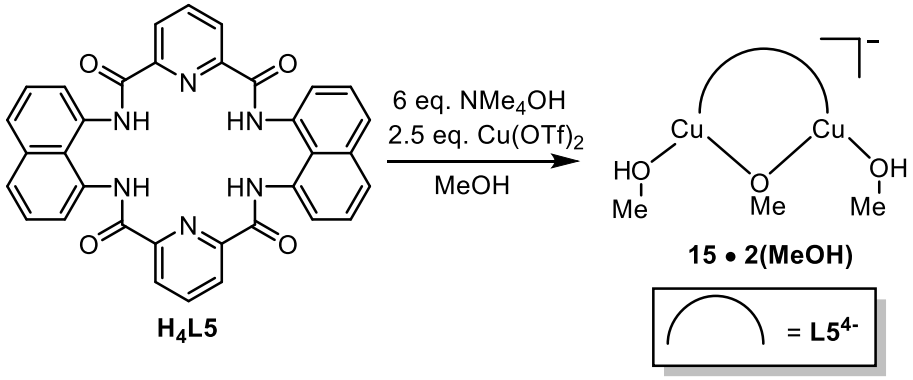

Scheme 3.8. Synthetic procedure for generation of compound [**L5**Cu_2(OMe)]$^-$•2(MeOH) (**15**•2(MeOH))

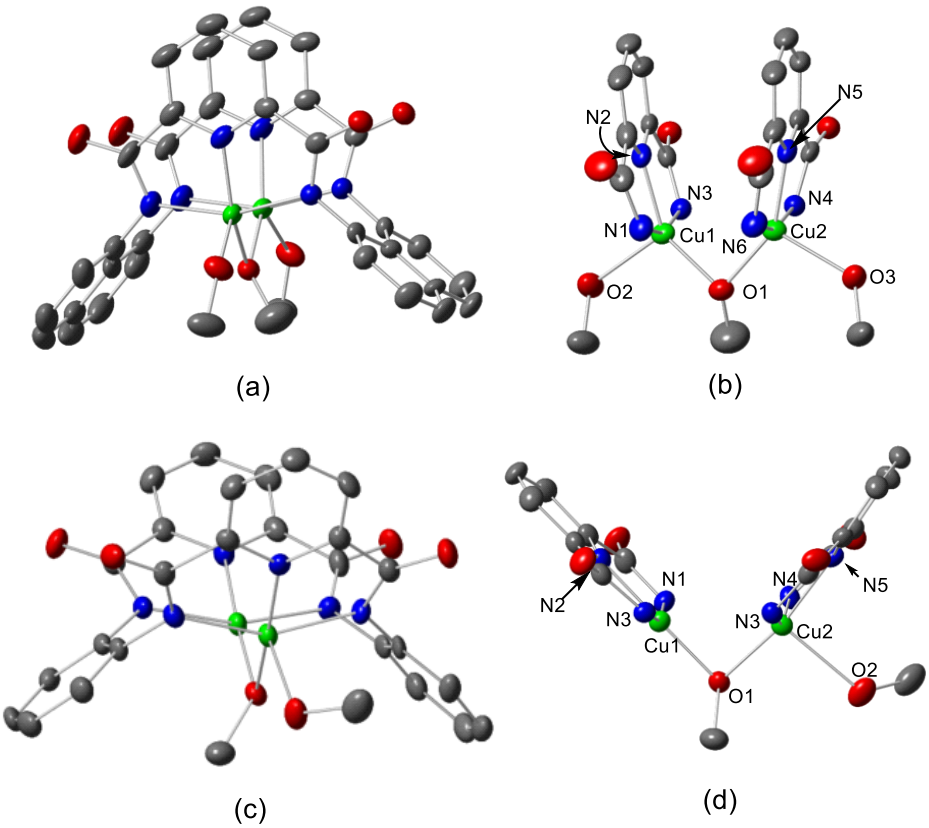

Figure 3.15. Representations of the anionic portion of the X-ray structure of [NMe_4][**L5**Cu_2(OMe)] • 2(MeOH) ([NMe_4][**15**] • 2(MeOH)) from front-on view (a) and the side-on dicopper core with naphthyl linkers omitted for clarity (b), the anionic portion of the X-ray structure of [NMe_4][**L2**Cu_2(OMe)] • MeOH (c), and the side-on dicopper core with phenyl linkers omitted for clarity (d). All nonhydrogen atoms shown as 50% thermal ellipsoids.

Table 3.5. Selected interatomic distances (Å) and angles (deg) for [NMe_4][**L5**Cu_2(OMe)]•2(MeOH) ([NMe_4][**15**]•2(MeOH)) and [NMe_4][**L2**Cu_2(OMe)]•MeOH.

[NMe_4][**L5**Cu_2(OMe)] • 2(MeOH) ([NMe_4][**15**] • 2(MeOH))			
Cu1 – N1	2.024(6)	N2 – Cu1 – O1	148.04(23)
Cu1 – N2	1.938(6)	N2 – Cu1 – N1	79.75(25)
Cu1 – N3	2.024(6)	O1 – Cu1 – N1	100.39(22)
Cu1 – O1	1.952(5)	N2 – Cu1 – N3	79.51(27)
Cu1 – O2	2.228(6)	O1 – Cu1 – N3	95.67(24)

Cu1 – Cu2	2.729(1)	N1 – Cu1 – N3	159.05(26)
Cu2 – N4	2.023(6)	N5 – Cu2 – O1	148.09(24)
Cu2 – N5	1.932(6)	N5 – Cu2 – N4	79.80(27)
Cu2 – N6	2.024(6)	O1 – Cu2 – N4	95.58(24)
Cu2 – O1	1.949(5)	N5 – Cu2 – N6	79.90(26)
Cu1 – O3	2.226(6)	O1 – Cu2 – N6	100.06(22)
		N4 – Cu2 – N6	159.48(26)
		Cu1 – O1 – Cu2	88.79(20)
[NMe_4][**L2**Cu_2(OMe)] • MeOH			
Cu1 – N1	2.020(4)	N2 – Cu1 – O1	169.14(15)
Cu1 – N2	1.913(4)	N2 – Cu1 – N1	80.34(16)
Cu1 – N3	2.020(4)	O1 – Cu1 – N1	96.01(14)
Cu1 – O1	1.921(3)	N2 – Cu1 – N3	80.04(16)
Cu1 – O2	2.337(3)	O1 – Cu1 – N3	100.26(14)
Cu1 – Cu2	2.740(1)	N1 – Cu1 – N3	154.50(15)
Cu2 – N4	1.994(4)	N5 – Cu2 – O1	176.62(15)
Cu2 – N5	1.907(4)	N5 – Cu2 – N4	80.59(16)
Cu2 – N6	1.979(4)	O1 – Cu2 – N4	102.75(14)
Cu2 – O1	1.898(3)	N5 – Cu2 – N6	81.27(16)
		O1 – Cu2 – N6	95.35(14)
		N4 – Cu2 – N6	160.16(15)
		Cu1 – O1 – Cu2	91.71(13)

The geometric parameters about the copper centers in **15** and [**L2**Cu_2(OMe)]$^-$ are similar with Cu1-Cu2 distances of 2.729(1) and 2.740(5) Å respectively (Table 3.5). Additionally, the Cu1-O1-Cu2 bond angles were found to be similar at 88.89(20)° for **15** and 91.71(13)° for [**L2**Cu_2(OMe)]$^-$. The largest difference can be seen in the N2-Cu1-O1 and N5-Cu2-O1 bond angles that are ~20° less in **15** than [**L2**Cu_2(OMe)]$^-$. This

difference is easily observed when looking at the side-on views of the dicopper cores in Figure 3.13 where the methoxo ligand in **15** is bent out of the NNN plane whereas the methoxide in [**L2**Cu_2(OMe)]$^-$ is significantly more coplanar. The τ_4 values of the Cu1 centers for **15** and [**L2**Cu_2(OMe)]$^-$ are 0.38 and 0.26, respectively, with a τ_4 value of 0 corresponding to perfect square planar geometry and a value of 1 being a perfect tetrahedral geometry. Thus, **15** falls further from square planar on the geometric spectrum.

The bulk purification of complexes of **11**-**15** was not obtained despite multiple efforts to obtain clean EPR, elemental analysis, and HR-ESI-MS data. We tentatively attribute this to monocopper impurities in the bulk sample whereby only a single coordination site is occupied by copper. Monocopper species have been evidenced by preliminary X-ray crystallographic determination of a monocopper-chlorido complex ([$\mathbf{H_2L5}$Cu(Cl)]$^-$•H_2O) shown in Figure 3.16. This structure is subject to crystal twinning as well as several symmetrical and positional disorder issues of solvents and cations and as such we have not reported the bond metrics as we feel they are not appropriate to report at this time. This species was prepared from identical methods as reported above but with $CuCl_2$ as the copper source in lieu of $Cu(OTf)_2$. In the crystal structure we observe a single pyridine dicarboxiamido pocket occupied by a copper while the second pocket remains protonated and is engaged in hydrogen bonding interactions with the chlorido anion (similar to complex **1**). The presence of monocopper contaminants in the other complexes is proposed based on the existence of this $\mathbf{H_2L5}^{2-}$monocopper complex although further evidence is needed to confirm this proposal. Due to the lack of confidence in bulk purity only crude yields and scale of product is reported in the experimental section of this chapter (Section 3.6.).

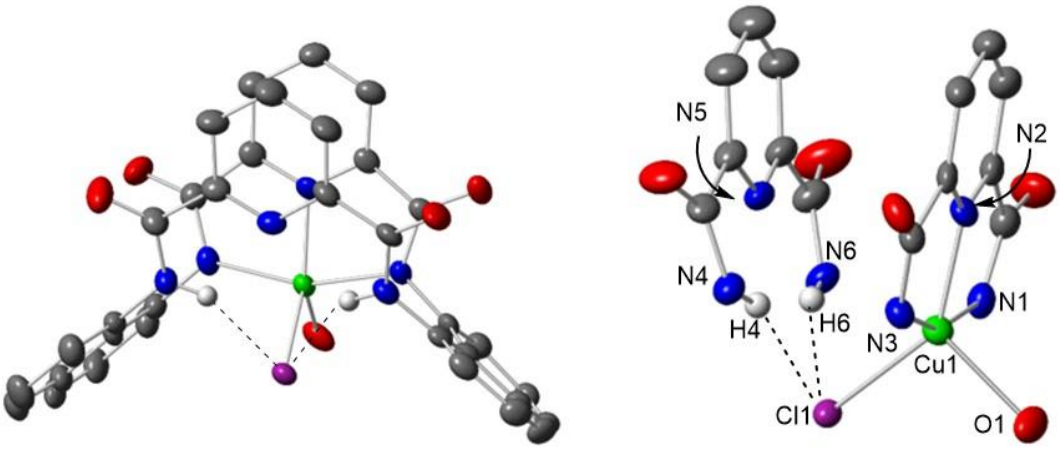

Figure 3.16. Representations of the anionic portion of the X-ray structure of [NMe_4][**H_2L5**Cu(Cl)] • H_2O from front-on view (a) and the side-on dicopper core with naphthyl linkers omitted for clarity (b). Hydrogen bond interactions displayed as dashed lines. All nonhydrogen atoms shown as 50% thermal ellipsoids.

3.4 Conclusions

The target macrocyclic proligand **H_4L5** was generated and found to exhibit interesting topological characteristics which allow for unique metal coordination chemistry that is different from that of its analogous **$L2^{4-}$** counterpart. The synthesis of **H_4L5** is reported for the first time in this work utilizing "fast addition" macrocyclization methods allowing for synthetically simplistic generation of the product. Additionally, the exploration of a synthetic route to **H_4L5** also allowed for the discovery of the novel compound **H_2L6** along with a synthetic route to generate **H_2L6** cleanly. **H_2L6** may also prove useful as a ligand as its structure suggests it may be capable of NNN coordination of metals as the proligand **H_2L6** or in its singly (**$HL6^-$**) or doubly deprotonated (**$L6^{2-}$**) states.

The compound **$L5^{4-}$** was found to be proficient at stabilizing dicopper cores and attempts to generate complex **16** led to the formation of products **11-15.** Evidence for support of monocopper cores by this framework was noted by this the observation of the

structure of the monocopper-chlorido complex [**H$_2$L5**Cu(Cl)]$^-$•H$_2$O. The observed dicopper compounds **11-14** are supposed products of hydrolytic and nucleophilic reactions which have been identified by structural determination through X-ray crystallography analysis with both μ(1,1) and μ(1,3) coordination modes observed. The unique ligand geometry has been shown to enforce short Cu-Cu distance and allows for cis-labile coordination sites in close proximity. The observed dicopper cores in **11-14** are found to be geometrically reminiscent of known carboxylate bridged paddle-wheel complexes.[129-133]

3.4.1 Insights into formation of dicopper-hydroxo species

The structural determination of **15** suggests that despite the topological differences between **L2**$^{4-}$ and **L5**$^{4-}$ the similarly short Cu-Cu distances of their dicopper complexes allow for monoatomic bridging modes between the metal centers in both ligand frameworks. The analogous (μ-hydroxo)Cu$^{II}_2$ core is quite possibly an accessible core for the **L5**$^{4-}$ framework to give the complex [**L5**Cu$_2$(OH)]$^-$ (**17**). With these structural insights in mind, the possibility of formation of **17** does not necessarily preclude the formation of target compound **16**. Examples of dicopper complexes with multiple binding modes and protonation states have shown that interconversion between different cores is possible by variation of the pH of the solution (Figure 3.17).[134]

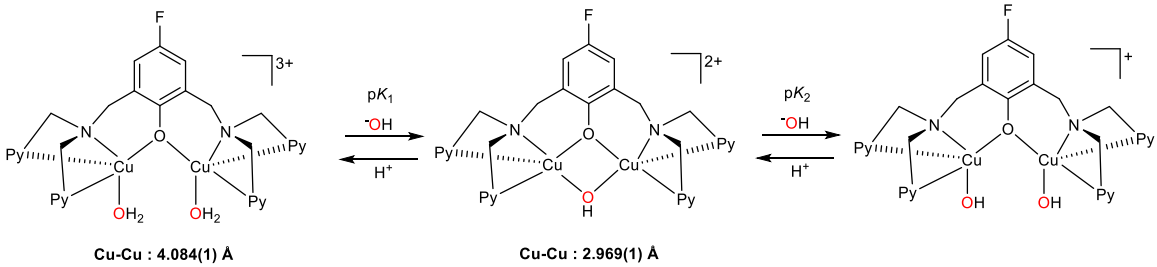

Figure 3.17. Interconversion of different cores in previously described dicopper complex as a function of pH. Figure adapted from ref. 134.

The ability of $\mathbf{L5^{4-}}$ dicopper complexes to adopt different coordination modes suggest it is entirely possible that the cores **16** and **17** lie on a pH-dependent continuum and may be interconvertible along with other possible $[\mathbf{L5}Cu_2(H_3O_2)]^-$ (**18**) or bis-aqua $[\mathbf{L5}Cu_2(OH_2)_2]^0$ (**19**) moieties (Figure 3.18). We speculate that in organic solvents, synthetic strategies may be developed to preferentially form one species over another as a function of the concentration of base. Additionally, if isolated, any species may be able to interconvert to any other proposed species through the addition or loss of a proton allowing a synthetic foothold to generate this family of complexes. It is worth noting literature reports for conversion from a μ-hydroxo mode to a bis(hydroxo) or bis(aqua) moiety have been shown to be accompanied by significant metal-metal distance elongation (~0.5 – 1.0 Å) in bimetallic compounds. The inflexibility of $\mathbf{L5^{4-}}$ in tandem with the short Cu-Cu distance of its observed dicopper complexes (2.7- 2.8 Å) may suggest a favored formation of **17** over the bis(hydroxo) compound **16** but currently no experimental evidence for preferential formation of a particular compound has been found.

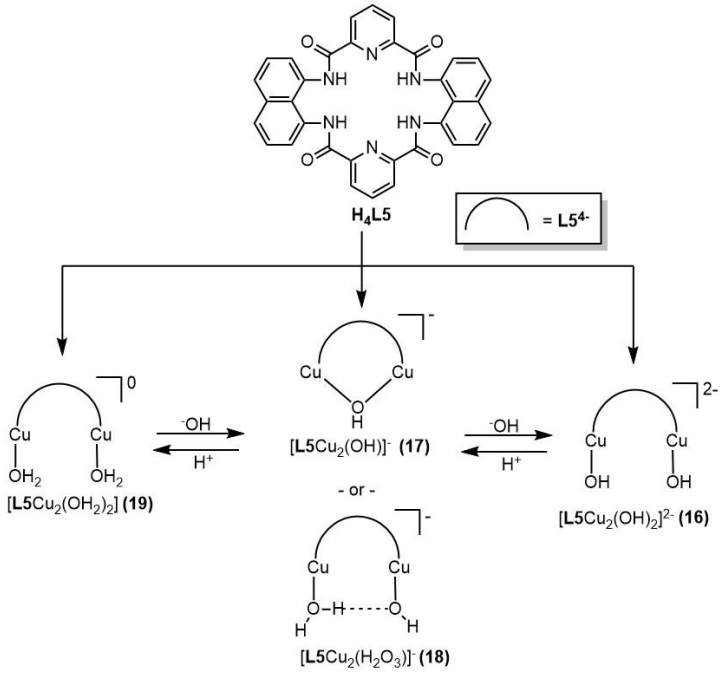

Figure 3.18. Potential pH dependent dicopper moieties in the $\mathbf{L5^{4-}}$ framework.

*3.4.2 Insights into products of nucleophilic reactivity (**11-14**)*

The observed compounds **11-14** all are proposed to be products of nucleophilic attack by an in-situ generated copper intermediate during their respective metallation reactions. The conversion of nitriles to amides, amides to acetates, and CO_2 to carbonates, is consistent with previous reports of dinuclear systems that have been shown to be hydrolytically competent.[135-139] The nucleophilic reactivity of many of these dinuclear complexes is largely attributed to a coordination-insertion mechanism, whereby the substrate coordinates to a metal site, thereby activating the substrate by increasing the electrophilicity at the point of insertion.[5,140,141] Once the substrate is bound, a hydroxide on the neighboring site can react with the activated molecule to give the final hydrolytic product. Binuclear compounds have been found to be particularly effective at this type of reactivity due to their ability to allow a metal site for coordination and a second site set to perform insertion.

Several proposals for a mechanism of reaction of the our reactive dicopper species with substrate can be suggested, however, a coordination-insertion mechanism route by complex **17** or **18** seems to be the most attractive due to the existing literature precedence in binuclear chemistry. Analogous routes can be proposed for either terminal or bridging hydroxo species, whereby substrate coordinates to one copper center (most likely displacing a molecule of solvent) and the hydroxo ligand inserts (Figure 3.19). It should be noted hydrolytic chemistry such as this is traditionally considered more facile with terminal metal-hydroxo cores as opposed to bridging hydroxo cores.[2] This is due to the reduced nucleophilicity of a hydroxo ligand when coordinated to two lewis acidic metals instead of one. The proficiency of terminal hydroxo compounds to perform nucleophilic reactions may argue for the existence of compound **16** and **18**.

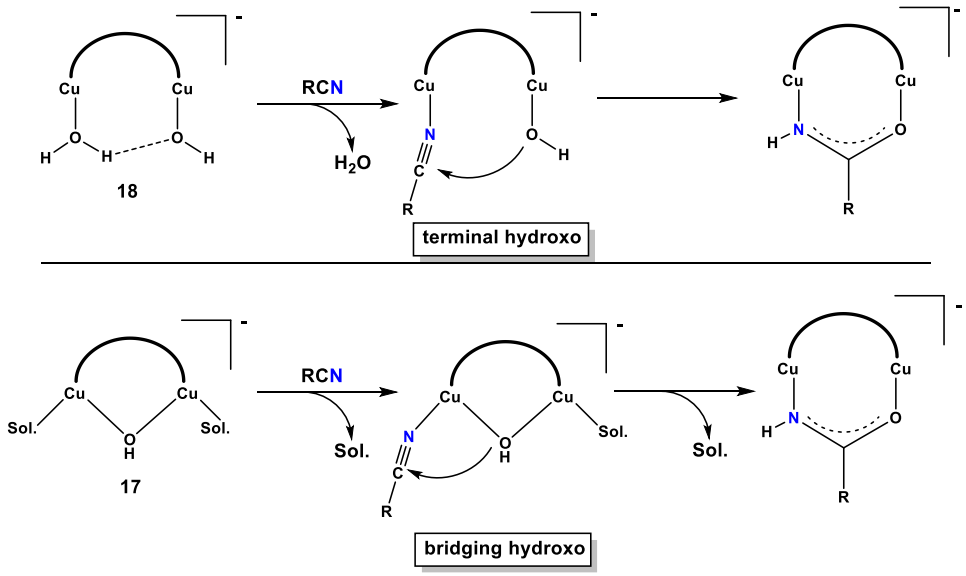

Figure 3.19. Proposed hydrolytically competent dicopper cores and their potential coordination-insertion mechanisms in the presence of nitrile substrate.

Isolation of the products of nucleophilic reaction **11-14** are suggestive that $\mathbf{L5^{4-}}$ is capable of supporting a reactive dicopper species that is proficient at nucleophilic reactions with amides, nitriles, and carbon dioxide under mild conditions. We attribute

this degree of reactivity to the high degree of electron donation of the tetraanionic framework of $\mathbf{L5^{4-}}$.The identity of this reactive intermediate is unknown but compounds **16**-**19** all have been proposed as possible intermediates. The isolation and characterization of these proposed intermediates as well as their ability to produce oxidized cores for C-H bond hydroxylation is an ongoing component of this project.

3.5 Experimental section

3.5.1 Materials and methods.

All reactions and manipulations were performed under an inert gas atmosphere using Schlenk techniques or a Glove box unless otherwise noted. HPLC grade Water was distilled and degassed by three freeze–pump–thaw cycles. The solvents tetrahydrofuran (THF), diethyl ether (Et_2O), pentane were passed through solvent purification columns (Glass Contour, Laguna, CA). Pyridine was purified by distillation prior to use. All chemicals were purchased from Aldrich and used without purification unless stated otherwise.

3.5.2 Preparation of compounds

H_4L5. To a flask of 150 mL dry THF, 2,6 pyridine dicarbonyl dichloride (4.0 g, 0.02 mol) was added along with 20 mL (0.12 mol)of *N*,*N*-diisopropylethylamine. This mixture was allowed to stir until all reagents were dissolved and then the solution was cooled to 0°C using an ice bath. In a separate flask, 3.08 g (0.02 mol) of 1,8-diaminonaphthalene was dissolved in 10 mL of dry THF. Using a 20 mL syringe, the solution of 1,8-diaminonaphthalene was then added to the flask containing 2,6 pyridine dicarbonyl dichloride and *N*,*N*-diisopropylethylamine over 60 seconds. A resulting cloudy off-white mixture was formed and allowed to stir at 0°C for 2 hours. The reaction solution was then vacuum-filtered using a frit funnel to give an off-white solid. The solid was then washed with 40 mL boiling methanol (3x) and subsequently washed with 20 mL

of diethyl ether. This solid was then allowed to dry over 8 hours under vacuum. The resulting powder was found to be **H_4L5** (4.0 g, 71%). ^{1}H-NMR (DMSO-*d6*, 300 MHz) δ (ppm): 11.25 (s, 4H, NHCO), 7.99 (m, 4H, CHPy), 7.89 (m, 6H, CH), 7.60 (m, 8H, C-H). HR-MS (ESI, MeOH) *m/z*: [**H_3L5**]$^-$ Calcd. for $[C_{34}H_{21}N_6O_4]^-$ 577.162; found 577.129; *m/z*: [**H_4L5** + Cl]$^-$ Calcd. for $[C_{34}H_{22}ClN_6O_4]^-$ 613.139; found 613.102.

H_4L6. To a flask of 200 mL dry THF, 1.0 g (0.006 mol) of 1,8-diaminonaphthalene was added and allowed to dissolve to give a deep red solution. In a separate flask, 2,6 pyridine dicarbonyl dichloride (1.30 g, 0,006 mol) was dissolved in 25 mL of dry THF. Using a 50 mL syringe, the solution of 2,6 pyridinedicarbonyl dichloride was added via syringe pump at a rate of ~ 1 drop/sec over 8 hours. A resulting clear red solution was observed and all solvent removed under vacuum to give a resulting red powder. This powder was washed with 20 mL of pentane and allowed to dry under vacuum. A deep red powder resulted that was found to be **H_4L6** (1.71g, 70%). ^{1}H-NMR (DMSO-*d6*, 300 MHz) δ (ppm): 8.58 (d, 2H, CHPy), 8.30 (s, 1H, CHPy), 7.26 (t, 4H, CH), 7.18 (d, 4H, CH), 6.91 (d, 4H, CH).

[NMe_4][L5Cu_2(OAc)] ([NMe_4][11]). To a 50 mL schlenk flask, 200 mg (0.35 mmol) **H_4L5** and 310 mg (0.86 mmol) of $Cu(OTf)_2$ was added. To the flask, 20 mL of dry DMA was added and the resulting mixture allowed to stir for 10 minutes, resulting in a suspension. To the suspension, 1.0 mL of a 2.18 M solution of NMe_4OH in MeOH was added resulting a color change to a deep green. The solution was allowed to stir for one hour and the solution concentrated to ~ 5 milliliters. Diethyl ether (20 mL) was added to the DMA solution resulting in the precipitation of green powder that was subsequently filtered by vacuum filtration and a frit funnel. The green solid was washed with diethyl ether (20 mL. 2x) and allowed to dry on the filter. The resulting solid was taken up again in minimal DMA (~5 mL) and recrystallized by vapor diffusion of diethyl ether into the

DMA solution over the course of 48 hours. Green crystals were obtained and identified by X-ray crystallography to be [NMe_4][**11**] (115mg, 40%). Repeated attempts to obtain correct CHN analysis were unsuccessful, which we attribute to incomplete combustion.

[NMe_4][L5Cu(CH_3CONH)] ([NMe_4][12]). Compound [NMe_4][**12**] was prepared analogously to [NMe_4][**11**] except CH_3CN was used as the solvent medium instead of DMA to afford a green powder (96 mg, 33%). Crystals could only be obtained by addition of potassium triflate to the DMA solution to produce green crystals of [K][**12**]**.** Repeated attempts to obtain correct CHN analysis were unsuccessful, which we attribute to incomplete combustion.

[NMe_4][L5Cu(CH_3CH_2CONH)] ([NMe_4][13]). Compound [NMe_4][**13**] was prepared analogously to [NMe_4][**11**] except CH_3CH_2CN (propionitrile) was used as the solvent medium instead of DMA to afford a green powder (124 mg, 42%). Single crystals were obtained by slow evaporation of Et_2O in concentrated DMA solutions of [NMe_4][**11**]**.** Repeated attempts to obtain correct CHN analysis were unsuccessful, which we attribute to incomplete combustion.

[NMe_4]$_2$[L5Cu(CO_3)] ([NMe_4]$_2$[14]). Compound [NMe_4][**14**] was prepared analogously to [NMe_4][**11**] except a 3:1 mixture of pyridine/water was used as the solvent medium instead of DMA. The resulting mixture was then allowed to crystallize open to air to afford green crystals of [NMe_4][**14**] (165 mg, 52%). Repeated attempts to obtain correct CHN analysis were unsuccessful, which we attribute to incomplete combustion.

[NMe_4][L5Cu(OMe)] ([NMe_4][15]). Compound [NMe_4][**15**] was prepared analogously to [NMe_4][**11**] except MeOH was used as the solvent medium instead of DMA to afford a green powder (76 mg, 25%). Single crystals were obtained by slow evaporation of Et_2O in concentrated MeOH solutions of [NMe_4][**15**]**.** Repeated attempts

to obtain correct CHN analysis were unsuccessful, which we attribute to incomplete combustion.

[NMe_4][L2Cu(OMe)]. Compound [NMe_4][**L2**Cu(OMe)] was prepared analogously to [NMe_4][**15**] except **H_4L2** was used instead **H_4L5**. (114 mg, 38%). Single crystals were obtained by slow evaporation of Et_2O in concentrated MeOH solutions of [NMe_4][**L2**Cu(OMe)]**.**

[NMe_4][H_2L5Cu(Cl)]. Compound [NMe_4][**H_2L5**Cu(Cl)] was prepared analogously to [NMe_4][**11**] except $CuCl_2$ was used instead of $Cu(OTf)_2$ to afford a green powder (76 mg, 25%). Single crystals were obtained by slow evaporation of Et_2O in concentrated DMF solutions of [NMe_4][**H_2L5**Cu(Cl)]. Repeated attempts to obtain correct CHN analysis were unsuccessful, which we attribute to incomplete combustion.

X-ray Crystallography. All crystals were placed onto the tip of a 0.1 mm diameter glass capillary or mitogen polymer tip and mounted on a Bruker APEX II Platform CCD diffractometer or a Bruker D8 Photon 100 CMOS diffractometer for data collection. The data collections were carried out using MoKα or CuKα radiation with a graphite monochromator (λ = 0.71073 Å or 1.54184 Å) at 173 K or 123 K respectively. Structure solutions were performed by direct methods using SHELXS-2013 software and refined against F2 using full-matrix-least-squares using SHELXL-97 and SHELXL-2013 software.

Chapter 4

Formally Cu^{III}-alkylperoxo complexes as models of intermediates in monoxygenase enzymes.[a]

[a] The results presented in this chapter were previously published in:

[a]Benjamin D. Neisen, Nicole L. Gagnon, Debanjan Dhar, Andrew D. Spaeth, and William B. Tolman* Formally Copper(III)-alkylperoxo complexes as models of possible intermediates in monooxygenase enzymes. *J. Am. Chem. Soc.* **2017**. ASAP

4.1 Introduction

Understanding the mechanism(s) of monooxygenase reactions promoted by monocopper sites in enzymes[142] and other catalysts[143] is an important research goal of our work. A generalized mechanistic scheme that highlights several key oxidants and processes under active discussion for many of these systems is shown in Figure 4.1. The first step in monooxygenases is reaction of the Cu^{I} form with O_2 to yield a 1:1 Cu/O_2 adduct typically formulated as a Cu^{II}-superoxide,[11,44,82,144] but which in some model compounds can have Cu^{III}-peroxide character.[145] This intermediate may undergo proton-coupled electron transfer (PCET or "H^+/e^-") via attack at a substrate C-H bond or delivery of a proton and an electron in another way to yield a $[Cu^{II}(OOH)]^+$ species (also written as $[Cu(OOH)]^+$), which may also attack substrate or undergo PCET. Alternatively, protonation of the Cu^{II}-superoxide to yield a $[Cu(OOH)]^{2+}$ species (formally $Cu^{III}(OOH)$) species that then attacks the substrate has been suggested on the basis of theory for peptidylglycine α-hydroxylating monooxygenase (PHM).[146] A $[Cu(OOH)]^{2+}$ species also is implicated in a proposed mechanism for catalytic alkane oxidations, where reaction of a putative $[Cu^{III}(OH)]^{2+}$ species with H_2O_2 to yield a hydroperoxyl radical and Cu^{II} presumably involves initial formation of $[Cu(OOH)]^{2+}$.[147]

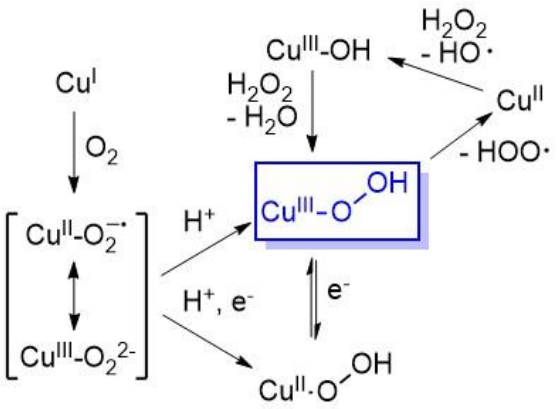

Figure 4.1. Generalized mechanistic scheme for O_2 activation by monocopper sites with formal oxidation states indicated.

The characterization and study of the reactivity of discrete complexes comprising these and other copper-oxygen intermediates is an important strategy for determining their viability in catalytic systems.[7,81,148-150] Examples of 1:1 Cu/O_2 adducts,[151] $[Cu(OH)]^{2+}$,[23,34,35,152] and $[Cu(OOR)]^{+}$ (R = alkyl) complexes[7] have been characterized, but to our knowledge there are no reports of compounds with a $[Cu(OOR)]^{2+}$ unit.[153] The existence of the $[Cu(OOR)]^{2+}$would have significant biological relevancy towards monooxygenase chemistry.

This chapter discusses efforts to generate model systems containing a $[Cu(OOR)]^{2+}$ (where R= alkyl) using experimental methods previously utilized in the characterization of $[Cu(OH)]^{2+}$ containing species.[23,34,35,152] To access these high valent cores, pyridine dicarboxamido Cu^{II}-alkylperoxo precursors were initially synthesized and one-electron oxidation used to generate the desired $[Cu(OOR)]^{2+}$ copper core. The spectroscopic and reactivity characteristics of the subsequent $[Cu(OOR)]^{2+}$ containing model species are subsequently investigated to draw comparisons to the proposed biorelevant $[Cu(OOH)]^{2+}$ intermediates.

4.2 Synthesis and Characterization of Cu^{II}-alkylperoxo complexes

4.2.1 Synthesis of Cu^{II}-alkylperoxo complexes

The generation of alkylperoxo compounds was performed by reacting the previously described [NBu_4][**L1b**Cu(OH)] complex with excess equivalents of ROOH (R = Cm, *t*Bu) to afford the corresponding anionic Cu^{II}-alkylperoxo complexes [NBu_4][**L1b**Cu(OOCm)] ([NBu_4][**20**]: 160mg, 68%) or [NBu_4][**L1b**Cu(OO*t*Bu)] ([NBu_4][**21**]: 190 mg, 81%), respectively (Scheme 4.1). The reactions were performed in the presence of activated 3 Å molecular sieves to sequester the equivalent of water that is produced from the reaction and drive it towards the desired Cu^{II}-alkylperoxo products. The reactions were carried out at ~ -20 °C because both **20** and **21** were found to decay in solution state at room temperature over a matter of several hours. Unlike many other Cu^{II}-alkylperoxo compounds previously reported in the literature, [NBu_4][**20**] and [NBu_4][**21**] could be isolated as dark crimson powders that could be stored over a period months with no appreciable signs of decay.

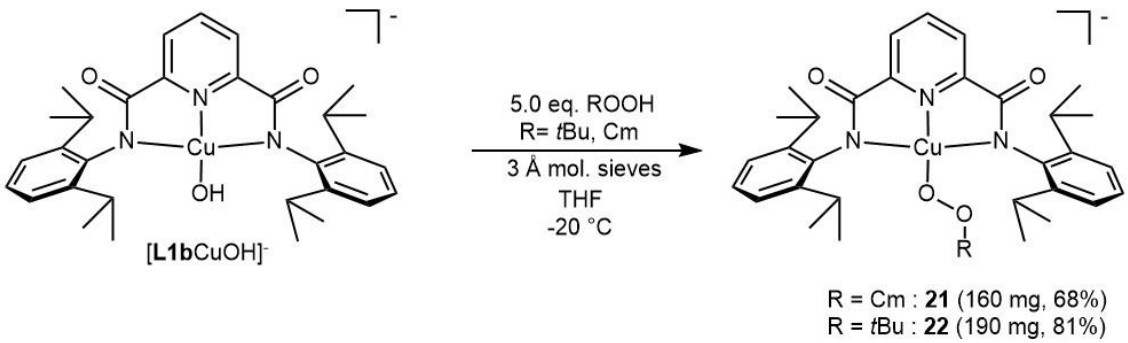

Scheme 4.1. Syntheses of [NBu_4][**L1b**Cu(OOCm)] ([NBu_4][**20**]) and [NBu_4][**L1b**Cu(OOCm)] ([NBu_4][**21**] from [NBu_4][**L1b**Cu(OH)].

4.2.2 EPR, UV-vis spectroscopy, and HR-ESI-MS of Cu^{II}-alkyperoxo complexes

Frozen solution EPR measurements of **20** and **21** show very similar features consistent with S = ½ Cu^{II} complexes (Figure 4.2, a,b). The spectra for **20** and **21** are similar to the EPR signal observed for the precursor compound [**L1b**Cu(OH)]$^-$ but key differences in the Cu hyperfine region is consistent with the desired ligand exchange to give products **20** and **21** (Figure 4.2, c). Simulated spectral parameters of **20** and **21** are

nearly identical to one another in accordance with both compounds having nearly similar electronic environments, as expected for the absence of significant electronic differences between *tert*-butylperoxo or cumylperoxo ligands.

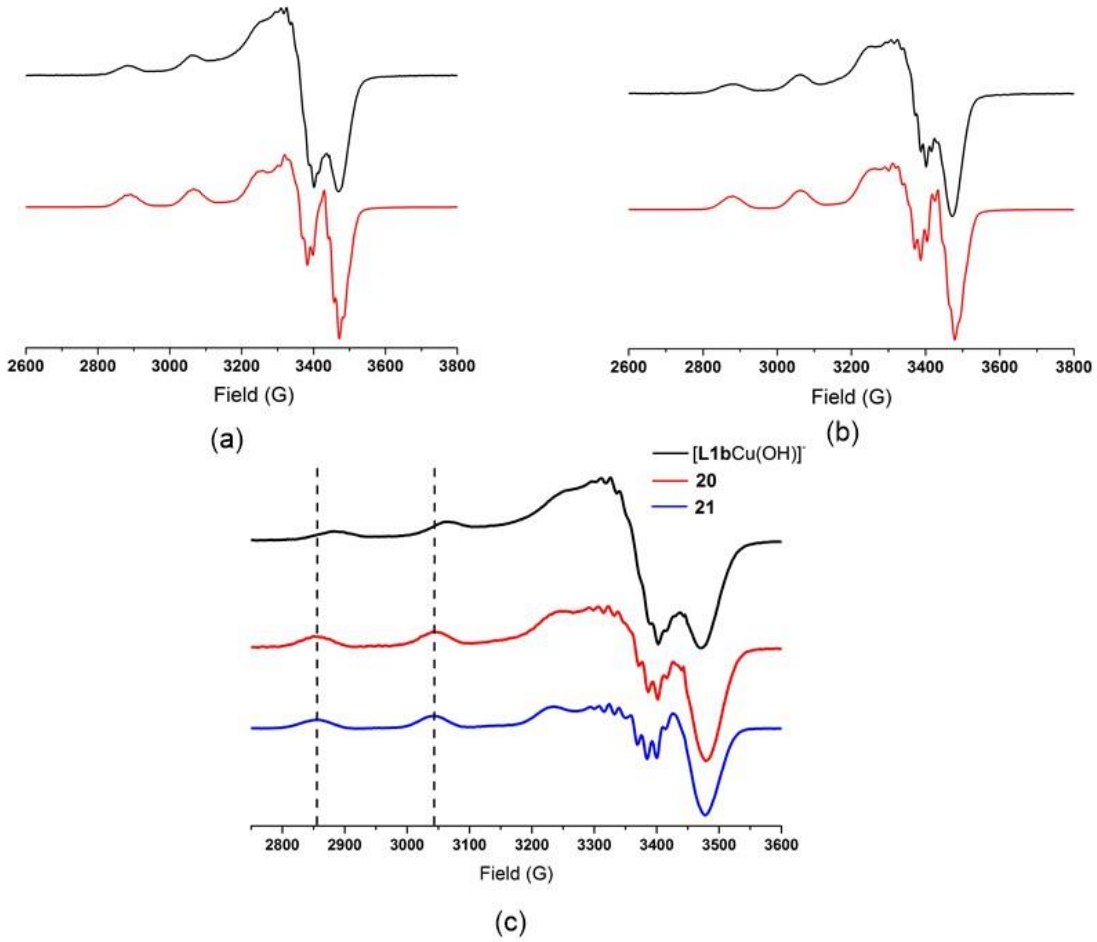

Figure 4.2. Continuous wave X-band (9.64 GHz) EPR spectra (black trace) and simulation (red trace) spectra of [NBu_4][**20**] (a), [NBu_4][**21**] (b), and overlay of [**L1b**Cu(OH)]$^-$ EPR spectrum with **20** and **21** (c). All samples obtained at 1 mM concentrations in THF solution at 30 K. EPR parameters are listed in Table 4.1.

Table 4.1. EPR parameters from spectral simulations.

Compound	$[NBu_4][\mathbf{L1b}Cu(OH)]^2$	$[NBu_4][\mathbf{20}]$	$[NBu_4][\mathbf{21}]$
g(x)	2.026	2.044	2.042
g(y)	2.047	2.041	2.042
g(z)	2.194	2.183	2.185
$A^{Cu}(x)$	57	45	60
$A^{Cu}(y)$	57	45	60
$A^{Cu}(z)$	567	535	550
A^{Py} (x)	30	40	55
$A^{Py}(y)$	50	40	55
$A^{Py}(z)$	30	50	50
$A^{am}(x)$	32	45	45
$A^{am}(y)$	50	50	45
$A^{am}(z)$	30	45	45

Ultraviolet-visible (UV-vis) spectra of 2 mM solutions of **20** and **21** in THF solution exhibit similar features. A sharp absorption at ~552 nm and a broad shoulder at ~695 nm were observed for both **20** and **21**. These features have been assigned as d→d transitions of the corresponding Cu^{II} complexes.

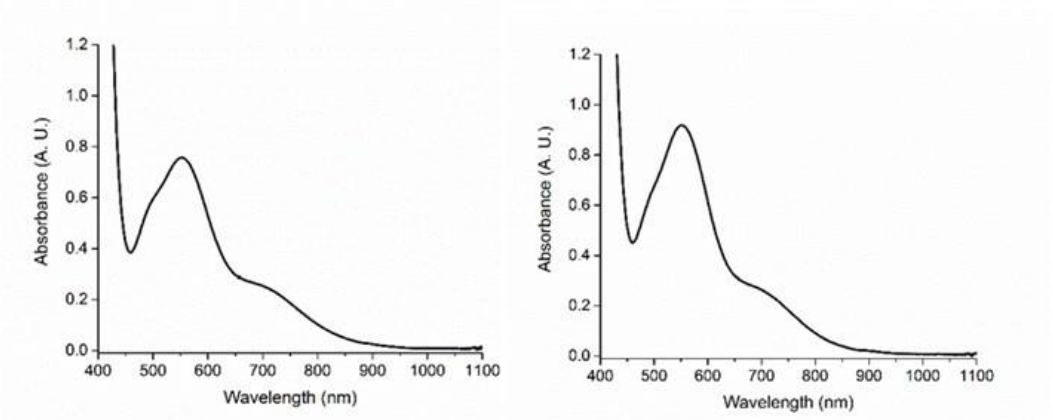

Figure 4.3. UV-visible spectra of $[NBu_4][\mathbf{20}]$ (left) and $[NBu_4][\mathbf{21}]$ (right) in THF at -80 °C (2 mM).

Negative mode HR-ESI-MS was also performed on both alkylperoxo compounds to observe target anionic molecules **20** and **21** (Figure 4.4). A feature at *m/z* = 697.208 corresponding to **20** and a feature at *m/z* = 635.270 corresponding to **21** were observed. Simulations of isotopic patterns for **20** and **21** are in accordance with monocopper compounds containing their respective alkylperoxo moieties. In summary, the HR-ESI-MS, UV-vis, and EPR spectroscopic data support the indicated structures for **20** and **21** in solution.

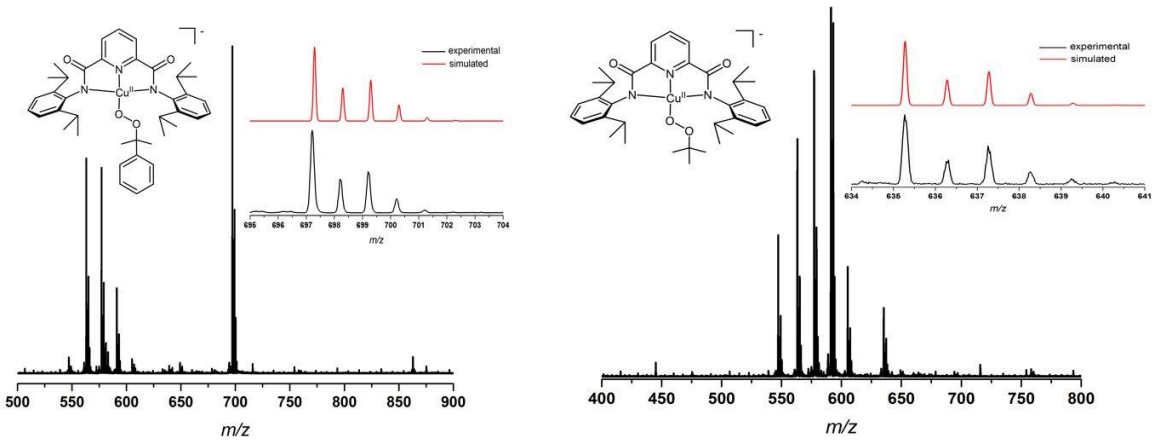

Figure 4.4. Negative mode HR-ESI-MS of [NBu_4][**20**] (left) and [NBu_4][**21**] (right), simulated isotopic patterns inset.

4.2.3 X-ray crystallography of Cu^{II} alkylperoxo complexes

Efforts to crystallize complexes of **20** and **21** as their respective tetrabutylammonium salts proved to be difficult due their high solubility in many organic solvents. Performing the analogous synthesis as described in Scheme 4.1 but with the starting material having a different counterion, [NEt_4][**L1b**Cu(OH)], the corresponding [NEt_4][**20**] and [NEt_4][**21**] salts were obtained and were subsequently crystallized. X-ray quality crystals of [NEt_4][**20**] were obtained by removal of THF solvent in the presence of excess cumene hydroperoxide, whereas [NEt_4][**21**] crystals was obtained through slow evaporation of diethyl ether into a THF solution of [NEt_4][**21**]. X-ray crystal structures were subsequently solved (Figure 4.5).

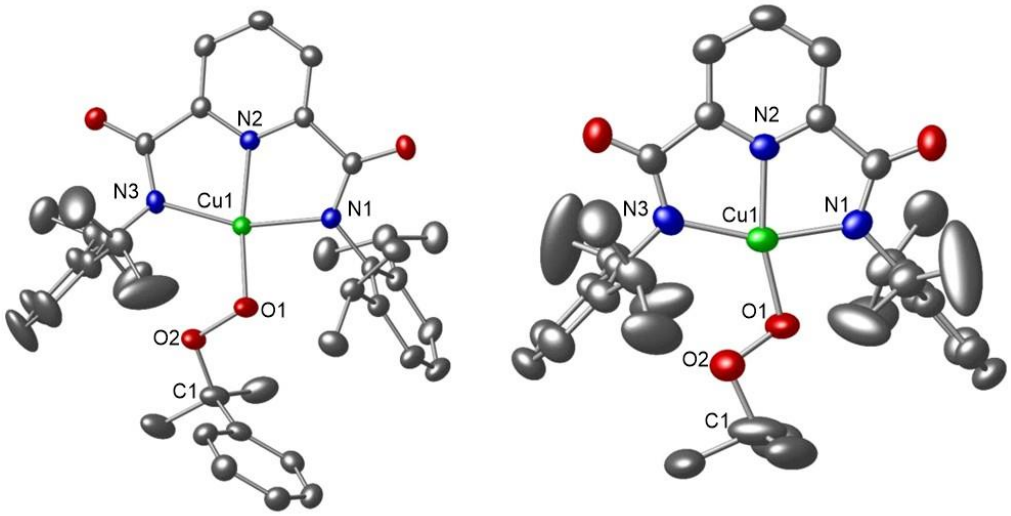

Figure 4.5. Representation of the X-ray crystal structure of anionic species **20** (left) and **21** (right), shown as 50% thermal ellipsoids (H atoms and disordered component of –OO*t*Bu group omitted for clarity).

Bond metrics determined from the X-ray crystal structures of **20** and **21** are in line with typical pseudo-square planar **L1b**$^{2-}$ Cu^{II} complexes.[35] Two distinct anionic complexes of **20** are present in its asymmetric unit and metrics for both units are listed in Table 4.2, whereas only half of **21** is located in the asymmetric unit as it lies on a two-fold rotation axis, resulting in a symmetrically disordered *tert*-butyl-peroxo group. We observe O1-O2 peroxo bond distances of 1.4689(19) Å and 1.469(2) Å for the two units of **20** and a O1-O2 distance of 1.416(6) Å for **21**. These peroxo bond distances are similar to those measured for the only other two [Cu(OOR)]$^{+}$ (R = H, alkyl) complexes reported (both of which are coincidentally 1.460(6) Å).[68,69] DFT geometry optimizations of **20** and **21** also show good correlation to the X-ray structures (further discussion of DFT optimized structures is presented in Section 4.4.3).

Table 4.2. Selected interatomic distances (Å) and angles (deg) for both units of [NEt_4][**L1b**Cu(OOCm)] ([NEt_4][**20]**) and [NEt_4][**L1b**Cu(OO*t*Bu)] ([NEt_4][**21]**).

[NEt_4][**L1b**Cu(OOCm)] ([NEt_4][**20],** unit 1)			
Cu1 – N1	2.0194(15)	N2 – Cu1 – O1	170.40(6)
Cu1 – N2	1.9336(15)	N2 – Cu1 – N1	79.50(6)
Cu1 – N3	2.0258(15)	O1 – Cu1 – N1	108.80(6)
Cu1 – O1	1.8410(14)	N2 – Cu1 – N3	79.67(6)
O1 – O2	1.4689(19)	O1 – Cu1 – N3	92.08(6)
C1 – O2	1.433(3)	N1 – Cu1 – N3	159.12(6)
		N1-Cu1-O1-O2	22.93(15)
		Cu1-O1-O2-C1	150.04(14)
[NEt_4][**L1b**Cu(OOCm)] ([NEt_4][**20],** unit 2)			
Cu2 – N4	2.0171(15)	N5 – Cu2 – O5	169.68(7)
Cu2 – N5	1.9303(16)	N5 – Cu2 – N4	79.48(6)
Cu2 – N6	2.0260(16)	O5 – Cu2 – N4	90.57(7)
Cu2 – O5	1.8240(17)	N5 – Cu2 – N6	80.22(6)
O5 – O6	1.469(2)	O5 – Cu2 – N6	109.63(7)
C2 – O6	1.414(3)	N4 – Cu2 – N6	159.66(6)
		N4-Cu2-O5-O6	22.93(15)
		Cu2-O5-O6-C2	150.04(14)
[NEt_4][**L1b**Cu(OO*t*Bu)] ([NEt_4][**21]**)			
Cu1 – N1	2.0073(19)	N2 – Cu1 – O1	165.48(13)
Cu1 – N2	1.931(2)	N2 – Cu1 – N1	79.71(6)
Cu1 – N3	2.0074(19)	O1 – Cu1 – N1	114.74(14)
Cu1 – O1	1.855(4)	N2 – Cu1 – N3	79.71(6)
O1 – O2	1.416(6)	O1 – Cu1 – N3	85.83(14)
C1 – O2	1.524(6)	N1 – Cu1 – N3	159.42(11)
		N1-Cu1-O1-O2	6.32

	Cu1-O1-O2-C1	179.61

4.2.4 Electrochemistry of Cu^{II}-alkylperoxo complexes

Cyclic voltammetry measurements of both **20** and **21** in solution were performed to identify potential Cu^{III}/Cu^{II} redox features (Figure 4.6). In THF solution both **20** and **21** were found to exhibit quasi-reversible electrochemical features (i_{pa}/i_{pc} = 2.9 and 2.3 for **20** and **21** respectively, scan rate = 500 mV/s). Increasing the scan-rate did not show a linear increase of reversibility as a function of scan rate, although a cathodic feature was observed at high scan rates (>100 mV/s). The growth of a return wave at high scan rates is consistent with an ECE mechanism, involving a reversible 1-electron redox process followed by a chemical (decomposition?) event, although the poor scan-rate dependence hints at additional complications. Nevertheless, we estimated $E_{1/2}$ values from the high scan rate results.

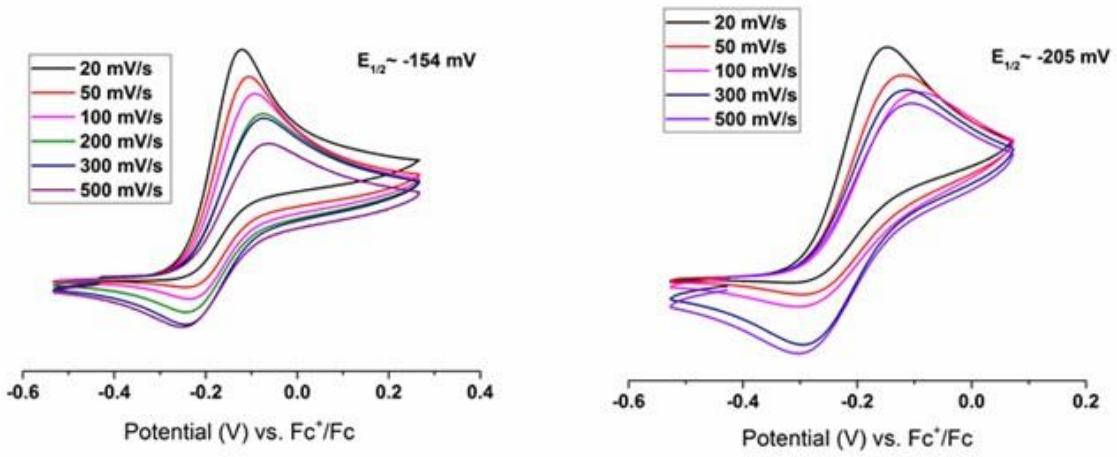

Figure 4.6. Scan rate normalized (where current is divided by square root of scan rate) cyclic voltammograms of [NBu_4][**20**] (left) and [NBu_4][**21**] (right) in 0.3 M NBu_4PF_6 THF solution at room temperature.

From the electrochemical data, $E_{1/2}$ values were calculated for **20** and **21** to be -154 mV and -205 mV vs. Fc^+/Fc, respectively. The redox processes associated with these $E_{1/2}$ values were tentatively assigned as the Cu^{III}/Cu^{II} redox couple. Notably, the oxidation potentials for these alkylperoxo compounds are lower than the hydroxo compound [**L1b**Cu(OH)]$^-$, which has a reported $E_{1/2}$ of -67 mV vs. Fc^+/Fc. Importantly, the redox potentials for **20** and **21** suggest that both compounds can be oxidized by mild chemical oxidants such as ferrocenium salts (see section 4.4.1).

4.3 Decay of Cu^{II}-alkylperoxo to Cu^{II}-hydroxo complexes

Decomposition of **20** and **21** in solution to a new Cu^{II} complex was observed at temperatures greater than -20 °C. Visually, the crimson solutions of **20** and **21** were observed to turn blue over the course of ~12 h at room temperature in THF. EPR spectra of the decay products were showed close similarity to that of the known Cu^{II}-OH compound [**L1b**Cu^{II}(OH)]$^-$ (Figure 4.7). Note the close correspondence of the g(x) and A(x) values.

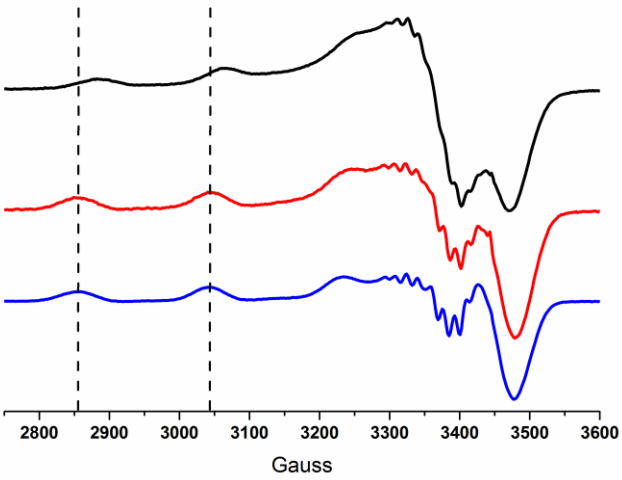

Figure 4.7. Continuous wave X-band (9.64 GHz) EPR spectra of [NBu_4][**20**] (black), [NBu_4][**20**] decay product (red), and [NBu_4][**L1b**Cu(OH)]$^-$ (blue) in THF at 30 K.

Additional confirmation of the identity of the decay product of **20** and **21** was obtained by treating the decay solutions with ferrocenium tetrakis[3,5-bis(trifluoromethyl)phenyl]borate ([Fc][B(Ar^F)$_4$]). When the oxidation of the decay product in THF was monitored by UV-vis spectroscopy at -80 °C the intense absorption features associated with **L1b**Cu^{III}(OH) were observed (Figure 4.8).[35] We take this spectroscopic data as confirmation of the identity of the decay product as [**L1b**Cu^{II}(OH)]$^-$

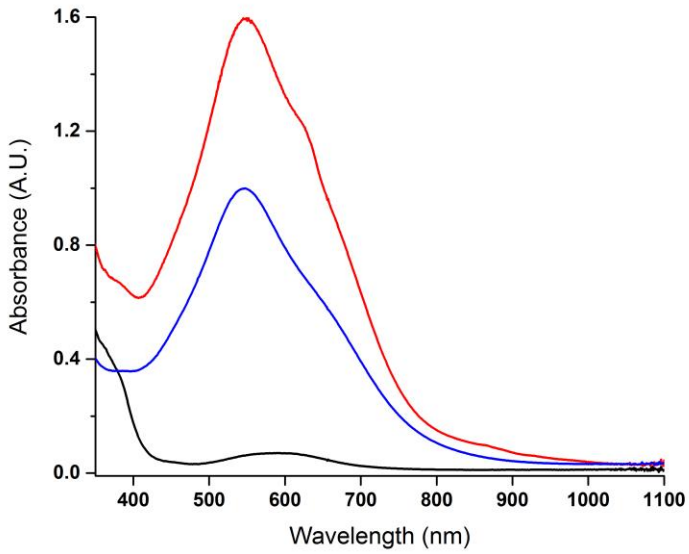

Figure 4.8. UV-vis spectra of [NBu_4][**20**] decay product (~0.1 mM) (black), and the product of reaction of that decay product with an equiv. of [Fc][B(Ar^F)$_4$] (red) in THF at -80 °C. This latter spectrum matches that reported previously for **L1b**Cu^{III}(OH) (blue trace).

Both EPR and UV-vis spectroscopic techniques support the assignment of the product of decay of **20** or **21** as [**L1b**Cu^{II}(OH)]$^-$. This result is precedented, as there are several examples of metal-alkylperoxo complexes that decompose to give the corresponding metal-hydroxo complex.[31,32] Most Cu^{II}-alkylperoxo complexes that have been shown to decay in this manner are thought to undergo homolytic O-O bond breakage.[31] These homolytic events are proposed to occur in a concerted fashion

accompanied by either inter- or intramolecular X-H bond activation (X = C, N, O) which produces the Cu^{II}-hydroxo species and an equivalent of alkoxyl radical (Scheme 4.2). Decomposition of alkylperoxo complexes in this homolytic fashion is reported to be a thermally sensitive process, in line with our observation of increased stability of **20** and **21** at low temperatures. Further exploration of the capability of **20** and **21** to activate X-H bonds through the mechanism proposed above is an ongoing topic of research.

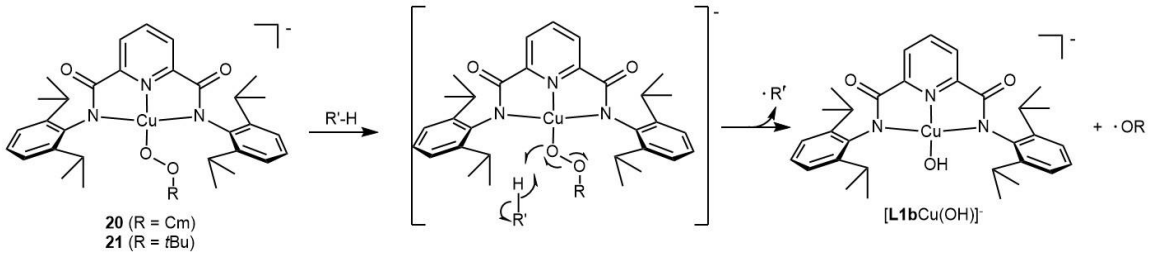

Scheme 4.2. Proposed homolytic decomposition pathway of **20** and **21** to [**L1b**Cu(OH)]$^{-}$.

4.4 Generation and characterization of $[CuOOR]^{2+}$ species

4.4.1 UV-vis and EPR spectroscopic studies of $[Cu(OOR)]^{2+}$ complexes

With complexes **20** and **21** in hand, we attempted the oxidation of the Cu^{II}-alkylperoxo species using $[Fc][B(Ar^F)_4]$ chosen as oxidant due to its oxidation potential being ~200 mV higher than those observed for either **20** or **21** by CV measurements. Additionally, the $[B(Ar^F)_4]^-$ anion is non-coordinating, preventing it from playing any significant role in the subsequent copper oxidation chemistry. Oxidation reactions of the precursor Cu^{II}-alkylperoxo complexes were initially monitored by UV-vis spectroscopy at 0.1mM concentrations in THF solution at -80 °C (Scheme 4.3). The THF solutions of **20** and **21** were found to change from crimson to a deep purple color upon addition of $[Fc][B(Ar^F)_4]$.

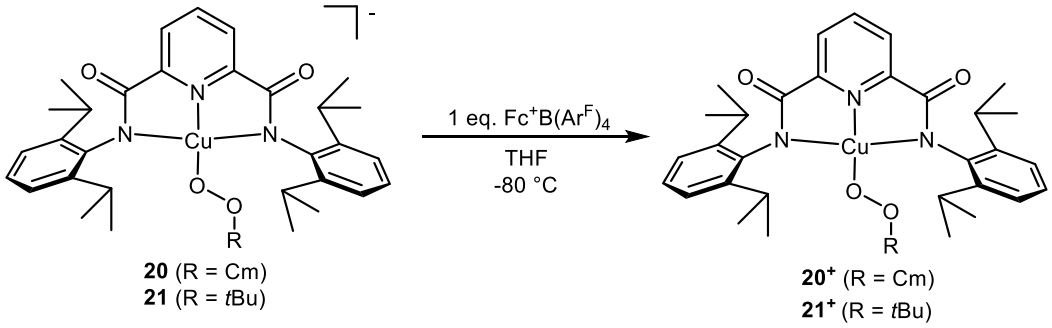

Scheme 4.3. Oxidation of [**L1b**Cu(OOCm)]$^{-}$ (**20**) and [**L1b**Cu(OOCm)]$^{-}$ (**21**) with an equivalent of [Fc][B(Ar^{F})$_4$] to **L1b**Cu(OOCm) (**20**$^{+}$) and **L1b**Cu(OO*t*Bu) (**21**$^{+}$) respectively.

Resulting UV-vis spectra from the oxidation reactions using [Fc][B(Ar^{F})$_4$] showed the formation of intense charge-transfer bands in the 500-700 nm region for both oxidized species (Figure 4.9). Several bands are observed for both **L1b**Cu(OOCm) (**20**$^{+}$) and **L1b**Cu(OO*t*Bu) (**21**$^{+}$). The oxidized species have an approximate $t_{1/2}$ of 4.0 h at -80 °C in THF solution and are stable only for ~5.0 seconds at room temperature. Self-decay products have not currently been identified for either **20**$^{+}$ or **21**$^{+}$.

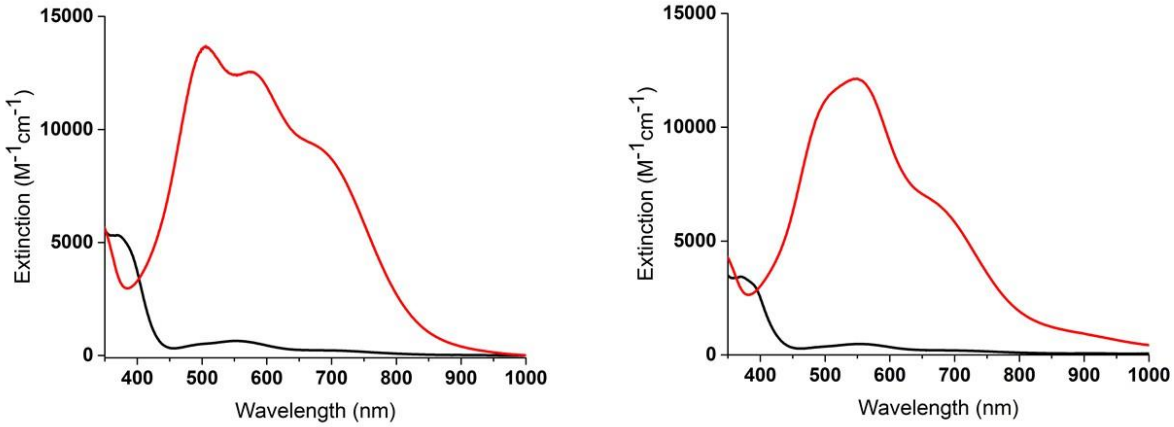

Figure 4.9. UV-vis spectra of [**L1b**Cu(OOCm)]$^{-}$ (**20,** black trace) and **L1b**Cu(OOCm) (**20**$^{+}$, red trace) (left) and [**L1b**Cu(OO*t*Bu)]$^{-}$ (**21,** black trace) and **L1b**Cu(OO*t*Bu) (**21**$^{+}$, red trace) (right) at 0.1 mM in THF at -80 °C.

The observed UV-vis absorption features are similar to those reported previously for **L1b**Cu^{III}(OH) and analogs, which were assigned by TD-DFT as ligand aryl π → Cu

$d_{x^2-y^2}$ transitions.[34] Overlaid UV-vis spectra of **20**$^+$, **21**$^+$, and **L1b**Cu^{III}(OH) are shown in Figure 4.10. Their absorption features all have intense absorptions with extinction coefficients all in the range of 10,000 – 15,000 $M^{-1}cm^{-1}$. The similarity between the spectra for **20**$^+$, **21**$^+$ and **L1b**Cu^{III}(OH) supports similar electronic structures for the complexes.

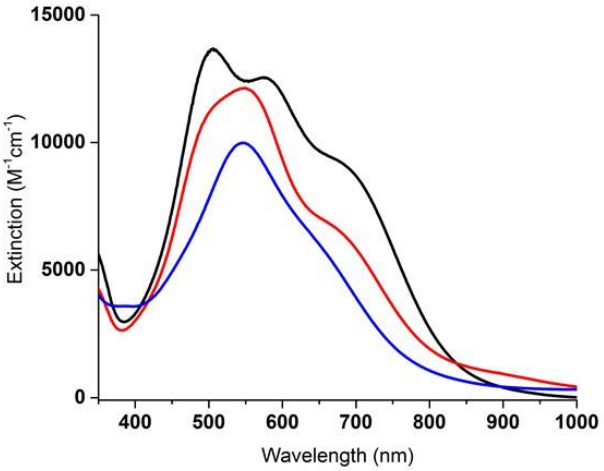

Figure 4.10. Overlaid UV-vis spectra of **L1b**Cu(OOCm) (**20**$^+$, black trace), **L1b**Cu(OOCm) (**21**$^+$, red trace), and **L1b**Cu^{III}(OH) (blue trace) at 0.1 mM in THF at -80 °C.

Additional data support the formulations of **20**$^+$ and **21**$^+$ as $[Cu(OOR)]^{2+}$ complexes. Both **20**$^+$ and **21**$^+$ exhibit no signal in perpendicular mode EPR spectra (Figure 4.11), consistent with S = 0 Cu^{III} but not ruling out an anti-ferromagnetically coupled (S = 0) Cu^{II}-ligand radical, or a ferromagnetically coupled (S = 1) Cu^{II}-ligand radical species.[154-156] The electronic structure of **20**$^+$ and **21**$^+$ is explored and discussed further using computational methods in Section 4.4.3.

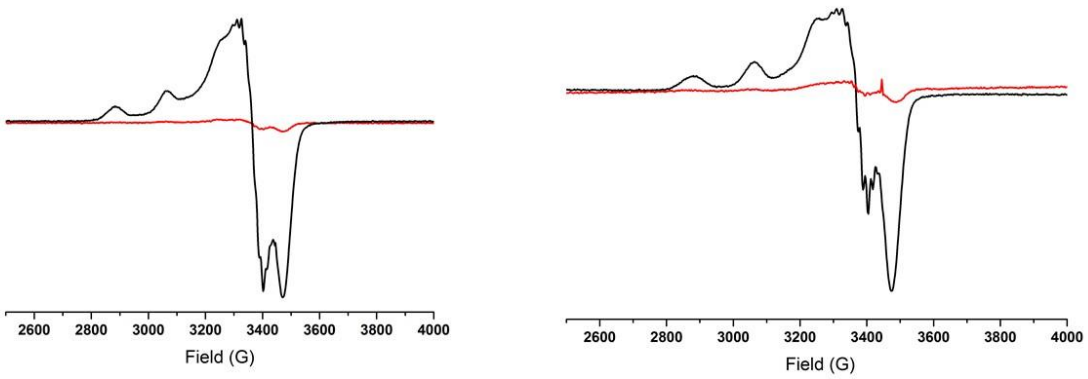

Figure 4.11. Starting (black trace) and oxidized (red trace) EPR spectra of 1 mM [NBu_4][**20**] (left) and 1 mM [NBu_4][**21**] (right) at -243 °C in THF (oxidation performed using [Fc][$B(Ar^F)_4$]).

Titration experiments with **20** showed that the absorption features generated upon oxidation reached maximum intensity upon addition of 1 equiv. of [Fc][$B(Ar^F)_4$] (Figure 4.12), consistent with a one-electron process. The results of the oxidation titration data are in alignment with the hypothesis that $\mathbf{20}^+$ is the one-electron oxidized form of **20**. Stronger oxidants such as acetylferrocenium tetrakis[3,5-bis(trifluoromethyl)phenyl]borate ([AcFc][$B(Ar^F)_4$]) gave similar spectra to those generated with [Fc][$B(Ar^F)_4$].

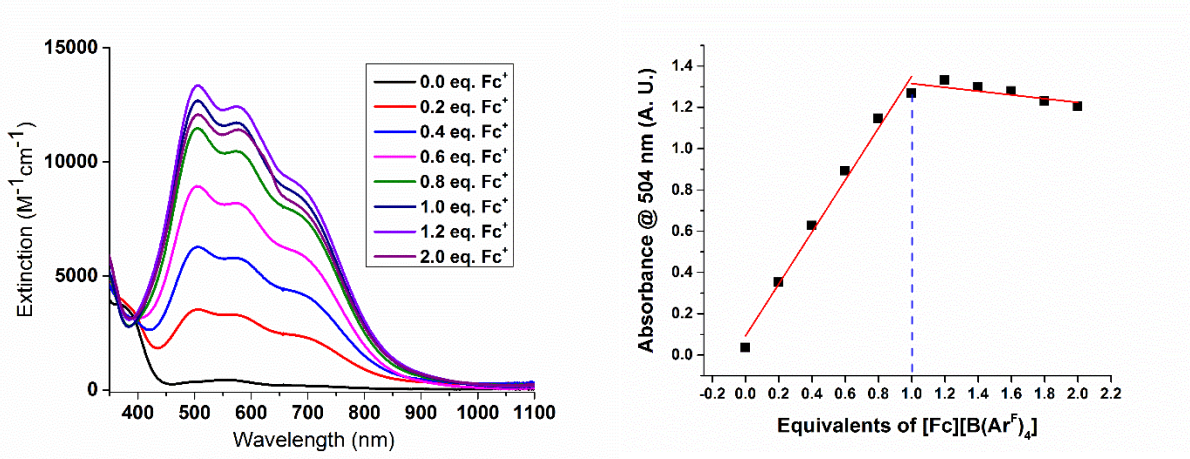

Figure 4.12. UV-vis absorption spectra upon addition of varying equivalents of [Fc][B(Ar^F)$_4$] to 0.1 mM THF solution of [NBu$_4$][**20**] at -80 °C (left) and plot of corresponding absorbance values at λ = 504 nm as a function of varying equivalents of [Fc][B(Ar^F)$_4$](right).

To better understand whether the oxidized feature associated with **20**$^+$ contains the proposed [Cu(OOR)]$^{2+}$ core, we conducted experiments to test the chemical reversibility of the oxidation process of **20** to **20**$^+$. If **20**$^+$ is something other than the one-electron oxidized form of **20** then one would not expect this process to be reversible by subsequent oxidation and reduction processes. In the experiments, UV-vis monitored titrations employing equivalents of [Fc][B(Ar^F)$_4$] oxidant and subsequent addition of decamethylferrocene (Fc*) as a reductant were performed in THF at -80 °C (Figure 4.13). Addition of Fc* to the oxidized species under these conditions resulted in bleaching of the UV-vis spectrum. Subsequent addition of a second equivalent of [Fc][B(Ar^F)$_4$] was shown to reform the associated UV-vis features of **20**$^+$. This process was repeated twice, albeit with some loss of intensity due to decomposition (Figure 4.13). These UV-vis data convincingly demonstrate the reversibility of the one-electron redox processes.

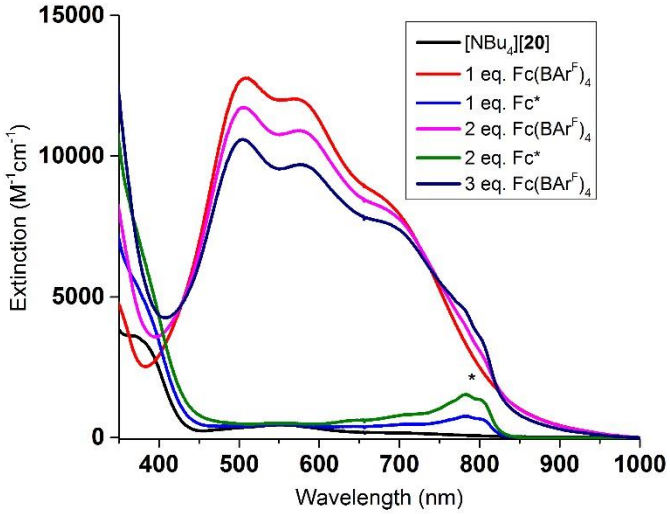

Figure 4.13. UV-vis titration of [Fc][$B(Ar^F)_4$] and decamethyl ferrocene (Fc*) to a 0.1 mM THF solution of [NBu_4][**2a**] at -80 °C (* denotes decamethyl ferrocenium signal).

EPR spectroscopic studies were employed as additional confirmation that $\mathbf{20}^+$ can be reduced back to **20** and that the 1-electron redox process occurs with no accompanying chemical reactions. Separate EPR samples were generated of **20**, **20** oxidized with an equiv. of [Fc][$B(Ar^F)_4$], and **20** oxidized with [Fc][$B(Ar^F)_4$] and subsequently treated with an equiv. of Fc* (1 mM in THF). The three respective EPR spectra show the typical $g = 2$ signal associated with **20**, an EPR silent spectrum associated with $\mathbf{20}^+$, and a spectrum that is essentially identical to the initial spectrum of **20** (Figure 4.14). This EPR data in conjunction with the electrochemical reversibility titrations of **20** monitored by UV-vis spectroscopy support the identity of $\mathbf{20}^+$ as the one-electron oxidized form of **20**.

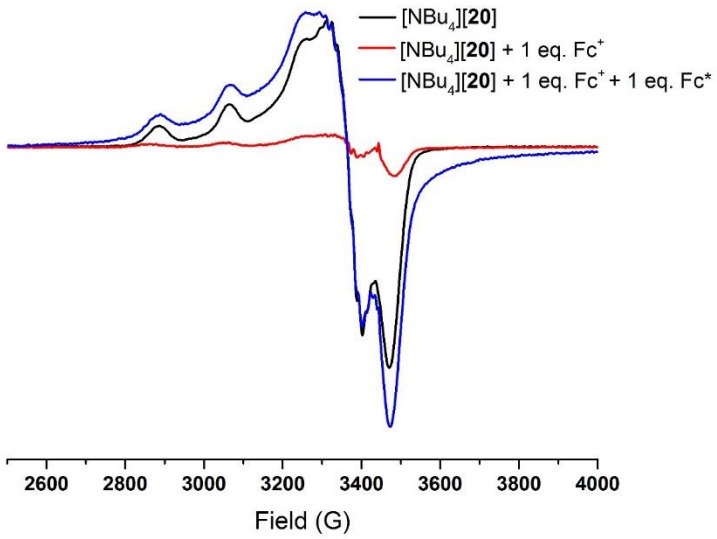

Figure 4.14. Overlaid EPR spectra of [NBu_4][**20**], [NBu_4][**20**] after addition of [Fc][$B(Ar^F)_4$]), and [NBu_4][**20**] after subsequent addition of [Fc][$B(Ar^F)_4$] and then Fc*. All Spectra taken at 1 mM in THF at 30 K.

4.4.2 Resonance Raman studies of [Cu(OOR)]$^{2+}$ complexes

All resonance Raman spectra were run in collaboration with Nicole Gagnon. To confirm the presence of the alkylperoxo ligand in the 1-electron oxidized product, we obtained resonance Raman spectra for frozen solutions of **20**$^+$ in THF (λ_{ex} = 561 nm) with samples prepared from natural abundance $Cm^{16}O^{16}OH$ or labeled $Cm^{18}O^{18}OH$. Isotopically enriched cumene hydroperoxide was synthesized by known literature procedures[157] and subsequently used for generation of ^{18}O-enriched [NBu_4][**20]** by the analogous synthetic procedure described in Scheme 4.1. Incorporation of ^{18}O into complex **20** was evaluated by negative mode ESI-MS methods (Figure 4.15). The degree of ^{18}O incorporation was calculated using relative peak heights of the feature corresponding to ^{16}O alkylperoxo complex (*m/z* = 697) and the ^{18}O enriched complex (*m/z* = 701) using Equation 4.1. In Equation 4.1, M_{701b} is the total peak height at *m/z* =

701, M_{701a} is the predicted contribution to the *m/z* = 701 feature due to naturally occurring isotopes of the unlabeled complex and M_{697} is the total peak height of the feature at *m/z* = 697. No mixed labeled ^{16}O-^{18}O alkylperoxo species was detected by ESI-MS. The ^{18}O incorporation of complex **20** was calculated to be ~60% using this method.

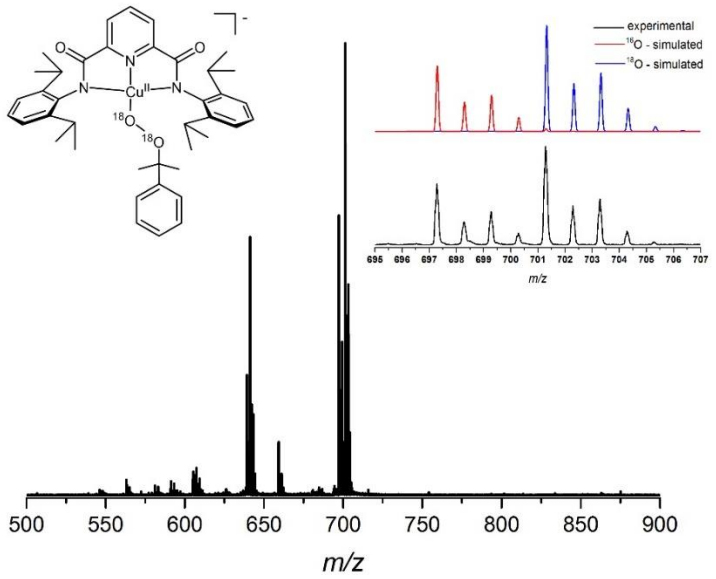

Figure 4.15. Negative mode low-res ESI-MS of ^{18}O isotopically labeled [NBu_4][**20**], with simulated isotopic pattern for the parent ion shown in the inset (60% incorporation of label).

$$\%^{18}O \text{ incorporation} = \left(\frac{(M_{701b} - M_{701a})}{((M_{701b} - M_{701a}) + M_{697})} \right) \times 100\% \qquad (\mathbf{4.1})$$

A resonance Raman feature at 831 cm^{-1} in the ^{16}O sample of $\mathbf{20}^{+}$ shifts to 813 cm^{-1} upon ^{18}O-labeling (Figure 4.16); it is the only feature that is sensitive to isotopic labeling. The $\Delta_{16O-18O}$ = 18 cm^{-1} is smaller than calculated from Hooke's law for ν(O-O) (48 cm^{-1}),

but close to values reported previously for Cu^{II}-alkylperoxo complexes ($\Delta_{16O-18O}$ in the range 24-89 cm^{-1} with most between 24-30 cm^{-1}).[62] To rationalize these smaller values, mixing of the ν(O-O), ν(C-O), and ν(C-C) modes was proposed, and we surmise that similar mixing occurs for **20**$^{+}$. Consistent with this hypothesis, DFT numerical frequency calculations performed by Dr. Andrew Spaeth yielded $\Delta_{16O-18O}$ = 26 cm^{-1} for a highly delocalized vibration at 856 cm^{-1} for the ^{16}O isotopomer.[158] The presence of the isotopically identified O-O stretching frequency supports our assignment of **20**$^{+}$ as the one-electron oxidized product of **20** containing a $[Cu(OOR)]^{2+}$ core.

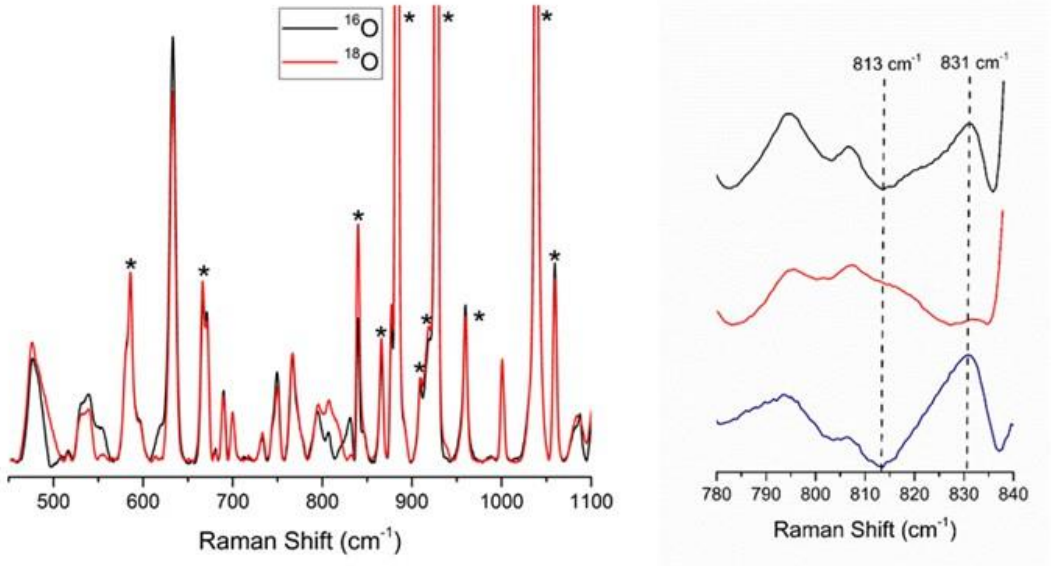

Figure 4.16. Full resonance Raman spectra of [NBu4][**20**] with ^{16}O (black) and ^{18}O (red) showing a shift of the peak at 831 cm^{-1} to 813 cm^{-1} (right) and enlarged region of interest (right). (* denotes solvent).

4.4.3 Computational assessment of $[Cu(OOR)]^{2+}$ complexes

All computational work reported in this section was performed in collaboration with Dr. Andrew Spaeth. In prior work on the $[Cu(OH)]^{2+}$ moiety, we showed this core was best described as a singlet Cu^{III} species.[35] For the $[Cu(OOR)]^{2+}$ complexes, the electronic energies of the singlet and triplet states were tracked running relaxed surface scans about the N1-Cu1-O1-O2 torsion angle (*m*PWPW / Def2-TZVP, Figures 4.17). The

data show that the torsion angle changes the energy of the singlet-triplet gap ($E_{S\text{-}T}$) such that the singlet state is favored at 0° but the $E_{S\text{-}T}$ gap becomes much smaller at 90°. Spin density plots of **20**$^{+}$ and **21**$^{+}$ as singlet and triplet configurations show the expected opposite spin on the copper center and ligands for the singlet state with positive spin on both for triplet states (Figure 4.18).

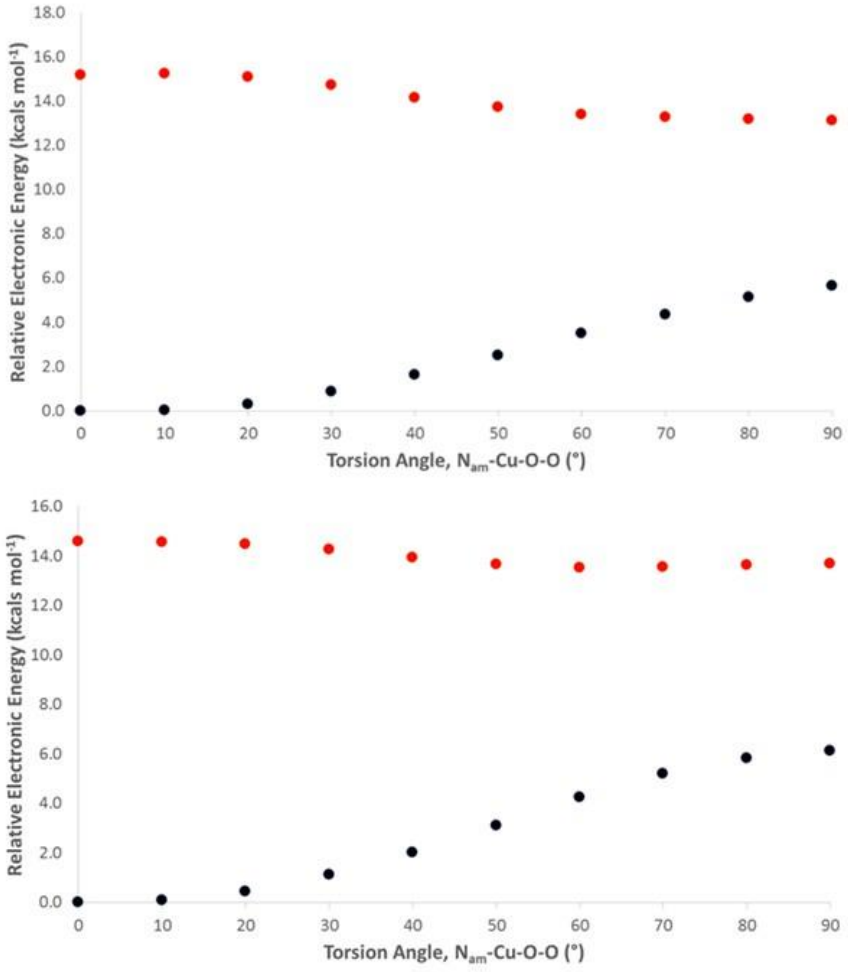

Figure 4.17. Relaxed surface scan of **20**$^{+}$ (top) and **21**$^{+}$ (bottom) [*m*PWPW / Def2-TZVP] tracking the electronic energy of the singlet (black) and triplet (red) states by varying the torsion angle about the N1-Cu1-O1-O2. Note that the electronic energy of the singlet state has not been spin purified.

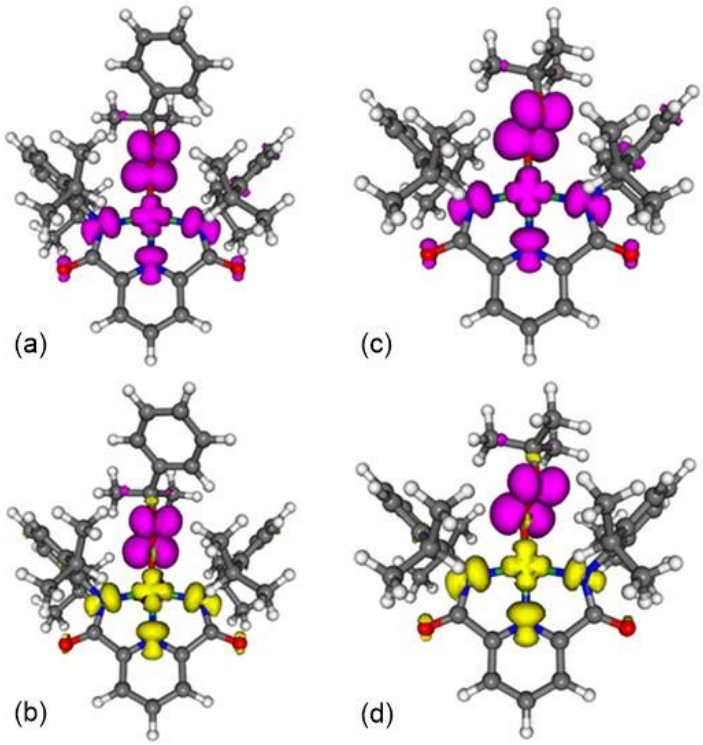

Figure 4.18. Spin density plots (pink is positive density, yellow is negative density) of $[Cu(OOR)]^{2+}$ for [(a,b) R = cumyl **20**$^{+}$; (c,d) R = *t*Bu **21**$^{+}$] where (a & c) are the triplet states and (b & d) are the broken-symmetry solution singlet states using PBE0 / Def2-TZVP | Def2-QZVP(Cu) level of theory where gray, white, blue, red, and green atoms represent C, H, N, O, and Cu, respectively.

Density functional theory (DFT) geometric optimization of the structures of both triplet and singlet electronic states indicate several differences in structural metrics between the two proposed electronic configurations (metrics listed in Table 4.3). As mentioned above, the N1-Cu1-O1-O2 torsion angle is significantly different between the calculated singlet and triplet geometries with values of 4° and 3° in singlet states and 80° and 63° in triplet states for **20**$^{+}$ and **21**$^{+}$ respectively. Additionally, longer Cu1-O1 (1.929 and 1.923 Å) and shorter O1-O2 distances (1.363 and 1.364 Å) are predicted for triplet states in both **20**$^{+}$ and **21**$^{+}$ respectively whereas the inverse is seen for their singlet states (Cu1-O2 = 1.860 and 1.856 Å; O1-O2 = 1.407 and 1.405 Å). Notably, with respect to the DFT calculated O1-O2 bond distances of the reduced form **20** (O-O = 1.449 Å) and **21**

(O1-O2 = 1.449 Å), **20**$^{+}$ (singlet O1-O2 = 1.407 Å; triplet O1-O2 = 1.364 Å) and **21**$^{+}$ (singlet O1-O2 = 1.405 Å; triplet O1-O2 = 1.363 Å) both have shortened O1-O2 bond distances consistent with previous reports suggesting electron deficient groups can withdraw electron density from antibonding orbitals of peroxo units resulting in a contraction of O1-O2 bond distance.[159] The DFT predicted O1-O2 contraction suggests that the peroxo bond is actually stronger in **20**$^{+}$ and **21**$^{+}$ than their reduced counterparts.

Table 4.3. Geometric parameters compared between XRD data and DFT optimized structures.
[a] Density Functional Theory (DFT) structures calculated at the *m*PWPW / Def2-TZVP | Def2-QZVP(Cu) level where (S) is singlet state and (T) is triplet state.

Complex		**20**	**20**$^{+}$	**20**$^{+}$	**21**	**21**$^{+}$	**21**$^{+}$
Method[a]		DFT	DFT (S)	DFT (T)	DFT	DFT (S)	DFT (T)
Bond Length (Å)	**Cu1-O1**	1.881	1.860	1.929	1.874	1.856	1.923
	Cu1-N2	1.964	1.911	1.961	1.960	1.908	1.958
	Cu1-N1	2.095	2.006	2.059	2.101	1.995	2.058
	Cu1-N3	2.115	1.995	2.053	2.110	2.001	2.044
	O1-O2	1.449	1.407	1.364	1.449	1.405	1.363
	O2-C1	1.461	1.493	1.523	1.452	1.482	1.507
Torsion Angle (°)	**N1-Cu1-O1-O2**	9	4	80	5	3	63
	Cu1-O1-O2-C1	129	127	175	136	128	178

To better estimate the $E_{S\text{-}T}$ gap, broken-symmetry (BS) calculations starting at the singlet state optimized geometries (torsion angles of 4° (**20**$^{+}$) or 3° (**21**$^{+}$)) were performed and shown to favor the singlet state by >10 kcal/mol after spin purification (using eq. 4.4; Table 4.4). However, BS calculations starting at the triplet state optimized geometries (torsion angles of 80° (**20**$^{+}$) or 63° (**21**$^{+}$)) favored the singlet state by ~4 kcal/mol when using GGA or meta-GGA functionals, while hybrid-GGA, meta-hybrid-GGA, and double hybrid functionals predominantly favored the triplet ground state by ~2 kcal/mol (Table 4.5).

Table 4.4. Functional screen of the broken-symmetry calculations for **20**$^+$ and **21**$^+$starting from the *singlet* state optimized geometry [*m*PWPW / Def2-TZVP | Def2-QZVP(Cu)] where a negative number indicates the singlet state is favored and a positive number means the triplet state is favored for the ground state. Electronic energy of the singlet state (E_S) was spin purified according to eq. 4.4.

Complex	Functional[a]	E_T (Eh)	E_{BS} (Eh)	$\langle S^2_T \rangle$	$\langle S^2_{BS} \rangle$	Spin Purified E_S (kcal/mol)
20$^+$	*m*PWPW	-3659.529426	-3659.566989	2.005	0.000	-23.7
	M06-L	-3659.303285	-3659.338407	2.011	0.000	-22.1
	PBE0	-3656.952555	-3656.976949	2.012	0.326	-18.4
	M06-2X	-3658.679340	-3658.692578	2.013	0.791	-13.8
21$^+$	*m*PWPW	-3467.757952	-3467.795736	2.005	0.000	-23.8
	M06-L	-3467.529614	-3467.564999	2.011	0.000	-22.3
	PBE0	-3465.38489	-3465.408997	2.012	0.332	-18.2
	M06-2X	-3466.955196	-3466.968200	2.012	0.792	-13.6

[a] All calculations used the Def2-TZVP | Def2-QZVP(Cu) basis set, see experimental section for further details.

Table 4.5. Functional screen of the broken-symmetry calculations for **20**$^{+}$ (top series) and **21**$^{+}$(bottom series) starting from the *triplet* state optimized geometry [*m*PWPW / Def2-TZVP | Def2-QZVP(Cu)] where a negative number indicates the singlet state is favored and a positive number means the triplet state is favored for the ground state. Electronic energy of the singlet state (E_S) was spin purified according to eq. 4.4.

Complex	Functional[a]	E_T (Eh)	E_{BS} (Eh)	$\langle S^2_T \rangle$	$\langle S^2_{BS} \rangle$	Spin Purified E_S (kcals/mol)
20^{+}	*m*PWPW	-3659.545698	-3659.550960	2.005	0.553	-4.6
	BP86	-3659.226612	-3659.230524	2.007	0.562	-3.4
	OLYP	-3659.877159	-3659.882306	2.005	0.553	-4.5
	TPSS	-3659.988592	-3659.993048	2.006	0.575	-3.9
	M06-L	-3659.314125	-3659.316289	2.010	0.580	-1.9
	B3LYP	-3658.284841	-3658.282856	2.010	0.924	2.3
	PBE0	-3656.974595	-3656.972625	2.011	1.008	2.5
	TPSSh	-3659.733747	-3659.733713	2.009	0.765	0.0
	PW6B95	-3663.008901	-3663.006935	2.010	1.008	2.5
	M06	-3658.099305	-3658.095872	2.012	0.937	4.1
	M06-2X	-3658.701729	-3658.700219	2.012	1.010	1.9
	PWPB95	-3664.091592	-3664.090095	2.015	1.014	1.9
Complex	**Functional[a]**	**E_T (Eh)**	**E_{BS} (Eh)**	**$\langle S^2_T \rangle$**	**$\langle S^2_{BS} \rangle$**	**Spin Purified E_S (kcals/mol)**
21^{+}	mPWPW	-3467.773868	-3467.779513	2.005	0.555	-4.9
	BP86	-3467.504909	-3467.509186	2.006	0.564	-3.8
	OLYP	-3468.082143	-3468.087702	2.005	0.555	-4.8
	TPSS	-3468.156636	-3468.161426	2.006	0.577	-4.2
	M06-L	-3467.541244	-3467.543870	2.010	0.590	-2.3
	B3LYP	-3466.607097	-3466.605961	2.010	0.899	1.3
	PBE0	-3465.405376	-3465.403522	2.011	0.994	2.3
	TPSSh	-3467.923568	-3467.924091	2.009	0.774	-0.5
	PW6B95	-3470.953343	-3470.951542	2.010	0.992	2.3
	M06	-3466.450587	-3466.448062	2.012	0.884	2.9
	M06-2X	-3466.975813	-3466.974268	2.012	1.010	2.0
	PWPB95	-3472.438347	-3472.436818	2.016	1.014	2.0

[a] All calculations used the Def2-TZVP | Def2-QZVP(Cu) basis set, see experimental section for further details.

Comparison of TD-DFT spectra calculated for both states (PBE0/Def2-TZVP) to the experimental UV-Vis spectra for **20**$^+$ and **21**$^+$ indicated marginally better agreement for the singlet, but do not rule out the triplet (Figures 4.19–4.20, Table 4.6). Additionally, no significant difference in the Raman stretching frequencies is predicted between the singlet and triplet states (within 2 cm^{-1}). We conclude at this juncture that more extensive work is needed to unambiguously determine the ground state, and note that because the accuracy of broken-symmetry predictions is notoriously difficult for transition metals,[160-162] future studies will involve reevaluation of the $E_{S\text{-}T}$ gap using multireference calculations.

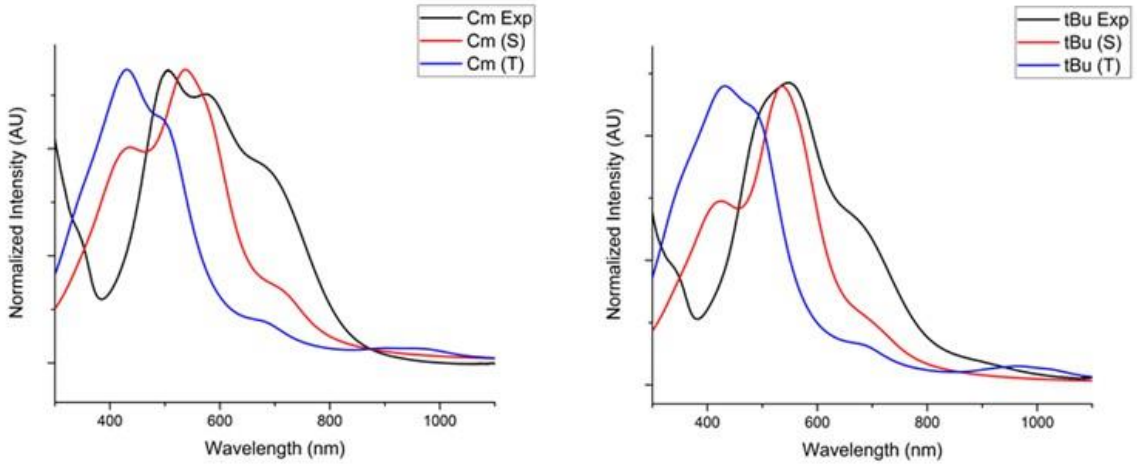

Figure 4.19. Overlay of **20**$^+$ (left) and **21**$^+$ (right) experimental UV-Vis spectrum [THF, -80°C, black line] with the TD-DFT predicted [PBE0 / Def2-TZVP] spectrum of the singlet state (red line) and triplet state (blue line) using a Lorentzian lineshape (half-width = 50 nm), normalized to the λ_{max} of the experimental spectrum.

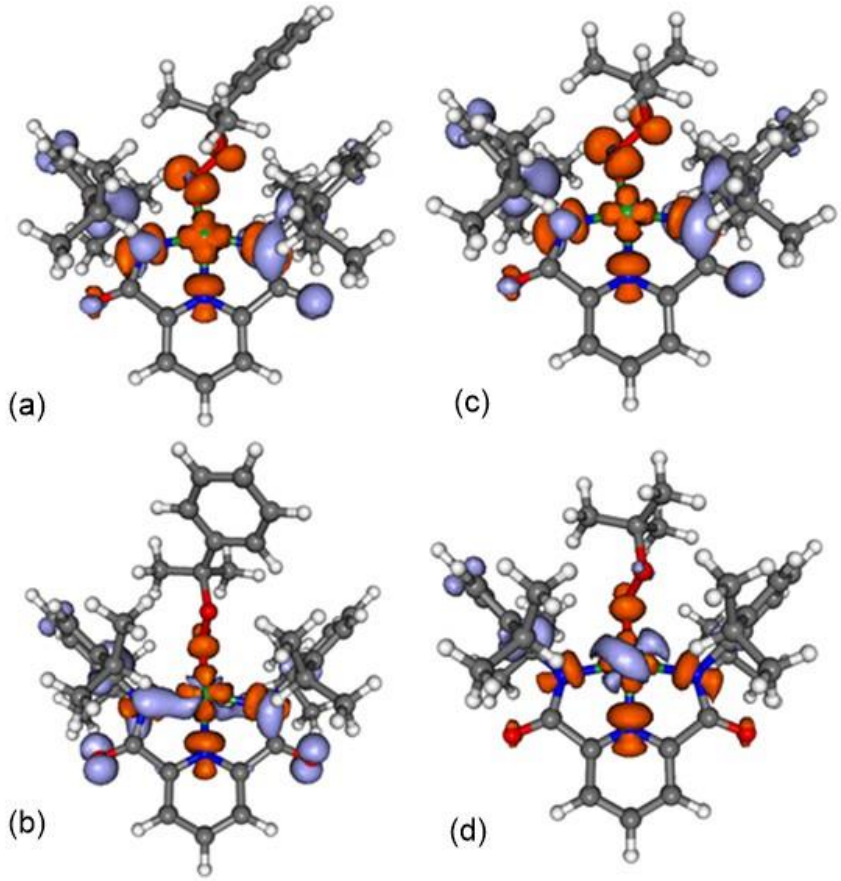

Figure 4.20. TD-DFT difference density plots of the most intense oscillator strength transition (purple is loss of electron density, orange gain of electron density) of $[Cu(OOR)]^{2+}$ for [(a,b) R = cumyl, **20**$^{+}$; (c,d) R = *t*Bu, **21**$^{+}$ where (a & c) are the singlet states and (b & d) are the triplet states using PBE0 / Def2-TZVP level of theory where gray, white, blue, red, and green atoms represent C, H, N, O, and Cu, respectively.

Table 4.6. TD-DFT for **20**$^+$ and **21**$^+$ in the singlet and triplet states using PBE0 / Def2-TZVP of the first 40 excited states with an oscillator strength threshold of >0.001. Bolded values are pictured as difference density plots in Figure 4.20.

20$^+$ (S)		**20**$^+$ (T)		**21**$^+$ (S)		**21**$^+$ (T)	
Energy (nm)	$f_{osc.}$	Energy (nm)	$f_{osc.}$	Energy (nm)	$f_{osc.}$	Energy (nm)	$f_{osc.}$
722	0.038	1453	0.005	719	0.019	1444	0.009
690	0.020	995	0.001	682	0.027	1177	0.002
605	0.008	972	0.002	579	0.039	1030	0.003
584	0.180	946	0.001	568	0.150	985	0.001
564	0.007	895	0.002	561	0.007	964	0.004
531	**0.262**	685	0.008	**527**	**0.294**	915	0.002
479	0.033	588	0.001	433	0.067	689	0.008
447	0.035	543	0.003	429	0.025	649	0.001
434	0.046	509	0.063	405	0.096	637	0.001
429	0.056	499	0.011	391	0.019	**501**	**0.056**
405	0.067	449	0.018	367	0.002	493	0.027
396	0.031	**430**	**0.072**	364	0.002	466	0.001
370	0.001	425	0.001	360	0.010	453	0.023
364	0.004	408	0.009	347	0.015	427	0.029
360	0.003	395	0.002	344	0.015	425	0.034
351	0.008	394	0.001	342	0.007	405	0.011
347	0.027	393	0.003	338	0.004	396	0.006
		388	0.002			391	0.002
		386	0.017			388	0.003
		377	0.001			382	0.003
		373	0.001			371	0.010
		365	0.002			368	0.002
		359	0.001			365	0.006
		355	0.001			364	0.002
		350	0.001			358	0.001
		348	0.004			351	0.003
		344	0.002			351	0.001
		341	0.017			345	0.002
		338	0.001			345	0.002
		337	0.005			340	0.008
		334	0.001			338	0.004
						335	0.008
						332	0.002

			330	0.006
			328	0.001

4.5 Reactivity studies of L1bCu(OOCm) (20^+)

Preliminary investigation into the reactivity of $\mathbf{20}^+$ with various substrates revealed notable differences relative to **L1b**$Cu^{III}OH$.[23,34,35] UV-vis spectroscopic monitoring showed that the rate of decay of solutions of $\mathbf{20}^+$ was not enhanced and no new spectral features were observed upon addition of excess (200 equiv.) 9,10-dihydroanthracene, 1,4-cyclohexadiene, phenol, 2,4,6-tri-*tert*-butyl phenol, 2,4-di-*tert*-butyl phenol, 4-*tert*-butyl phenol, or 4-methyl-2,6-*tert*-butyl-phenol. These substrates have relatively weak C-H or O-H bonds that react rapidly with **L1b**$Cu^{III}OH$ via proton coupled electron transport (PCET) mechanisms.[152,163] The indifference of $\mathbf{20}^+$ towards even weak O-H bonds of phenolic substrates was initially surprising to us as these substrates have been shown to react nearly instantaneously under identical conditions with **L1b**$Cu^{III}OH$.[152]

4.5.1 Reactions with TEMPO-H

After the initial observation of a lack of reactivity of $\mathbf{20}^+$ with most substrates it was observed that upon addition of 1-hydroxy-2,2,6,6-tetramethyl-piperidine (TEMPO-H) to $\mathbf{20}^+$ (THF, -80 °C) rapid exponential decay of its UV-vis feature resulted. The concentration of TEMPO-H was varied (25-200 equiv.) and monitoring the decay by UV-vis spectroscopy showed the reaction to be first-order in TEMPO-H with an overall second order rate constant of ~2.4 $M^{-1}s^{-1}$ (Figures 4.21- 4.22). The final decay spectrum resembles a Cu^{II} species with what appears to be a d→d feature at ~570 nm. Clean isosbestic points at ~375 nm and ~425 nm indicate that this is a single step reaction with no observable intermediate species formed.

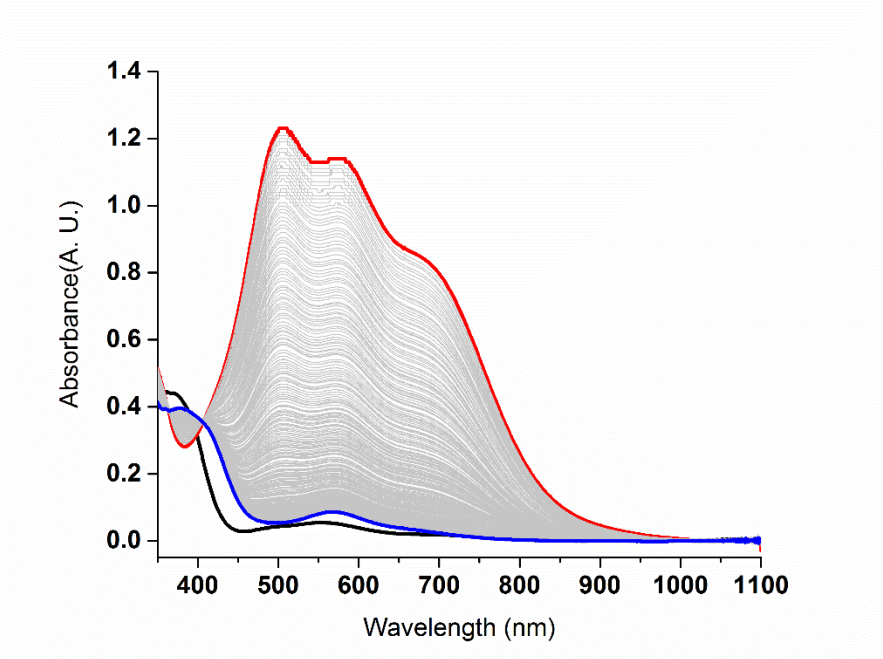

Figure 4.21. Reaction of 0.1 mM **20**$^{+}$ with 100 equiv. TEMPO-H at -80 °C in THF. Starting spectrum [NBu$_4$][**20**] (black), oxidized spectrum **20**$^{+}$ (red), and final decay spectrum (blue).

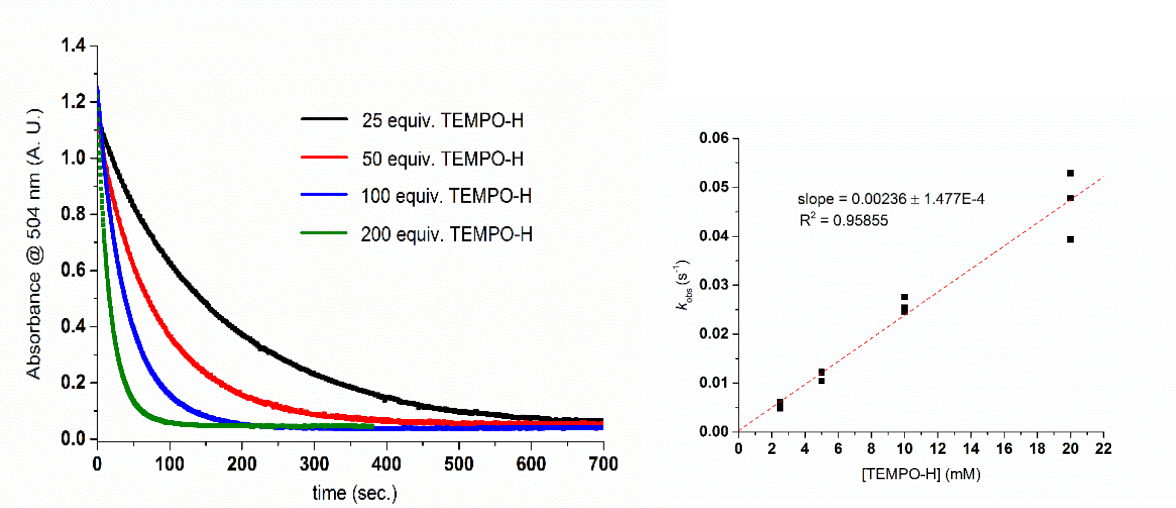

Figure 4.22. Plot of observed rates of reaction of **20**$^{+}$ with TEMPO-H vs. concentration of TEMPO-H (left). Plot of decay of 504 nm feature over time with varying equivalents of TEMPO-H (right).

EPR studies of the final reaction solution indicate the presence of a Cu^{II} complex the identity of which is still unknown. EPR spin quantification studies also indicate production of the expected TEMPO• radical (~70% yield) consistent with a PCET mechanism of **20**$^{+}$ with TEMPO-H. TEMPO-H is a useful substrate in gauging even mild competency at PCET as it exclusively proceeds through concerted proton electron transfer processes. The bond dissociation free energy (BDFE) of the O-H bond in TEMPO-H is reported to be ~67.5 kcal/mol[71] giving us a potential lower limit for strengths of bonds that **20**$^{+}$ can activate.

If a simple single PCET mechanism with TEMPO-H occurs then the expected products of this reaction would be CmOOH, TEMPO•, and a Cu^{II}-solvato species, presumably **L1b**Cu(THF) (Scheme 4.4). Identification of the final Cu^{II} decay complex has not implicated conclusively the presence of **L1b**Cu(THF) possibly due to a mixture of products being present at the end of the reaction. Unfortunately, other than the presence of TEMPO•, we still are pursuing the identification of all reaction products.

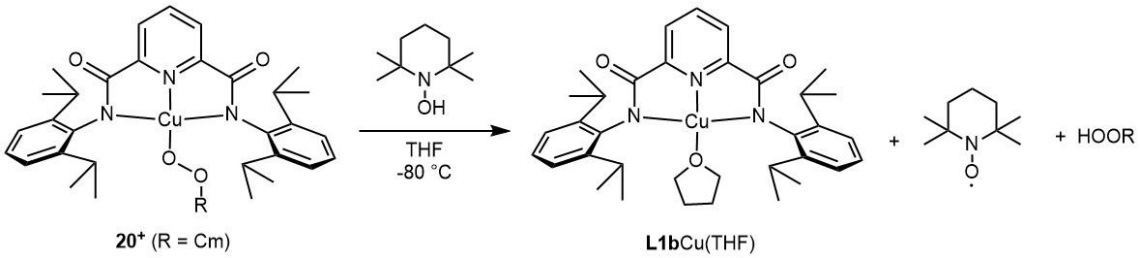

Scheme 4.4. Proposed products formed from reaction of **20**$^{+}$ with TEMPO-H.

4.5.2 Reactivity with phenols

During our initial substrate reactivity screenings of **20**$^{+}$ with phenols several substrates showed reactivity with **20**$^{+}$ that upon further investigation were found to undergo more complicated mechanisms than single PCET as was observed with TEMPO-H. Addition of 4-dimethylamino-phenol (^{NMe2}PhOH) to **20**$^{+}$ (THF, -80 °C) resulted in

instantaneous loss of the UV-vis features associated with **20**$^{+}$ and generation of a new feature at ~740 nm (Figure 4.23, blue trace). This spectrum is identical to that reported previously to form upon reaction of **L1b**Cu^{III}(OH) with ^{NMe2}PhOH and was tentatively assigned as the Cu^{II}-phenoxyl radical complex **L1b**Cu(•OPh^{NMe2}) (**22**$^{+}$).[152]

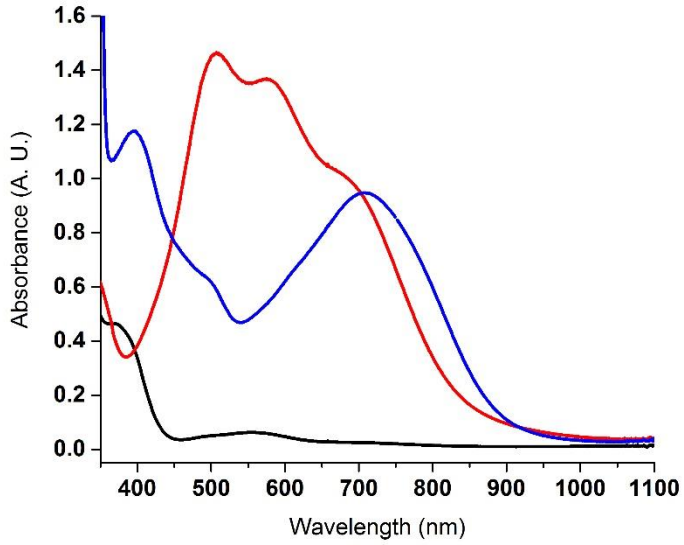

Figure 4.23. Reaction of 0.1 mM **20**$^{+}$ with 200 equiv. ^{NMe2}PhOH at -80 °C in THF. Starting spectrum [NBu$_4$][**20**] (black), oxidized spectrum **20**$^{+}$ (red), and spectrum after addition of ^{NMe2}PhOH (blue).

To buttress the assignment of **22**$^{+}$ as the product of reaction of **20**$^{+}$ with ^{NMe2}PhOH, an independent synthetic route was used to prepare the Cu^{II}-phenolate complex [NBu$_4$][**L1b**Cu(OPh^{NMe2})] ([NBu$_4$][**22**]). The complex [NBu$_4$][**22**] was synthesized in an analogous route to that used for generation of [NBu$_4$][**20**] and [NBu$_4$][**21**] where excess ^{NMe2}PhOH was reacted with [NBu$_4$][**L1b**Cu(OH)] in the presence of activated molecular sieves (Scheme 4.5). The final product could be isolated as a stable deep purple powder (155 mg, 90 %).

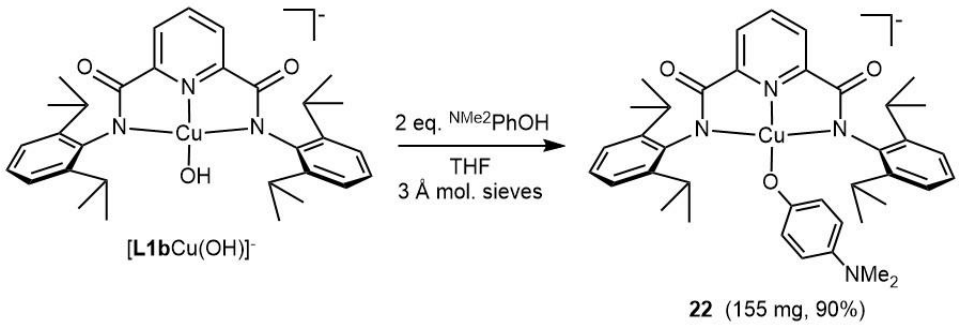

Scheme 4.5. Synthetic route for generation of **22** from [**L1b**Cu(OH)]$^-$. Reaction performed with tetrabutylammonoium salts of copper complexes.

The complex [NBu$_4$][**22**] was characterized by HR-ESI-MS, UV-vis spectroscopy, and CV measurements (Figures 4.24 - 4.25). Negative ion mode HR-ESI-MS of [NBu$_4$][**22**] displays a parent ion peak at *m/z* = 682.187 consistent with the anionic complex of **22**. UV-vis spectroscopy of [NBu$_4$][**22**] in THF at -80 °C displays several observable features at 462 nm, 533 nm, and 726 nm; distinctly identifiable from the UV-vis features associated with **20**. A quasi-reversible redox feature (i_{pa}/i_{pc} = 1.6 at 50 mV/s) is observed upon CV measurements of **22** in solution with a calculated $E_{1/2}$ of -639 mV vs. Fc^+/Fc. The low redox potential of **22** is in agreement with the coordination of the electron rich 4-dimethylamino-phenoxide ligand in the complex and is also suggestive that this species can be easily oxidized by even mild chemical oxidants. We tentatively assign the observed redox process as a phenoxide centered oxidation to give the Cu^{II}-phenoxyl species **22**$^+$. The high reversibility of the redox process also suggests to us that **22**$^+$ is reasonably long lived.

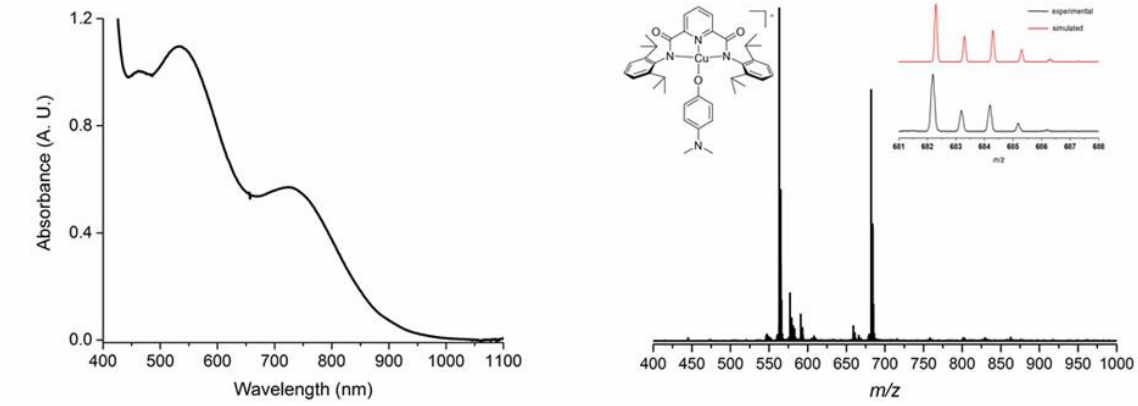

Figure 4.24. UV-vis spectrum of 2 mM solution in THF at -80 °C (left) and HR-ESI-MS (right) of [NBu_4][**L1b**Cu(OPh^{NMe2})] ([NBu_4][**22**]).

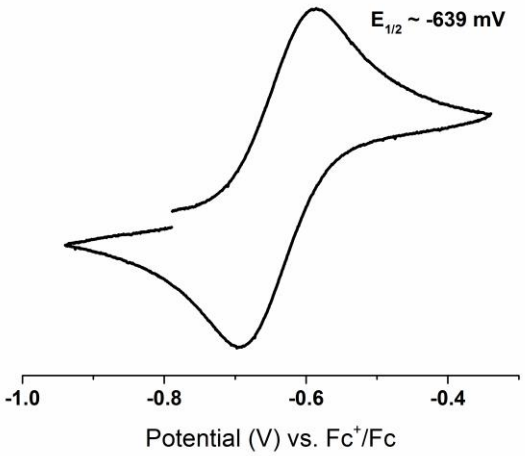

Figure 4.25. Cyclic voltammogram of 2 mM solution [NBu_4][**22**] in THF (0.3 M NBu_4PF_6) with a scan rate of 50 mV/s.

Treatment of [NBu_4][**22**] (THF, -80 °C) with [Fc][$B(Ar^F)_4$] yielded the same UV-vis spectrum as that seen for the reaction of $\mathbf{20}^+$ with ^{NMe2}PhOH,[152] consistent with formation of $\mathbf{22}^+$ (Figure 4.26). The conversion of $\mathbf{20}^+$ to $\mathbf{22}^+$ involves a net proton transfer (Scheme 4.6), but multiple possible mechanisms may be envisaged, including simple proton transfer, PCET, stepwise proton transfer -electron transfer (PT/ET), or stepwise electron transfer - proton transfer (ET/PT) pathways. We note that ^{NMe2}PhOH is the least acidic phenol (p*K*a = 19.8 in DMSO)[71] and contains the lowest O-H bond dissociation free energy (BDFE = 78.7 kcal/mol in DMSO)[71] of all the phenolic substrates that we screened. Thus, at this juncture we view simple proton transfer to be unlikely and a PCET or ET/PT pathway to be more appropriate (further mechanistic work is underway).

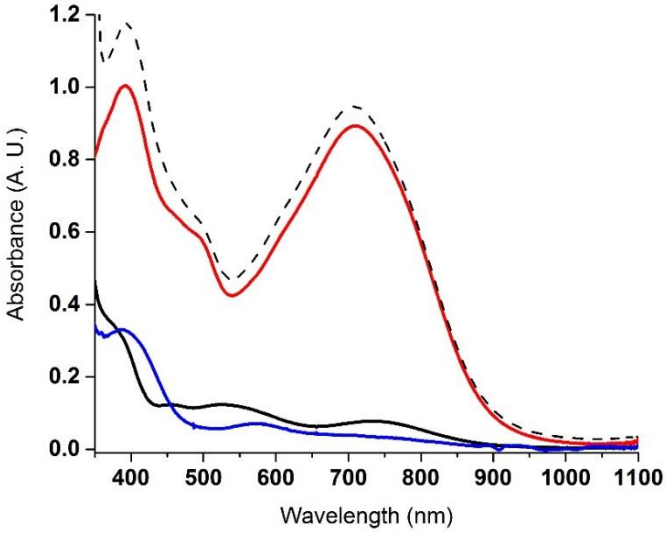

Figure 4.26. UV-vis spectra of 0.1 mM of starting [NBu_4][**20**] (solid black) after addition of 1 equiv, of [Fc][$B(Ar^F)_4$](solid red), decomposition spectrum (solid blue), and overlaid spectrum of reaction of $\mathbf{20}^+$ with ^{NMe2}PhOH (dashed black). All spectra collected in THF at -80 °C.

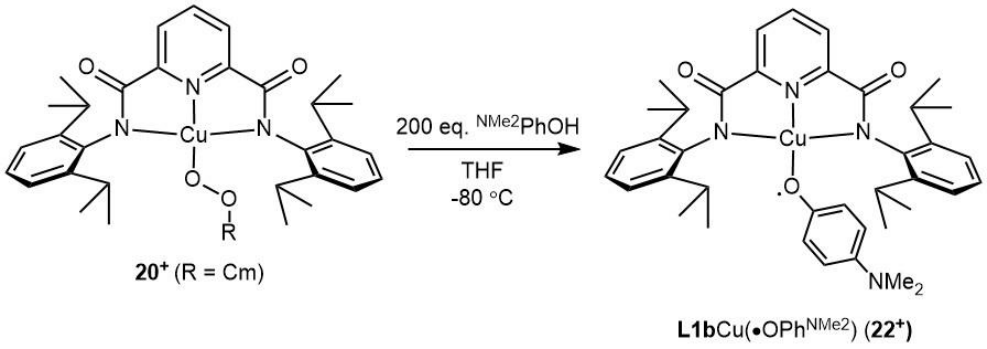

Scheme 4.6. Reaction of **20**$^{+}$ with ^{NMe2}PhOH to give **L1b**Cu(•OPh^{NMe2}) (**22**$^{+}$).

Screening phenolic derivatives for potential reactivity also showed decay of the UV-vis spectral features associated with **20**$^{+}$ when reacted with 4-nitrophenol (^{NO2}PhOH) at -80 °C in THF (Figure 4.27). In the reaction of **20**$^{+}$ with excess ^{NO2}PhOH (200 equiv.) no intermediate species was detected by UV-vis spectroscopy like what had been observed previously with ^{NMe2}PhOH. Exponential decay of the characteristic band at 504 nm was monitored over time and full decay of the **20**$^{+}$ species was completed after ~300 seconds. The resulting spectrum contained a band at 625 nm consistent with the known UV-visible features associated with ferrocenium (Fc^{+}) in solution. Due to the high acidity of ^{NO2}PhOH (p*K*a = 10.8 in DMSO)[71] with respect to other unreactive phenolic substrates (p*K*a =17.7 - 19.8 in DMSO),[71] we speculated that a protonation event of **20**$^{+}$ may be occurring to generate a formally Cu^{III}-cumenehydroperoxide adduct [**L1b**Cu(HOOCm)]$^{+}$. The protonation of **20**$^{+}$ is proposed to increase the redox potential of the complex such that it can then reoxidize the ferrocene in solution, resulting in rapid decay of **20**$^{+}$ and the observed formation of Fc^{+} (Scheme 4.7). This type of behavior has been previously reported with the reaction of phenols with the **L1b**Cu^{III}(OH) whereby protonation by the phenols was found to generate the corresponding [**L1b**Cu^{III}(OH$_2$)]$^{+}$ species and subsequent regeneration of Fc^{+} was observed.[152] The identity of the final copper complex is still under investigation in these reactions but we believe the most likely species to

exist are **L1b**Cu(X) adducts where X is either THF, CmOOH, or 4-nitrophenoxide ($^{NO2}PhO^-$).

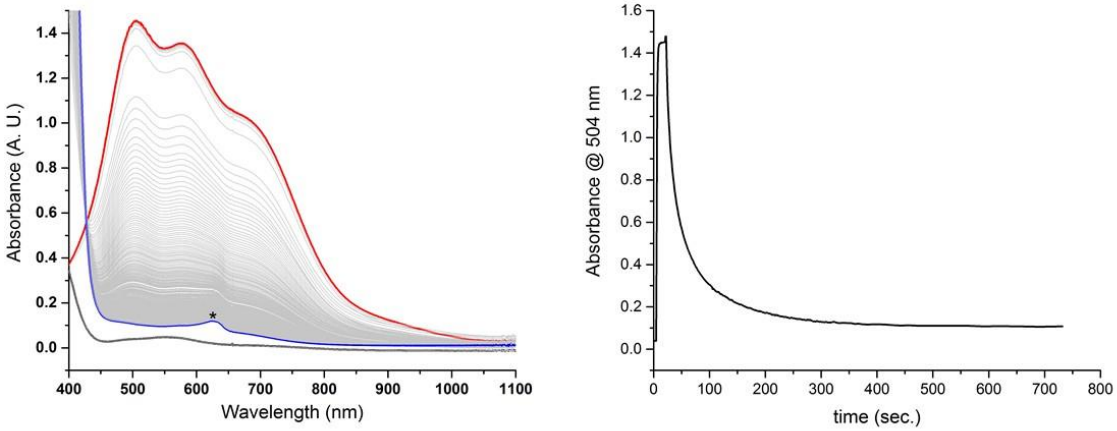

Figure 4.27. UV-vis spectra of 0.1 mM of starting [NBu_4][**20**] (black trace), after addition of 1 equiv of [Fc][$B(Ar^F)_4$] to generate **20**$^+$ (red trace), after addition of 200 equiv. of ^{NO2}PhOH (blue trace) (left) and plot of absorbance at λ = 504nm vs. time of ongoing reaction (right).

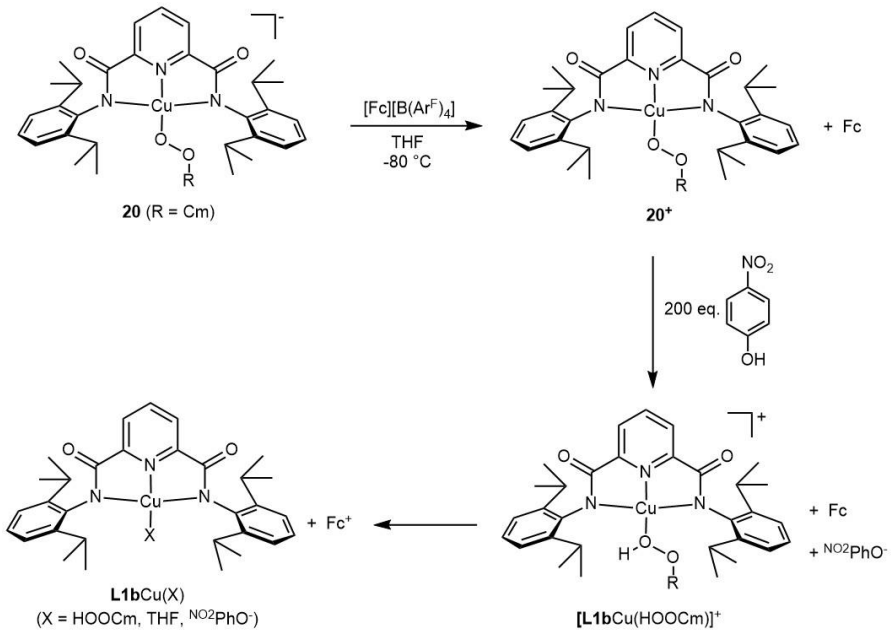

Scheme 4.7. Proposed mechanistic route for protonation of **20**$^{+}$ by ^{NO2}PhOH to generate [**L1b**Cu(HOOCm)]$^{+}$ and its subsequent reduction by Fc to generate Fc^{+} and **L1b**Cu(X) (where X = CmOOH, THF, or ^{NO2}PhO^{-}).

If the proposed protonation of **20**$^{+}$ occurs as drawn in Scheme 4.7 then using a chemical oxidant with a redox potential higher than that of the protonated species [**L1b**Cu(HOOCm)]$^{+}$ should allow direct spectroscopic identification of the protonated intermediate. Employing [AcFc][B(Ar^{F})$_4$] as the chemical oxidant for generation of **20**$^{+}$ from **20**, we were able to observe the diagnostic spectrum we associate with **20**$^{+}$. Upon addition of excess ^{NO2}PhOH to the solution, however, no obvious change to the absorption spectrum was observed that could be attributed to the generation of a new compound. The resulting reaction mixture showed no increase in decay rate of the features of **20**$^{+}$ indicating that **20**$^{+}$ is indifferent to the presence of ^{NO2}PhOH under these reaction conditions (Figure 4.28). After ~90 sec. with no change of the UV-vis absorption features, one equivalent of external Fc was added to the reaction solution, resulting in the

rapid loss of absorption features associated with **20**$^{+}$ and a new feature formed at 625 nm consistent with Fc^{+}.

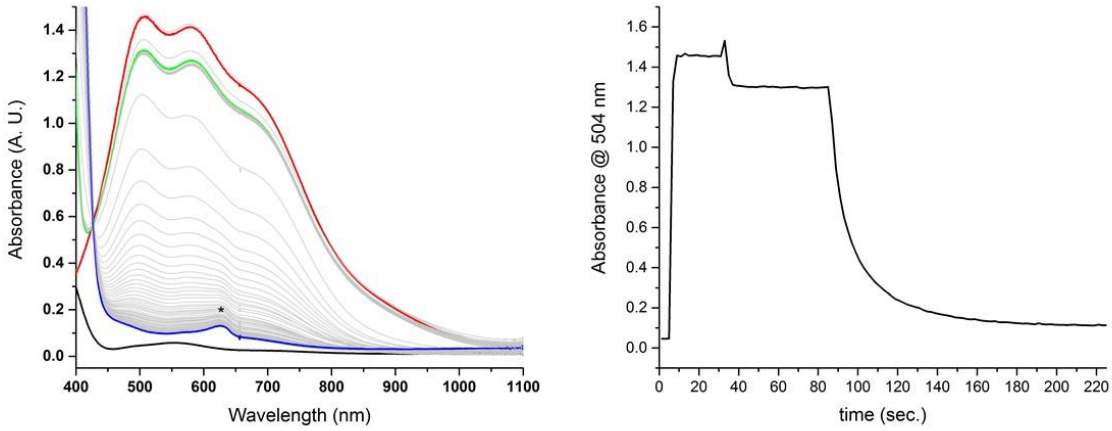

Figure 4.28. UV-vis spectra of 0.1 mM of starting [NBu_4][**20**] (black trace), after addition of 1 equiv of [AcFc][$B(Ar^F)_4$] to generate **20**$^{+}$ (red trace), after addition of 200 equiv. of ^{NO2}PhOH (green trace), after addition of 1 equiv. of Fc (blue trace) (left) and plot of absorbance at λ = 504nm vs. time of ongoing reaction (right). Reaction run in THF at -80 °C.

The lack of an observable intermediate spectrum that can be assigned to [**L1b**Cu(HOOCm)]$^{+}$ is suggestive that our initial proposal of ^{NO2}PhOH protonation of **20**$^{+}$ was incorrect. The decay of **20**$^{+}$ after the addition of external Fc to the solution is notably similar to what is observed when [Fc][$B(Ar^F)_4$] is used as an oxidant initially. The fact that **20**$^{+}$ is stable in the presence of ^{NO2}PhOH or Fc but unstable when both compounds are present points to an alternative reaction pathway. We therefore propose a revised mechanism involving a bidirectional PCET pathway from ^{NO2}PhOH and Fc by **20**$^{+}$. In a bidirectional PCET mechanism a reagent abstracts the proton and electron from two independent sources in a concerted fashion. In the case of **20**$^{+}$, ^{NO2}PhOH is the source of the proton, and Fc is the source of the electron (Scheme 4.8). The experimental observations of the required presence of both reactants for decay of **20**$^{+}$, a lack of discrete

observable intermediates, and the presence of Fc^+ at the end of the reaction all are supportive of a bidirectional mechanism.[164] We reason that while **L1b**Cu^{III}(OH) was shown to undergo PT/ET mechanisms with ^{NO2}PhOH,[152] the expected lower basicity of **20**$^+$ may disallow an initial proton transfer, and a PCET mechanism is instead observed.

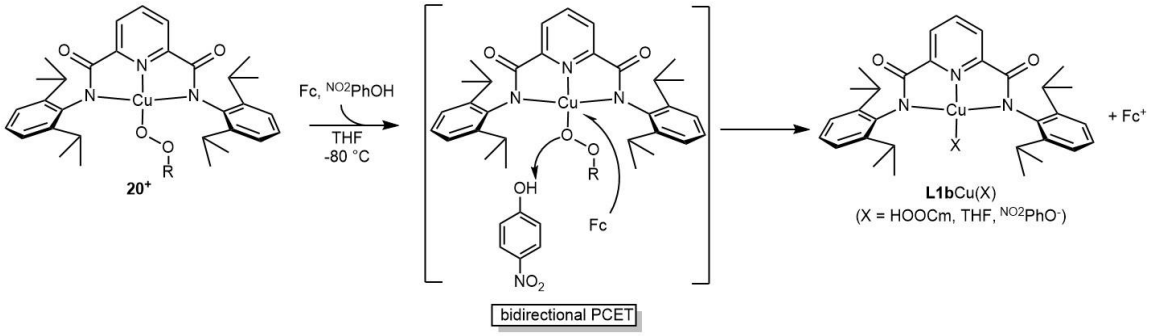

Scheme 4.8. Proposed mechanistic route for bidirectional PCET from ^{NO2}PhOH and Fc by **20**$^+$ to generate Fc^+ and **L1b**Cu(X) (where X = CmOOH, THF, or $^{NO2}PhO^-$).

To further support the proposal of a bidirectional PCET mechanism of **20**$^+$, we performed analogous reactivity experiments using benzoic acid instead of ^{NO2}PhOH (Figure 4.29). Benzoic acid has a reported p*K*a of 11.0 in acetonitrile,[165] similar to that of ^{NO2}PhOH, and is relatively redox innocent. If ^{NO2}PhOH is simply a proton donor in the reaction mechanism then benzoic acid should undergo a similar reaction when subjected to **20**$^+$ in the presence of Fc. Upon addition of excess benzoic acid (200 equiv.) to **20**$^+$ (generated from [AcFc][$B(Ar^F)_4$]), no new features and no significant decay of **20**$^+$ was observed. Addition of an equivalent of external Fc to the reaction solution caused a gradual decay of the UV-vis absorption bands of **20**$^+$ and resulted in a decay spectrum containing the same 625 nm feature assigned as Fc^+. These results suggest that benzoic acid undergoes a similar bidirectional PCET as proposed for ^{NO2}PhOH. We noted that the reaction with benzoic acid exhibited a slower overall decay of **20**$^+$ than with ^{NO2}PhOH, the basis for which is unclear and is a topic of ongoing research.

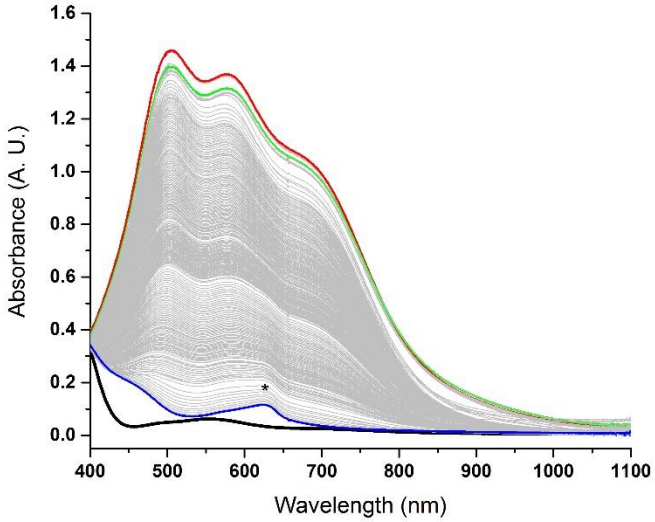

Figure 4.29. UV-vis spectra of 0.1 mM of starting [NBu_4][**20**] (black trace), after addition of 1 equiv of [AcFc][$B(Ar^F)_4$] to generate **20**$^+$ (red trace), after addition of 200 equiv. of benzoic acid (green trace), and after addition of 1 equiv. of Fc (blue trace). Reaction carried out in THF at -80 °C.

4.6 Conclusions

In this work we have prepared and characterized two new, and relatively stable, anionic Cu^{II}-alkylperoxo complexes **20** and **21.** Evidence from spectroscopy and theory shows that one-electron oxidation at low temperature yields novel $[Cu(OOR)]^{2+}$ (R = alkyl) species **20**$^+$ and **21**$^+$. The exact electronic configuration of the $[Cu(OOR)]^{2+}$ core in these systems was explored and whether the complexes are singlet or triplet in nature is not immediately evident, although spectroscopic evidence coincides better with predicted singlet spectral features. Regardless, the discovery of a $[Cu(OOR)]^{2+}$ core provides initial precedent for the possible existence of such species in oxidations catalyzed by copper enzymes. For example, one could envision the involvement of a related $[Cu(OOH)]^{2+}$ species in lytic polysaccharide monooxygenase, an intriguing enzyme due to its utility in

lignocellulosic degradation for biofuel generation (Figure 4.30).[166] We hypothesize that deprotonation of the amino group of the histidine brace enhances the basicity of the initial Cu^{II}-superoxide intermediate **S** (the formation of which may also be promoted by such deprotonation). Such deprotonation of the amino group has been suggested on the basis of X-ray crystallography.[20,25] The enhanced basicity of **S** would facilitate protonation to yield a $[Cu(OOH)]^{2+}$ species ($\mathbf{HP}^{+}$) analogous to the species we have prepared, and similarly stabilized by an anionic supporting ligand (for $\mathbf{HP}^{+}$, a *trans* amide donor). Whether $\mathbf{HP}^{+}$ is sufficiently reactive to be a viable oxidizing intermediate is an open question. Preliminary studies indicate significantly decreased reactivity of $\mathbf{20}^{+}$ with C-H and O-H bonds compared to **L1b**$Cu^{III}(OH)$, consistent with the low oxidation potential and expected low p*K*a for the ROO^{-} ligand of the former. The preliminary indications that $\mathbf{20}^{+}$ is capable of bidirectional PCET, however, may be suggestive of similar mechanisms in LPMO although no experimental observations for this currently exist. Still, further work is needed to understand the reactivity of the $[CuOOR]^{2+}$ core, key issues being the relative propensity for Cu-O vs. O-O bond scission.

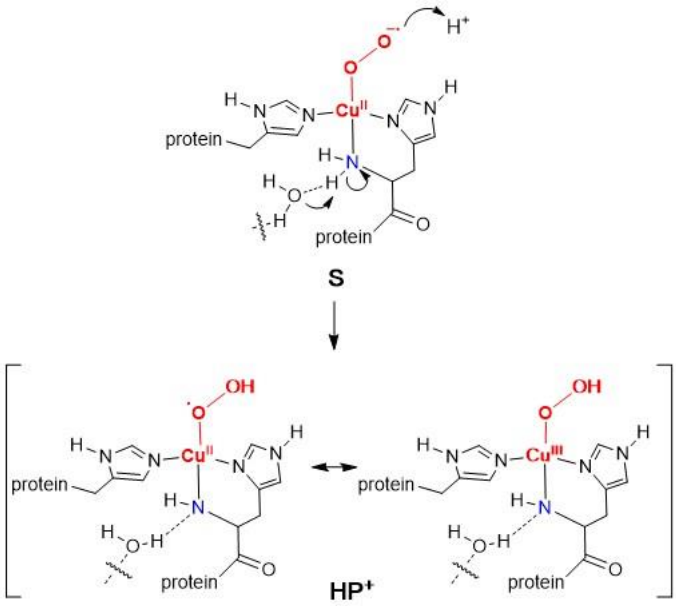

Figure 4.30. Proposed intermediates in LPMO.

4.7 Experimental section

4.7.1 Materials and methods

Preparation and handling of the air-sensitive compounds were carried out under a dinitrogen atmosphere either in a glovebox or using standard Schlenk techniques. All reagents and solvents were purchased from commercial sources and used as received unless otherwise noted. Tetrahydrofuran (THF) was dried over sodium/benzophenone and vacuum distilled. Diethyl ether and pentane was passed through solvent purification columns (Glass Contour, Laguna, California). All solvents were stored over 3 Å molecular sieves in a N_2 filled glove-box prior to use. The compounds (**H_2L1b**, **L1b^{2-}** = N,N'-Bis(2,6-diisoproylphenyl)-2,6-pyridinedicarboxamido),[167] [NBu_4][**L1b**Cu(OH)],[34] ferrocenium tetrakis(3,5-bis(trifluoromethyl)phenyl)borate ([Fc][B(Ar^F)$_4$]),[168] acetylferrocenium tetrakis(3,5-bis(trifluoromethyl)phenyl)borate ([AcFc][B(Ar^F)$_4$]),[168] 4-dimethylamino-phenol (^{NMe2}PhOH),[169] and 1-hydroxy-2,2,6,6-tetramethyl-

piperidine (TEMPO-H)[170] were synthesized by known published procedures. The compound [NEt_4][**L1b**Cu(OH)] was prepared using the same procedure as reported for the synthesis of [NBu_4][**L1b**Cu(OH)],[34] except tetraethylammonium hydroxide was used instead of tetrabuytlammonium hydroxide. The 80% cumene hydroperoxide (CmOOH) and 9 M *tert*-butyl-hydroperoxide (*t*BuOOH) in nonane were procured from Sigma Aldrich Chemical Co. ^{18}O-enriched cumene hydroperoxide (~ 60% ^{18}O incorporation by ESI-MS) was synthesized by using cumene and $^{18}O_2$ (procured from ICON isotopes) according to a literature procedure.[157] Decamethylferrocene (Fc*) was procured from Sigma-Aldrich.

UV-vis spectra were collected on a HP8453 (190-1100nm) diode array spectrophotometer. Low-temperature UV-vis experiments were performed using a Unisoku low-temp UV-vis cell holder. EPR data was collected on a Bruker Elexsys E500 spectrophotometer using X-band radiation at 35 dB and 30 K. EPR spectral simulations were performed using EasySpin software (version 4.5.5).[171] Cyclic voltammograms were recorded using an EC Epsilon potentiostat from BASi, a platinum working electrode, and an $AgNO_3$/Ag reference electrode. All cyclic voltammograms were internally referenced using Fc* and then the potentials converted with respect to the standard Fc^+/Fc couple.[172] X-ray diffraction measurements were collected with a Cu Kα radiation and a Bruker D8 Photon II CPAD diffractometer using normal parabolic mirrors as monochromators. Resonance Raman (rR) spectra were collected on an Acton 506 spectrometer using a Princeton Instruments LN/CCD-11100-PB/UBAR detector and ST-1385 controller interfaced with *Winspec* software. The spectra were obtained at 77 K using a backscattering geometry. Excitation at 561 nm was provided by a Cobalt Jive 100 mW laser. Raman shifts were externally referenced to indene and internally referenced to solvent (THF). Spectra were baseline corrected and normalized to solvent using *Origin*

(2016) software. Hooke's law was used to determine the force constant (*k*) and the expected shift upon isotopic labeling:

$$\nu = \frac{1}{2\pi}\sqrt{\frac{k}{\mu}} \;\Rightarrow\; k = \mu(2\pi\nu)^2 \tag{4.2}$$

$$\mu = \frac{m_1 m_2}{m_1 + m_2} \tag{4.3}$$

where ν is the stretching frequency (in Hz), μ is the reduced mass (in kg), and m_1 and m_2 are the masses of the atoms involved in the vibration (in kg).[1] The final units of *k* are N m^{-1}, which are converted to mdyn $Å^{-1}$ by dividing by 100.

4.7.2 Preparation of compounds

[NBu$_4$][L1bCu^{II}OOCm], ([NBu$_4$][20]). To a 25 mL Schleck flask, 200 mg (0.25 mmol) of solid [NBu$_4$][**L1b**Cu(OH)] was added along with activated 3 Å molecular sieves and placed under Argon atmosphere. To this flask 10 mL of anhydrous THF was added, which resulted in dissolution of the [NBu$_4$][**L1b**Cu(OH)] to give a blue solution. After stirring the solution for 30 min, it was cooled to -20 °C using a salt/ice bath and 0.1 mL of an 80% solution (5 equiv.) of cumene hydroperoxide was added dropwise resulting in a color change from blue to a dark crimson. After stirring for 15 min., the reaction mixture was syringe-filtered using a 25 mM diameter, 0.2 µm hydrophobic polytetrafluoroethylene (PTFE) syringe filter, into a separate dry, flask to remove all molecular sieve particulate. The solvent was removed from the reaction solution in vacuo while at -20 °C and the resulting crimson oil was subsequently dissolved in minimal anhydrous diethyl ether (Et_2O, ~ 5.0 mL) and triturated with pentane 3x until a more powdery product was obtained. The product was then stirred over 10 mL of anhydrous pentane for 12 hours and filtered using a frit funnel to give a crimson colored solid that was washed with pentane 3x and dried on a vacuum line (160 mg, 68% yield). UV-vis (THF, -80 °C) λ_{max}, nm (ε, M^{-1} cm^{-1}): 552 (380), 698 (130). HR-MS (ESI, MeCN) *m/z*:

20 Calcd. for $[C_{40}H_{48}CuN_3O_4]^-$ 697.294; found 697.208. Repeated attempts to obtain correct CHN analysis were unsuccessful with consistently low carbon composition in the analyses, which we attribute to incomplete combustion. The compound [NEt_4][**20**] was prepared specifically for crystallization purposes using the analogous synthetic procedure for compound [NBu_4][**20**] but using [NEt_4][**L1b**Cu(OH)] as a precursor in lieu of [NBu_4][**L1b**Cu(OH)] X-ray quality crystals were formed from the crude reaction mixture after being subjected to vacuum over a 12 hour period.

[NBu_4][L1bCu(OO*t*Bu)], ([NBu_4][21]). The analogous synthetic method for [NBu_4][**20**] was used except *tert*-butyl-hydroperoxide in nonane was used to give [NBu_4][**21**] (190 mg, 81% yield). UV-vis (THF, -80 °C) λ_{max}, nm (ε, M^{-1} cm^{-1}): 551 (450), 694 (135). HR-MS (ESI, MeCN) *m/z*: **2b** Calcd. for $[C_{35}H_{46}CuN_3O_4]^-$ 635.278; found 635.270. Repeated attempts to obtain correct CHN analysis were unsuccessful, which we attribute to incomplete combustion. Compound [NEt_4][**2b**] was prepared specifically for crystallization purposes using the analogous synthetic procedure for compound [NBu_4][**21**] but using [NEt_4][**L1b**Cu(OH)] as a precursor in lieu of [NBu_4][**L1b**Cu(OH)] X-ray quality crystals were formed by the slow evaporation of pentane solvent into a concentrated THF solution of [NEt_4][**21**] in a -20 °C freezer.

[NBu_4][L1bCu(OPh^{NMe2})], ([NBu_4][22]). Solid [NBu_4][**L1b**Cu(OH)] (150 mg, 0.186 mmol) and 38 mg (0.279 mmol) of 4-dimethylamino-phenol was mixed along with activated 3 Å molecular sieves in a 20 ml vial inside a N_2 filled dry box. To this mixture 10 mL of anhydrous THF was added, which resulted in the immediate formation of a deep purple solution. After stirring for 30 min. the reaction mixture was syringe-filtered using a 25 mM diameter, 0.2 µm hydrophobic polytetrafluoroethylene (PTFE) syringe filter, into a separate vial to remove all the molecular sieve particulate. The residual pulverized sieves were rinsed with anhydrous THF (3 x 2 mL) to extract all adhered

compound and the resulting solution was syringe-filtered analogously and combined with the original filtrate. The combined solution was then concentrated *in vacuo* to ~ 2 mL and to the resulting solution excess diethyl ether (Et_2O, ~ 15 mL) was added and the mixture was stirred vigorously. The fine solid that precipitated out was isolated by filtration on a fine-pore size frit and washed with copious amounts of Et_2O and dried thoroughly to yield a deep purple colored solid (155 mg, 90 %). UV-vis (THF, -80 °C) λ_{max}, nm (ε, M^{-1} cm^{-1}): 462 (1,000), 533 (1,100), 726 (570). HR-MS (ESI, MeCN) *m/z*: **22** Calcd. for $[C_{39}H_{47}CuN_4O_3]^-$ 682.294; found 682.187.

Oxidation Reactions. A necked 1 cm UV-vis cuvette in the Unisoku low-temp UV-vis cell holder containing 1.8 mL of THF and a stir bar was cooled to -80 °C. To this cell, 0.1 mL of a 2 mM THF solution of [NBu_4][**20**], [NBu_4][**21**], or [NBu_4][**22**] was added. After mixing and allowing for temperature stabilization (5 min), a UV-vis spectrum was recorded. To the stirring mixture, 0.1 mL of a 2 mM solution of [Fc][$B(Ar^F)_4$] was injected and stirred. The spectrum was immediately recorded upon addition of oxidant. EPR samples were prepared by injecting a 0.15 mL aliquot of a 2 mM THF solution of [NBu_4][**20**] or [NBu_4][**21**] to a quartz EPR sample tube and cooling to ~-80 °C using a liquid N_2/acetone bath. To this cooled tube a 0.15 mL aliquot of a 2 mM THF solution of [Fc][$B(Ar^F)_4$] was added, mixed using the tip of the syringe needle, and then immediately frozen in liquid nitrogen for storage and analysis.

Preparation of resonance Raman samples of [NBu_4][20]. To a dry schlenk flask with 3 Å molecular sieves, 40.3 mg of [NBu_4][**L1b**Cu(OH)] was added and dissolved in 4.9 mL of anhydrous THF. The blue reaction solution was cooled to -20 °C using a salt/ice bath and 0.1 mL of cumene hydroperoxide in cumene or ^{18}O-enriched cumene hydroperoxide in cumene was added, producing a color change from blue to light crimson. This mixture was allowed to stir for 20 min. and then a 0.15 mL aliquot was

injected into a septa covered quartz EPR sample tube under dry N_2 atmosphere and cooled to ~-80 °C using a liquid N_2/acetone bath. To this cooled tube a 0.15 mL aliquot of a 10 mM THF solution of [Fc][B(Ar^F)$_4$], was added, mixed using the tip of the syringe needle and then immediately frozen in liquid nitrogen for storage and analysis.

Oxidation titration of [NBu$_4$][20]. To a cuvette with 1.8 mL of THF and a stir bar in the Unisoku low temperature cell holder at -80 °C was added 0.1 mL of a stock solution of [NBu$_4$][**20**] (2 mM). After temperature equilibration (10 min), 0.1 mL of THF solutions [Fc][B(Ar^F)$_4$] of varying concentration (corresponding to 0.0–2.0 equivalents) were added and the UV-vis spectra were recorded. This was repeated 11 times, where one titration data point corresponds to a single reaction with specific equivalent amount of [Fc][B(Ar^F)$_4$] (Figure 4.12).

Reversible oxidation/reduction of [NBu$_4$][20]. To a cuvette with 1.8 mL of THF and a stir bar in the Unisoku low temperature cell holder at -80 °C was added 0.1 mL of a stock solution of [NBu$_4$][**20**] (2 mM). After temperature equilibration (10 min), 0.1 mL of a 2 mM solution of [Fc][B(Ar^F)$_4$] was injected and stirred and the spectrum immediately recorded. To this oxidized solution, 0.1 mL of a 2 mM solution of Fc* was added and the resulting spectrum recorded. The addition of 0.1 mL of [Fc][B(Ar^F)$_4$] (oxidant) and Fc* (reductant) was repeated with spectra taken after each addition. The UV-vis spectra shown in Figure S11 were corrected for concentration as a function of volume change due to addition of reagents.

Kinetics analysis of the reactions of 20$^+$. A necked 1 cm UV-vis cuvette in the Unisoku low-temp UV-vis cell holder, containing 1.7 mL of THF was cooled to -80 °C or -25 °C respectively. To this cell 0.1 mL of a 2 mM THF solution of [NBu$_4$][**20**] was added. Continuous collection of the UV-vis absorption spectrum was initiated as soon as 0.1 mL of a 2 mM solution of [Fc][B(Ar^F)$_4$] was injected to the mixture. Upon

observation of the full growth of the oxidized feature of **20**$^{+}$**.** 0.1 mL of a solution of the desired substrate was added to the cell. The decay of **20**$^{+}$ was monitored until no changes to the UV-vis spectrum could be detected. The single wavelength kinetic trace was determined by the disappearance of the UV-vis feature due to **20**$^{+}$ at 504 nm. The pseudo first order rate constants, k_{obs}, were determined from the decay of **20**$^{+}$ as a function of time. Second order rate constants for TEMPO-H reactions were approximated by producing a linear fit using the plot of k_{obs} vs. [TEMPO-H] and obtaining the second order rate constant from the slope of the linear fit of this data (Figure 4.22).

4.7.3 Theoretical methods.

Density Functional Theory (DFT) calculations were performed using the *ORCA* (v.3.0.2) program.[173] Starting geometries for copper-alkylperoxo complexes were based on the respective X-ray crystal structures. Complexes were optimized spin-unrestricted (UKS) using the *m*PWPW functional with a Def2-QZVP basis set on Cu and other atoms set to a Def2-TZVP basis set, the Resolution of Identity (RI) approximation, Def2-TZV/J auxiliary basis set, tight SCF convergence (VeryTightSCF), and a large integration grid (Grid6).[174-176] The *m*PWPW functional was previously shown to give acceptable geometries for copper-oxygen complexes.[177] Numerical frequency calculations on all complexes confirmed stable structures with no imaginary frequencies observed. A comparison of the bond metrics for the DFT optimized structures with the crystal structures is shown in Table 4.2. To determine the O-O vibration, the generated Hessian file was rerun through the '*orca_vib*' program where the mass of oxygen was changed to 18 amu, as documented in the *ORCA* manual. Large shifts in energy were used to assign the stretching vibration, which was confirmed upon visualization of the highly-coupled vibration.

Spin density plots for **20** and **21** were generated from single point calculations using the BP86 functional[178,179] with the 'Partridge-3' basis set,[180,181] the RI approximation, and a TZV/J auxiliary basis set, as used previously.[35] Broken-symmetry calculations were computed using the 'Flipspin' command on the Cu atom starting from the singlet or triplet state geometries with the same basis set mentioned above using a range of functionals: *m*PWPW,[182] BP86,[14] OLYP,[183] TPSS,[184] M06-L,[185,186] B3LYP,[187,188] PBE0,[187] TPSSh,[189] M06,[190] PW6B95,[182] and M06-2X. Hybrid- and meta-hybrid-GGA functionals additionally used the Resolution of Identity – Chain of Spheres (RIJCOSX) approximation with an elevated COSX integration grid (GridX4).[191] The 'double-hybrid' functional PWPB95[192] was utilized (including the RIJK approximation with Def2-TZVP/JK and Def2-TZVP/C auxiliary basis sets using a frozen core) by running single-point energy calculations on the triplet state optimized geometry and the broken-symmetry solution from the PBE0 calculation. The singlet-triplet energy gaps were 'spin purified' by the following, equation 4.4,[161,193]

$$E_S = E_T - 2\left[\frac{E_T - E_{BS}}{2 - \langle S^2_{BS}\rangle}\right] \quad (4.4)$$

where E_T, E_S, and E_{BS} are the electronic energies of the triplet, singlet, and broken-symmetry singlet states, respectively, and $\langle S^2_{BS}\rangle$ is the expectation value of the spin operator from the broken-symmetry singlet state. Time-dependent DFT (TD-DFT) calculations were performed with the PBE0 functional, Def2-TZVP basis set, Def2-SVP/J auxiliary basis set, the Zero-Order Regular Approximation (ZORA)[194] for Cu, RIJCOSX, Grid4, TightSCF, and the Tamm-Dancoff approximation for 40 excited states. Surface contour plots were generated using the *Molekel* (v.5.4.0.8) program with isodensity values set to ±0.003 for spin density plots, ±0.002 for TD-DFT difference plots

and ±0.02 for Kohn-Sham molecular orbitals.[195] The programs *Avogadro* (v.1.2.0) and *Gabedit* (v.2.4.8) were also utilized.[196,197]

Chapter 5
Research Perspectives and Future Directions

Through generations of evolutionary refinement, monooxygenases have become capable of catalyzing thermodynamically difficult and industrially desirable chemical processes such as the selective conversion of methane to methanol and the degradation of cellulose to its base glucose monomers. Attempts to replicate these natural processes in artificial settings requires the fundamental physical and chemical understanding of these enzymes. Investigation of the chemistry surrounding copper monooxygenases, has incited the chemical studies reported within this dissertation. The utilization of biomimetic synthetic models have been described in an effort to glean mechanistically relevant information. This work has served to progress these fields of research with both biological and inorganic insights into enzymatic modeling.

5.1 Advances and future directions in modeling secondary sphere interactions

Small molecule modeling of enzymatic active sites often requires development of specialized ligand frameworks to better mimic the complexity of a protein environment. Chapter 2 of this dissertation describes the utilization of pyridine dicarboxamido macrocycles **H_2L3^{2-}**, **H_2L4a^{2-}**, and **H_2L4b^{2-}**as supporting frameworks to better model secondary sphere interactions on copper metal sites. The nuances of non-covalent interactions on the behavior of metal ions are difficult to ascertain via small molecule analogs, with only a small subset of known ligand frameworks capable of enforcing these interactions.[198,199] Select examples of previously reported ligands utilized for the study of secondary sphere effects are shown in Figure 5.1.

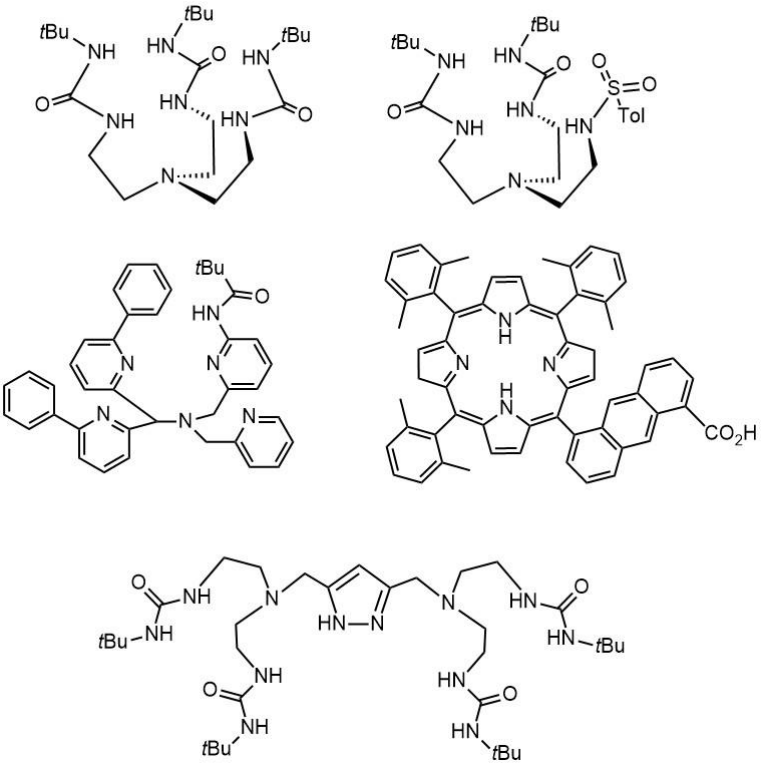

Figure 5.1. Selected examples of proligands utilized in the generation of metal complexes with intramolecular non-covalent interactions.

The work reported in Chapter 2 has contributed to the collective understanding of ligand design concepts for the study of secondary sphere interactions by establishing pyridine dicarboxamide macrocycles as supporting ligands for metalloenzyme model compounds. Previously such compounds were primarily used as anion receptors (as shown in Figure 5.2) with no mention of their ability support transition metals in the coordination environments we describe in Chapter 2.[95,126,200,201]

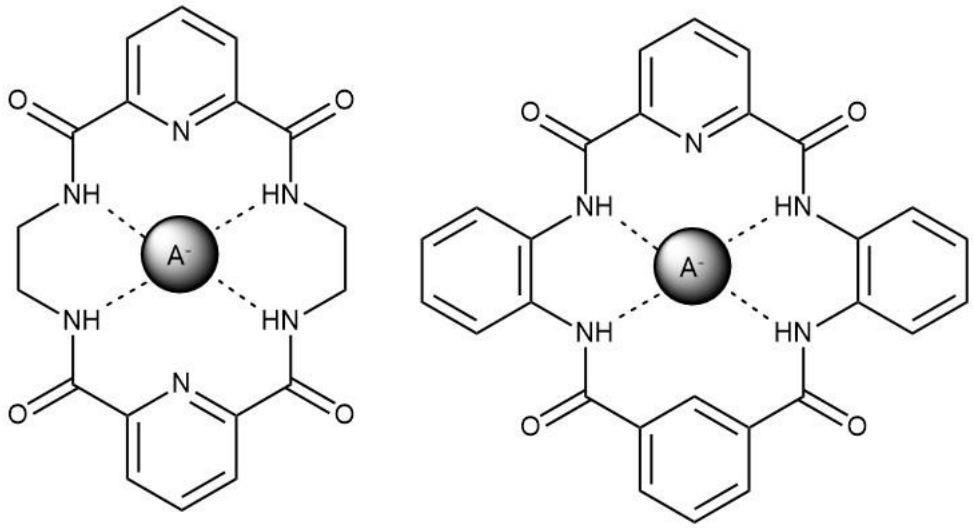

Figure 5.2. Generic depiction of pyridine dicarboxamide macrocycles as anion receptors through carboxamide proton interactions.

The electrochemical relationship that was established in Chapter 2 between hydrogen bonding interactions and the copper complexes' redox behavior is an important relationship to understand in the context of enzymatic chemistry. The knowledge of the direction and magnitude of the shifts in reduction potential as a function of secondary coordination sphere interactions aids researchers in their understanding of the structure-function relationship in enzyme active sites. Biological systems have been shown to utilize these interactions to discretely modulate the characteristics of their metal sites.[202] Model systems, such as the ones reported in Chapter 2, offer direct experimental evidence to which to refer when proposing the role of biological residues in enzymatic reaction mechanisms.

Possible future directions include modeling other copper-oxygen cores utilizing our described ligand systems and studying the effects of hydrogen bonding with respect to non-hydrogen bound analogs. For example, Cu^{II}-superoxo ([**L1b**Cu(OO)]$^-$), Cu^{II}-alkylperoxo ([**L1b**Cu(OOR)]$^-$), and formally Cu^{III}-alkylperoxo (**L1b**Cu(OOR))

complexes have all been described in literature as enzymatic model complexes in the **L1b**$^{2-}$ ligand framework.[34,203,204] The coordination modes observed in **H$_2$L3**$^{2-}$ monocopper complexes in Chapter 2 provide a possible extension of this research whereby generation of a series of copper-oxygen complexes with intramolecular hydrogen-bonding interactions may be obtained (Figure 5.3). The possibility for the generation of a series of cores across the **L1b**$^{2-}$ and **H$_2$L3**$^{2-}$ ligand scaffolds may produce important insights into to the effects of hydrogen bonding for particular copper-oxygen cores currently proposed to be relevant to monooxygenase mechanisms.

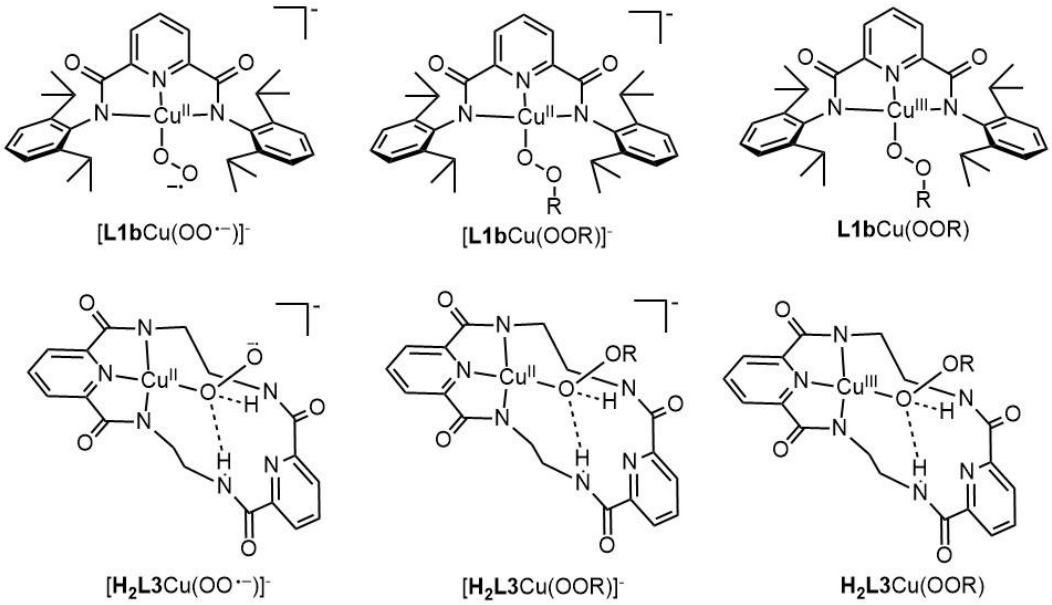

Figure 5.3. Known copper complexes of **L1b**$^{2-}$ and possible analogs supported by **H$_2$L3**$^{2-}$ containing biorelevant cores (Cu^{II}-superoxo, Cu^{II}-alkylperoxo, Cu^{III}-alkylperoxo).

5.2 Advances and future directions for bimetallic chemistry

Chapter 3 discusses the development of a macrocyclic ligand capable of accommodating bimetallic cores and the characterization of a series of dicopper complexes by X-ray crystallography. Although the initial goals of the project to model the proposed dicopper active site of pMMO have not yet been met (i.e. generation of

target compound **16**), the larger contributions of this work should be discussed in regards to bioinorganic modeling chemistry as a whole. This is to say that the ligand $\mathbf{L5^{4-}}$ may prove useful in the modeling of dinuclear active sites beyond pMMO can be extended to the modeling of other bimetallic systems.

One extension of the modeling work with the $\mathbf{L5^{4-}}$ framework, is its utilization as a supporting ligand for model systems of the diiron enzyme, soluble methane monooxygenase (sMMO). The enzyme sMMO, like pMMO, is responsible for the selective conversion of methane to methanol selectively and as such is an equally attractive target in modeling studies.[43,205] The diiron active site of sMMO contains two neutral histidine residues and four deprotonated glutamate residues providing a tetraanionic ligand environment with an Fe-Fe distance of ~3.04 Å (Figure 5.4).[206] The overall charge and metal-metal distances are consistent with those observed in the reported dicopper complexes of $\mathbf{L5^{4-}}$ (~2.8 Å).

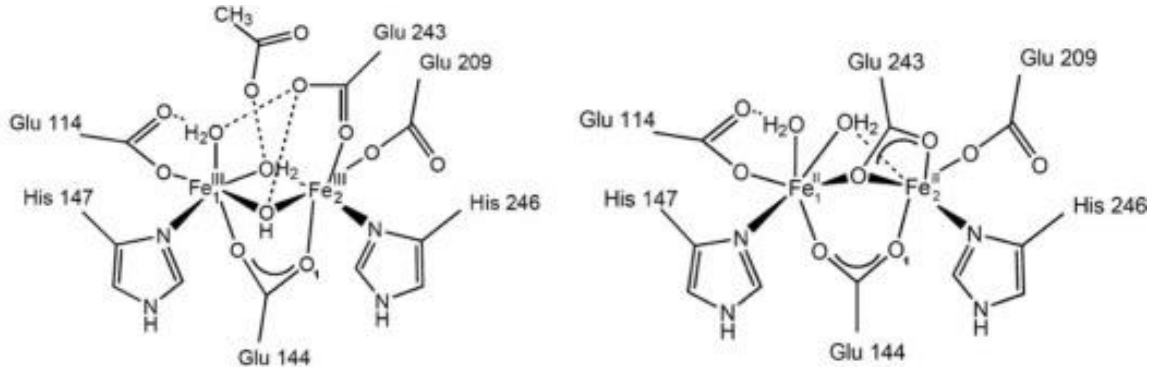

Figure 5.4. Oxy-form (left) and reduced form (right) of the diiron active site of sMMO. Reprinted with permission from reference 13.

Beyond bioinorganic modeling studies, the development of ligand $\mathbf{L5^{4-}}$ and its specific coordination chemistry may prove to be useful in other fields. Bimetallic catalysis has been shown to be particularly proficient in a number of chemical processes including polymerization, depolymerization, hydrolysis, and hydrogenation

reactions.[137,140,207,208] Precedence for the ability of bimetallic catalysts to outperform monometallic analogs has been established in many catalytic systems. This enhanced proficiency is largely attributed to observed cooperativity of binding and activation between two metal ions in close proximity.[207,209] The **L5^{4-}** framework may provide a suitable ligand environment for the development of new bimetallic catalysts suitable to the aforementioned reactions resulting from its ability to support bimetallic cores in multiple coordination modes (Figure 5.5).

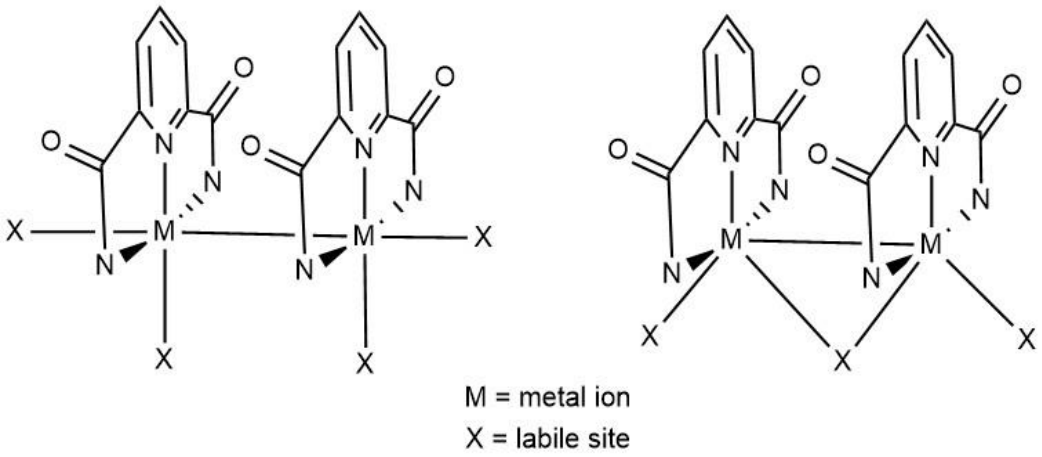

Figure 5.5. Generic coordination modes for bimetallic systems utilizing **L5^{4-}** (naphthyl bridge omitted for clarity).

5.3 Advances and future directions in modeling the Cu^{III}-OOR core

As described in Chapter 1, modeling biorelevant copper-oxygen cores using small molecule systems has been utilized in the study of potential intermediates in enzymatic pathways. Proposal concerning the role of copper-oxygen intermediates in monooxygenases often refers to experimental precedence of modeling work in order to better refine existing mechanistic theories. The evidence provided in these modeling studies can then be used to generate new mechanistic proposals based on experimental precedent. The work reported in Chapter 4 encompasses the first experimental report of a

formal Cu^{III}-alkylperoxo core which can be viewed as a model for a Cu^{III}-hydroperoxo core. The Cu^{III}-hydroperoxo core has been suggested as an alternative reactive intermediate to those currently found in existing mechanistic proposals (Figure 5.6). The existence of a discrete $[Cu(OOR)]^{2+}$ (R = alkyl) core provides the necessary experimental precedent for a Cu^{III}-hydroperoxo species to be invoked in new theories involving C-H bond activation pathways in monooxygenase enzymes.

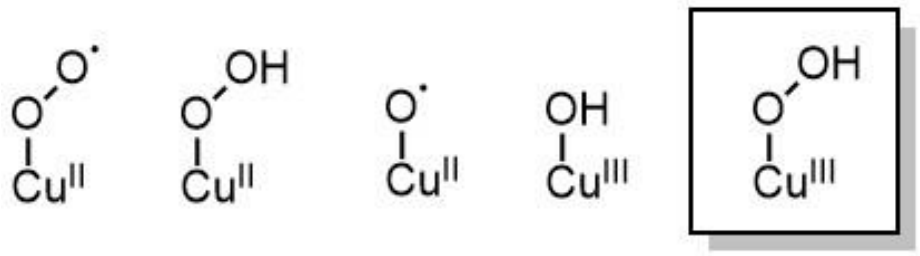

Figure 5.6. Proposed reactive cores of LPMO.

Additionally, the investigation of the proton-coupled electron-transfer (PCET) capabilities of compound $\mathbf{20}^{+}$ have further provided evidence for the possibility of related species as H-atom abstraction reagents in the presence of substrates. As such, this work has added an additional point of comparison for discussing other copper-oxygen cores and their respective oxidative capabilities. In addition to the reports of **20**, **21**, $\mathbf{21}^{+}$and $\mathbf{20}^{+}$, the $\mathbf{L1b}^{2-}$ framework has also been shown to support Cu^{II}-superoxo[8] and Cu^{III}-hydroxo[34,35] cores (Figure 5.7). Both Cu^{II}-superoxo and Cu^{III}-hydroxo complexes have shown varying degrees of reactivity towards substrates. Direct comparison of this series of copper-oxygen complexes has generated a spectrum of reactivity for which the likelihood of individual cores as reactive intermediates in monooxygenase enzymes can be assessed.

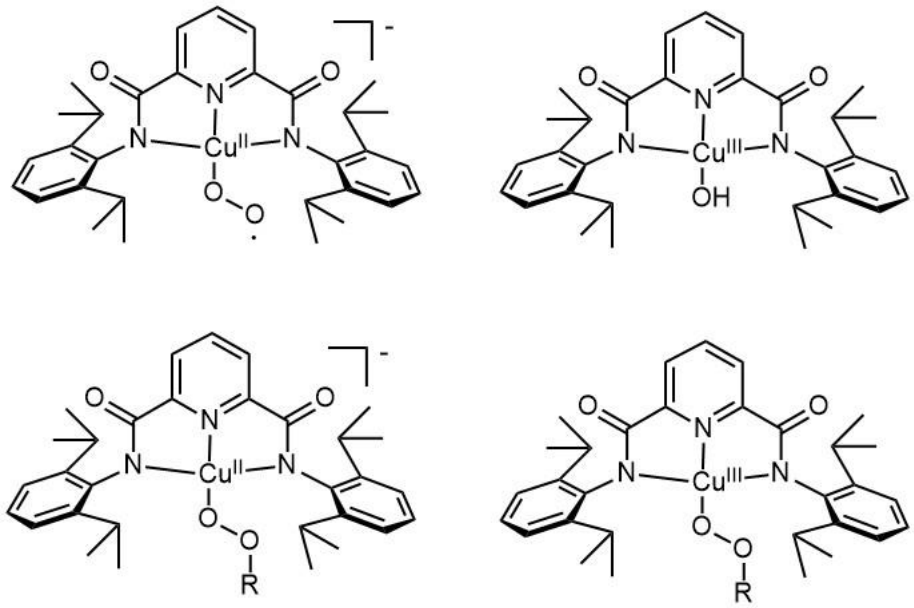

Figure 5.7. Several reported complexes containing copper-oxygen cores relevant to biological monocopper enzyme intermediates with **L1b**$^{2-}$ ligand scaffolds.

Extensions of this work include the investigation of ligand perturbations on the $[Cu(OOR)]^{2+}$ core, such that electronic and steric effects can be determined based on the relative stability/reactivity of variant complexes. Previous work in the Tolman lab has already produced several dicarboxamido frameworks designed to perturb the electronic and steric effects of **L1b**$^{2-}$. These ligand variants of **L1b**$^{2-}$ can be employed in the study of discrete perturbations to the $[Cu(OOR)]^{2+}$ core. In addition to the comparisons that can be made across a series $[Cu(OOR)]^{2+}$ cores generated in each framework, the Cu^{III}-hydroxo systems previously described in each of the ligand variants shown in Figure 5.8, may lend insight into understanding how ligand variations affect the $[Cu(OOR)]^{2+}$ differently. Understanding the structure-function relationship of the ligand environment on proposed copper-oxygen intermediates will help to develop arguments for the presence a particular core based on enzymatic residues present in individual active sites.

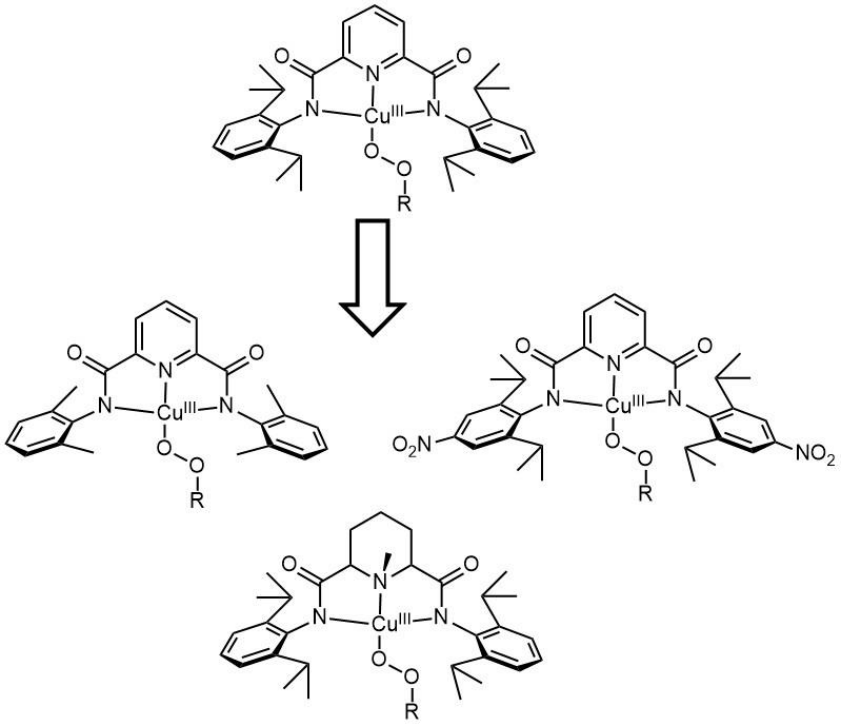

Figure 5.8. Steric and electronic variants of formal Cu^{III}-alkylperoxo complexes utilizing previously reported ligands for further study of electronic and steric perturbations on chemical and physical properties.

With respect to the investigation of a Cu^{II}-superoxo intermediate undergoing protonation to produce a formal Cu^{III}-hydroperoxo intermediate, there is still more experimental work to be done. The work reported in Chapter 4 provides a useful spectroscopic handle for which protonation mechanisms may be investigated in future work. Studies directed at the protonation of the previously reported [**L1b**Cu(OO)]$^-$ complex by proton donors can now be performed using the spectroscopic features of **20**$^+$ as a point of comparison in determining whether discrete Cu^{III}-hydroperoxo species are generated (Figure 5.9). If a Cu^{III}-hydroperoxo species can be produced from the protonation of a Cu^{II}-superoxo complex, then the mechanistic proposal for the formation of the Cu^{III}-hydroperoxo intermediate in LPMO will be further substantiated.

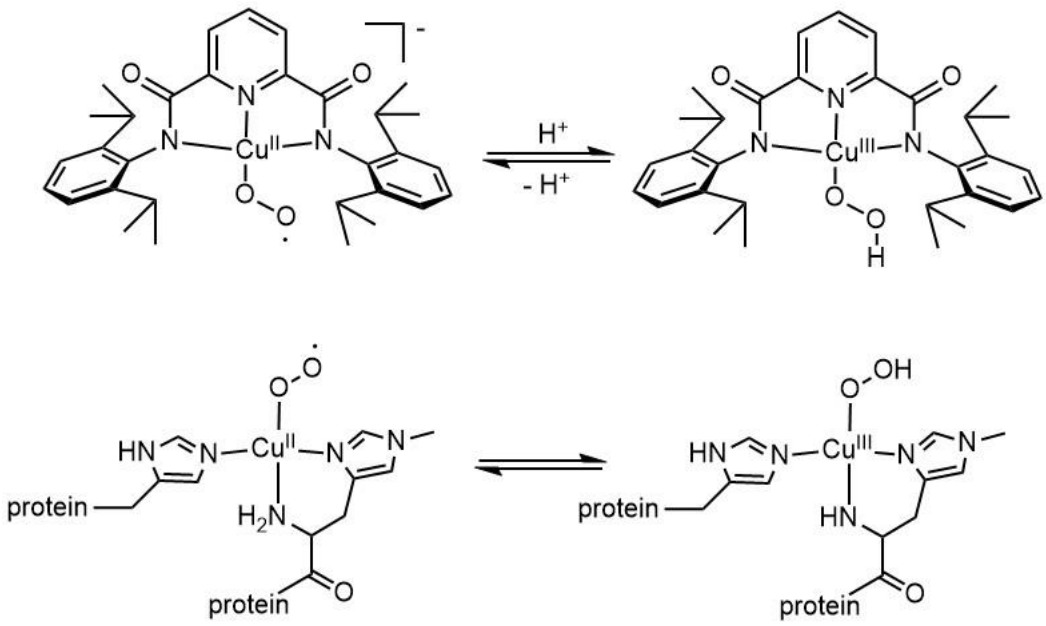

Figure 5.9. Proposed protonation of [**L1b**Cu(OO)]$^{-}$ to give the proposed **L1b**Cu(OOH) complex (top) in relation to the proposed tautomeric relationship of a Cu^{II}-superoxo core with a Cu^{III}-hydroperoxo core with a singly deprotonated amino terminus.

Establishing the relevance of the $[Cu(OOR)]^{2+}$ core and its properties relative to other better described copper-oxygen species has allowed this research to enrich the existing literature surrounding LPMO and its chemistry. Whether the $[Cu(OOR)]^{2+}$ core is an appropriate model for the proposed biologically relevant Cu^{III}-hydroperoxo core remains to be fully established, but it has provided the first experimental insight into its structural, spectroscopic, and reactivity characteristics. The continuation of this work will hopefully elucidate its relevance as a legitimate biological intermediate.

Bibliography

(1) Waldron, K. J.; Rutherford, J. C.; Ford, D.; Robinson, N. J. *Nature* **2009**, *460*, 823.

(2) Carter, E. L.; Flugga, N.; Boer, J. L.; Mulrooney, S. B.; Hausinger, R. P. *Metallomics* **2009**, *1*, 207.

(3) Que, L., Jr.; Tolman, W. B. *Nature* **2008**, *455*, 333.

(4) Rosenzweig, A. C. *Nat. Chem. Biol.* **2013**, *9*, 220.

(5) Wilcox, D. E. *Chem. Rev.* **1996**, *96*, 2435.

(6) Zhao, M.; Wang, H.-B.; Ji, L.-N.; Mao, Z.-W. *Chem.Soc. Rev.* **2013**, *42*, 8360.

(7) Elwell, C. E.; Gagnon, N. L.; Neisen, B. D.; Dhar, D.; Spaeth, A. D.; Yee, G. M.; Tolman, W. B. *Chem. Rev.* **2017**, *117*, 2059.

(8) Fukuzumi, S.; Kotani, H. *Rsc Catal Ser* **2012**, *9*, 89.

(9) Solomon, E. I.; Ginsbach, J. W.; Heppner, D. E.; Kieber-Emmons, M. T.; Kjaergaard, C. H.; Smeets, P. J.; Tian, L.; Woertink, J. S. *Faraday Discuss.* **2011**, *148*, 11.

(10) In *Encyclopedic Reference of Genomics and Proteomics in Molecular Medicine*; Springer Berlin Heidelberg: Berlin, Heidelberg, 2006, p 408.

(11) Klinman, J. P. *J. Biol. Chem.* **2006**, *281*, 3013.

(12) Vendelboe, T. V.; Harris, P.; Zhao, Y.; Walter, T. S.; Harlos, K.; El Omari, K.; Christensen, H. E. M. *Sci. Adv.* **2016**, *2*.

(13) Chufán, E. E.; Prigge, S. T.; Siebert, X.; Eipper, B. A.; Mains, R. E.; Amzel, L. M. *J. Am. Chem. Soc.* **2010**, *132*, 15565.

(14) Rudzka, K.; Moreno, D. M.; Eipper, B.; Mains, R.; Estrin, D. A.; Amzel, L. M. *J. Biol. Inorg. Chem.* **2013**, *18*, 223.

(15) Hemsworth, G. R.; Davies, G. J.; Walton, P. H. *Curr. Opin. Struct. Biol.* **2013**, *23*, 660.

(16) Balasubramanian, R.; Rosenzweig, A. C. *Acc. Chem. Res.* **2007**, *40*, 573.

(17) Kamachi, T.; Kihara, N.; Shiota, Y.; Yoshizawa, K. *Inorg. Chem.* **2005**, *44*, 4226.

(18) Kunishita, A.; Ertem, M. Z.; Okubo, Y.; Tano, T.; Sugimoto, H.; Ohkubo, K.; Fujieda, N.; Fukuzumi, S.; Cramer, C. J.; Itoh, S. *Inorg. Chem.* **2012**, *51*, 9465.

(19) Chen, P.; Bell, J.; Eipper, B. A.; Solomon, E. I. *Biochemistry* **2004**, *43*, 5735.

(20) Frandsen, K. E. H.; Simmons, T. J.; Dupree, P.; Poulsen, J.-C. N.; Hemsworth, G. R.; Ciano, L.; Johnston, E. M.; Tovborg, M.; Johansen, K. S.; von Freiesleben, P.; Marmuse, L.; Fort, S.; Cottaz, S.; Driguez, H.; Henrissat, B.; Lenfant, N.; Tuna, F.; Baldansuren, A.; Davies, G. J.; Lo Leggio, L.; Walton, P. H. *Nat. Chem. Biol.* **2016**, *12*, 298.

(21) Quinlan, R. J.; Sweeney, M. D.; Lo Leggio, L.; Otten, H.; Poulsen, J.-C. N.; Johansen, K. S.; Krogh, K. B. R. M.; Joergensen, C. I.; Tovborg, M.; Anthonsen, A.; Tryfona, T.; Walter, C. P.; Dupree, P.; Xu, F.; Davies, G. J.; Walton, P. H. *Proc. Natl. Acad. Sci.* **2011**, 1.

(22) Chaplin, A. K.; Wilson, M. T.; Hough, M. A.; Svistunenko, D. A.; Hemsworth, G. R.; Walton, P. H.; Vijgenboom, E.; Worrall, J. A. R. *J. Biol. Chem.***2016**.

(23) Dhar, D.; Tolman, W. B. *J. Am. Chem. Soc.* **2015**, *137*, 1322.

(24) Hemsworth, G. R.; Henrissat, B.; Davies, G. J.; Walton, P. H. *Nat. Chem. Biol.* **2014**, *10*, 122.

(25) Bacik, J.-P.; Mekasha, S.; Forsberg, Z.; Kovalevsky, A. Y.; Vaaje-Kolstad, G.; Eijsink, V. G. H.; Nix, J. C.; Coates, L.; Cuneo, M. J.; Unkefer, C. J.; Chen, J. C. H. *Biochemistry* **2017**, *56*, 2529.

(26) Reynolds, A. M.; Gherman, B. F.; Cramer, C. J.; Tolman, W. B. *Inorg. Chem.* **2005**, *44*, 6989.

(27) Gherman, B. F.; Heppner, D. E.; Tolman, W. B.; Cramer, C. J. *J. Biol. Inorg. Chem* **2006**, *11*, 197.

(28) Kim, S.; Stahlberg, J.; Sandgren, M.; Paton, R. S.; Beckham, G. T. *Proc. Natl. Acad. Sci. USA* **2014**, *111*, 149.

(29) Hedegård, E. D.; Ryde, U. *J. Biol. Inorg. Chem.* **2017**.

(30) Klinman, J. P. *Chem. Rev.* **1996**, *96*, 2541.

(31) Kunishita, A.; Ishimaru, H.; Nakashima, S.; Ogura, T.; Itoh, S. *J. Am. Chem. Soc.* **2008**, *130*, 4244.

(32) Tano, T.; Ertem, M. Z.; Yamaguchi, S.; Kunishita, A.; Sugimoto, H.; Fujieda, N.; Ogura, T.; Cramer, C. J.; Itoh, S. *Dalton Trans.* **2011**, *40*, 10326.

(33) Tian, G.; Berry, J. A.; Klinman, J. P. *Biochemistry* **1994**, *33*, 226.

(34) Donoghue, P. J.; Tehranchi, J.; Cramer, C. J.; Sarangi, R.; Solomon, E. I.; Tolman, W. B. *J. Am. Chem. Soc.* **2011**, *133*, 17602.

(35) Dhar, D.; Yee, G. M.; Spaeth, A. D.; Boyce, D. W.; Zhang, H.; Dereli, B.; Cramer, C. J.; Tolman, W. B. *J. Am. Chem. Soc.* **2016**, *138*, 356.

(36) Gagnon, N.; Tolman, W. B. *Acc. Chem. Res.* **2015**, *48*, 2126.

(37) Ismaya, W. T.; Rozeboom, H. J.; Weijn, A.; Mes, J. J.; Fusetti, F.; Wichers, H. J.; Dijkstra, B. W. *Biochemistry* **2011**, *50*, 5477.

(38) Lieberman, R. L.; Rosenzweig, A. C. *Dalton Trans.* **2005**, 3390.

(39) Lieberman, R. L.; Rosenzweig, A. C. *Crit. Rev. Biochem. Mol. Biol.* **2004**, *39*, 147.

(40) Culpepper, M. A.; Rosenzweig, A. C. *Crit. Rev. Biochem. Mol. Biol.* **2012**, *47*, 483.

(41) Wang, V. C. C.; Maji, S.; Chen, P. P. Y.; Lee, H. K.; Yu, S. S. F.; Chan, S. I. *Chem. Rev.* **2017**, *117*, 8574.

(42) Balasubramanian, R.; Smith, S. M.; Rawat, S.; Yatsunyk, L. A.; Stemmler, T. L.; Rosenzweig, A. C. *Nature* **2010**, *465*, 115.

(43) Ross, M. O.; Rosenzweig, A. C. *J. Biol. Inorg. Chem.* **2017**, *22*, 307.

(44) Kjaergaard, C. H.; Qayyum, M. F.; Wong, S. D.; Xu, F.; Hemsworth, G. R.; Walton, D. J.; Young, N. A.; Davies, G. J.; Walton, P. H.; Johansen, K. S.; Hodgson, K. O.; Hedman, B.; Solomon, E. I. *Proc. Natl. Acad. Sci. USA* **2014**, *111*, 8797.

(45) Matoba, Y.; Kumagai, T.; Yamamoto, A.; Yoshitsu, H.; Sugiyama, M. *J. Biol. Chem.* **2006**, *281*, 8981.

(46) Yoon, J.; Fujii, S.; Solomon, E. I. *Proc. Natl. Acad. Sci.* **2009**, *106*, 6585.

(47) Mirica, L. M.; Vance, M.; Rudd, D. J.; Hedman, B.; Hodgson, K. O.; Solomon, E. I.; Stack, T. D. P. *Science* **2005**, *308*, 1890.

(48) Hatcher, L. Q.; Vance, M. A.; Narducci Sarjeant, A. A.; Solomon, E. I.; Karlin, K. D. *Inorg. Chem.* **2006**, *45*, 3004.

(49) Liang, H.-C.; Henson, M. J.; Hatcher, L. Q.; Vance, M. A.; Zhang, C. X.; Lahti, D.; Kaderli, S.; Sommer, R. D.; Rheingold, A. L.; Zuberbühler, A. D.; Solomon, E. I.; Karlin, K. D. *Inorg. Chem.* **2004**, *43*, 4115.

(50) Cahoy, J.; Holland, P. L.; Tolman, W. B. *Inorg.Chem.* **1999**, *38*, 2161.

(51) Itoyama, S.; Doitomi, K.; Kamachi, T.; Shiota, Y.; Yoshizawa, K. *Inorg. Chem.* **2016**, *55*, 2771.

(52) Shiota, Y.; Yoshizawa, K. *Inorg. Chem.* **2009**, *48*, 838.

(53) Himes, R. A.; Karlin, K. D. *Proc. Natl. Acad. Sci.* **2009**, *106*, 18877.

(54) Aboelella, N. W.; Lewis, E. A.; Reynolds, A. M.; Brennessel, W. W.; Cramer, C. J.; Tolman, W. B. *J. Am. Chem. Soc.* **2002**, *124*, 10660.

(55) Aboelella, N. W.; Kryatov, S. V.; Gherman, B. F.; Brennessel, W. W.; Young, V. G.; Sarangi, R.; Rybak-Akimova, E. V.; Hodgson, K. O.; Hedman, B.; Solomon, E. I.; Cramer, C. J.; Tolman, W. B. *J. Am. Chem. Soc.* **2004**, *126*, 16896.

(56) Würtele, C.; Gaoutchenova, E.; Harms, K.; Holthausen, M. C.; Sundermeyer, J.; Schindler, S. *Angew. Chem. Int. Ed.* **2006**, *45*, 3867.

(57) Sanchez-Eguia, B. N.; Flores-Alamo, M.; Orio, M.; Castillo, I. *Chem. Comm.* **2015**, *51*, 11134.

(58) Yoshizawa, K.; Kihara, N.; Kamachi, T.; Shiota, Y. *Inorg. Chem.* **2006**, *45*, 3034.

(59) Schröder, D.; Schwarz, H. *Angew. Chem. Int. Ed.* **1995**, *34*, 1973.

(60) Dietl, N.; van der Linde, C.; Schlangen, M.; Beyer, M. K.; Schwarz, H. *Angew. Chem. Int. Ed.* **2011**, *50*, 4966.

(61) Schröder, D.; Holthausen, M. C.; Schwarz, H. *J. Phys. Chem. B.* **2004**, *108*, 14407.

(62) Chen, P.; Fujisawa, K.; Solomon, E. I. *J. Am. Chem. Soc.* **2000**, *122*, 10177.

(63) Choi, Y. J.; Cho, K.-B.; Kubo, M.; Ogura, T.; Karlin, K. D.; Cho, J.; Nam, W. *Dalton Trans.* **2011**, *40*, 2234.

(64) Kunishita, A.; Teraoka, J.; Scanlon, J. D.; Matsumoto, T.; Suzuki, M.; Cramer, C. J.; Itoh, S. *J. Am. Chem. Soc.* **2007**, *129*, 7248.

(65) Chaloner, L.; Askari, M. S.; Kutteh, A.; Schindler, S.; Ottenwaelder, X. *Eur. J. Inorg. Chem.* **2011**, *2011*, 4204.

(66) Li, L.; Sarjeant, A. A. N.; Karlin, K. D. *Inorg. Chem.* **2006**, *45*, 7160.

(67) Maiti, D.; Narducci Sarjeant, A. A.; Karlin, K. D. *J. Am. Chem. Soc.* **2007**, *129*, 6720.

(68) Kitajima, N.; Katayama, T.; Fujisawa, K.; Iwata, Y.; Morooka, Y. *J. Am. Chem. Soc.* **1993**, *115*, 7872.

(69) Syuhei, Y.; Hideki, M. *Sci. Tech. Adv. Mater.* **2005**, *6*, 34.

(70) Donoghue, P. J.; Tehranchi, J.; Cramer, C. J.; Sarangi, R.; Solomon, E. I.; Tolman, W. B. *J. Am. Chem. Soc.* **2011**, *133*, 17602.

(71) Warren, J. J.; Tronic, T. A.; Mayer, J. M. *Chem. Rev.* **2010**, *110*, 6961.

(72) Kim, S.; Ginsbach, J. W.; Billah, A. I.; Siegler, M. A.; Moore, C. D.; Solomon, E. I.; Karlin, K. D. *J. Am. Chem. Soc.* **2014**, *136*, 8063.

(73) Maiti, D.; Woertink, J. S.; Narducci Sarjeant, A. A.; Solomon, E. I.; Karlin, K. D. *Inorg. Chem.* **2008**, *47*, 3787.

(74) Citek, C.; Lyons, C. T.; Wasinger, E. C.; Stack, T. D. P. *Nature Chem.* **2012**, *4*, 317.

(75) Citek, C.; Gary, J. B.; Wasinger, E. C.; Stack, T. D. P. *J. Am. Chem. Soc.* **2015**, *137*, 6991.

(76) Citek, C.; Lin, B.-L.; Phelps, T. E.; Wasinger, E. C.; Stack, T. D. P. *J. Am. Chem. Soc.* **2014**, *136*, 14405.

(77) Cole, A. P.; Mahadevan, V.; Mirica, L. M.; Ottenwaelder, X.; Stack, T. D. P. *Inorg. Chem.* **2005**, *44*, 7345.

(78) Herres-Pawlis, S.; Verma, P.; Haase, R.; Kang, P.; Lyons, C. T.; Wasinger, E. C.; Floerke, U.; Henkel, G.; Stack, T. D. P. *J. Am. Chem. Soc.* **2009**, *131*, 1154.

(79) Halvagar, M. R.; Solntsev, P. V.; Lim, H.; Hedman, B.; Hodgson, K. O.; Solomon, E. I.; Cramer, C. J.; Tolman, W. B. *J. Am. Chem. Soc.* **2014**, *136*, 7269.

(80) Isaac, J. A.; Gennarini, F.; López, I.; Thibon-Pourret, A.; David, R.; Gellon, G.; Gennaro, B.; Philouze, C.; Meyer, F.; Demeshko, S.; Le Mest, Y.; Réglier, M.; Jamet, H.; Le Poul, N.; Belle, C. *Inorg. Chem.* **2016**, *55*, 8263.

(81) Mirica, L. M.; Ottenwaelder, X.; Stack, T. D. P. *Chem. Rev.* **2004**, *104*, 1013.

(82) Crespo, A.; Martí, M. A.; Roitberg, A. E.; Amzel, L. M.; Estrin, D. A. *J. Am. Chem. Soc.* **2006**, *128*, 12817.

(83) Vanelderen, P.; Hadt, R. G.; Smeets, P. J.; Solomon, E. I.; Schoonheydt, R. A.; Sels, B. F. *J. Catal.* **2011**, *284*, 157.

(84) Haack, P.; Limberg, C. *Angew. Chem. Int. Ed.* **2014**, *53*, 4282.

(85) Tehranchi, J.; Donoghue, P. J.; Cramer, C. J.; Tolman, W. B. *Eur. J. Inorg. Chem.* **2013**, *2013*, 4077.

(86) E., Weber. *Chemie.* **1976**, *5*, 891.

(87) Lin, I. J.; Gebel, E. B.; Machonkin, T. E.; Westler, W. M.; Markley, J. L. *Proc. Natl. Acad. Sci. U. S.A.* **2005**, *102*, 14581.

(88) Yikilmaz, E.; Porta, J.; Grove, L. E.; Vahedi-Faridi, A.; Bronshteyn, Y.; Brunold, T. C.; Borgstahl, G. E. O.; Miller, A.-F. *J. Am. Chem. Soc.* **2007**, *129*, 9927.

(89) Borovik, A. S. *Acc. Chem. Res.* **2005**, *38*, 54.

(90) Natale, D.; Mareque-Rivas, J. C. *Chem. Comm.* **2008**, 425.

(91) Rivas, J. C. M.; Hinchley, S. L.; Metteau, L.; Parsons, S. *Dalton Trans.* **2006**, 2316.

(92) Wada, A.; Honda, Y.; Yamaguchi, S.; Nagatomo, S.; Kitagawa, T.; Jitsukawa, K.; Masuda, H. *Inorg. Chem.* **2004**, *43*, 5725.

(93) Wang, D.; Lindeman, S. V.; Fiedler, A. T. *Eur. J. Inorg. Chem.* **2013**, *2013*, 4473.

(94) Higashi, F.; Mochizuki, A. *J. Polym. Sci. A Polym. Chem.* **1983**, *21*, 3337.

(95) Sessler, J. L.; Katayev, E.; Pantos, G. D.; Scherbakov, P.; Reshetova, M. D.; Khrustalev, V. N.; Lynch, V. M.; Ustynyuk, Y. A. *J. Am. Chem. Soc.* **2005**, *127*, 11442.

(96) Dannenberg, J. J. *J. Am. Chem. Soc.* **1998**, *120*, 5604.

(97) Neisen, B. D.; Solntsev, P.; Halvagar, M. R.; Tolman, W. B. *Eur. J. Inorg. Chem.* **2015**, *2015*, 5856.

(98) Escuer, A.; Mautner, F. A.; Peñalba, E.; Vicente, R. *Inorg. Chem.* **1998**, *37*, 4190.

(99) Bernhardt, P. V. *Inorg. Chem.* **2001**, *40*, 1086.

(100) Schneider, J. L.; Young, V. G.; Tolman, W. B. *Inorg. Chem.* **1996**, *35*, 5410.

(101) Kolks, G.; Lippard, S. J.; Waszczak, J. V. *J. Am. Chem. Soc.* **1980**, *102*, 4832.

(102) Patra, A. K.; Ray, M.; Mukherjee, R. *Polyhedron* **2000**, *19*, 1423.

(103) Sheldrick, G. *Acta. Crys. Sec. A* **2008**, *64*, 112.

(104) Gong, J.; Luque, R. *Chem. Soc.Rev.***2014**, *43*, 7466.

(105) Nocera, D. G. *Inorg. Chem.* **2009**, *48*, 10001.

(106) Shamsul, N. S.; Kamarudin, S. K.; Rahman, N. A. *Renew. Sustainable Energy Rev.* **2017**, *80*, 538.

(107) Rady, A. C.; Giddey, S.; Badwal, S. P. S.; Ladewig, B. P.; Bhattacharya, S. *Energy Fuels* **2012**, *26*, 1471.

(108) Han, B.; Yang, Y.; Xu, Y.; Etim, U. J.; Qiao, K.; Xu, B.; Yan, Z. *Chinese J. Catal.* **2016**, *37*, 1206.

(109) Khirsariya, P.; Mewada, R. K. *Procedia Eng.* **2013**, *51*, 409.

(110) Yoshizawa, K.; Wiley-VCH Verlag GmbH & Co. KGaA: 2008, p 317.

(111) Zakaria, Z.; Kamarudin, S. K. *Renew. Sustainable Energy Rev.* **2016**, *65*, 250.

(112) Tomkins, P.; Ranocchiari, M.; van Bokhoven, J. A. *Acc. Chem. Res.* **2017**, *50*, 418.

(113) Narsimhan, K.; Iyoki, K.; Dinh, K.; Román-Leshkov, Y. *ACS Cent. Sci.* **2016**, *2*, 424.

(114) Božović, A.; Feil, S.; Koyanagi, G. K.; Viggiano, A. A.; Zhang, X.; Schlangen, M.; Schwarz, H.; Bohme, D. K. *Chem. Eur. J.* **2010**, *16*, 11605.

(115) Hutchings, G. J. *Topics in Catalysis* **2016**, *59*, 658.

(116) Periana, R. A.; Mironov, O.; Taube, D.; Bhalla, G.; Jones, C. J. *Science* **2003**, *301*, 814.

(117) Periana, R. A.; Taube, D. J.; Gamble, S.; Taube, H.; Satoh, T.; Fujii, H. *Science* **1998**, *280*, 560.

(118) Lipscomb, J. D. *Annu. Rev. Microbiol.* **1994**, *48*, 371.

(119) Rosenzweig, A. C.; Nordlund, P.; Takahara, P. M.; Frederick, C. A.; Lippard, S. *J. Biol. Chem.* **1995**, *2*, 409.

(120) Tinberg, C. E.; Lippard, S. J. *Biochem.***2010**, *49*, 7902.

(121) Lieberman, R. L.; Kondapalli, K. C.; Shrestha, D. B.; Hakemian, A. S.; Smith, S. M.; Telser, J.; Kuzelka, J.; Gupta, R.; Borovik, A. S.; Lippard, S. J.; Hoffman, B. M.; Rosenzweig, A. C.; Stemmler, T. L. *Inorg. Chem.* **2006**, *45*, 8372.

(122) Rosenzweig, Amy C. *Biochem. Soc. Trans.* **2008**, *36*, 1134.

(123) Himes, R. A.; Karlin, K. D. *Curr. Opin. Chem. Biol.* **2009**, *13*, 119.

(124) Lieberman, R.; Rosenzweig, A. *Crit. Rev. Biochem. Mol. Biol.* **2004**, *39*, 147.

(125) Halvagar, M. R.; Neisen, B.; Tolman, W. B. *Inorg. Chem.* **2013**, *52*, 793.

(126) Kumar, P.; Gupta, R. *Dalton Trans.* **2016**, *45*, 18769.

(127) Sharghi, H.; Zare, A. *Synthesis* **2006**, *2006*, 999.

(128) Rao, V. M.; Sathyanarayana, D. N.; Manohar, H. *Dalton Trans.* **1983**, 2167.

(129) Agterberg, F. P. W.; Provó Kluit, H. A. J.; Driessen, W. L.; Oevering, H.; Buijs, W.; Lakin, M. T.; Spek, A. L.; Reedijk, J. *Inorg. Chem.* **1997**, *36*, 4321.

(130) Agterberg, F. P. W.; Provo Kluit, H. A. J.; Driessen, W. L.; Reedijk, J.; Oevering, H.; Buijs, W.; Veldman, N.; Lakin, M. T.; Spek, A. L. *Inorg. Chim. Acta.* **1998**, *267*.

(131) Hassanein, K.; Castillo, O.; Gómez-García, C. J.; Zamora, F.; Amo-Ochoa, P. *Cryst. Growth Des.* **2015**, *15*, 5485.

(132) Jenniefer, S. J.; Muthiah, P. T. *Chem. Cent. J.* **2013**, *7*, 35.

(133) Selvakumar, P. M.; Suresh, E.; Subramanian, P. S. *Inorg. Chim. Acta.* **2008**, *361*.

(134) Belle, C.; Beguin, C.; Gautier-Luneau, I.; Hamman, S.; Philouze, C.; Pierre, J. L.; Thomas, F.; Torelli, S.; Saint-Aman, E.; Bonin, M. *Inorg. Chem.* **2002**, *41*, 479.

(135) Chapman, W. H.; Breslow, R. *J. Am. Chem. Soc.* **1995**, *117*, 5462.

(136) Frey, S. T.; Murthy, N. N.; Weintraub, S. T.; Thompson, L. K.; Karlin, K. D. *Inorg. Chem.* **1997**, *36*, 956.

(137) Göbel, M. W. *Angew. Chem. Int. Ed.* **1994**, *33*, 1141.

(138) Kukushkin, V. Y.; Pombeiro, A. J. L. *Inorg. Chim. Acta.* **2005**, *358*, 1.

(139) Tsubouchi, A.; Bruice, T. C. *J. Am. Chem. Soc.* **1995**, *117*, 7399.

(140) Mitić, N.; Smith, S. J.; Neves, A.; Guddat, L. W.; Gahan, L. R.; Schenk, G. *Chem. Rev.* **2006**, *106*, 3338.

(141) Schenk, G.; Mitić, N.; Gahan, L. R.; Ollis, D. L.; McGeary, R. P.; Guddat, L. W. *Acc. Chem. Res.* **2012**, *45*, 1593.

(142) Solomon, E. I.; Heppner, D. E.; Johnston, E. M.; Ginsbach, J. W.; Cirera, J.; Qayyum, M.; Kieber-Emmons, M. T.; Kjaergaard, C. H.; Hadt, R. G.; Tian, L. *Chem. Rev.* **2014**, *114*, 3659.

(143) Allen, S. E.; Walvoord, R. R.; Padilla-Salinas, R.; Kozlowski, M. C. *Chem. Rev.* **2013**, *113*, 6234.

(144) Chen, P.; Solomon, E. I. *Proc. Natl. Acad. Sci. USA* **2004**, *101*, 13105.

(145) Cramer, C. J.; Tolman, W. B. *Acc. Chem. Res.* **2007**, *40*, 601.

(146) Abad, E.; Rommel, J. B.; Kästner, J. *J. Biol. Inorg. Chem.* **2014**, *289*, 13726.

(147) Garcia-Bosch, I.; Siegler, M. A. *Angew. Chem. Int. Ed.* **2016**, *55*, 12873.

(148) Liu, J. J.; Diaz, D. E.; Quist, D. A.; Karlin, K. D. *Isr. J. Chem.* **2016**, *56*, 738.

(149) Itoh, S. *Acc. Chem. Res.* **2015**, *48*, 2066.

(150) Lewis, E. A.; Tolman, W. B. *Chem. Rev.* **2004**, *104*, 1047.

(151) Itoh, S. *Curr. Opin. Chem. Biol.* **2006**, *10*, 115.

(152) Dhar, D.; Yee, G. M.; Markle, T. F.; Mayer, J. M.; Tolman, W. B. *Chem. Sci.* **2017**, *8*, 1075.

(153) Paria, S.; Ohta, T.; Morimoto, Y.; Ogura, T.; Sugimoto, H.; Fujieda, N.; Goto, K.; Asano, K.; Suzuki, T.; Itoh, S. *J. Am. Chem. Soc.* **2015**.

(154) Lane, A. C.; Barnes, C. L.; Antholine, W. E.; Wang, D.; Fiedler, A. T.; Walensky, J. R. *Inorg. Chem.* **2015**, *54*, 8509.

(155) Matsuda, Y.; Uchida, T.; Hori, H.; Kitagawa, T.; Arata, H. *Biochimica et Biophysica Acta (BBA) - Bioenergetics* **2004**, *1656*, 37.

(156) Nakano, M.; Fukuda, K.; Ito, S.; Matsui, H.; Nagami, T.; Takamuku, S.; Kitagawa, Y.; Champagne, B. *J. Phys. Chem. A* **2017**, *121*, 861.

(157) Finn, M. G.; Sharpless, K. B. *J. Am. Chem. Soc.* **1991**, *113*, 113.

(158) Lehnert, N.; Ho, R. Y. N.; Que, L.; Solomon, E. I. *J. Am. Chem. Soc.* **2001**, *123*, 8271.

(159) Hatcher, L. Q.; Lee, D.-H.; Vance, M. A.; Milligan, A. E.; Sarangi, R.; Hodgson, K. O.; Hedman, B.; Solomon, E. I.; Karlin, K. D. *Inorg. Chem.* **2006**, *45*, 10055.

(160) Aboelella, N. W.; York, J. T.; Reynolds, A. M.; Fujita, K.; Kinsinger, C. R.; Cramer, C. J.; Riordan, C. G.; Tolman, W. B. *Chem. Commun.* **2004**, 1716.

(161) Cramer, C. J.; Truhlar, D. G. *Phys. Chem. Chem. Phys.* **2009**, *11*, 10757.

(162) Neese, F. *Coord. Chem. Rev.* **2009**, *253*, 526.

(163) Mayer, J. M. *Acc. Chem. Res.* **2011**, *44*, 36.

(164) Hodgkiss, J. M.; Rosenthal, J.; Nocera, D. G. In *Hydrogen-Transfer Reactions*; Wiley-VCH Verlag GmbH & Co. KGaA: 2007, p 503.

(165) Kütt, A.; Leito, I.; Kaljurand, I.; Sooväli, L.; Vlasov, V. M.; Yagupolskii, L. M.; Koppel, I. A. *J. Org. Chem.* **2006**, *71*, 2829.

(166) Hemsworth, G. R.; Johnston, E. M.; Davies, G. J.; Walton, P. H. *Trends Biotechnol.* **2015**, *33*, 747.

(167) Wasilke, J.-C.; Wu, G.; Bu, X.; Kehr, G.; Erker, G. *Organometallics* **2005**, *24*, 4289.

(168) Le Bras, J.; Jiao, H.; Meyer, W. E.; Hampel, F.; Gladysz, J. A. *J. Organomet. Chem.* **2000**, *616*, 54.

(169) Seim, K. L.; Obermeyer, A. C.; Francis, M. B. *J. Am. Chem. Soc.* **2011**, *133*, 16970.

(170) Mader, E. A.; Davidson, E. R.; Mayer, J. M. *J. Am. Chem Soc.* **2007**, *129*, 5153.

(171) Stoll, S.; Schweiger, A. *J. Magn. Reson.* **2006**, *178*, 42.

(172) Noviandri, I.; Brown, K. N.; Fleming, D. S.; Gulyas, P. T.; Lay, P. A.; Masters, A. F.; Phillips, L. *J. Chem. Phys. B.* **1999**, *103*, 6713.

(173) Neese, F. *Wiley Interdisciplinary Reviews: Computational Molecular Science* **2012**, *2*, 73.

(174) Perdew, J. P.; Wang, Y. *Phys. Rev. B.* **1992**, *45*, 13244.

(175) Adamo, C.; Barone, V. *J. Chem. Phys.* **1998**, *108*, 664.

(176) Neese, F. *J. Comput. Chem.* **2003**, *24*, 1740.

(177) Spaeth, A. D.; Gagnon, N. L.; Dhar, D.; Yee, G. M.; Tolman, W. B. *J. Am. Chem. Soc.* **2017**, *139*, 4477.

(178) Becke, A. D. *J. Chem. Phys.* **1986**, *84*, 4524.

(179) Perdew, J. P. *Phys. Rev. B.* **1986**, *33*, 8822.

(180) Partridge, H. *J. Chem. Phys.* **1987**, *87*, 6643.

(181) Partridge, H. *J. Chem. Phys.* **1989**, *90*, 1043.

(182) Zhao, Y.; Truhlar, D. G. *J. Phys. Chem. A.* **2005**, *109*, 5656.

(183) Handy, N. C.; Cohen, A. J. *Mol. Phys.* **2001**, *99*, 403.

(184) Tao, J.; Perdew, J. P.; Staroverov, V. N.; Scuseria, G. E. *Phys. Rev. Lett.* **2003**, *91*, 146401.

(185) Zhao, Y.; Truhlar, D. G. *J. Chem. Phys.* **2006**, *125*, 194101.

(186) Ekström, U.; Visscher, L.; Bast, R.; Thorvaldsen, A. J.; Ruud, K. *J. Chem. Theory Comput.* **2010**, *6*, 1971.

(187) Lee, C.; Yang, W.; Parr, R. G. *Phys. Rev. B.* **1988**, *37*, 785.

(188) Adamo, C.; Barone, V. *J. Chem. Phys.* **1999**, *110*, 6158.

(189) Staroverov, V. N.; Scuseria, G. E.; Tao, J.; Perdew, J. P. *J. Chem. Phys.* **2003**, *119*, 12129.

(190) Zhao, Y.; Truhlar, D. G. *Theor. Chem. Acc.* **2008**, *120*, 215.

(191) Izsák, R.; Neese, F. *J. Chem. Phys.* **2011**, *135*, 144105.

(192) Goerigk, L.; Grimme, S. *J. Chem. Theory Comput.* **2011**, *7*, 3272.

(193) Noodleman, L. *J. Chem. Phys.* **1981**, *74*, 5737.

(194) Pantazis, D. A.; Chen, X.-Y.; Landis, C. R.; Neese, F. *J. Chem. Theory Comput.* **2008**, *4*, 908.

(195) Portmann, S.; Lüthi, H. P. *CHIMIA International Journal for Chemistry* **2000**, *54*, 766.

(196) Hanwell, M. D.; Curtis, D. E.; Lonie, D. C.; Vandermeersch, T.; Zurek, E.; Hutchison, G. R. *J. Cheminform.* **2012**, *4*, 17.

(197) Allouche, A.-R. *J. Comput. Chem.* **2011**, *32*, 174.

(198) Borovik, A. S. *Acc. Chem. Res.* **2005**, *38*, 54.

(199) Nagaraju, P.; Ohta, T.; Liu, J.-G.; Ogura, T.; Naruta, Y. *Chem. Comm.***2016**, *52*, 7213.

(200) Chmielewski, M.; Jurczak, J. *Tetrahedron Lett.* **2004**, *45*, 6007.

(201) Chmielewski, M. J.; Jurczak, J. *Chem. Eur. J.* **2005**, *11*, 6080.

(202) Vance, C. K.; Miller, A.-F. *Biochem.* **2001**, *40*, 13079.

(203) Donoghue, P. J.; Gupta, A. K.; Boyce, D. W.; Cramer, C. J.; Tolman, W. B. *J. Am. Chem. Soc.* **2010**, *132*, 15869.

(204) Neisen, B. D.; Gagnon, N. L.; Dhar, D.; Spaeth, A. D.; Tolman, W. B. *J. Am. Chem. Soc.* **2017**.

(205) Westerheide, L.; Pascaly, M.; Krebs, B. *Curr. Opin. Chem. Biol.* **2000**, *4*, 235.

(206) Visvaganesan, K.; Suresh, E.; Palaniandavar, M. *Dalton Trans.* **2009**, 3814.

(207) Hetterscheid, D. G. H.; Chikkali, S. H.; de Bruin, B.; Reek, J. N. H. *ChemCatChem.* **2013**, *5*, 2785.

(208) Radlauer, M. R.; Day, M. W.; Agapie, T. *J. Am. Chem. Soc.* **2012**, *134*, 1478.

(209) Koike, T.; Inoue, M.; Kimura, E.; Shiro, M. *J. Am. Chem. Soc.* **1996**, *118*, 3091.